



# Modelling Parkinson's Disease Using Human iPSC-derived Neurons

Roy Masius



# **Modelling Parkinson's Disease Using Human iPSC-derived Neurons**

**Roy Geordi Masius**

The research described in this thesis was performed at the Department of Clinical Genetics, Erasmus MC, Rotterdam, the Netherlands, and was financially supported by:  
Dorpmans-Wigmans stichting  
Erasmus MC MRace  
European Union's Horizon 2020  
JPND, the EU Joint Programme - Neurodegenerative Disease Research  
Memorabel, ZonMw, Dutch organisation for healthcare research and innovation  
NWO, Netherlands Organisation for Scientific Research  
Stichting ParkinsonFonds

Printing of this thesis was financially supported by Stichting ParkinsonFonds.



ISBN: 978-94-6375-163-6

Cover design: Roy Masius

Layout: Wesley Masius and Roy Masius

Printing: Ridderprint BV

Copyright © Roy Masius 2018

No part of this thesis may be reproduced, stored in a retrieval system or transmitted in any form or by any means, electronic, mechanical, photocopying, translating, recording or otherwise, without written permission of the author. Some chapters of this thesis are based on published or submitted papers, and were reproduced with permission of the coauthors. Copyright of these papers is held by the publisher.



# Modelling Parkinson's Disease Using Human iPSC-derived Neurons

De ziekte van Parkinson modelleren middels  
humane iPSC afstammende neuronen

## Proefschrift

ter verkrijging van de graad van doctor aan de  
Erasmus Universiteit Rotterdam  
op gezag van de rector magnificus

Prof. dr. R.C.M.E. Engels

en volgens besluit van het College voor Promoties.

De openbare verdediging zal plaatsvinden op  
woensdag 24 oktober 2018 om 13.30 uur

door

**Roy Geordi Masius**

geboren te Vlissingen

**Promotiecomissie**

**Promotor:** Prof. dr. V. Bonifati

**Overige leden:** Prof. dr. R.J. Pasterkamp  
Prof. dr. J.C. Schwaborn  
Prof. dr. R. Willemsen

**Co-promotor:** Dr. W.J. Mandemakers

# Table of contents

<b>List of abbreviations</b>	6
<b>Chapter 1</b>	9
Modelling Parkinson's disease with induced pluripotent stem Cells: overview of available protocols and developments	
<b>Chapter 2</b>	37
The SAC1 domain in Synaptojanin is required for autophagosome maturation at presynaptic terminals	
<b>Chapter 3</b>	87
Analysis of <i>PARK20</i> patient iPSC-derived dopaminergic neurons implies a role for Synaptojanin-1 in neurodevelopment and mitochondrial function	
<b>Chapter 4</b>	113
<i>LRP10</i> genetic variants in familial Parkinson's disease and dementia with Lewy bodies: a genome-wide linkage and sequencing study	
<b>Chapter 5</b>	163
General discussion	
<b>Appendix</b>	177
Summary	178
Samenvatting	180
List of publications	183
Curriculum Vitae	184
PhD portfolio	186
Dankwoord	188

# List of abbreviations

AA	Ascorbic acid
BDNF	Brain derived neurotrophic factor
cAMP	Cyclic adenosine monophosphate
CCCP	Carbonyl cyanide m-chlorophenyl hydrazone
CHIR	CHIR99021
CLEM	Correlative light and electron microscopy
CPX	Complexin
CRE	Clinical Relevant Exons
CTCF	Corrected total cell fluorescence
DA	Dopaminergic
DAn	Dopaminergic neuron
DAT	Dopamine Active Transporter
DIV	Days in vitro
DLB	Dementia with Lewy Bodies
DMSO	Dimethylsulfoxide
DNA	Deoxyribonucleic acid
EB	Embryoid body
EJP	Excitatory junctional potentials
EM	Electron microscopy
EMCCD	Electron-multiplying charge-coupled device
ER	Endoplasmic Reticulum
ERG	Electroretinogram
ESP	Exome Sequencing Project
ExAC	Exome Aggregation Consortium
FACS	Fluorescence-activated cell sorting
FGF-8	Fibroblast growth factor 8
FRAP	Fluorescence recovery after photobleaching
GDNF	Glial derived neurotrophic factor
GoNL	Genome of the Netherlands
GPI	Globus pallidus pars interna
GTM	Medial temporal gyrus
hESC	Human embryonic stem cell
HKG	House-keeping genes
HRM	High-resolution melting
IP	Immunoprecipitation
iPSC	Induced pluripotent stem cell
LB	Lewy Body
LDS	Lithium dodecyl sulfate
LUT	Lookup table

MAF	Minor allele frequency
MAP2	Microtubule-associated protein 2
M-CAP	Mendelian Clinically Applicable Pathogenicity
mDAN	Midbrain dopaminergic neurons
MEF	Mouse Embryo Fibroblast
mEJC	Miniature excitatory junctional currents
MLPA	Multiple ligation probe amplification assay
MPTP	1-Methyl-4-phenyl-1,2,3,6-tetrahydropyridine
MSD	Mean square displacement
NIRB	Near-infrared branding
NMJ	Neuromuscular junction
NPC	Neural progenitor cell
PD	Parkinson's disease
PDD	Parkinson's disease dementia
PDL	Poly-D-lysine
PI	Phosphatidylinositol
PMA	Purmorphamine
PtdInsP	Phosphoinositide phosphate
PTP	Protein tyrosine phosphatase
qPCR	Real-time quantitative PCR
RIPA	RadioImmunoPrecipitation Assay
RNA	Ribonucleic Acid
ROS	Reactive Oxygen Species
SAG	Smoothened agonist
SD	Standard deviation
SDS	Sodium Dodecyl Sulphate
SEM	Standard error of the mean
smNPC	Small-molecule neural progenitor cell
SN	Substantia nigra
SNc	Substantia nigra pars compacta
SNP	Single nucleotide polymorphism
sptPALM	Single-particle tracking photoactivation localization
STN	Subthalamic nucleus
TEM	Transmission electron microscopy
TEVC	Two-electrode voltage clamp
TGF-B3	Transforming growth factor B3
TH	Tyrosine hydroxylase
TIRF	Total internal reflection microscopy
TUJ1	$\beta$ III-tubulin
WES	whole exome sequencing
WM	Wortmannin
YM	YM201636
$\alpha$ -syn	$\alpha$ -synuclein



Chapter 1

# Modelling Parkinson's disease with induced pluripotent stem cells: overview of available protocols and developments

**Roy Masius**, Bella Banjanin, Vincenzo Bonifati, Wim Mandemakers

Manuscript in preparation

# Summary

Parkinson's disease (PD) is a common neurodegenerative disease characterized mainly by the degeneration of dopaminergic (DA) neurons resulting in motor symptoms. The underlying molecular mechanisms of PD have remained elusive due to the lack of availability of a representative model for the affected human midbrain dopaminergic neurons. However, the recent technological advancement of induced pluripotent stem cells (iPSC) generation opened new avenues to generate human midbrain DA neurons from PD patients and unaffected individuals by directed differentiation of iPSC. This offers an unprecedented platform to model PD in patient derived cells with the focus on the underlying mechanism of PD. In this review we briefly discuss the available PD models and highlight how iPSC have brought a new dimension to fundamental research. We will focus on the various established genetic iPSC PD models, and compare the various established neuronal differentiation protocols. Despite the hurdles in cultivating iPSC, they offer great promise for translation into therapeutic applications.



# Introduction

Parkinson's disease (PD) is the second most common progressive neurodegenerative disorder, affecting an estimated 1 to 2 in every 1000 individuals at any time, and 1% of the population above 60 years (1). Patients with PD suffer from numerous motor symptoms, such as bradykinesia, resting tremor, rigidity, and postural instability. The symptoms become more pronounced as the disease progresses and eventually become a source of disability (2). In addition to motor problems, PD patients often experience fatigue, sleep disturbances, depression, and anxiety (3). Pathologic investigation of PD patient brains shows a characteristic loss of neuromelanin-containing monoamine neurons, particularly midbrain A9 dopamine (DA) neurons in the substantia nigra pars compacta (SNc) as a hallmark of the disease. The loss of these specific neurons leads to reduced nigrostriatal dopamine levels causing many of the motor symptoms (4). At the onset of motor symptoms, putamenal dopamine is depleted ~80% and ~60% of the SNc DA neurons have been lost (5). However, progressively, many other neuronal cell populations are also affected and account for the presence of non-motor symptoms. A second hallmark of PD is the accumulation of Lewy bodies (LB), cytoplasmic inclusions of protein aggregates mainly composed of abnormally folded  $\alpha$ -synuclein (6). These two hallmarks are used as criteria for definite diagnosis of PD at post-mortem pathological examination.

Currently, the main method of therapy is based on managing symptoms where the focus lies on improving the quality of life of the patients and can be achieved in two ways. Firstly, the most conventional treatment is based on medication to increase the dopamine levels in the brain to adjust for the loss of the dopamine secreting neurons. The most common medication is Levodopa, a natural chemical that passes the blood-brain barrier (BBB), and is converted to dopamine (7). In addition, other dopaminergic agents are used to repress symptoms, including dopamine agonists and dopamine release stimulators (7, 8). However, these drugs are prone to side effects and, over time, the benefits of these drugs frequently diminish or become less consistent (9). The second method of therapy is called Deep Brain Stimulation (DBS), a non-drug based treatment that uses implanted electrodes to suppress neuronal activity of the subthalamic nucleus (STN) or globus pallidus pars interna (GPi), resulting in increased motor signalling (10). Although these treatments may provide temporary benefit to suppress Parkinson's symptoms, they do not keep Parkinson's disease from progressing.

# Obstacles for disease modifying therapies

## The origin of Parkinson's Disease

The problem in finding a therapy to halt neuron degeneration in PD, or to replenish lost neurons, lies in the incomplete understanding of the underlying disease causing mechanism in affected cells in PD patients. The difficulty lies in part in the origin of PD. The vast majority of patients are considered to be sporadic in origin, meaning that no clear cause can be appointed. Most likely the origins of these cases lie in a combination of environmental and genetic factors (11). There have been implications that agricultural exposure to herbicides and pesticides could also cause PD, but these have never been substantiated (12). In addition to the sporadic PD cases, there are approximately 10% of PD patients that are considered to be familial cases, with a heritable disease causing genetic mutation. Interestingly, sporadic and familial forms of PD are phenotypically similar (13). This raises the question, whether the two forms of PD share common pathways fundamental for the pathophysiology of PD.

The genetic investigation of these familial cases has led to the discovery of many genes and loci involved in PD and Parkinsonism, which have been reviewed extensively previously (14). However, most recently, a novel disease causing genetic variant has been found in the *LRP10* gene, found in familial PD, PD dementia (PDD), and dementia with Lewy bodies (DLB) (15). Quadri et al. describe nine rare *LRP10* variants, and show that the mutations are influencing protein expression, stability and/or function (15). This work shows that LRP10 is shared disease causing gene between the Lewy body diseases, that are characterized by widespread cortical and subcortical  $\alpha$ -synuclein / Lewy body plus  $\beta$ -amyloid and tau pathologies, and puts forward LRP10 as an important novel therapeutic target, not only for PD, but Lewy Body diseases in general. In conclusion, taking careful consideration of the full complexity of PD and associated disorders, investigation of genetic causes of PD might bring us another step closer to understanding the disease.

## Available models – Toxin based PD models

To better understand the etiology of PD, various approaches have been used to model

the disease. Great progress has been made with animal models based on toxins and the genes involved in PD. Toxin based models represent the first experimental PD models; these aim to reproduce the pathological and behavioural changes of the human disease in rodents or primates by using neurotoxins. The major toxins used that induce the selective degeneration of nigrostriatal neurons are 1-Methyl-4-phenyl-1,2,3,6-tetrahydropyridine (MPTP), Oxidopamine, Rotenone, and Paraquat (16) (Table 1). Each of these is able to replicate DA neuron degeneration in the SNc and MPTP and Oxidopamin show striatal DA reduction in animal models (17-22). The effect of MPTP in humans is also described, as the effect of MPTP was first discovered in users that developed PD like motor features after using MPTP contaminated heroin (23). MPTP treatment is the most tested and was originally used in high doses to induce acute models (24). Recent advancements in administration protocols have obtained also more progressive models, which mimic better the course of the disease in PD patients (22, 25, 26). Furthermore, primates treated with MPTP develop motor symptoms and respond well to L-DOPA therapy and even develop dyskinesias after long term therapy (27). Lastly the MPTP and the Paraquat models develop  $\alpha$ -synuclein aggregations, however these are dissimilar to LBs (28, 29). In contrast, models with herbicide Rotenone are able to reproduce LB pathology (30). Together, these toxin based models have been indispensable for the development of the symptomatic treatments (31). Further examination of the downstream molecular effects of these toxic substances causing PD-like pathology has pointed towards Reactive Oxygen Species (ROS) and mitochondrial dysfunction as possible disease mechanisms (32).

## Available models – Genetic based PD models

Genetic animal PD models were created following the discovery of disease causing genes and the development of new genetic tools, enabling gene deletion, over-expression, and mutation in vivo (33). Strikingly, most of these genetic models have failed to demonstrate significant loss of DA neurons, the main pathological hallmark of PD (34-37) (Table 2). Nevertheless, these models have been instrumental for further elucidation of the possible disease mechanisms. Especially, the  $\alpha$ -synuclein genetic models have given insight into the  $\alpha$ -synuclein misfolding, aggregation and even determined a possible prion-like propagation (38-41). Unresolved questions remain whether the progressive accumulation of  $\alpha$ -synuclein aggregates contributes to neuronal cell loss in PD and which cellular mechanisms would mediate this process (42, 43).

**Table 1. Most widely used and successful toxin based PD models**

Toxin	Organism	Pathologic Phenotype	Behavioral Phenotype	Lewy Body Pathology	Method	Limitations	Reference
6-OHDA	Primates Cats Dogs Rats	DAn degeneration ROS Oxidative stress	Behavior deficits Slower locomotion Akinesia L-DOPA Responding	no	Injection	No effect on olfactory bulbs, lower brainstem, or locus coeruleus.	(16, 19, 31, 32)
MPTP	Primates DAT+ Mice	DAn degeneration Striatal DA reduction Oxidative stress ROS Inflammation	Rigidity Tremor Slower locomotion Altered behavior L-DOPA Responding	no	High dose acute model, Crosses blood brain barrier	Mice do not develop the same impairment. Does not work on rats.	(16, 18, 22, 24-26, 28, 31, 32)
Rotenone	Rats	DAn degeneration Striatal DA reduction	Slower locomotion Bradykinesia Rigidity L-DOPA Responding	$\alpha$ -synuclein positive inclusions	Crosses blood brain barrier	Mice and monkey, not succesful.	(16, 17, 30-32)
Paraquat	Mice	DAn degeneration	Slower locomotion Bradykinesia Rigidity L-DOPA Responding	Increased expression and aggregation of $\alpha$ -synuclein		Variable Needs amino acid transporter.	(16, 20, 21, 29, 31, 32)

MPTP=1-methyl-4-fenyl-1,2,3,6-tetrahydropyridine, DAT=Dopamine Transporter, DA=Dopamine, DAn=Dopaminergic neuron, ROS=Reactive Oxygen Species.

Genetic models have also shown that many of the identified PD genes seem to converge towards several specific pathological pathways, indicating multiple possible disease mechanisms. Firstly, the PD causing genes *SNCA*, *LRRK2*, *DNAJC6*, and *SYNJ1* have been shown to be involved in regulating synaptic function and dopamine neurotransmission (44, 45). Secondly, PD associated mutations in *SNCA*, *Parkin*, *PINK1*, *FBXO7*, *DJ-1*, and *CHCHD2* have been shown to affect mitochondrial function and mitophagy (45-47). Third, *LRRK2*, *VPS35*, *DNAJC13*, *ATP13A2*, *SYNJ1* and *GBA* converge on the lysosome-autophagy pathway (44, 45, 48). Fourth *LRRK2*, *VPS35*, and *DNAJC13* also function in protein and membrane trafficking (45). Lastly, *Parkin* and *FBXO7* are thought to play a role in the ubiquitin-proteasome system (45, 49). In spite of this compelling evidence for the presence of converging pathological pathways, they still need to be linked to the neuronal degeneration. So far none of these models have shown convincing evidence for this PD pathological hall mark. Additionally, discrepancies between species make it difficult to accurately extrapolate animal experimental data to PD in humans (50). Therefore, in addition to the currently available genetic models, a human derived model of PD neurons might allow investigation of the underlying molecular mechanisms and how PD causing genetic mutations lead to neuronal death.

# Generation of novel PD models

Recent advancements in the field of stem cell research have opened up new possibilities for modelling of difficult to obtain cell types in humans. Initially, human embryonic stem cells and neural stem cells were coaxed to differentiate into DA neurons as early steps in cell replacement strategies for PD (51-53). Different routes of differentiation ranged from overexpression of transcription factors (51-53), to co-culture with stromal cells (54), and growth factor manipulation (55, 56).

## Induced pluripotent stem cells

A major breakthrough was the discovery that adult cells can be reversed in development to a pluripotent state by over-expressing a handful of transcription factors (57). This new source of induced pluripotent stem cells (iPSC) is readily available and allows for vast new possibilities for disease modelling in human cells. For instance, iPSCs generated from familial PD patients carrying a genetic mutation can be differentiated into DA neurons, which then allows not only for in vitro analysis of the resulting mature human DA neurons, but of the entire neuro-developmental process.

The current and most common methods for human iPSC generation use non-integrating reprogramming technologies, such as episomes, synthetic mRNAs or Sendai virus (95-97). Another recently established tool, the CRISPRCas9 system, combined with piggyback technology allows for relatively easy, footprint-free, targeted genome editing (98-100). This mutagenesis tool is perfect for the correcting or introducing the mutation in patient or control iPSCs. Together these advancements have paved the way for a new generation of in vitro human midbrain DA neuron PD models (Table 3), aimed at understanding the disease and halting or curing the neurodegeneration.

**Table 2. Mouse models of PD based on familial PD gene mutations**

Gene	Gene product	Animal model	Dopaminergic cell death	Protein accumulation/aggregation	Motor phenotype	Dopamine metabolism/homeostasis alterations	Oxidative stress/altered mitochondria	Ref
<b>SNCA</b>	SNCA A30P $\alpha$ -synuclein	Transgenic knock-in	Not reported	Not reported	$\downarrow$ motor coordination; $\downarrow$ stride length, catalepsy	$\downarrow$ striatal DA and metabolite	Not reported	(58)
	SNCA A53T $\alpha$ -synuclein	Tet-off inducible	Loss of DA and motor neurons but no change in striatal DA	$\alpha$ -syn accumulation in several brain regions including SN	$\downarrow$ Spontaneous locomotor activity progressing to paralysis and death	Not reported	Not reported	(59, 60)
	SNCA wildtype $\alpha$ -synuclein	Transgenic	SN inclusions but no death; $\downarrow$ neurogenesis in adult hippocampus	Widespread $\alpha$ -syn + ubiquitin inclusions; $\downarrow$ S129 phospho- $\alpha$ -syn; $\downarrow$ autophagic vacuoles and enlarged lysosomes; $\downarrow$ Astroglial $\alpha$ -syn inclusion	Motor coordination impaired	$\downarrow$ Striatal TH nerve terminals; $\downarrow$ striatal TH levels and enzymatic activity	Not reported	(61-65)
	SNCA Y39C mutant $\alpha$ -synuclein	Transgenic	No	Widespread LB-like $\alpha$ -syn- and ubiquitin+ inclusions including SN, $\downarrow$ S129 phospho- $\alpha$ -syn	$\downarrow$ Coordination learning memory impairment	No, but, pathology and cognitive decline suggest diffuse LB disease	Not reported	(66)
	SNCA truncated 1-119 $\alpha$ -synuclein	Transgenic	No	No SN $\alpha$ -syn inclusions observed	Unknown	$\downarrow$ Striatal DA and metabolite levels	Not reported	(67)
	SNCA truncated 1-120 $\alpha$ -synuclein	Knockout/transgenic	No cell loss despite pathological changes	$\alpha$ -syn inclusions in SN and olfactory bulb	Progressive $\downarrow$ motor activity	$\downarrow$ Striatal DA and metabolite levels	Microgliosis	(68)
	SNCA truncated 1-130 $\alpha$ -synuclein	Transgenic	Congenital .SN neuron number	LB-like $\alpha$ -syn inclusions	$\downarrow$ Spontaneous locomotor activity (L-DOPA responsive)	$\downarrow$ Striatal DA and metabolites, impaired striatal axon terminals	No signs of gliosis; mitochondrial dysfunction unknown	(69)
	$\alpha$ -synuclein-eGFP fusion protein	Transgenic	Not reported but lysosomal pathology was observed in frontal cortex and hippocampus	Prominent $\alpha$ -syn aggregates in neurons of neocortex and hippocampus	Not reported	Not reported	Not reported	(70)
	DJ-1 knockout	Knockout	No	$\downarrow$ autophagic activity may prevent protein accumulation	Progressively $\downarrow$ locomotion and grip strength; Gait impairment	$\downarrow$ DA reuptake $\downarrow$ striatal DA	Dysfunctional skeletal muscle mitochondria may explain motor deficit; $\uparrow$ ROS	(72-75)
	VPS35 knockout	Knockout	$\downarrow$ DA neurons	Accumulation of endocytic proteins	$\downarrow$ performance in open field test	Not reported	Not reported	(76)
<b>VPS35</b>	VPS35 D620N	Knock-in	No	Accumulation of endocytic proteins	No	$\downarrow$ Evoked striatal DA release	$\downarrow$ Mitochondrial fusion	(77)

**Table 2. (continued)**

Gene	Gene product	Animal model	Dopaminergic cell death	Protein accumulation / aggregation	Motor phenotype	Dopamine metabolism / homeostasis alterations	Oxidative stress/ altered mitochondria	Ref
<b>LRRK2</b>	LRRK2 knockout	Knockout	No loss of TH+ SN neurons but apoptotic cell death in kidneys	Extensive $\alpha$ -syn and ubiquitin aggregates in kidneys with autophagy lysosome dysfunction	Not reported	No change in striatal DA	Not reported	(78)
	LRRK2 R1441C	Knock-in	No	No	No	DA D2 receptor-mediated impairments, $\downarrow$ DA neurotransmission	Not reported	(79)
	LRRK2 wildtype	BAC transgenic	No	No	Hyperactive; $\uparrow$ motor function	$\uparrow$ Striatal DA release	Not reported	(80)
	LRRK2 R1441G	BAC transgenic	Loss of TH+dendrites in SN and $\downarrow$ SN neuron size	$\uparrow$ Phospho-tau, axonal pathology in nigrostriatal pathway	Progressive $\downarrow$ locomotor activity (L-DOPA responsive)	$\downarrow$ DA release and uptake	Not reported	(81, 82)
	LRRK2 G2019S	BAC transgenic	No neuron death; $\downarrow$ neurogenesis	No	No	Progressive $\downarrow$ striatal DA, DA release and uptake	Altered distribution Abnormal morphology	(80, 83, 84)
<b>PRKN</b>	Parkin knockout	Knockout	Loss of TH+ catecholaminergic neurons in locus coeruleus; $\downarrow$ TH+ SN neurons in geriatric mice; $\downarrow$ Neurogenesis	$\uparrow$ p53 mRNA and protein levels; $\uparrow$ tau levels in geriatric mice but no inclusion formation	$\downarrow$ Coordination; $\downarrow$ Startle response	$\uparrow$ Striatal DA; $\downarrow$ striatal synaptic excitability; $\uparrow$ midbrain DA levels; $\uparrow$ striatal DA receptor binding; $\downarrow$ noradrenaline; $\downarrow$ striatal DAT and VMAT	Mitochondrial dysfunction; $\uparrow$ protein and lipid peroxidation; $\downarrow$ mitochondria complex I activity; $\uparrow$ abnormal glial mitochondria; $\uparrow$ GSH may compensate for oxidant stress	(85-90)
	Parkin truncated mutant Q311X	BAC transgenic	Age-dependent DA neuron degeneration in SN	Accumulation of proteinase K resistant $\alpha$ -syn in SN	$\downarrow$ Motor activity	$\downarrow$ Striatal DA and metabolite levels; loss of striatal DA nerve terminals	3-Nitrotyrosine associated with accumulated $\alpha$ -syn	(91)
<b>PINK1</b>	PINK1 knockout	Knockout	No	Not reported	Progressive weight loss accompanied by $\downarrow$ locomotion	$\downarrow$ Striatal DA release, impaired corticostriatal plasticity rescued by LDOPA; progressive $\downarrow$ striatal DA	Mitochondrial and respiratory deficits; enlarged mitochondria; age-dependent impairment of mitochondrial respiration	(92, 93)
<b>SYNJ1</b>	SYNJ1 R258Q	Knock-in	No	Accumulation of endocytic proteins	$\downarrow$ Coordination; $\uparrow$ Seizures	Not reported	Not reported	(94)

DA=Dopamine,  $\alpha$ -syn= $\alpha$ -synuclein, SN=Substantia nigra, TH=Tyrosine Hydroxylase, LB=Lewy Body, SDS=Sodium Dodecyl Sulphate, ROS=Reactive Oxygen Species.

## Dopaminergic neuron differentiation

Numerous protocols for differentiation of midbrain DA neurons from stem cells have been described over the last decade. Currently the most efficient way of generating midbrain DA neurons from stem cells is via the use of dual SMAD inhibitors at the beginning of the differentiation protocol to ensure Floor Plate induction (101), followed by or combined with inhibition of GSK3 $\beta$  to activate WNT/ $\beta$ -catenin signalling (102, 103). These principles were first implemented by the Studer group, producing 80% FOXA2+ cells and 75% TH+ cells, respectively indicating floor plate and dopaminergic cell lineage (104). The resulting cells exhibited biochemical and electrophysiological properties of mature midbrain DA neurons. Furthermore, long-term engraftment in oxidopamine treated mice and rats demonstrated robust survival of midbrain DA neurons and induced recovery of motor function. Other groups have developed comparable protocols based on the same principles, using variations in timing and types of SMAD inhibitors (105-108). Some DA neuron differentiation protocols have been developed to generate a three dimensional structure consisting of multiple cell types, but enriched for the presence of DA neurons, termed midbrain organoids (109, 110).

## iPSC models

### SNCA

Based on its central role in PD,  $\alpha$ -synuclein has been one of the main candidates for iPSC based modelling for PD. Models for triplication of *SNCA* showed multiple phenotypes (Table 3), starting with the double amount of  $\alpha$ -synuclein protein in generated midbrain dopamine neurons, is an important finding linking the model to  $\alpha$ -synuclein aggregations found in LBs in patients (111). This accumulation was also observed in combination with an increased sensitivity to oxidative stress, in a similar model (112). Later, Flierl and Oliveira et al. reported an impaired neuronal differentiation and maturation as a consequence of the triplication in their iPSC model (113, 114) and recently transcriptomic analysis revealed an ER stress phenotype in neurons derived from patient iPSCs (115). An effect of  $\alpha$ -synuclein on the ER was already described in yeast and in *Drosophila*, supporting the ER stress phenotype, however, it was not yet observed in animal or human models (116, 117). An *SNCA* p.A53T mutation model has been set up for multiple patient lines, including corrected isogenic controls using either CRISPR-Cas9 or Zinc



Finger Nuclease editing. One of these models has been differentiated to DA neurons, where a difference in oxidative stress response was observed in inhibition of myocyte enhancer factor 2C, which is normally required for peroxisome proliferator-activated receptor- $\gamma$  coactivator-1 $\alpha$  transcription (PGC-1 $\alpha$ ) (118). Disruption of this pathway would contribute to mitochondrial dysfunction PGC-1 $\alpha$  acts as an inducer of mitochondrial biogenesis. Furthermore, increased ROS, decreased mitochondrial membrane potential, and altered mitochondrial morphology is observed in the iPSC-derived neurons with a *SNCA* triplication, the latter two are also seen in the p.A53T model (114, 119). These mitochondrial defects are in line with, and grant insight into, the mitochondrial degeneration found in *SNCA* p.A53T transgenic mice (60). A second p.A53T model focuses on the  $\alpha$ -synuclein structure in neural precursor cells and neurons; p.A53T and p.E46K *SNCA* mutations shift native helically folded tetrameric to monomeric  $\alpha$ -synuclein (120). Further decrease of the tetramer to monomer ratio pairs with decreased  $\alpha$ -synuclein solubility and induces neurotoxicity and accumulation of  $\alpha$ -synuclein in round cytoplasmic inclusions, these inclusions may be the origin of the LBs seen in PD patients (120).

## LRRK2

Mutations in the *LRRK2* gene are the most common cause of autosomal dominant familial PD and various patient derived iPSCs have been generated (Table 3). In particular the *LRRK2* p.G2019S mutation has been modelled in numerous studies. Differentiation of the *LRRK2* p.G2019S iPSCs into DA neurons resulted in phenotypes including an increased sensitivity to oxidative stress, and  $\alpha$ -synuclein accumulation as seen in the *SNCA* models (121-124). Another study used *LRRK2* p.G2019S-iPSC-derived DA neurons to show an increase in mitochondrial DNA damage that was not present after zinc finger nuclease-mediated correction of the mutation (125). Moreover, a role of *LRRK2* in mitochondrial physiology was further supported as delayed mitophagy, increased mitochondrial fission and mitochondrial mobility were observed in DA neurons from p.G2019S-iPSCs (121, 126-128). In p.G2019S knock-in mice, mitochondria were also found to be affected; however, mitochondria appeared as "beads-on-a-string" in mice, standing in direct contrast to the finding of increased mitochondrial fission (83). This disparity requires further clarification of the effect of *LRRK2* on mitochondrial fission mechanisms. Further, *LRRK2* p.G2019S-iPSC-derived DA neurons had increased sensitivity to proteasomal stress induced apoptosis (129). In addition, impaired autophagic clearance and morphological alterations (including reduced number, length and branching of neurites) can be seen in these human DA neurons (122, 128, 130-133).

Table 3. Overview of phenotypes observed in iPSC derived models with PD patient mutations

Gene	Mutation	General Phenotype	Mitochondrial Phenotype	$\alpha$ -synuclein Phenotype	Developmental Phenotype	References
SNCA	Triplication	<ul style="list-style-type: none"><li>↑ Oxidative stress sensitivity</li><li>↑ PTP opening</li><li>↓ Phagocytosis capability</li><li>↓ VAPB-PTPIP51 tethers</li><li>↓ GCase activity</li><li>↑ Fe-dependent DNA breaks</li><li>↓ ER-mitochondria associations combined with Fe significantly promotes neuronal cell death</li></ul> ER stress phenotype	<ul style="list-style-type: none"><li>↑ ROS production</li><li>↓ Mitochondrial membrane potential</li><li>Altered mitochondrial morphology</li></ul>	<ul style="list-style-type: none"><li>↑ <math>\alpha</math>-synuclein accumulation</li><li>↑ <math>\alpha</math>-synuclein aggregation</li><li>↑ Intracellular <math>\alpha</math>-synuclein pSer129-<math>\alpha</math>Syn accumulation</li><li>Aggregated <math>\alpha</math>-synuclein interacts with ATP synthase</li></ul>	<ul style="list-style-type: none"><li>↓ Differentiation capacity</li><li>↓ Neurite outgrowth and lower neuronal activity</li></ul>	13 Studies (111-115, 119, 135, 147, 156-160)
	A53T	<ul style="list-style-type: none"><li>↑ Oxidative stress sensitivity</li><li>↑ Nitrosative stress</li><li>↑ ER stress</li><li>↑ ER-associated degradation</li><li>↓ PGC1<math>\alpha</math> and mitochondrial function in response to oxidative stress</li></ul>	<ul style="list-style-type: none"><li>↓ Mitochondrial membrane potential</li><li>Altered mitochondrial morphology</li></ul>	<ul style="list-style-type: none"><li>↑ Protein aggregation</li><li>Shift in <math>\alpha</math>-synuclein native tetramers to monomers</li></ul>	<ul style="list-style-type: none"><li>↓ Neuritic outgrowth</li><li>↓ Axon integrity</li></ul>	4 Studies (118-120, 161)
	G2019S	<ul style="list-style-type: none"><li>↑ Oxidative stress sensitivity</li><li>↓ NF-<math>\kappa</math>B pathway</li><li>↑ Monoocyte production</li><li>↑ Expression of p21</li><li>↑ Caspase-3 activation sensitivity</li><li>↑ Proteasomal stress sensitivity</li><li>↑ Release of pro-inflammatory cytokines</li><li>LRRK2 interaction with ASK1-MAPK pathway</li><li>Differential expression of 10 miRNA</li><li>Altered patterns of genome methylation and gene expression</li></ul>	<ul style="list-style-type: none"><li>↓ Mitochondrial transport</li><li>↑ mtDNA damage</li><li>↑ Mitochondrial fission</li><li>↑ Mitochondrial mobility</li><li>↓ Oxygen consumption</li><li>Delayed Mitophagy</li><li>Potential role for sirtuin dysfunction</li></ul>	<ul style="list-style-type: none"><li>↑ <math>\alpha</math>-synuclein protein</li></ul>	<ul style="list-style-type: none"><li>↓ Precursor cell formation</li><li>↓ Neural differentiation</li><li>↓ Neurite length</li><li>↓ Neurite branching</li><li>↓ TH neurons with long neurites</li><li>↑ Neurite aggregation and calcium dysfunction</li><li>↑ Autophagic vacuoles</li></ul>	25 Studies (121-129, 131-135, 138, 162-171)
LRRK2	I2020T	<ul style="list-style-type: none"><li>↓ Phospho-AKT level</li><li>↑ Apoptosis</li></ul>			<ul style="list-style-type: none"><li>↓ Dopamine release</li></ul>	1 Study (136)
	R1441G	<ul style="list-style-type: none"><li>↑ Oxidative stress sensitivity</li><li>↓ NF-<math>\kappa</math>B pathway</li></ul>	<ul style="list-style-type: none"><li>↑ mtDNA damage</li><li>↑ Mitochondrial mobility</li><li>↓ Oxygen consumption</li></ul>			3 Studies (121, 125, 166)
	R42P				<ul style="list-style-type: none"><li>↓ Differentiation</li></ul>	1 Study (144)
PRKN	R275W				<ul style="list-style-type: none"><li>↓ Differentiation</li></ul>	1 Study (144)

Table 3. (continued)

Gene	Mutation	General Phenotype	Mitochondrial Phenotype	α-synuclein Phenotype	Developmental Phenotype	References
PRKN	V324A		↑ Abnormal mitochondrial size	↑ α-synuclein accumulation		1 Study (143)
	R42P; del exon 3				↓ Differentiation	1 Study (144)
	del exon 2-4	↑ Oxidative stress sensitivity ↓ GHSR expression	Abnormal mitochondrial morphology ↓ Mitochondrial turnover	↑ α-synuclein accumulation		2 Studies (142, 172)
	del exon 3	↑ Oxidative stress sensitivity			Altered dopamine metabolism	1 Study (141)
	del exon 3; del exon 5	↑ Oxidative stress sensitivity			Altered dopamine metabolism	1 Study (141)
	del exon 3-4; 1-BP del255A				↓ Differentiation	1 Study (144)
	del exon 6-7	↑ Oxidative stress sensitivity	Abnormal mitochondrial morphology ↓ Mitochondrial turnover	↑ α-synuclein accumulation		1 Study (142)
	del202-203AG; IVS1+1G/A				↓ Precursor cell formation	1 Study (134)
	G309D	↑ LRRK2 expression				1 Study (146)
	Q456X	↑ Oxidative stress sensitivity	↓ Parkin recruitment ↑ Mitochondrial copy number ↑ PGC-1α ↑ Oxygen consumption ↑ Abnormal mitochondrial size	↑ α-synuclein accumulation		3 Studies (121, 139, 143)
ATP13A2	L1059R; L1085W fsX1088	↓ GCase activity		↑ α-synuclein accumulation		1 Study (147)
SYNJ1	R258Q	↓ Autophagosome maturation	↑ Parkin ↑ Mitochondrial respiration		↓ PAX6	2 Studies Chapters 2 & 3 (48)

PTP=Protein tyrosine phosphatase, ER=Endoplasmic Reticulum, ROS=Reactive Oxygen Specie, TH=Tyrosine Hydroxylase.

Various iPSC models for p.G2019S also presented impaired neuronal differentiation (129, 133-135). These changes in neuron development match the impaired neurogenesis and neurite outgrowth described in an adult p.G2019S knock-in mouse model (84). The increased sensitivity to oxidative stress, increased levels of mitochondrial DNA damage and mitochondrial mobility were reproduced in models with the LRRK2 p.R1441G mutation (121, 125). Recently, one LRRK2 p.I2020T model has been developed, producing neurons that release less dopamine and have an increased incidence of apoptosis (136). Furthermore, it was demonstrated that these patient iPSC derived neurons had a lower phospho-AKT level than control iPSC derived neurons (136). This impaired activation of AKT was further described in *Drosophila* models for p.G2019S and p.R1441C and the iPSC-derived neurons suggest these associations are also supported in humans (137). Besides these phenotypes the models are also used to identify new interactions and possible proteins of interest for PD pathogenesis. Schwab et al. describe role for Sirtuin dysfunction in disease-associated mitochondrial damage (127). Further, LRRK2 interaction with the ASK1-MAPK pathway was identified and inhibition of ASK1 suppresses LRRK2-induced apoptosis (138).

## Parkin and PINK1

Parkin and PINK1 are proteins implicated in regulating the autophagic flux of damaged mitochondria, termed mitophagy. Interestingly, mutations in *PRKN* and *PINK1* genes have been linked to autosomal recessive familial PD, and many of these mutations are replicated in iPSC based PD modelling (Table 3). Modelled iPSC derived neurons of one such mutation, the PINK1 p.Q456X, showed impaired recruitment of Parkin to mitochondria upon depolarization, increased mtDNA copy number, and upregulation of the mitochondrial biogenesis inducer, PGC-1 $\alpha$  (139). Overexpression of wild type PINK1 in p.Q456X DA neurons was able to restore the recruitment of Parkin to mitochondria (139). This was further supported by Rakovic et al., who demonstrated impaired mitophagy in PINK1 p.V170G iPSC derived neurons (140). Furthermore, iPSC modelling of Parkin compound heterozygous deletions of exon 3 and exon 5, and homozygous deletion of exon 3 lead to decreased dopamine uptake and increased spontaneous dopamine release in DA neurons (141). This altered dopamine metabolism is supported by the finding of decreased striatal dopamine transporter and increased levels of dopamine in the midbrains of Parkin Q311X knock-in and knockout mice (85-89). Moreover, a homozygous deletion of exon 2 to 4 and a homozygous deletion of exons 6 and 7 of Parkin result in increased reactive oxygen species in iPSC derived DA neurons (142). Also,

these cells exhibited similar pathological changes seen in LRRK2 p.G2019S-iPSC-derived neurons, including accumulation of  $\alpha$ -synuclein. Next, Chung et al. described two models for PINK1 p.Q456X and Parkin p.V324A that both show aberrant mitochondria and  $\alpha$ -synuclein accumulation, confirming earlier findings in the homozygous deletion model for Parkin (143). These findings of mitochondrial accumulation and impaired mitophagy in PINK1 and Parkin iPSC based models are in line with the mitochondrial dysfunction found in mouse PINK1 and Parkin knockout models. As was observed with the LRRK2 p.G2019S-iPSC-derived neurons, neuronal differentiation and neurite complexity was impaired in cultures with various mutations in Parkin (134, 144, 145). This change in neurogenesis was later also observed in Parkin knockout mice (90). Recently, LRRK2 gene expression was found to be upregulated in a model for PINK1 p.G309D, this finding is in line with the many similar phenotypes between the models for PINK1, Parkin and LRRK2, suggesting a common pathogenic mechanism (146).

## Other genes

One patient derived iPSC model has been set up for a compound heterozygous p.L1059R and c.3253delC mutation in *ATP13A2*. This model presented accumulation of  $\alpha$ -synuclein, which is in agreement with the Lewy Bodies found in the *ATP13A2* mutant form of PD, called Kufor-Rakeb syndrome (147, 148). Furthermore, it is important to note that mutation of *ATP13A2* also causes hereditary spastic paraplegia, indicating depending on the mutation, the effects of *ATP13A2* are not limited to DA neurons (149). Lastly, one patient derived iPSC based model was created for the homozygous *SYNJ1* mutation p.R258Q (48). The mutant and control iPSCs were differentiated to neurons and a blockade in autophagy cycling was observed, suggested to be caused by the lack of the SAC1 domain function of Synaptojanin-1 (48). Furthermore, DA neuron degeneration was also observed in *Drosophila* model for the Synaptojanin-1 p.R258Q mutation, yet the iPSC-derived neuron model possibly needs to be developed further to gain mature DA neurons that progress from autophagosome accumulation to neuron death (48). Alternatively to the *SYNJ1* mutation in the SAC1 domain, loss of *SYNJ1* dual phosphatase activity leads to a much more severe disease of neonatal refractory epilepsy with progressive neurological decline (150-152). Whereas, increased *SYNJ1* expression has been associated with Alzheimer's disease (153, 154). Interestingly, autolysosome accumulation and impaired lysosomal-autophagy function was observed in PD patient derived fibroblasts with mutations in *ATP13A2* (155). This finding further highlights the importance of autophagy in PD.

Though iPSCs derived from patients with causative mutations have successfully modelled PD and further illustrated the pathogenic pathway of the disease, the DA neuronal models fail to demonstrate increased neuronal death without applying additional stress to the cells. Moreover, the LBs are not clearly observed in the cell culture models, although many of the patient mutation iPSCs-derived neurons display some form of  $\alpha$ -synuclein accumulation or aggregation (111, 112, 120, 123, 142, 143, 156, 157, 160, 161). Overcoming these shortfalls of reproducing the pathological phenotypes could decisively link pathogenesis to the described pathways. However, currently the pathogenesis of neurodegeneration in PD remains elusive. Further studies of iPSC-derived DA neurons from patients with other genetic mutations (such as VPS35, DJ-1, and PLA2G6) are needed to model PD and elucidate the pathogenesis.

## Opportunities to optimize human iPSC-derived dopaminergic neuronal models

The full potential of iPSC-derived DA neurons in PD modelling is not yet reached as high variability in observed effects of the generated neurons of the different models is observed, a possible explanation for this could be the diversity in differentiation protocols. Characterising and minimizing the variability between differentiated neurons could allow for better comparison between generated models. Furthermore, reliable methods for PD like neurodegeneration are required to conclusively identify the mechanisms and pathways that are pathogenic.

Most of the iPSC based studies mainly depend on tyrosine hydroxylase (TH), the rate-limiting enzyme in dopamine synthesis, as a marker of DA neurons. The differentiation protocols are optimized for floor plate DA neurons, however, to assess the maturity of these cells TH might not be suitable as TH is a marker of cells that are still mitotic or very early postmitotic (176). Additionally, in response to repeated or chronic stress, TH can also be expressed in the adrenal medulla, sympathetic ganglia, and locus coeruleus neurons, further diminishing the suitability of TH as a specific marker (177). In addition, the differentiation duration varies between the studies, which could have grave implications on the maturity of the neuronal populations. An alternative way to characterize the

differentiated midbrain DA neurons would be electrophysiological analysis. Adult SNc DA neurons are autonomous pacemakers whose basal activity is driven by L-type Ca<sup>2+</sup> channels (178). The fast-spiking pacemakers are also the ones most affected in PD, and through electrophysiology the diseased neurons can be pinpointed (179). Therefore, electrophysiology of the differentiated midbrain DA neurons could prove a more reliable way of characterizing mature midbrain DA neurons, as opposed to using TH. This would safe-guard the maturity of the investigated cells and could create a standard for the duration of differentiation. Unfortunately, few studies characterize the neurons as functional using electrophysiology.

Next, novel surface markers for midbrain DA neurons for flowcytometry-based sorting could further increase the efficiency of the different differentiation protocols. It was recently shown that the positive cell surface markers CORIN and CD166, in addition to a negative selection cell surface marker CXCR4, could enrich floor plate neural progenitor to 90% purity (173). The increased purity of the intermediate stage translated into more efficient differentiation of cells to mature midbrain DA neurons (173).

This homogenisation of the cell population stands in stark contrast to the multitude of cell types that are generated by using the recent midbrain organoid based models (109, 110). These organoids however, offers great opportunities as an advanced experimental in vitro model that mimics the cytoarchitecture and network connectivity of the brain. The self-organisation of these organoids allows for the interaction between glial cells and the generated neurons, which could support the formed neurons in formation of synapses and regular neuronal activity (174). In addition, a high degree of axonal myelination can be achieved (109); this is done by oligodendrocytes, a celltype difficult to differentiate in most stem cell-based differentiation protocols (175). Astrocytes also play critical roles in neuroprotection mechanisms involved in PD pathogenic pathways, by scavenging ROS, modulating oxidative stress, and expressing growth factors (180). Furthermore, they inhibit excessive inflammatory responses by regulating microglial activation (180). The oligodendrocytes also are thought to play a protective role in PD, and  $\alpha$ -synuclein depositions have been described in both oligodendrocytes and astrocytes (181, 182).

Finally, human iPSC-derived DA neurons have currently a relatively short lifespan of several weeks, which is only a fraction of the age compared to that of the midbrain DA neuronal populations in patients. This reduced lifespan can be limiting in studying PD which primarily affects the adult brain (183). Therefore, to improve the iPSC derived DA neuronal model system, either the lifespan of DA neurons should be expanded, or the aging process should be sped up. For example, one way to overcome this problem

is by making use of progerin, a protein involved in the premature aging disorder Hutchinson–Gilford progeria. Overexpression of this protein in human iPSC-derived midbrain DA neurons induces age-related deficits, such as mitochondrial abnormality and AKT deregulation (184). Even though overexpressing progerin does not reproduce all aspects of normal aging, it may prove useful for modelling late-onset disorders in vitro. These opportunities may yet unlock the full potential of the iPSC based PD model in decisive determination of the pathogenic pathways and screening of drug libraries in search for possible treatments.

## Challenges for iPSC models

### Intrinsic concerns regarding iPSC cultures

Despite the advancements of iPSC cultures, there are still several hurdles in using iPSCs to model PD. First, there is great variation in efficiency of neuronal differentiation between iPSC clones. Even within iPSC clones from the same patient differences in the pan neuronal marker Pax6 have been described (185). This means to achieve reproducible results larger numbers of cell lines should be investigated, also the application of isogenic controls could offer solution as the differences would be minimal between control and mutant iPSC lines.

Another problem with the iPSCs is that multiple analyses have shown that the transcriptome and epigenome differs from human embryonic stem cells. The cells seem to retain a DNA methylation profile influenced by their pre-iPSC cell type (186). The effect of this ‘primed state’ on the eventual model cell is unknown. Little is also known about the effect of leftover mitochondrial DNA from the fibroblast. However, the DNA methylation profile diminishes over time as the iPSC passage increases. The primed state can also be overcome by converting them into the so-called “naive” state (187, 188). In any case, the current methods for differentiation are fully overpowering the possible primed state, generating large amounts of neurons.

Risk of teratoma formation upon transplantation of iPSC derived neurons remains a problem as often during differentiation, a subpopulation of cells remains undifferentiated (189). This was particularly the case when in the past the oncogene c-myc was used to induce pluripotency (190). For this purpose the use of the non-integrating



reprogramming technologies is critical. Additionally, Flow cytometry cell sorting can be applied to filter out any unwanted celltypes. Nevertheless, residual transgene expression of the reprogramming factors has been shown to cause a differential gene expression profile in iPSCs (191). This finding demands caution and highlights not only the need for integration-free, but also factor-free iPSC.

## Applications of PD iPSC in clinical practice

iPSC-derived models of PD have a high translational potential into clinical practice. This includes the identification of novel new pathways of PD and testing of known and novel therapeutic agents in disease relevant tissue. Moreover, iPSC provide a source of patient own DA neurons for Stem Cell-based cell replacement therapies. Long term engraftment has already been shown to be possible and effective for mice and rats shown up to 5 months and rhesus monkeys up to 1 month (104). With the arrival of non-viral, non-integration and non-DNA mediated iPSC reprogramming techniques, it could be possible in the near future to perform safe iPSC-mediated midbrain DA neuron transplantations in PD patients. Applying the CRISPR-Cas9 system, a library of iPSCs may be built for all known PD mutations and risk factors for phenotypical investigation and drug screening in a large number of lines with minimal variation. This can be expanded to include other neurodegenerative disorders to find common pathways. Recently, Kirkeby et al. have revealed a subset of predictive markers that can be used to improve graft outcome of transplanted human embryonic stem cells. They found that markers expressed by midbrain cells close to the midbrain-hindbrain boundary (i.e., EN1, ETV5, CNPY1, PAX8, and SPRY1) correlated with a successful graft outcome, which could possibly also be used for purification of iPSCs before transplantation (192).

## Conclusion

Among the existing human patient derived iPSC-based DA neuronal models, most of the key features of the disease have been demonstrated, and therefore these models could serve as novel platforms for the development of disease modifying therapies. However, generation of a PD model that fully captures the disease causing mechanism and pathology will be difficult. Especially, midbrain DA neuron loss, the pathological hallmark in PD patients, seems to be difficult to reproduce in PD patient derived iPSC

model systems. On the other hand, the high-speed progression of the field and research over the last decade is still on-going and opportunities are still to be exploited. Currently, the CRISPR-Cas9 system is incorporated to correct mutations in PD patient-derived iPS lines, and to introduce mutations in control iPS lines. This doubles the amount of lines available and at the same time provides with the best controls with minimal variation. Variation could further be reduced by cell sorting for desired cell types. Reduced iPS clone variation would also support accurate investigation of phenotypes with a small effect-size. Lastly, the formation of brain organoids can be used to add complexity, once a phenotype is found in the iPSC models, but would also allow for the detection of phenotypes that could otherwise not be detected in a 2D-culture system. Further development and investigation of the iPSC-derived DA neuron models will contribute, not only to our understanding of PD and related disease, but also aid in finding drug targets for a curative therapy. Finally, the patient based DA neurons may even be used for cell replacement therapy, providing a readily available source of cells and circumventing transplant rejection issues.

## Aim and scope of the thesis

### Aim

Since the initial description of the disease by James Parkinson over two centuries ago, the Parkinson's disease (PD) causing mechanisms still remain obscure. One of the problems in investigating this disease lies in the lack of availability of a representative model system of human substantia nigra dopaminergic neurons, the cells affected in PD. The recent development of the induced pluripotent stem cell (iPSC) technique opened up new possibilities in modelling PD, by differentiating PD patient derived iPSCs towards dopaminergic neurons, providing a very important model system for these otherwise unavailable cells. The aim of this thesis is to gain insight into the function of PD related genes and the effect of their associated disease causing mutations by generating and investigating patient iPSC derived model neurons. Furthermore, a better understanding of the affected pathways could lead to development of new therapies. Additionally, a cellular phenotype could enable the model to be used for drug screening.

## Scope

In **chapter 1** we provided a comprehensive outline of PD modelling and the challenges and opportunities of the new generation of iPSC models. **Chapter 2** combines *Drosophila syn<sup>RO</sup>* and *PARK20* iPSC derived neuron modelling to functionally investigate the effect of the SYNJ1 p.Arg258Gln mutation on synaptic endocytosis and macroautophagy. These models were able to pinpoint the driving role of the SAC1 domain in autophagosome biogenesis within synapses. Furthermore, the mutation impairs dephosphorylation of the autophagosome membrane lipids PI(3)P and PI(3,5)P2 causing a stop in autophagosome maturation. In **chapter 3** the *PARK20* iPSC derived model was used to specifically form DA neurons, which are used to further address the effect of the p.Arg258Gln mutation on neuron development, endocytosis, and mitochondrial function. The patient lines do not display any changes in differentiation of the neurons, nor is endocytosis noticeably affected. However, evidence was found pointing towards a neurodevelopmental function of Synaptojanin-1 at the smNPC stage. Further, a strong increase in Parkin levels and improved mitochondrial function were observed. Based on functions of Parkin described in literature, there may be a connection between Parkin upregulation and mitochondrial function. **Chapter 4** then proposes LRP10 as a new gene for Parkinson's disease, Parkinson's disease dementia, and dementia with Lewy bodies. We discovered nine rare variants associated with the Lewy body diseases by genome-wide linkage analysis, followed by sequencing of the gene in unrelated probands and finally screening for specific variants. Furthermore, we identify the effects of the mutations on the protein expression, stability and/or function. Together these findings indicate loss of LRP10 function as the pathogenic mechanism. To give first insights into the workings of the LRP10 gene, we used a novel human iPSC derived dopaminergic neuron model to generate and investigate 12-week-old neuronal cultures. Immunocytochemical analysis shows co-localisation with GGA1 and partial co-localisation with VPS35. Interestingly both GGA1 and VPS35 may link LRP10 to  $\alpha$ -synuclein aggregation and Lewy Body disease. In **chapter 5** we discuss our iPSC models and our findings in the context of recent literature, their contribution to understanding Parkinson's disease and the next steps in validating our findings and testing our new hypotheses.

# References

- von Campenhausen S, Bornschein B, Wick R, Botzel K, Sampaio C, Poewe W, et al. Prevalence and incidence of Parkinson's disease in Europe. *Eur Neuropsychopharmacol*. 2005;15(4):473-90.
- von Coelln R, Shulman LM. Clinical subtypes and genetic heterogeneity: of lumping and splitting in Parkinson disease. *Curr Opin Neurol*. 2016;29(6):727-34.
- Schapira AHV, Chaudhuri KR, Jenner P. Non-motor features of Parkinson disease. *Nat Rev Neurosci*. 2017;18(7):435-50.
- Antony PM, Diederich NJ, Kruger R, Balling R. The hallmarks of Parkinson's disease. *FEBS J*. 2013;280(23):5981-93.
- Liu LX, Du D, Zheng T, Fang Y, Chen YS, Yi HL, et al. Detecting dopaminergic neuronal degeneration using diffusion tensor imaging in a rotenone-induced rat model of Parkinson's disease: fractional anisotropy and mean diffusivity values. *Neural Regen Res*. 2017;12(9):1485-91.
- Dickson DW, Braak H, Duda JE, Duyckaerts C, Gasser T, Halliday GM, et al. Neuropathological assessment of Parkinson's disease: refining the diagnostic criteria. *Lancet Neurol*. 2009;8(12):1150-7.
- LeWitt PA. Levodopa therapy for Parkinson's disease: Pharmacokinetics and pharmacodynamics. *Mov Disord*. 2015;30(1):64-72.
- Stayte S, Vissel B. Advances in non-dopaminergic treatments for Parkinson's disease. *Front Neurosci*. 2014;8:113.
- Guttman M, Kish SJ, Furukawa Y. Current concepts in the diagnosis and management of Parkinson's disease. *CMAJ*. 2003;168(3):293-301.
- Chiken S, Nambu A. Disrupting neuronal transmission: mechanism of DBS? *Front Syst Neurosci*. 2014;8:33.
- Wirdefeldt K, Adami HO, Cole P, Trichopoulos D, Mandel J. Epidemiology and etiology of Parkinson's disease: a review of the evidence. *Eur J Epidemiol*. 2011;26 Suppl 1:S1-58.
- Costello S, Cockburn M, Bronstein J, Zhang X, Ritz B. Parkinson's disease and residential exposure to maneb and paraquat from agricultural applications in the central valley of California. *Am J Epidemiol*. 2009;169(8):919-26.
- Klein C, Westenberger A. Genetics of Parkinson's disease. *Cold Spring Harb Perspect Med*. 2012;2(1):a008888.
- Bonifati V. Genetics of Parkinson's disease--state of the art, 2013. *Parkinsonism Relat Disord*. 2014;20 Suppl 1:S23-8.
- Quadri M, Mandemakers W, Grochowska MM, Masius R, Geut H, Fabrizio E, et al. LRP10 genetic variants in familial Parkinson's disease and dementia with Lewy bodies: a genome-wide linkage and sequencing study. *Lancet Neurol*. 2018;17(7):597-608.
- Tieu K. A guide to neurotoxic animal models of Parkinson's disease. *Cold Spring Harb Perspect Med*. 2011;1(1):a009316.
- Cannon JR, Tapias V, Na HM, Honick AS, Drolet RE, Greenamyre JT. A highly reproducible rotenone model of Parkinson's disease. *Neurobiol Dis*. 2009;34(2):279-90.
- Forno LS, DeLanney LE, Irwin I, Langston JW. Similarities and differences between MPTP-induced parkinsonism and Parkinson's disease. *Neuropathologic considerations*. *Adv Neurol*. 1993;60:600-8.
- Przedborski S, Levivier M, Jiang H, Ferreira M, Jackson-Lewis V, Donaldson D, et al. Dose-dependent lesions of the dopaminergic nigrostriatal pathway induced by intrastriatal injection of 6-hydroxydopamine. *Neuroscience*. 1995;67(3):631-47.
- Thiruchelvam M, Brockel BJ, Richfield EK, Baggs RB, Cory-Slechta DA. Potentiated and preferential effects of combined paraquat and maneb on nigrostriatal dopamine systems: environmental risk factors for Parkinson's disease? *Brain Res*. 2000;873(2):225-34.
- Thiruchelvam M, Richfield EK, Baggs RB, Tank AW, Cory-Slechta DA. The nigrostriatal dopaminergic system as a preferential target of repeated exposures to combined paraquat and maneb: implications for Parkinson's disease. *J Neurosci*. 2000;20(24):9207-14.
- Blesa J, Juri C, Collantes M, Penuelas I, Prieto E, Iglesias E, et al. Progression of dopaminergic depletion in a model of MPTP-induced Parkinsonism in non-human primates. An (18)F-DOPA and (11)C-DTBZ PET study. *Neurobiol Dis*. 2010;38(3):456-63.
- Langston JW. The MPTP Story. *J Parkinsons Dis*. 2017;7(s1):S11-S22.
- Blandini F, Armentero MT. Animal models of Parkinson's disease. *FEBS J*. 2012;279(7):1156-66.
- Bezard E, Imbert C, Deloire X, Bioulac B, Gross CE. A chronic MPTP model reproducing the slow evolution of Parkinson's disease: evolution of motor symptoms in the monkey. *Brain Res*. 1997;766(1-2):107-12.
- Hantraye P, Varastet M, Peschanski M, Riche D, Cesaro P, Willer JC, et al. Stable parkinsonian syndrome and uneven loss of striatal dopamine fibres following chronic MPTP administration in baboons. *Neuroscience*. 1993;53(1):169-78.
- Johnston TM, Fox SH. Symptomatic Models of Parkinson's Disease and L-DOPA-Induced Dyskinesia in Non-human Primates. *Curr Top Behav Neurosci*. 2015;22:221-35.
- Huang B, Wu S, Wang Z, Ge L, Rizak JD, Wu J, et al. Phosphorylated alpha-Synuclein Accumulations and Lewy Body-like Pathology Distributed in Parkinson's Disease-Related Brain Areas of Aged Rhesus Monkeys Treated with MPTP. *Neuroscience*. 2018;379:302-15.
- Manning-Bog AB, McCormack AL, Purisai MG, Bolin LM, Di Monte DA. Alpha-synuclein overexpression protects against paraquat-induced neurodegeneration. *J Neurosci*. 2003;23(8):3095-9.
- Sherer TB, Kim JH, Betarbet R, Greenamyre JT. Subcutaneous rotenone exposure causes highly selective dopaminergic degeneration and alpha-synuclein aggregation. *Exp Neurol*. 2003;179(1):9-16.
- Ko WKD, Bezard E. Experimental animal models of Parkinson's disease: A transition from assessing symptomatology to alpha-synuclein targeted disease modification. *Exp Neurol*. 2017;298(Pt B):172-9.
- Dauer W, Przedborski S. Parkinson's disease: mechanisms and models. *Neuron*. 2003;39(6):889-909.
- Capecchi MR. Gene targeting in mice: functional analysis of the mammalian genome for the twenty-first century. *Nat Rev Genet*. 2005;6(6):507-12.
- Goldberg MS, Fleming SM, Palacino JJ, Cepeda C, Lam HA, Bhatnagar A, et al. Parkin-deficient mice exhibit nigrostriatal deficits but not loss of dopaminergic neurons. *J Biol Chem*. 2003;278(44):43628-35.
- Hinkle KM, Yue M, Behrouz B, Dachsel JC, Lincoln SJ, Bowles EE, et al. LRRK2 knockout mice have an intact dopaminergic system but display alterations in exploratory and motor co-ordination behaviors. *Mol Neurodegener*. 2012;7:25.
- Andres-Mateos E, Perier C, Zhang L, Blanchard-Fillion B, Greco TM, Thomas B, et al. DJ-1 gene deletion reveals that DJ-1 is an atypical peroxiredoxin-like peroxidase. *Proc Natl Acad Sci U S A*. 2007;104(37):14807-12.

37. Chesselet MF, Fleming S, Mortazavi F, Meurers B. Strengths and limitations of genetic mouse models of Parkinson's disease. *Parkinsonism Relat Disord.* 2008;14 Suppl 2:S84-7.
38. Li JY, Englund E, Holton JL, Soulet D, Hagell P, Lees AJ, et al. Lewy bodies in grafted neurons in subjects with Parkinson's disease suggest host-to-graft disease propagation. *Nat Med.* 2008;14(5):501-3.
39. Brundin P, Li JY, Holton JL, Lindvall O, Revesz T. Research in motion: the enigma of Parkinson's disease pathology spread. *Nat Rev Neurosci.* 2008;9(10):741-5.
40. Stöpschinski BE, Diamond MI. The prion model for progression and diversity of neurodegenerative diseases. *Lancet Neurol.* 2017;16(4):323-32.
41. Steiner JA, Quansah E, Brundin P. The concept of alpha-synuclein as a prion-like protein: ten years after. *Cell Tissue Res.* 2018;373(1):161-73.
42. Wong YC, Krainc D. Alpha-synuclein toxicity in neurodegeneration: mechanism and therapeutic strategies. *Nat Med.* 2017;23(2):1-13.
43. Lashuel HA, Overk CR, Oueslati A, Masliah E. The many faces of alpha-synuclein: from structure and toxicity to therapeutic target. *Nat Rev Neurosci.* 2013;14(1):38-48.
44. Bras J, Guerreiro R, Hardy J. Snapshot: Genetics of Parkinson's disease. *Cell.* 2015;160(3):570-e1.
45. Kalia LV, Lang AE. Parkinson's disease. *Lancet.* 2015;386(9996):896-912.
46. Vicario M, Cieri D, Brini M, Cali T. The Close Encounter Between Alpha-Synuclein and Mitochondria. *Front Neurosci.* 2018;12:388.
47. Kinghorn KJ, Castillo-Quan JL, Bartolome F, Angelova PR, Li L, Pope S, et al. Loss of PLA2G6 leads to elevated mitochondrial lipid peroxidation and mitochondrial dysfunction. *Brain.* 2015;138(Pt 7):1801-16.
48. Vanhauwaert R, Kuenen S, Masius R, Bademosi A, Manetsberger J, Schoovaerts N, et al. The SAC1 domain in synaptotagmin is required for autophagosome maturation at presynaptic terminals. *EMBO J.* 2017;36(10):1392-411.
49. Nelson DE, Randle SJ, Laman H. Beyond ubiquitination: the atypical functions of F-box and other F-box proteins. *Open Biol.* 2013;3(10):130131.
50. La Manno G, Gyllborg D, Codeluppi S, Nishimura K, Salto C, Zeisel A, et al. Molecular Diversity of Midbrain Development in Mouse, Human, and Stem Cells. *Cell.* 2016;167(2):566-80 e19.
51. Wagner J, Akerud P, Castro DS, Holm PC, Canals JM, Snyder EY, et al. Induction of a midbrain dopaminergic phenotype in Nurr1-overexpressing neural stem cells by type 1 astrocytes. *Nat Biotechnol.* 1999;17(7):653-9.
52. Andersson E, Tryggvason U, Deng Q, Friling S, Alekseenko Z, Robert B, et al. Identification of intrinsic determinants of midbrain dopamine neurons. *Cell.* 2006;124(2):393-405.
53. Cai J, Donaldson A, Yang M, German MS, Enikolopov G, Jacobowitz L. The role of Lmx1a in the differentiation of human embryonic stem cells into midbrain dopamine neurons in culture and after transplantation into a Parkinson's disease model. *Stem Cells.* 2009;27(1):220-9.
54. Kawasaki H, Mizuseki K, Nishikawa S, Kaneko S, Kuwana Y, Nakanishi S, et al. Induction of midbrain dopaminergic neurons from ES cells by stromal cell-derived inducing activity. *Neuron.* 2000;28(1):31-40.
55. Lee SH, Lumelsky N, Studer L, Auerbach JM, McKay RD. Efficient generation of midbrain and hindbrain neurons from mouse embryonic stem cells. *Nat Biotechnol.* 2000;18(6):675-9.
56. Kim JH, Auerbach JM, Rodriguez-Gomez JA, Velasco I, Gavin D, Lumelsky N, et al. Dopamine neurons derived from embryonic stem cells function in an animal model of Parkinson's disease. *Nature.* 2002;418(6893):50-6.
57. Takahashi K, Yamanaka S. Induction of pluripotent stem cells from mouse embryonic and adult fibroblast cultures by defined factors. *Cell.* 2006;126(4):663-76.
58. Crews L, Spencer B, Desplats P, Patrick C, Paulino A, Rockenstein E, et al. Selective molecular alterations in the autophagy pathway in patients with Lewy body disease and in models of alpha-synucleinopathy. *PLoS One.* 2010;5(2):e9313.
59. Kitada T, Pisani A, Karouani M, Haburcak M, Martella G, Tschertner A, et al. Impaired dopamine release and synaptic plasticity in the striatum of parkin-/- mice. *J Neurochem.* 2009;110(2):613-21.
60. Martin LJ, Pan Y, Price AC, Sterling W, Copeland NG, Jenkins NA, et al. Parkinson's disease alpha-synuclein transgenic mice develop neuronal mitochondrial degeneration and cell death. *J Neurosci.* 2006;26(1):41-50.
61. Marx FP, Holzmann C, Strauss KM, Li L, Eberhardt O, Gerhardt E, et al. Identification and functional characterization of a novel R621C mutation in the synphilin-1 gene in Parkinson's disease. *Hum Mol Genet.* 2003;12(11):1223-31.
62. Jensen PH, Nielsen MS, Jakes R, Dotti CG, Goedert M. Binding of alpha-synuclein to brain vesicles is abolished by familial Parkinson's disease mutation. *J Biol Chem.* 1998;273(41):26292-4.
63. Conway KA, Harper JD, Lansbury PT. Accelerated in vitro fibril formation by a mutant alpha-synuclein linked to early-onset Parkinson disease. *Nat Med.* 1998;4(11):1318-20.
64. Vogiatzi T, Xilouri M, Vekrellis K, Stefanis L. Wild type alpha-synuclein is degraded by chaperone-mediated autophagy and macroautophagy in neuronal cells. *J Biol Chem.* 2008;283(35):23542-56.
65. Navarro A, Boveris A. Brain mitochondrial dysfunction and oxidative damage in Parkinson's disease. *J Bioenerg Biomembr.* 2009;41(6):517-21.
66. Tong Y, Pisani A, Martella G, Karouani M, Yamaguchi H, Pothos EN, et al. R1441C mutation in LRRK2 impairs dopaminergic neurotransmission in mice. *Proc Natl Acad Sci U S A.* 2009;106(34):14622-7.
67. Dufty BM, Warner LR, Hou ST, Jiang SX, Gomez-Isla T, Leenhouts KM, et al. Calpain-cleavage of alpha-synuclein: connecting proteolytic processing to disease-linked aggregation. *Am J Pathol.* 2007;170(5):1725-38.
68. Chen L, Thiruchelvam MJ, Madura K, Richfield EK. Proteasome dysfunction in aged human alpha-synuclein transgenic mice. *Neurobiol Dis.* 2006;23(1):120-6.
69. Maskri L, Zhu X, Fritzen S, Kuhn K, Ullmer C, Engels P, et al. Influence of different promoters on the expression pattern of mutated human alpha-synuclein in transgenic mice. *Neurodegener Dis.* 2004;1(6):255-65.
70. Fuchs J, Nilsson C, Kachergus J, Munz M, Larsson EM, Schule B, et al. Phenotypic variation in a large Swedish pedigree due to SNCA duplication and triplication. *Neurology.* 2007;68(12):916-22.
71. van Duijn CM, Dekker MC, Bonifati V, Galjaard RJ, Houwing-Duistermaat JJ, Snijders PJ, et al. Park7, a novel locus for autosomal recessive early-onset parkinsonism, on chromosome 1p36. *Am J Hum Genet.* 2001;69(3):629-34.
72. Su X, Maguire-Zeiss KA, Giuliano R, Prifti L, Venkatesh K, Federoff HJ. Synuclein activates microglia in a model of Parkinson's disease. *Neurobiol Aging.* 2008;29(11):1690-701.
73. Rockenstein E, Mallory M, Hashimoto M, Song D, Shults CW, Lang I, et al. Differential neuropathological alterations in transgenic mice expressing alpha-synuclein from the platelet-derived growth factor and Thy-1 promoters. *J Neurosci Res.* 2002;68(5):568-78.
74. Baik JH, Picetti R, Saiardi A, Thiriet G, Dierich A, Depaulis A, et al. Parkinsonian-like locomotor impairment in mice lacking dopamine D2 receptors. *Nature.* 1995;377(6548):424-8.

75. Kitada T, Tong Y, Gautier CA, Shen J. Absence of nigral degeneration in aged parkin/DJ-1/PINK1 triple knockout mice. *J Neurochem*. 2009;111(3):696-702.
76. Tang FL, Liu W, Hu JX, Erion JR, Ye J, Mei L, et al. VPS35 Deficiency or Mutation Causes Dopaminergic Neuronal Loss by Impairing Mitochondrial Fusion and Function. *Cell Rep*. 2015;12(10):1631-43.
77. Ishizu N, Yui D, Hebisawa A, Aizawa H, Cui W, Fujita Y, et al. Impaired striatal dopamine release in homozygous Vps35 D620N knock-in mice. *Hum Mol Genet*. 2016;25(20):4507-17.
78. Wakamatsu M, Ishii A, Ukai Y, Sakagami J, Iwata S, Ono M, et al. Accumulation of phosphorylated alpha-synuclein in dopaminergic neurons of transgenic mice that express human alpha-synuclein. *J Neurosci Res*. 2007;85(8):1819-25.
79. Su X, Federoff HJ, Maguire-Zeiss KA. Mutant alpha-synuclein overexpression mediates early proinflammatory activity. *Neurotox Res*. 2009;16(3):238-54.
80. Kitada T, Pisani A, Porter DR, Yamaguchi H, Tschertner A, Martella G, et al. Impaired dopamine release and synaptic plasticity in the striatum of PINK1-deficient mice. *Proc Natl Acad Sci U S A*. 2007;104(27):11441-6.
81. Gispert S, Ricciardi F, Kurz A, Azizov M, Hoepken HH, Becker D, et al. Parkinson phenotype in aged PINK1-deficient mice is accompanied by progressive mitochondrial dysfunction in absence of neurodegeneration. *PLoS One*. 2009;4(6):e5777.
82. Liu HF, Lu S, Ho PW, Tse HM, Pang SY, Kung MH, et al. LRRK2 R1441G mice are more liable to dopamine depletion and locomotor inactivity. *Ann Clin Transl Neurol*. 2014;1(3):199-208.
83. Yue M, Hinkle KM, Davies P, Trushina E, Fiesel FC, Christenson TA, et al. Progressive dopaminergic alterations and mitochondrial abnormalities in LRRK2 G2019S knock-in mice. *Neurobiol Dis*. 2015;78:172-95.
84. Winner B, Melrose HL, Zhao C, Hinkle KM, Yue M, Kent C, et al. Adult neurogenesis and neurite outgrowth are impaired in LRRK2 G2019S mice. *Neurobiol Dis*. 2011;41(3):706-16.
85. Shigemitsu K, Tsujishita Y, Hara K, Nanahoshi M, Avruch J, Yonezawa K. Regulation of translational effectors by amino acid and mammalian target of rapamycin signaling pathways. Possible involvement of autophagy in cultured hepatoma cells. *J Biol Chem*. 1999;274(2):1058-65.
86. Mori H, Kondo T, Yokochi M, Matsumine H, Nakagawa-Hattori Y, Miyake T, et al. Pathologic and biochemical studies of juvenile parkinsonism linked to chromosome 6q. *Neurology*. 1998;51(3):890-2.
87. Calabresi P, Saiardi A, Pisani A, Baik JH, Centonze D, Mercuri NB, et al. Abnormal synaptic plasticity in the striatum of mice lacking dopamine D2 receptors. *J Neurosci*. 1997;17(12):4536-44.
88. Hao LY, Giasson BI, Bonini NM. DJ-1 is critical for mitochondrial function and rescues PINK1 loss of function. *Proc Natl Acad Sci U S A*. 2010;107(21):9747-52.
89. Hatano Y, Sato K, Eliab B, Yoshino H, Yamamura Y, Bonifati V, et al. PARK6-linked autosomal recessive early-onset parkinsonism in Asian populations. *Neurology*. 2004;63(8):1482-5.
90. Park MH, Lee HJ, Lee HL, Son DJ, Ju JH, Hyun BK, et al. Parkin Knockout Inhibits Neuronal Development via Regulation of Proteasomal Degradation of p21. *Theranostics*. 2017;7(7):2033-45.
91. Martinat C, Shendelman S, Jonason A, Leete T, Beal MF, Yang L, et al. Sensitivity to oxidative stress in DJ-1-deficient dopamine neurons: an ES-derived cell model of primary Parkinsonism. *PLoS Biol*. 2004;2(11):e327.
92. Drolet RE, Behrouz B, Lookingland KJ, Goudreau JL. Mice lacking alpha-synuclein have an attenuated loss of striatal dopamine following prolonged chronic MPTP administration. *Neurotoxicology*. 2004;25(5):761-9.
93. Yu WH, Dorado B, Figueroa HY, Wang L, Planel E, Cookson MR, et al. Metabolic activity determines efficacy of macroautophagic clearance of pathological oligomeric alpha-synuclein. *Am J Pathol*. 2009;175(2):736-47.
94. Cao M, Wu Y, Ashrafi G, McCartney AJ, Wheeler H, Bushong EA, et al. Parkinson Sac Domain Mutation in Synaptotagmin 1 Impairs Clathrin Uncoating at Synapses and Triggers Dystrophic Changes in Dopaminergic Axons. *Neuron*. 2017;93(4):882-96 e5.
95. Fusaki N, Ban H, Nishiyama A, Saeki K, Hasegawa M. Efficient induction of transgene-free human pluripotent stem cells using a vector based on Sendai virus, an RNA virus that does not integrate into the host genome. *Proc Jpn Acad Ser B Phys Biol Sci*. 2009;85(8):348-62.
96. Warren L, Manos PD, Ahfeldt T, Loh YH, Li H, Lau F, et al. Highly efficient reprogramming to pluripotency and directed differentiation of human cells with synthetic modified mRNA. *Cell Stem Cell*. 2010;7(5):618-30.
97. Okita K, Matsumura Y, Sato Y, Okada A, Morizane A, Okamoto S, et al. A more efficient method to generate integration-free human iPS cells. *Nat Methods*. 2011;8(5):409-12.
98. Gasiunas G, Barrangou R, Horvath P, Siksnys V. Cas9-crRNA ribonucleoprotein complex mediates specific DNA cleavage for adaptive immunity in bacteria. *Proc Natl Acad Sci U S A*. 2012;109(39):E2579-86.
99. Jinek M, Chylinski K, Fonfara I, Hauer M, Doudna JA, Charpentier E. A programmable dual-RNA-guided DNA endonuclease in adaptive bacterial immunity. *Science*. 2012;337(6096):816-21.
100. Wang G, Yang L, Grishin D, Rios X, Ye LY, Hu Y, et al. Efficient, footprint-free human iPSC genome editing by consolidation of Cas9/CRISPR and piggyBac technologies. *Nat Protoc*. 2017;12(1):88-103.
101. Chambers SM, Fasano CA, Papapetrou EP, Tomishima M, Sadelain M, Studer L. Highly efficient neural conversion of human ES and iPS cells by dual inhibition of SMAD signaling. *Nat Biotechnol*. 2009;27(3):275-80.
102. Chung S, Leung A, Han BS, Chang MY, Moon JJ, Kim CH, et al. Wnt1-Imx1a forms a novel autoregulatory loop and controls midbrain dopaminergic differentiation synergistically with the SHH-FoxA2 pathway. *Cell Stem Cell*. 2009;5(6):646-58.
103. Joksimovic M, Yun BA, Kittappa R, Anderegg AM, Chang WW, Taketo MM, et al. Wnt antagonism of Shh facilitates midbrain floor plate neurogenesis. *Nat Neurosci*. 2009;12(2):125-31.
104. Kriks S, Shim JW, Piao J, Ganat YM, Wakeman DR, Xie Z, et al. Dopamine neurons derived from human ES cells efficiently engraft in animal models of Parkinson's disease. *Nature*. 2011;480(7378):547-51.
105. Kirkeby A, Grealish S, Wolf DA, Nelander J, Wood J, Lundblad M, et al. Generation of regionally specified neural progenitors and functional neurons from human embryonic stem cells under defined conditions. *Cell Rep*. 2012;1(6):703-14.
106. Denham M, Bye C, Leung J, Conley BJ, Thompson LH, Dottori M. Glycogen synthase kinase 3beta and activin/nodal inhibition in human embryonic stem cells induces a pre-neuroepithelial state that is required for specification to a floor plate cell lineage. *Stem Cells*. 2012;30(11):2400-11.
107. Xi J, Liu Y, Liu H, Chen H, Emborg ME, Zhang SC. Specification of midbrain dopamine neurons from primate pluripotent stem cells. *Stem Cells*. 2012;30(8):1655-63.
108. Doi D, Samata B, Katsukawa M, Kikuchi T, Morizane A, Ono Y, et al. Isolation of human induced pluripotent stem cell-derived dopaminergic progenitors by cell sorting for successful transplantation. *Stem Cell Reports*. 2014;2(3):337-50.
109. Monzel AS, Smits LM, Hemmer K, Hachi S, Moreno EL, van Wuellem T, et al. Derivation of Human Midbrain-Specific Organoids from Neuroepithelial Stem Cells. *Stem Cell Reports*. 2017;8(5):1144-54.



110. Jo J, Xiao Y, Sun AX, Cukuroglu E, Tran HD, Goke J, et al. Midbrain-like Organoids from Human Pluripotent Stem Cells Contain Functional Dopaminergic and Neuromelanin-Producing Neurons. *Cell Stem Cell*. 2016;19(2):248-57.
111. Devine MJ, Ryten M, Vodicka P, Thomson AJ, Burdon T, Houlden H, et al. Parkinson's disease induced pluripotent stem cells with triplication of the alpha-synuclein locus. *Nat Commun*. 2011;2:440.
112. Byers B, Cord B, Nguyen HN, Schule B, Fenno L, Lee PC, et al. SNCA triplication Parkinson's patient's iPSC-derived DA neurons accumulate alpha-synuclein and are susceptible to oxidative stress. *PLoS One*. 2011;6(11):e26159.
113. Oliveira LM, Falomir-Lockhart LJ, Botelho MG, Lin KH, Wales P, Koch JC, et al. Elevated alpha-synuclein caused by SNCA gene triplication impairs neuronal differentiation and maturation in Parkinson's patient-derived induced pluripotent stem cells. *Cell Death Dis*. 2015;6:e1994.
114. Flierl A, Oliveira LM, Falomir-Lockhart LJ, Mak SK, Hesley J, Soldner F, et al. Higher vulnerability and stress sensitivity of neuronal precursor cells carrying an alpha-synuclein gene triplication. *PLoS One*. 2014;9(11):e112413.
115. Heman-Ackah SM, Manzano R, Hoozemans JJM, Scheper W, Flynn R, Haerty W, et al. Alpha-synuclein induces the unfolded protein response in Parkinson's disease SNCA triplication iPSC-derived neurons. *Hum Mol Genet*. 2017;26(22):4441-50.
116. Cooper AA, Gitler AD, Cashikar A, Haynes CM, Hill KJ, Bhullar B, et al. Alpha-synuclein blocks ER-Golgi traffic and Rab1 rescues neuron loss in Parkinson's models. *Science*. 2006;313(5785):324-8.
117. Gitler AD, Bevis BJ, Shorter J, Strathearn KE, Hamamichi S, Su LJ, et al. The Parkinson's disease protein alpha-synuclein disrupts cellular Rab homeostasis. *Proc Natl Acad Sci U S A*. 2008;105(1):145-50.
118. Ryan SD, Dolatabadi N, Chan SF, Zhang X, Akhtar MW, Parker J, et al. Isogenic human iPSC Parkinson's model shows nitrosative stress-induced dysfunction in MEF2-PGC1alpha transcription. *Cell*. 2013;155(6):1351-64.
119. Little D, Luft C, Mosaku O, Lorvellec M, Yao Z, Paillasson S, et al. A single cell high content assay detects mitochondrial dysfunction in iPSC-derived neurons with mutations in SNCA. *Sci Rep*. 2018;8(1):9033.
120. Dettmer U, Newman AJ, Soldner F, Luth ES, Kim NC, von Saucken VE, et al. Parkinson-causing alpha-synuclein missense mutations shift native tetramers to monomers as a mechanism for disease initiation. *Nat Commun*. 2015;6:7314.
121. Cooper O, Seo H, Andrabi S, Guardia-Laguarta C, Graziotto J, Sundberg M, et al. Pharmacological rescue of mitochondrial deficits in iPSC-derived neural cells from patients with familial Parkinson's disease. *Sci Transl Med*. 2012;4(141):141ra90.
122. Reinhardt P, Schmid B, Burbulla LF, Schondorf DC, Wagner L, Glatz M, et al. Genetic correction of a LRRK2 mutation in human iPSCs links parkinsonian neurodegeneration to ERK-dependent changes in gene expression. *Cell Stem Cell*. 2013;12(3):354-67.
123. Nguyen HN, Byers B, Cord B, Shcheglovitov A, Byrne J, Gujar P, et al. LRRK2 mutant iPSC-derived DA neurons demonstrate increased susceptibility to oxidative stress. *Cell Stem Cell*. 2011;8(3):267-80.
124. Byers B, Lee HL, Reijo Pera R. Modeling Parkinson's disease using induced pluripotent stem cells. *Curr Neurol Neurosci Rep*. 2012;12(3):237-42.
125. Sanders LH, Laganieri J, Cooper O, Mak SK, Vu BJ, Huang YA, et al. LRRK2 mutations cause mitochondrial DNA damage in iPSC-derived neural cells from Parkinson's disease patients: reversal by gene correction. *Neurobiol Dis*. 2014;62:381-6.
126. Hsieh CH, Shaltouki A, Gonzalez AE, Bettencourt da Cruz A, Burbulla LF, St Lawrence E, et al. Functional Impairment in Mito Degradation and Mitophagy Is a Shared Feature in Familial and Sporadic Parkinson's Disease. *Cell Stem Cell*. 2016;19(6):709-24.
127. Schwab AJ, Sison SL, Meade MR, Broniowska KA, Corbett JA, Ebert AD. Decreased Sirtuin Deacetylase Activity in LRRK2 G2019S iPSC-Derived Dopaminergic Neurons. *Stem Cell Reports*. 2017;9(6):1839-52.
128. Su YC, Qi X. Inhibition of excessive mitochondrial fission reduced aberrant autophagy and neuronal damage caused by LRRK2 G2019S mutation. *Hum Mol Genet*. 2013;22(22):4545-61.
129. Liu GH, Qu J, Suzuki K, Nivet E, Li M, Montserrat N, et al. Progressive degeneration of human neural stem cells caused by pathogenic LRRK2. *Nature*. 2012;491(7425):603-7.
130. Sanchez-Danes A, Richaud-Patin Y, Carballo-Carbajal I, Jimenez-Delgado S, Caig C, Mora S, et al. Disease-specific phenotypes in dopamine neurons from human iPSC-based models of genetic and sporadic Parkinson's disease. *EMBO Mol Med*. 2012;4(5):380-95.
131. Orenstein SJ, Kuo SH, Tasset I, Arias E, Koga H, Fernandez-Carasa I, et al. Interplay of LRRK2 with chaperone-mediated autophagy. *Nat Neurosci*. 2013;16(4):394-406.
132. Borgs L, Peyre E, Alix P, Hanon K, Grobarczyk B, Godin JD, et al. Dopaminergic neurons differentiating from LRRK2 G2019S induced pluripotent stem cells show early neuritic branching defects. *Sci Rep*. 2016;6:33377.
133. Qing X, Walter J, Jarazo J, Arias-Fuenzalida J, Hillje AL, Schwamborn JC. CRISPR/Cas9 and piggyBac-mediated footprint-free LRRK2-G2019S knock-in reveals neuronal complexity phenotypes and alpha-Synuclein modulation in dopaminergic neurons. *Stem Cell Res*. 2017;24:44-50.
134. Kononova EV, Novosadova EV, Grivennikov IA, Illarionov SN. Phenotypical Differences in Neuronal Cultures Derived via Reprogramming the Fibroblasts from Patients Carrying Mutations in Parkinsonian Genes LRRK2 and PARK2. *Bull Exp Biol Med*. 2015;159(6):772-5.
135. Momcilovic O, Sivapatham R, Oron TR, Meyer M, Mooney S, Rao MS, et al. Derivation, Characterization, and Neural Differentiation of Integration-Free Induced Pluripotent Stem Cell Lines from Parkinson's Disease Patients Carrying SNCA, LRRK2, PARK2, and GBA Mutations. *PLoS One*. 2016;11(5):e0154890.
136. Ohta E, Nihira T, Uchino A, Imaizumi Y, Okada Y, Akamatsu W, et al. I2020T mutant LRRK2 iPSC-derived neurons in the Sagami-hara family exhibit increased Tau phosphorylation through the AKT/GSK-3beta signaling pathway. *Hum Mol Genet*. 2015;24(17):4879-900.
137. Chuang CL, Lu YN, Wang HC, Chang HY. Genetic dissection reveals that Akt is the critical kinase downstream of LRRK2 to phosphorylate and inhibit FOXO1, and promotes neuron survival. *Hum Mol Genet*. 2014;23(21):5649-58.
138. Yoon JH, Mo JS, Kim MY, Ann EJ, Ahn JS, Jo EH, et al. LRRK2 functions as a scaffolding kinase of ASK1-mediated neuronal cell death. *Biochim Biophys Acta*. 2017;1864(12):2356-68.
139. Seibler P, Graziotto J, Jeong H, Simunovic F, Klein C, Krainc D. Mitochondrial Parkin recruitment is impaired in neurons derived from mutant PINK1 induced pluripotent stem cells. *J Neurosci*. 2011;31(16):5970-6.
140. Rakovic A, Shurkewitsch K, Seibler P, Grunewald A, Zanon A, Hagenah J, et al. Phosphatase and tensin homolog (PTEN)-induced putative kinase 1 (PINK1)-dependent ubiquitination of endogenous Parkin attenuates mitophagy: study in human primary fibroblasts and induced pluripotent stem cell-derived neurons. *J Biol Chem*. 2013;288(4):2223-37.
141. Jiang H, Ren Y, Yuen EY, Zhong P, Ghaedi M, Hu Z, et al. Parkin controls dopamine utilization in human midbrain dopaminergic neurons derived from induced pluripotent stem cells. *Nat Commun*. 2012;3:668.
142. Imaizumi Y, Okada Y, Akamatsu W, Koike M, Kuzumaki N, Hayakawa H, et al. Mitochondrial dysfunction associated with increased oxidative stress and alpha-synuclein accumulation in PARK2 iPSC-derived neurons and postmortem brain tissue. *Mol Brain*. 2012;5:35.

143. Chung SY, Kishinevsky S, Mazzulli JR, Graziotto J, Mrejeru A, Mosharov EV, et al. Parkin and PINK1 Patient iPSC-Derived Midbrain Dopamine Neurons Exhibit Mitochondrial Dysfunction and alpha-Synuclein Accumulation. *Stem Cell Reports*. 2016;7(4):664-77.
144. Shaltouki A, Sivapatham R, Pei Y, Gerencser AA, Momcilovic O, Rao MS, et al. Mitochondrial alterations by PARK1 in dopaminergic neurons using PARK2 patient-specific and PARK2 knockout isogenic iPSC lines. *Stem Cell Reports*. 2015;4(5):847-59.
145. Ren Y, Jiang H, Hu Z, Fan K, Wang J, Janoschka S, et al. Parkin mutations reduce the complexity of neuronal processes in iPSC-derived human neurons. *Stem Cells*. 2015;33(1):68-78.
146. Azkona G, Lopez de Maturana R, Del Rio P, Sousa A, Vazquez N, Zubarrain A, et al. LRRK2 Expression Is Deregulated in Fibroblasts and Neurons from Parkinson Patients with Mutations in PINK1. *Mol Neurobiol*. 2018;55(1):506-16.
147. Mazzulli JR, Zunke F, Tsunemi T, Toker NJ, Jeon S, Burbulla LF, et al. Activation of beta-Glucocerebrosidase Reduces Pathological alpha-Synuclein and Restores Lysosomal Function in Parkinson's Patient Midbrain Neurons. *J Neurosci*. 2016;36(29):7693-706.
148. Murphy KE, Cottle L, Gysbers AM, Cooper AA, Halliday GM. ATP13A2 (PARK9) protein levels are reduced in brain tissue of cases with Lewy bodies. *Acta Neuropathol Commun*. 2013;1:11.
149. Parodi L, Coarelli G, Stevanin G, Brice A, Durr A. Hereditary ataxias and paraparesias: clinical and genetic update. *Curr Opin Neurol*. 2018;31(4):462-71.
150. Al Zaaibi N, Al Menhali N, Al-Jasmi F. SYNJ1 gene associated with neonatal onset of neurodegenerative disorder and intractable seizure. *Mol Genet Genomic Med*. 2018;6(1):109-13.
151. Dymont DA, Smith AC, Humphreys P, Schwartzentruber J, Beaulieu CL, Consortium F, et al. Homozygous nonsense mutation in SYNJ1 associated with intractable epilepsy and tau pathology. *Neurobiol Aging*. 2015;36(2):1222 e1-5.
152. Hardies K, Cai Y, Jardel C, Jansen AC, Cao M, May P, et al. Loss of SYNJ1 dual phosphatase activity leads to early onset refractory seizures and progressive neurological decline. *Brain*. 2016;139(Pt 9):2420-30.
153. Miranda AM, Herman M, Cheng R, Nahmani E, Barrett G, Micevska E, et al. Excess Synaptotagmin 1 Contributes to Place Cell Dysfunction and Memory Deficits in the Aging Hippocampus in Three Types of Alzheimer's Disease. *Cell Rep*. 2018;23(10):2967-75.
154. Cossec JC, Lavaur J, Berman DE, Rivals I, Hoischen A, Stora S, et al. Trisomy for synaptotagmin1 in Down syndrome is functionally linked to the enlargement of early endosomes. *Hum Mol Genet*. 2012;21(14):3156-72.
155. Dehay B, Ramirez A, Martinez-Vicente M, Perier C, Canon MH, Doudnikoff E, et al. Loss of P-type ATPase ATP13A2/PARK9 function induces general lysosomal deficiency and leads to Parkinson disease neurodegeneration. *Proc Natl Acad Sci U S A*. 2012;109(24):9611-6.
156. Ludtmann MHR, Angelova PR, Horrocks MH, Choi ML, Rodrigues M, Baev AY, et al. alpha-synuclein oligomers interact with ATP synthase and open the permeability transition pore in Parkinson's disease. *Nat Commun*. 2018;9(1):2293.
157. Haenseler W, Zambon F, Lee H, Vowles J, Rinaldi F, Duggal G, et al. Excess alpha-synuclein compromises phagocytosis in iPSC-derived macrophages. *Sci Rep*. 2017;7(1):9003.
158. Paillusson S, Gomez-Suaga P, Stoica R, Little D, Gissen P, Devine MJ, et al. alpha-Synuclein binds to the ER-mitochondria tethering protein VAPB to disrupt Ca(2+) homeostasis and mitochondrial ATP production. *Acta Neuropathol*. 2017;134(1):129-49.
159. Vasquez V, Mitra J, Hegde PM, Pandey A, Sengupta S, Mitra S, et al. Chromatin-Bound Oxidized alpha-Synuclein Causes Strand Breaks in Neuronal Genomes in vitro Models of Parkinson's Disease. *J Alzheimers Dis*. 2017;60(s1):S133-S50.
160. Lin X, Parisiadou L, Sgobio C, Liu G, Yu J, Sun L, et al. Conditional expression of Parkinson's disease-related mutant alpha-synuclein in the midbrain dopaminergic neurons causes progressive neurodegeneration and degradation of transcription factor nuclear receptor related 1. *J Neurosci*. 2012;32(27):9248-64.
161. Kouroupi G, Taoufik E, Vlachos IS, Tsiaras K, Antoniou N, Papastefanaki F, et al. Defective synaptic connectivity and axonal neuropathology in a human iPSC-based model of familial Parkinson's disease. *Proc Natl Acad Sci U S A*. 2017;114(18):E3679-E88.
162. Sanchez-Danes A, Consiglio A, Richaud Y, Rodriguez-Piza I, Dehay B, Edel M, et al. Efficient generation of A9 midbrain dopaminergic neurons by lentiviral delivery of LMX1A in human embryonic stem cells and induced pluripotent stem cells. *Hum Gene Ther*. 2012;23(1):56-69.
163. Fernandez-Santiago R, Carballo-Carbajal I, Castellano G, Torrent R, Richaud Y, Sanchez-Danes A, et al. Aberrant epigenome in iPSC-derived dopaminergic neurons from Parkinson's disease patients. *EMBO Mol Med*. 2015;7(12):1529-46.
164. Ho DH, Kim H, Kim J, Sim H, Ahn H, Kim J, et al. Leucine-Rich Repeat Kinase 2 (LRRK2) phosphorylates p53 and induces p21(WAF1/CIP1) expression. *Mol Brain*. 2015;8:54.
165. Schwab AJ, Ebert AD. Neurite Aggregation and Calcium Dysfunction in iPSC-Derived Sensory Neurons with Parkinson's Disease-Related LRRK2 G2019S Mutation. *Stem Cell Reports*. 2015;5(6):1039-52.
166. Lopez de Maturana R, Lang V, Zubarrain A, Sousa A, Vazquez N, Gorostidi A, et al. Mutations in LRRK2 impair NF-kappaB pathway in iPSC-derived neurons. *J Neuroinflammation*. 2016;13(1):295.
167. Speidel A, Felk S, Reinhardt P, Sterneckert J, Gillardon F. Leucine-Rich Repeat Kinase 2 Influences Fate Decision of Human Monocytes Differentiated from Induced Pluripotent Stem Cells. *PLoS One*. 2016;11(11):e0165949.
168. Sandor C, Robertson P, Lang C, Heger A, Booth H, Vowles J, et al. Transcriptomic profiling of purified patient-derived dopamine neurons identifies convergent perturbations and therapeutics for Parkinson's disease. *Hum Mol Genet*. 2017;26(3):552-66.
169. Son MY, Sim H, Son YS, Jung KB, Lee MO, Oh JH, et al. Distinctive genomic signature of neural and intestinal organoids from familial Parkinson's disease patient-derived induced pluripotent stem cells. *Neuropathol Appl Neurobiol*. 2017;43(7):584-603.
170. Tan KKB, Lim WWM, Chai C, Kukumberg M, Lim KL, Goh ELK, et al. Sequential Application of Discrete Topographical Patterns Enhances Derivation of Functional Mesencephalic Dopaminergic Neurons from Human Induced Pluripotent Stem Cells. *Sci Rep*. 2018;8(1):9567.
171. Tolosa E, Botta-Orfila T, Morato X, Calatayud C, Ferrer-Lorente R, Martí MJ, et al. MicroRNA alterations in iPSC-derived dopaminergic neurons from Parkinson disease patients. *Neurobiol Aging*. 2018;69:283-91.
172. Suda Y, Kuzumaki N, Sone T, Narita M, Tanaka K, Hamada Y, et al. Down-regulation of ghrelin receptors on dopaminergic neurons in the substantia nigra contributes to Parkinson's disease-like motor dysfunction. *Mol Brain*. 2018;11(1):6.
173. Paik EJ, O'Neil AL, Ng SY, Sun C, Rubin LL. Using intracellular markers to identify a novel set of surface markers for live cell purification from a heterogeneous hiPSC culture. *Sci Rep*. 2018;8(1):804.
174. Chung WS, Welsh CA, Barres BA, Stevens B. Do glia drive synaptic and cognitive impairment in disease? *Nat Neurosci*. 2015;18(11):1539-45.



175. Bunk EC, Ertaylan G, Ortega F, Pavlou MA, Gonzalez Cano L, Stergiopoulos A, et al. Prox1 Is Required for Oligodendrocyte Cell Identity in Adult Neural Stem Cells of the Subventricular Zone. *Stem Cells*. 2016;34(8):2115-29.
176. White RB, Thomas MG. Moving beyond tyrosine hydroxylase to define dopaminergic neurons for use in cell replacement therapies for Parkinson's disease. *CNS Neurol Disord Drug Targets*. 2012;11(4):340-9.
177. Tank AW, Xu L, Chen X, Radcliffe P, Sterling CR. Post-transcriptional regulation of tyrosine hydroxylase expression in adrenal medulla and brain. *Ann N Y Acad Sci*. 2008;1148:238-48.
178. Bevan MD, Magill PJ, Terman D, Bolam JP, Wilson CJ. Move to the rhythm: oscillations in the subthalamic nucleus-external globus pallidus network. *Trends Neurosci*. 2002;25(10):525-31.
179. Ellens DJ, Leventhal DK. Review: electrophysiology of basal ganglia and cortex in models of Parkinson disease. *J Parkinsons Dis*. 2013;3(3):241-54.
180. Joe EH, Choi DJ, An J, Eun JH, Jou I, Park S. Astrocytes, Microglia, and Parkinson's Disease. *Exp Neurobiol*. 2018;27(2):77-87.
181. Yan J, Fu Q, Cheng L, Zhai M, Wu W, Huang L, et al. Inflammatory response in Parkinson's disease (Review). *Mol Med Rep*. 2014;10(5):2223-33.
182. Bruck D, Wenning GK, Stefanova N, Fellner L. Glia and alpha-synuclein in neurodegeneration: A complex interaction. *Neurobiol Dis*. 2016;85:262-74.
183. LaMarca EA, Powell SK, Akbarian S, Brennand KJ. Modeling Neuropsychiatric and Neurodegenerative Diseases With Induced Pluripotent Stem Cells. *Front Pediatr*. 2018;6:82.
184. Miller JD, Ganat YM, Kishinevsky S, Bowman RL, Liu B, Tu EY, et al. Human iPSC-based modeling of late-onset disease via progerin-induced aging. *Cell Stem Cell*. 2013;13(6):691-705.
185. Hu BY, Weick JP, Yu J, Ma LX, Zhang XQ, Thomson JA, et al. Neural differentiation of human induced pluripotent stem cells follows developmental principles but with variable potency. *Proc Natl Acad Sci U S A*. 2010;107(9):4335-40.
186. de Boni L, Gasparoni G, Haubenreich C, Tierling S, Schmitt I, Peitz M, et al. DNA methylation alterations in iPSC- and hESC-derived neurons: potential implications for neurological disease modeling. *Clin Epigenetics*. 2018;10:13.
187. Honda A, Hatori M, Hirose M, Honda C, Izu H, Inoue K, et al. Naive-like conversion overcomes the limited differentiation capacity of induced pluripotent stem cells. *J Biol Chem*. 2013;288(36):26157-66.
188. Altshuler A, Verbuk M, Bhattacharya S, Abramovich I, Haklai R, Hanna JH, et al. RAS Regulates the Transition from Naive to Primed Pluripotent Stem Cells. *Stem Cell Reports*. 2018;10(3):1088-101.
189. Brederlau A, Correia AS, Anisimov SV, Elmi M, Paul G, Roybon L, et al. Transplantation of human embryonic stem cell-derived cells to a rat model of Parkinson's disease: effect of in vitro differentiation on graft survival and teratoma formation. *Stem Cells*. 2006;24(6):1433-40.
190. Ahrlund-Richter L, De Luca M, Marshak DR, Munsie M, Veiga A, Rao M. Isolation and production of cells suitable for human therapy: challenges ahead. *Cell Stem Cell*. 2009;4(1):20-6.
191. Soldner F, Hockemeyer D, Beard C, Gao Q, Bell GW, Cook EG, et al. Parkinson's disease patient-derived induced pluripotent stem cells free of viral reprogramming factors. *Cell*. 2009;136(5):964-77.
192. Lehnen D, Barral S, Cardoso T, Grealish S, Heuer A, Smiyakin A, et al. IAP-Based Cell Sorting Results in Homogeneous Transplantable Dopaminergic Precursor Cells Derived from Human Pluripotent Stem Cells. *Stem Cell Reports*. 2017;9(4):1207-20.



# The SAC1 domain in Synaptojanin is required for autophagosome maturation at pre-synaptic terminals

Roeland Vanhauwaert, Sabine Kuenen, [Roy Masius](#), Adekunle Bademosi, Julia Manetsberger, Nils Schoovaerts, Laura Bounti, Serguei Gontcharenko, Jef Swerts, Sven Vilain, Marina Picillo, Paolo Barone, Shashini T. Munshi , Femke M.S. de Vrij, Steven A. Kushner, Natalia V. Gounko, Wim Mandemakers, Vincenzo Bonifati, Frederic A. Meunier, Sandra-Fausia Soukup and Patrik Verstreken

EMBO Journal 2017; 36(10):1392-1411.

## Summary

Presynaptic terminals are metabolically active and accrue damage through continuous vesicle cycling. How synapses locally regulate protein homeostasis is poorly understood. We show that the presynaptic lipid phosphatase synaptojanin is required for macroautophagy, and this role is inhibited by the Parkinson's disease mutation R258Q. Synaptojanin drives synaptic endocytosis by dephosphorylating PI(4,5)P<sub>2</sub>, but this function appears normal in *Synaptojanin*<sup>RQ</sup> knock-in flies. Instead, R258Q affects the synaptojanin SAC1 domain that dephosphorylates PI(3)P and PI(3,5)P<sub>2</sub>, two lipids found in autophagosomal membranes. Using advanced imaging, we show that *Synaptojanin*<sup>RQ</sup> mutants accumulate the PI(3)P/PI(3,5)P<sub>2</sub>-binding protein Atg18a on nascent synaptic autophagosomes, blocking autophagosome maturation at fly synapses and in neurites of human patient induced pluripotent stem cell-derived neurons. Additionally, we observe neurodegeneration, including dopaminergic neuron loss, in *Synaptojanin*<sup>RQ</sup> flies. Thus, synaptojanin is essential for macroautophagy within presynaptic terminals, coupling protein turnover with synaptic vesicle cycling and linking presynaptic-specific autophagy defects to Parkinson's disease.

# Introduction

Presynaptic terminals are often distantly located from the neuronal cell body, hampering rapid transport of components between these subcellular compartments (1). Despite this physical separation, synapses maintain a functional protein pool to support efficient information transfer. They must do so even under conditions of intense synaptic activity that place high metabolic energy demands on this area of the cell. However, the mechanisms that regulate and maintain protein homeostasis at synapses are poorly characterized. Furthermore, impaired synaptic protein homeostasis is implicated in neurodegeneration where combined failure of protein quality control systems and synaptic defects are recurrent themes (2-4).

Parkinson's disease (PD) is a common neurodegenerative condition characterized by the loss of substantia nigra neurons alongside broader pathology in most patients. While ~90% of PD cases are idiopathic, at least 10% have a family history of disease and several causative genes are identified (5, 6). While these PD genes encode a functionally diverse set of proteins, there is an emerging theme that several act on synaptic vesicle trafficking (7-9). However, the nature and degree of synaptic vesicle trafficking impairment that is caused by pathogenic mutations remains unclear.

Synaptojanin1 (Synj1) is a lipid phosphatase that is essential for synaptic vesicle trafficking (10-13). It is also mutated in several different families with hereditary early-onset PD (14-17). Synj1 is evolutionarily well conserved and enriched at synapses (10, 11, 13, 18). The protein has two different lipid phosphatase domains, 5-phosphatase and SAC1, that target different phosphoinositide phosphate (PtdInsP) species. The 5-phosphatase domain specifically hydrolyzes phosphates on the 5' position of the inositol ring and has a preference for PI(4,5)P<sub>2</sub> as a substrate (19, 20). In contrast, the SAC1 domain hydrolyzes PI(3)P, PI(4)P, and PI(3,5)P<sub>2</sub> (21, 22).

Differently phosphorylated PtdInsP lipids concentrate on different organelles or membrane subdomains. Many proteins recognize particular PtdInsP, and thus are recruited to a specific membrane. This underlies the concept that PtdInsP lipids act as molecular tags that confer membrane identity (23-27). For example, patches of PI(4,5)P<sub>2</sub> at the synaptic membrane bind Clathrin adaptors and other endocytic factors to promote synaptic vesicle formation adjacent to active zones. This PI(4,5)P<sub>2</sub>-dependent binding underlies why Synj1 is essential for synaptic vesicle cycling, whereby the 5-phosphatase domain hydrolysis of PI(4,5)P<sub>2</sub> lowers the membrane-binding affinity of endocytic

adaptors and uncoats newly formed vesicles (10, 13, 28). Other PtdInsPs are critical as well, for example, PI(4)P in Golgi membranes and PI(3)P in endosomes recruit specific proteins to the surface of these organelles. In addition, PI(3)P and PI(3,5)P<sub>2</sub> are essential during the formation of autophagosomes where they are recognized by proteins like Atg18/WIPI2 that promote autophagosome biogenesis (29-32).

The PD causing mutations (R258Q and the newly identified R459P) reside in the Synj1 SAC1 domain (14-17). The R258Q mutation blocks the dephosphorylation of PI(3)P and PI(4)P, while leaving 5-phosphatase activity against PI(4,5)P<sub>2</sub> unaffected (15). This strongly implicates disturbed presynaptic PtdInsP signaling in PD pathogenesis. Although, blocking Synj1 5-phosphatase activity in mouse neurons causes severe endocytic defects during intense stimulation. When SAC1-enzymatic function is inhibited synaptic vesicle cycling is only mildly affected (during weak stimulation) (33). This suggests the SAC1 and 5-phosphatase domains have distinct presynaptic functions, but currently little is known about which aspects of presynaptic cell biology are controlled by the Synj1 SAC1 domain.

In this work, we show that the Synj1-SAC1 domain drives autophagosome biogenesis within synapses independent from and in parallel to the well-described importance of Synj in endocytosis. We also provide evidence that both in flies and human neurons differentiated from patient-derived induced pluripotent stem cells (iPSC), the Synj1 SAC1 domain removes the PI(3)P/PI(3,5)P<sub>2</sub>-binding protein, WIPI2/Atg18a, from immature autophagosomes. This function appears analogous to how hydrolysis of PI(4,5)P<sub>2</sub> by Synj1 uncoats endocytic vesicles. Together with our recent finding that another synapse-enriched protein, EndophilinA, is essential for synaptic autophagosome biogenesis (34), these data highlight that the presynaptic terminal has unique mechanisms to induce and regulate autophagosome formation. Furthermore, these processes appear tightly connected to PD, potentially explaining the recurrent themes of synaptic dysfunction and protein homeostasis defects found in models of this neurodegenerative disease.

## Results

### The Parkinson's disease mutation R228Q in the synaptojanin 1 SAC1 domain does not affect synaptic vesicle endocytosis at fly excitatory glutamatergic neurons and photoreceptors

SYNJ1 is evolutionarily conserved from yeast to humans (Figure 1A and B). The human Parkinson's disease-causing R258Q mutation in *SYNJ1* blocks the dephosphorylation of specific phosphoinositides including PI(3)P and to assess the functional consequences of this mutation, we used MiMIC technology and knocked in the R228Q mutation (corresponding to the human R258Q) into the endogenous *Drosophila synj* locus (*synj<sup>RQ</sup>*) (Appendix Figure S1A) (35, 36). This *synj<sup>RQ</sup>* knock-in allele expresses Synj at a comparable level to the wild-type *synj* locus, indicating that the mutation does not affect protein stability (Appendix Figure S1B, C, and H). We also developed a second system to study Synj function, where we use the UAS/Gal4 system to transgenically overexpress wild-type or R228Q Synj in neurons of *synj* null mutant flies that otherwise lack Synj expression (*synj<sup>-/-</sup>; nSyb>UAS synj<sup>+</sup>* or *synj<sup>RQ</sup>*). We confirm similar expression of these transgenically expressed Synj<sup>+</sup> and Synj<sup>RQ</sup> proteins (~1.2 fold over the levels produced from the endogenous *synj* locus (Appendix Figure S1D-E,I)). We compared the subcellular localization of endogenous Synj against that produced from the R228Q knock-in locus, or transgenically expressed wild-type Synj<sup>+</sup> and Synj<sup>RQ</sup> proteins. We find that all concentrate in the presynaptic terminals of the larval neuromuscular junction (NMJ) (Appendix Figure S1F-G'', and J-M''), indicating the mutant protein localizes correctly and similar to the presynaptic protein EndoA (37).

*Synj* null mutant animals are not viable (Figure 1C), and deletion of *synj* specifically in the eye severely affects the efficiency of synaptic transmission between eye photoreceptors and the brain detected by electroretinogram (ERG) recordings (Figure 1D, arrowheads). As expected, these *Synj* null phenotypes are rescued by neuronal transgenic expression (*nSyb-Gal4*) of wild-type Synj<sup>+</sup>. Surprisingly, however, transgenic expression of the Synj<sup>RQ</sup> mutant is as effective as the wild-type protein (Figure 1C and D). Since even a partially active mutant might result in rescue of the phenotype when overexpressed, we confirmed that *synj<sup>RQ</sup>* knock-in flies are viable and that they too display normal ERGs (Figure 1D). Hence, it appears that the Synj<sup>RQ</sup> mutant protein retains core Synj activities that are essential for viability and synaptic communication in the eye.

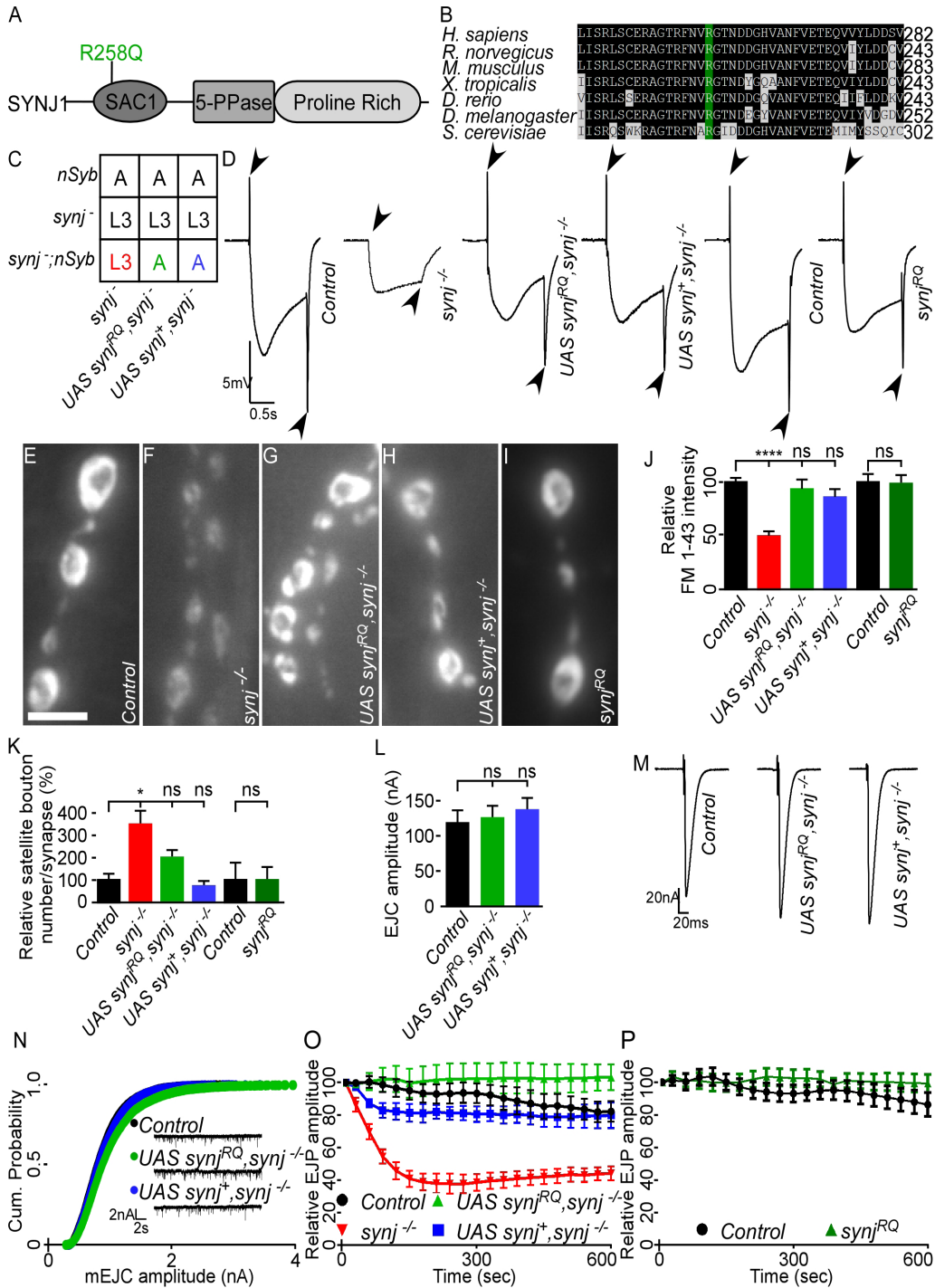




# Figure 1. The Parkinson's disease mutation R228Q in the Synj SAC1 domain does not affect synaptic vesicle cycling

- A** Diagram of human *Synj1* indicating the two polyphosphoinositide domains (SAC1 and 5-PPase) and the proline-rich domain. The SAC1 domain bears at position 258 an arginine to glutamine amino acid change causative for PD.
- B** Arginine at position 258 (green) in *Synj1* SAC1 domain and the surrounding region are highly conserved from yeast to human (R258 corresponds to R228 in *Drosophila*).
- C** Table indicating neuronal expression (*nSyb-Gal4*) of *Synj<sup>RQ</sup>* and *Synj<sup>\*</sup>* rescues the lethality of *synj* null mutants (*synj<sup>1/2</sup>* indicated as *synj<sup>-/-</sup>*), "A" and "L3" indicate lethality at the "adult stage" and at the "third-instar larval stage", respectively.
- D** Example average traces of ERGs of control animals (left, *nSyb-Gal4/+*), flies with *synj* null mutant eyes (*synj<sup>-/-</sup>*), flies with *synj* null mutant eyes expressing *synj<sup>RQ</sup>* or *synj<sup>\*</sup>* (UAS *synj<sup>RQ</sup>*, *synj<sup>-/-</sup>* and UAS *synj<sup>\*</sup>*, *synj<sup>-/-</sup>*), control animals (right, *w<sup>1118</sup>*), and *synj<sup>RQ</sup>* knock-in animals. Full genotypes appear in the Appendix Supplementary Methods. "ON" and "OFF" peaks are indicated with arrowheads. Note that while *synj* null mutants display severe defects in their ERG traces, *synj<sup>RQ</sup>* mutants do not. *n* > 20 animals per genotype.
- E–J** Representative images of boutons loaded (1 min, 90 mM KCl) with FM 1-43 (**E–I**) and quantification (**J**) of the following genotypes: control (left, *D42-Gal4/+*) (**E**), *synj* null mutants (*synj<sup>-/-</sup>*) (**F**), *synj* null mutants that express *synj<sup>RQ</sup>* (**G**), or *synj<sup>\*</sup>* (**H**) (UAS *synj<sup>RQ</sup>*, *synj<sup>-/-</sup>* and UAS *synj<sup>\*</sup>*, *synj<sup>-/-</sup>*), control animals (right, *w<sup>1118</sup>*; image not shown, only quantification is included) and *synj<sup>RQ</sup>* knock-in animals (**I**). Full genotypes appear in the Appendix Supplementary Methods. Scale bar, 5  $\mu$ m. Note that *synj<sup>RQ</sup>* internalizes as much FM 1-43 as controls do. For UAS experiments, statistical analysis with one-way ANOVA Kruskal–Wallis followed by Dunn's multiple comparison post hoc test, \*\*\*\**P* < 0.0001; ns, not significant; *n*  $\geq$  7 larvae and *n*  $\geq$  14 NMJs per genotype. For *synj<sup>RQ</sup>* experiment: t-test, *P* > 0.05, *n*=10 larvae and *n*=20 NMJs per genotype. Error bars represent SEM.
- K** Quantification of the number of satellite boutons per NMJ of the genotypes in (**E–I**). Note that while *synj* null mutants harbor numerous satellite boutons, *synj<sup>RQ</sup>* mutants do not. Statistical analysis for UAS experiments: one-way ANOVA Kruskal–Wallis followed by Dunn's multiple comparison post hoc test, \**P* < 0.05, *n*  $\geq$  4 larvae and *n*  $\geq$  16 NMJs per genotype. For *Synj<sup>RQ</sup>* experiment: t-test, *P* > 0.05, *n*=6 larvae and *n*  $\geq$  14 NMJs. Error bars represent SEM.
- L, M** Quantification (**L**) of the EJC amplitude recorded at third-instar larval NMJs of the indicated genotypes (see also **E–I**) and sample EJC traces (**M**). Statistical analysis, one-way ANOVA Kruskal–Wallis followed by Dunn's multiple comparison post hoc test, *P* > 0.05, *n*  $\geq$  8 larvae per genotype. Error bars represent SEM.
- N** Cumulative histograms of mEJC amplitudes and sample EJC traces recorded at third-instar larval NMJs of the indicated genotypes (see also **E–I**). *n*  $\geq$  7 larvae for indicated genotypes.
- O, P** Relative EJP amplitudes recorded during a 10-min 10-Hz stimulation train of the genotypes indicated in (**E–I**). Please see Materials and Methods for details. Data for the *synj* null mutants that express *synj<sup>RQ</sup>* or *synj<sup>\*</sup>* are not significantly different from control (*D42-Gal4/+*), whereas a significant difference is observed from data point 3 till the end of the recording of *synj* null mutants (*synj<sup>-/-</sup>*) compared to control (ns: data points 1–2, \**P* < 0.05; data point 3, \*\**P* < 0.01; data points 4, 16–21, \*\*\**P* < 0.001; data points 5, 13–15, \*\*\*\**P* < 0.0001; data points 6–12). Statistical analysis for UAS experiments: one-way ANOVA Kruskal–Wallis followed by Dunn's multiple comparison post hoc test, *n*  $\geq$  4 larvae indicated genotypes in (**O**). Data for *Synj<sup>RQ</sup>* compared to control are not significantly different. Statistical analysis by t-test, *P* > 0.05, and *n*  $\geq$  8 larvae for indicated genotypes in (**P**). Error bars represent the SEM. Note that *synj* null mutants do not maintain neurotransmitter release whereas the *synj<sup>RQ</sup>* mutants maintain release similar to controls.

*Synj* is best defined as the protein that uncoats newly endocytosed synaptic vesicles (10, 11, 13). To directly examine whether R228Q affects this endocytic function, we performed FM 1-43 fluorescent dye labeling at the excitatory glutamatergic *Drosophila* NMJ. FM 1-43 binds membranes and is incorporated into and labels newly formed synaptic vesicles, thereby labeling synaptic boutons proportional to the amount of vesicle recycling and thus synaptic endocytosis (38). As previously described, *synj* loss significantly reduces FM 1-43 labeling compared to controls (13). This labeling is restored by neuronal expression of wild-type *synj*, and again also by *Synj<sup>RQ</sup>* (Figure 1E–H and J). We confirmed that *Synj<sup>RQ</sup>* rescues the *synj*-knock out phenotype independent of overexpression by finding normal FM 1-43 dye uptake in *synj<sup>RQ</sup>* knock-in animals (Figure 1I and J). Thus FM 1-43 labeling suggests that *Synj<sup>RQ</sup>* supports presynaptic vesicle recycling and, under the conditions we tested, does so as efficiently as wild-type *Synj*.

The disruption of NMJ endocytosis often correlates with morphological defects. These also occur in the *synj* null mutants in the form of numerous satellite boutons that are small protrusions emanating from the primary axial branch (39). We therefore examined whether *Synj*<sup>RQ</sup> possesses sufficient *Synj* activity to suppress this defect. We find a significant rescue of this *synj*-null mutant-associated satellite bouton phenotype in *synj* null mutants that transgenically express wild-type *Synj*<sup>+</sup> or mutant *Synj*<sup>RQ</sup>. We also observe no difference in satellite bouton number between *synj*<sup>RQ</sup> knock-in animals and controls (Figure 1K). Hence, *Synj*<sup>RQ</sup> appears to allow enough endocytosis to suppress this classic read-out of NMJ endocytic defects, and is markedly different to the *synj* null allele.

We next directly examined how well *Synj*<sup>RQ</sup> supports neurotransmission at the larval NMJ. First, we measured basal release characteristics including miniature excitatory junctional currents (mEJC) and EJCs. In controls and *synj* null mutants expressing *Synj*<sup>+</sup> or *Synj*<sup>RQ</sup>, no difference is observed in mEJC and EJC amplitude nor in frequency (Figure 1LN). We then stimulated the motor nerves for 10 min at 10 Hz to continuously drive synaptic vesicle exo- and endocytosis, and measured the post synaptic excitatory junctional potentials (EJP). While control NMJs maintain neurotransmitter release under these conditions, *synj* null mutants fail to do so, and the block in endocytosis causes the EJP amplitude to drop to a low level in the first minutes of stimulation (Figure 1O) (13). This neurotransmission defect is rescued by transgenic neuronal expression of wild-type *Synj*<sup>+</sup>, or *Synj*<sup>RQ</sup> (Figure 1O). Here also, *synj*<sup>RQ</sup> knock-in animals maintain release during this 10 Hz stimulation train at a level comparable to controls (Figure 1P). *Synj*<sup>RQ</sup> was previously shown to lack SAC1 domain phosphatase activity (15) and our data now suggest that the *Synj*<sup>RQ</sup> mutant protein can support synaptic vesicle cycling. These results are consistent with data obtained in mouse cortical neurons using SAC1-dead *Synj1* mutants that also supported vesicle recycling during persistent activity (33).

## Synaptojanin is required for autophagosome formation in presynaptic terminals

Given that *Synj* is strongly enriched at presynaptic terminals (13), *Synj1*<sup>R258Q</sup> lacks PI(3)P phosphatase activity (15), and the importance of PI(3)P on autophagosomes (30, 32, 40-42), we hypothesized that the *Synj* SAC1 domain acts in synaptic autophagy. We and others recently showed the presence of autophagic markers at presynaptic terminals (34, 43-49). To determine if *Synj* localizes on autophagic membranes we examined the interaction between *Synj* and the transmembrane *Atg9* marker of early pre-autophagosomal membranes (45, 50-52). The distribution of a genomic *Atg9*<sup>HA</sup>

construct where Atg9<sup>HA</sup> is expressed under endogenous promotor control is broad (Appendix Figure S2A-A''), consistent with the idea that Atg9 decorates early autophagic vesicles and autophagosomes. Next, we used anti-HA to immunoprecipitate neuronal autophagosomal membranes from fly heads expressing Atg9<sup>HA</sup> at endogenous levels. We detect the co-immunoprecipitation of Synj with the Atg9-positive membrane fraction in both wild-type and *synj<sup>RQ</sup>* knock-in animals expressing Atg9<sup>HA</sup> (Figure 2A). In contrast and indicating specificity, other synaptic proteins (alpha-SNAP and Complexin) do not co-immunoprecipitate (Figure 2A).

Next, we assessed whether Synj is important for presynaptic autophagy. Such a role had recently been suggested in zebrafish cone photoreceptors (53). We expressed transgenes for the Atg8<sup>mCherry</sup> (fly LC-3) marker of mature autophagosomes (54) and Lamp1<sup>GFP</sup>, an autolysosomal marker (55, 56), in motor neurons using D42-Gal4. In control animals, autophagy induced by starvation (amino acid deprivation) is marked by the presence of punctate dots of Atg8<sup>mCherry</sup> signal within presynaptic terminals (Figure 2B, B', and G) that we previously characterized by correlative light and electron microscopy (CLEM) as synaptic autophagosome-like structures (34). Moreover, boutons of starved control animals also accumulate the Lamp1<sup>GFP</sup> marker (Appendix Figure S2B, B', and F). In contrast, in *synj* null mutants and *synj* null mutants that express Synj<sup>RQ</sup>, the Atg8<sup>mCherry</sup> and Lamp1<sup>GFP</sup> redistribution is blocked (Figure 2C-D' and G, and Appendix Figure S2C-D' and F). Unlike our findings with Synj-driven endocytosis, we observe that only wild-type Synj<sup>+</sup>, and not Synj<sup>RQ</sup>, can recover the Synj function in presynaptic autophagy (Figure 2F and G, and Appendix Figure S2E and F). Our results are also not unique to "starvation-induced autophagy" because when we induce the process by direct electrical motor neuron stimulation (30 min 20 Hz) (34), the clear increase in the number of Atg8 dots observed in controls is absent in *synj<sup>RQ</sup>* mutants (Figure 2H-J).

To scrutinize our results further and provide evidence that the block in synaptic autophagy is caused by the lack of SAC1 activity, we created flies that express Synj<sup>C396S</sup> (Synj<sup>CS</sup>), a SAC1 enzymatic dead mutant (33). We expressed Synj<sup>CS</sup> in *synj<sup>-/-</sup>* null mutants under the same conditions as used to express Synj<sup>RQ</sup> using *D42-Gal4* driver. We then assessed Atg8<sup>mCherry</sup> localization and found that Atg8<sup>mCherry</sup> also does not concentrate in dots upon induction of starvation (Figure 2E, E', and G). These data are in further support of the notion that Synj SAC1 domain function is required for synaptic autophagy and that the pathogenic PD mutant Synj behaves in this respect similar to a Synj-SAC1 domain mutant.



## Figure 2. Synptojanin is required for synaptic autophagy

- A** Western blot of an anti-HA immunoprecipitation from control fly heads (*w<sup>1118</sup>*), *Atg9<sup>HA</sup>*-expressing fly heads (*w<sup>1118</sup>;Atg9<sup>HA</sup>*) and *w<sup>1118</sup>;synj<sup>RQ</sup>;Atg9<sup>HA</sup>*. Blots probed with anti-Synj to assess whether Synj (predicted 134 kDa) is present on Atg9-positive structures; anti-HA to assess immunoprecipitation specificity, *Atg9<sup>HA</sup>* (predicted 96 kDa). As control alpha-SNAP (33 kDa) and complexin (*cpx*; 18 kDa) were probed. Experiments were performed in independent duplicates.
- B–G** Live imaging of fed (B–F) and 4-h-starved (B'–F') NMJ boutons of control (*D42-Gal4 > Atg8<sup>mCherry</sup>*) (B, B') and *synj<sup>-/-</sup>* null mutants (C, C') either expressing *synj<sup>RQ</sup>* (D, D') or *synjCS* (E, E') or *synj<sup>\*</sup>* (F, F') and also expressing *Atg8<sup>mCherry</sup>* (*D42-Gal4 > Atg8<sup>mCherry</sup>*). Full genotypes are included in the Appendix Supplementary Methods section. Quantification of the number of *Atg8<sup>mCherry</sup>* dots (arrowheads) (G). Statistical analysis with one-way ANOVA Kruskal–Wallis followed by Dunn's multiple comparison post hoc test, \*\*\*\**P* < 0.0001, \*\*\**P* < 0.001, and each genotype individually fed and starved by t-test, \*\*\*\**P* < 0.0001, *n* ≥ 9 larvae and *n* ≥ 18 NMJs per genotype. Error bars represent SEM; scale bar, 5 μm. Note that loss of Synj blocks the formation of *Atg8<sup>mCherry</sup>* dots and this is not rescued by expression of *synj<sup>RQ</sup>* nor *synjCS*.
- H–J** Live *Atg8<sup>mCherry</sup>* imaging following 30 min of 20-Hz electrical nerve stimulation of indicated genotypes (H, I). Full genotypes are included in the Appendix Supplementary Methods. Quantification of *Atg8<sup>mCherry</sup>* dots (arrowheads) (J). Statistical analysis by t-test, \*\**P* < 0.01, *n* ≥ 8 larvae and *n* ≥ 33 NMJs per genotype. Error bars represent SEM; scale bar, 5 μm.
- K–M** Images of NMJ boutons of *synj<sup>-/-</sup>* null mutants either expressing *synj<sup>\*</sup>* (K) or *synj<sup>RQ</sup>* (L) and also expressing *Atg8<sup>mCherry</sup>* (*D42-Gal4 > Atg8<sup>mCherry</sup>*) fed (data from G) and fed or starved for 4 h with chloroquine and labeled with anti-mCherry antibodies. Quantification of the number of *Atg8<sup>mCherry</sup>* dots (arrows) of indicated genotypes (in detail in the Appendix Supplementary Methods) (M). Statistical analysis by t-test, \*\*\*\**P* < 0.0001, \*\**P* < 0.01, *n* ≥ 9 larvae and *n* ≥ 18 NMJs per genotype. Error bars represent SEM; scale bar, 5 μm. Despite that chloroquine blocks autophagosome to lysosome fusion, *Atg8<sup>mCherry</sup>* dots still do not form in animals expressing *synj<sup>RQ</sup>*.

Next, to distinguish whether loss of Synj SAC1 function blocks autophagosome formation or promotes autophagosome degradation, we pharmacologically blocked the fusion of autophagosomes with late endosomes/lysosomes using chloroquine (57, 58). Subsequently, we monitored *Atg8<sup>mCherry</sup>* localization. As expected in wild-type controls, chloroquine under fed or starved conditions causes an increase in the number of *Atg8<sup>mCherry</sup>* dots. In contrast, in *synj<sup>RQ</sup>* mutants, chloroquine does not result in such an increase in the number of *Atg8<sup>mCherry</sup>* dots (Figure 2K–M), suggesting autophagosome biogenesis is slowed. We provide further evidence for this by using the flux marker Atg8 tagged with GFP and RFP in tandem. Here, Atg8-positive organelles are green and red fluorescent, but when they fuse with lysosomes, the GFP is quenched and autolysosomes are only red (59). We quantified the number of yellow and red Atg8-positive organelles in controls as well as the rare Atg8-positive organelles in *synj<sup>RQ</sup>* mutants. We do not observe a significant difference in the ratio of red (mature) over total Atg8-labeled organelles between control and *synj<sup>RQ</sup>* (Control: 55%; *synj<sup>RQ</sup>*: 57%). The data indicate that once a rare Atg8-positive autophagosome manages to form in *synj<sup>RQ</sup>* mutants, its further maturation is not impeded (Appendix Figure S2G–I).

## Synj mutants accumulate Atg18a within synaptic boutons

Members of the PROPPIN domain-containing protein family are key PI(3)P- and PI(3,5)P<sub>2</sub>-binding proteins with a role in autophagy (60). Given that Synj1<sup>RQ</sup> cannot dephosphorylate

PI(3)P (and likely PI(3,5)P<sub>2</sub>), we hypothesized that in the *synj* null mutants that express *Synj<sup>RQ</sup>*, autophagic PROPPIN-containing proteins would accumulate on synaptic pre-autophagosomal membranes. Therefore, we generated flies expressing N-terminal GFP-tagged *Drosophila* homologs of the PROPPIN WIPI2 (Atg18a, Atg18b, and CG11975; 70.8, 56.5, and 32.0% identity to human WIPI2 respectively). Both Atg18a<sup>GFP</sup> and CG11975<sup>GFP</sup> localize in puncta at synaptic boutons when expressed in motor neurons (*D42-Gal4*) (Appendix Figure S3A, B, G, and H). In contrast, Atg18b<sup>GFP</sup> is retained in neuronal cell bodies (Appendix Figure S3E and F). After starvation, we observe a clear upregulation of the number of Atg18a<sup>GFP</sup> puncta, while the number of CG11975<sup>GFP</sup> dots does not change (Appendix Figure S3C, D, I, and J and Figure 3A, A', and E). Additionally, Atg18a<sup>GFP</sup> puncta sometimes colocalize with Atg8<sup>mCherry</sup> puncta (Appendix Figure S3K and L) and expression of Atg18a<sup>GFP</sup> using the ubiquitous *Da-Gal4* driver in *atg18a* null mutants rescues their lethality. These data indicate that Atg18a<sup>GFP</sup> is a functional protein.

We then assessed Atg18a<sup>GFP</sup> localization in *synj* null mutants that express *synj<sup>RQ</sup>*. Consistent with *Synj<sup>RQ</sup>* not being able to dephosphorylate PI(3)P (15), we find a significant increase in the number of Atg18a<sup>GFP</sup> dots in fed *synj* mutants in comparison with fed controls (Figure 3A–C' and E). In addition, the number of Atg18a<sup>GFP</sup> dots is also increased in *synj* null mutant boutons that express *synj<sup>RQ</sup>* compared to *synj* null mutant boutons that express *synj<sup>+</sup>* (Figure 3C–E). Atg18a can bind PI(3)P and PI(3,5)P<sub>2</sub> that are both dephosphorylated by the SAC1 domain of Synj1. To delineate which phosphoinositide is involved, we took a pharmacological approach. We used wortmannin (WM) that inhibits Vps34, a kinase that produces PI(3)P, or YM201636 (YM) that inhibits PIKfyve, a kinase that produces PI(3,5)P<sub>2</sub>. We applied these drugs during starvation to control and *synj<sup>RQ</sup>* mutant animals that express Atg18a<sup>GFP</sup>. While Atg18a<sup>GFP</sup> accumulates in dots in starved controls, application of either drug blocks this effect and Atg18a<sup>GFP</sup> does not accumulate anymore, indicating that Atg18a<sup>GFP</sup> likely binds both PI(3)P and PI(3,5)P<sub>2</sub> during autophagy at synapses (Appendix Figure S3M). In *synj<sup>RQ</sup>* mutants, the number of Atg18a<sup>GFP</sup> dots is always upregulated. However, when we starve the larvae in the presence of either WM or YM, the number of Atg18a<sup>GFP</sup> is lower than in untreated starved *synj<sup>RQ</sup>* mutants (Appendix Figure S3M). These data suggest that consistent with the previously established function of the Synj SAC1 domain, both PI(3)P and PI(3,5)P<sub>2</sub> accumulate and bind Atg18a in *synj<sup>RQ</sup>* mutants.

We tried to find further evidence for upregulation of PI(3)P in *synj<sup>RQ</sup>* using expression of 2xFYVE-GFP, a probe that binds PI(3)P. We were however unsuccessful and did not detect obvious differences (not shown). Nonetheless, we do believe our results are consistent with the specific loss of SAC1 domain function in *synj<sup>RQ</sup>*. We assessed 5-phosphatase



domain activity of Synj using the PLC $\delta$ -PH-eGFP probe that detects PI(4,5)P<sub>2</sub>. We find that the synaptic labeling intensity of PLC $\delta$ -PH-eGFP is much less affected in *synj* null mutants that express Synj<sup>RQ</sup> (where 5-phosphatase activity is not affected) compared to *synj* null mutants (where 5-phosphatase activity is affected) (Appendix Figure S3N-R), suggesting *synj*<sup>RQ</sup> mutants support PI(4,5)P<sub>2</sub> dephosphorylation. Taken together, the data are consistent with normal PI(4,5)P<sub>2</sub> dephosphorylation activity of Synj1<sup>RQ</sup> measured *in vitro* (15), but altered PI(3)P dephosphorylation, thereby leading to the accumulation of Atg18a at synaptic boutons in *synj*<sup>RQ</sup> mutants.

## Visualization of Atg18a-labeled structures at synaptic boutons

Synapses in *synj* mutants expressing Synj<sup>RQ</sup> harbor increased synaptic Atg18a<sup>GFP</sup>-accumulations and largely lack Atg8<sup>mCherry</sup> accumulations. To further visualize the Atg18a<sup>GFP</sup>-labeled structures, we resorted to CLEM, a methodology that allows us to directly determine the ultrastructural appearance of Atg18a-positive structures within synaptic boutons. *Synj* mutants expressing Synj<sup>RQ</sup> and Atg18a<sup>GFP</sup> were dissected, fixed, and imaged. Subsequently, a near-infrared laser was used to produce burn marks in the vicinity of the imaged region. These marks are easily discernable at the light and EM level and help us when producing serial sections of the imaged boutons (Figure 3F-H). After alignment of the confocal images with the serial TEM images, we are able to identify the Atg18a<sup>GFP</sup>-positive structures (Figure 3I-K). As indicated in Figure 3L-P, Atg18a<sup>GFP</sup> marks profiles that have the appearance of cisternae that sometimes contain a few smaller vesicular structures in their lumen. Given that the flux of synaptic autophagy is blocked in *synj* mutants expressing Synj<sup>RQ</sup> and that these mutants do not harbor Atg8<sup>mCherry</sup> dots, we propose that these cisternae are early presynaptic autophagic intermediates.

Using the morphological features of Atg18a<sup>GFP</sup>-positive structures as a guide, we assessed the ultrastructural morphology of synapses in starved animals. We used TEM images to quantify the number of synaptic vesicles and the number of structures that have an appearance similar to the Atg18a-positive cisternae in our CLEM studies (Figure 3V). Compared to starved controls and *synj* null mutants expressing Synj<sup>+</sup>, starved *synj* null mutants show a strong reduction in the number of synaptic vesicles per bouton area, consistent with a defect in synaptic endocytosis. These mutants also show an increased number of cisternal structures (Figure 3Q, S, T, and V), correlating with an increased number of Atg18a-positive dots in *synj* null mutants. Starved *synj* null mutants that express *synj*<sup>RQ</sup> and *synj*<sup>RQ</sup> knock-in animals also show an increased number of

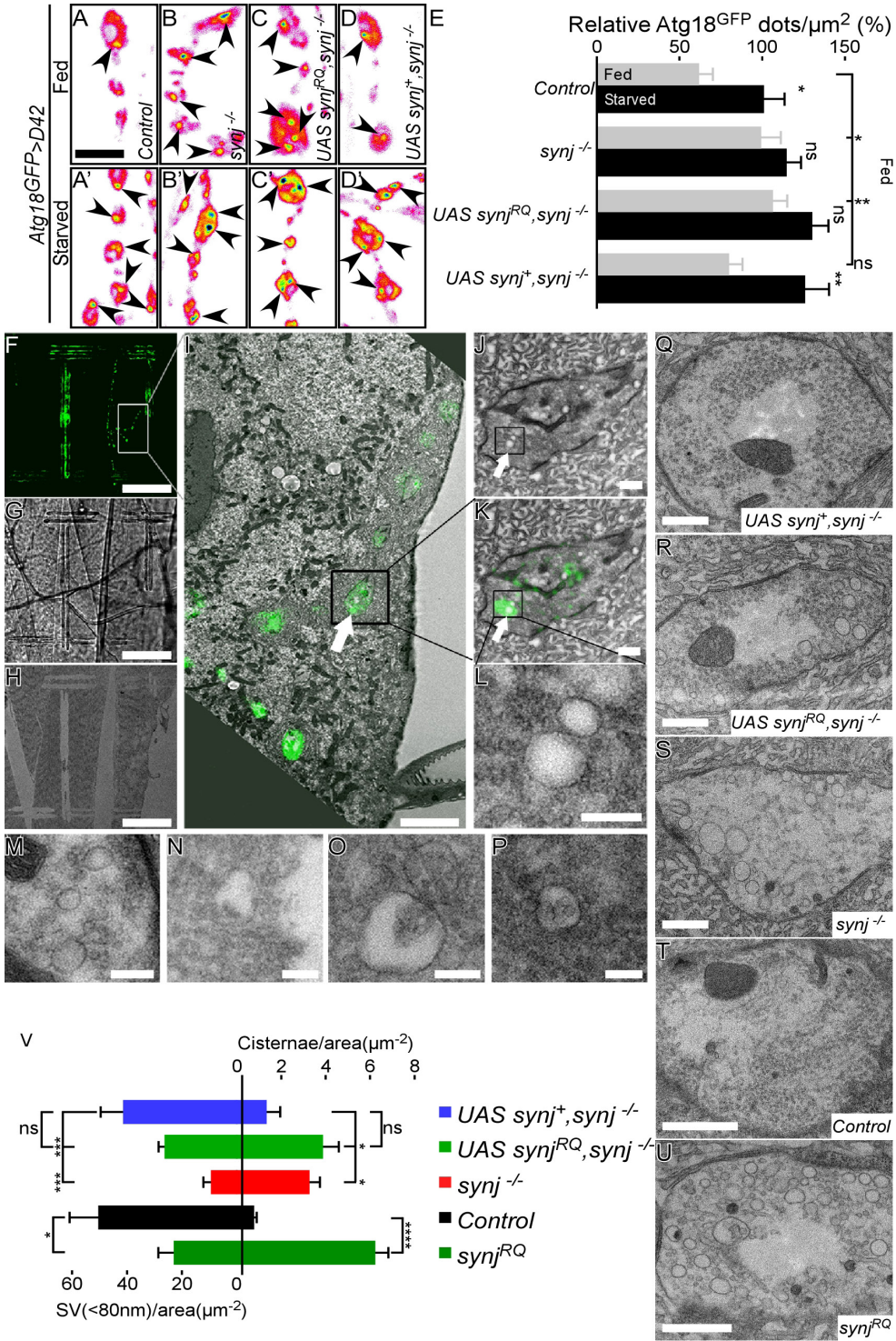




### Figure 3. Atg18a-positive structures accumulate at synaptic boutons of *synj* mutants

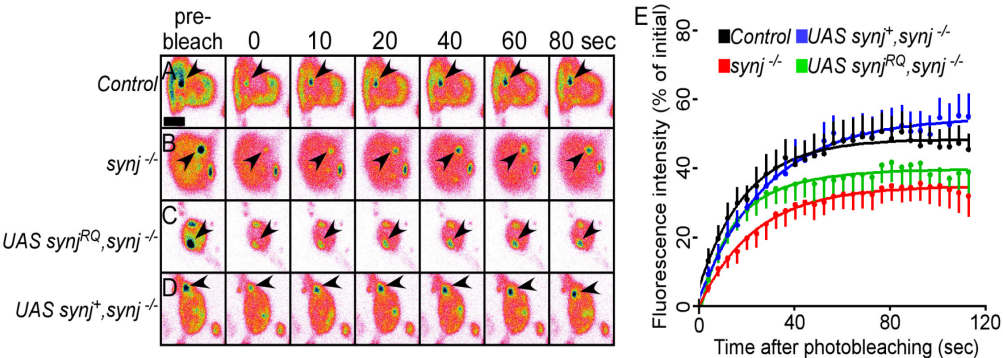
- A–E** Live imaging of fed (A–D) and 4-h-starved (A'–D') NMJ boutons in controls (D42-Gal4 > Atg18a<sup>GFP</sup>) (A, A') and *synj*<sup>-/-</sup> null mutants (B, B') or *synj*<sup>-/-</sup> null mutants expressing either *synj*<sup>RQ</sup> (C, C') or *synj*<sup>\*</sup> (D, D') and also expressing Atg18a<sup>GFP</sup> (D42-Gal4 > Atg18a<sup>GFP</sup>). Quantification of the number of Atg18a<sup>GFP</sup> dots (arrowheads) of indicated genotypes under fed and starved conditions (E). Full genotypes appear in the Appendix Supplementary Methods. Statistical analysis by t-test comparing control to individual genotypes separately in fed conditions and each genotype individually fed and starved, \*\**P* < 0.01, \**P* < 0.05, *n* ≥ 10 larvae and *n* ≥ 20 NMJs per genotype. Error bars represent SEM; scale bar, 5 μm. Note that loss of *Synj* increases the number of Atg18a<sup>GFP</sup> dots even under fed conditions. This is not rescued by expression of *synj*<sup>RQ</sup>.
- F–P** Correlative light and electron microscopy (CLEM) of 4-h-starved *synj*<sup>-/-</sup> null mutant NMJ boutons expressing Atg18a<sup>GFP</sup> and *synj*<sup>RQ</sup> under the control of D42-Gal4. NMJ boutons with Atg18a<sup>GFP</sup> fluorescence were imaged (F), and subsequently surrounded by burn marks using near-infrared branding (NIRB) (F–H). Branding marks are clearly visible in transmission and fluorescent mode due to autofluorescence of the marks (F, G). Branding marks allow subsequent detection of the same region of interest in electron micrographs (H). The marks then allow for the correlation of fluorescent and electron micrographs of Atg18a<sup>GFP</sup>-positive boutons (I–K). Arrows indicate Atg18a<sup>GFP</sup>-positive labeling (intensities were adjusted as to identify structures) in EM micrographs and boxes are enlarged in subsequent panels. Magnification of Atg18a<sup>GFP</sup>-positive structures identified in (I–K) is shown in (L) and further examples of Atg18a<sup>GFP</sup>-labeled structures are taken from independent CLEM experiments (M–P). Scale bars: 50 μm (F–H), 5 μm (I), 50 nm (J, K), and 200 nm (L–P).
- Q–U** Representative transmission electron micrographs of 4-h-starved *synj*<sup>-/-</sup> null mutants expressing either *synj*<sup>\*</sup> (Q) or *synj*<sup>RQ</sup> (R) using D42-Gal4, as well as of 4-h-starved *synj*<sup>-/-</sup> null mutants (S), controls (*w*<sup>1118</sup> (T)), and *synj*<sup>RQ</sup> knock-in animals (U). Full genotypes appear in the Appendix Supplementary Methods. Scale bars, 1 μm.
- V** Quantification of the number of synaptic vesicles (diameter < 80 nm) and cisternae that resemble Atg18a<sup>GFP</sup>-positive structures identified using CLEM. Note that at boutons of *synj*<sup>-/-</sup> null mutants, *synj*<sup>-/-</sup> null mutants expressing *synj*<sup>RQ</sup> and *synj*<sup>RQ</sup>, there are cisternae that resemble the Atg18a<sup>GFP</sup>-positive structures identified in CLEM; in *synj*<sup>-/-</sup> null mutants expressing *synj*<sup>RQ</sup> and in *synj*<sup>RQ</sup> knock-in, there are numerous synaptic vesicles detectable. For statistical analysis of both SV and cisternae, t-test comparing genotypes individually, \**P* < 0.05, \*\*\**P* < 0.001, \*\*\*\**P* < 0.0001. *n* ≥ 3 larvae and *n* ≥ 8 NMJs per genotype. Error bars represent SEM.

cisternal structures at boutons (Figure 3R, U, and V). However, there is a largely normal number of synaptic vesicles compared to controls (Figure 3Q–V), consistent with the normal synaptic vesicle endocytosis that we measured in these mutants (see Figure 1).

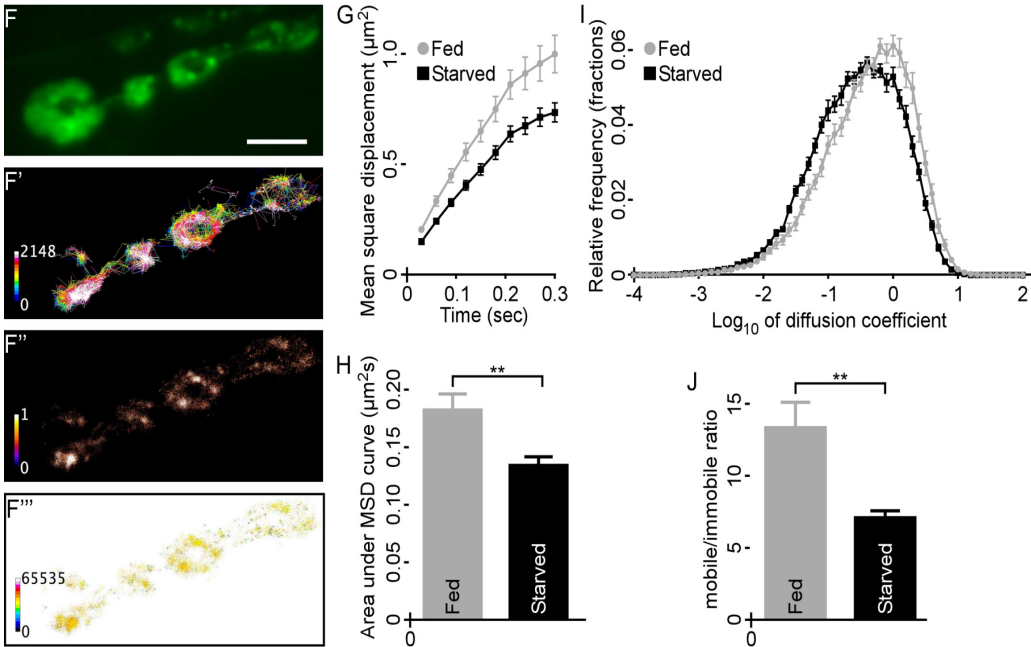
## Synaptojanin regulates Atg18a mobility at autophagosomal membranes

In synaptic vesicle endocytosis, the dephosphorylation of PI(4,5)P<sub>2</sub> by *Synj* on nascent vesicles regulates the detachment of adaptors with affinity for this lipid. We reasoned that a similar mechanism may be at play during autophagosome formation and tested whether *Synj* regulates Atg18a attachment and detachment. We expressed Atg18a<sup>GFP</sup> and assessed the fluorescence recovery after bleaching one specific Atg18a<sup>GFP</sup> dot. *Synj* null mutants and *synj* null mutants expressing *Synj*<sup>RQ</sup> show significantly slower recovery of Atg18a fluorescence in the bleached area compared to *synj* null mutants expressing *Synj*<sup>\*</sup> or compared to wild-type controls (Figure 4A–E).

FRAP Atg18a<sup>GFP</sup>



Single molecule tracking Atg18a<sup>mEOS3.2</sup>



Photoconversion Atg18a<sup>mEOS3.2</sup>

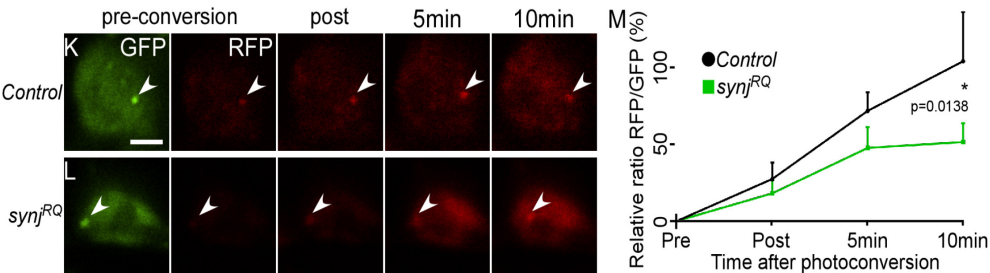


## Figure 4. Synaptojanin regulates Atg18a uncoating at autophagosomal membranes

- A–E Representative time-lapse images of a FRAP experiment where the fluorescence recovery after bleaching of an individual Atg18a<sup>GFP</sup> dot (D42-Gal4 > Atg18a<sup>GFP</sup>) was monitored at a synaptic bouton of a control (A) and of a *synj*<sup>-/-</sup> null mutant (B) and of a *synj*<sup>-/-</sup> null mutant expressing either *synj*<sup>RQ</sup> (C) or *synj*<sup>+</sup> (D) (expressed using the D42-Gal4). (E) Quantification of fluorescence intensities of a bleached Atg18a<sup>GFP</sup> dot (arrowheads) in the indicated genotypes (in % of initial fluorescence of the Atg18a<sup>GFP</sup> dot before bleaching), error bars represent SEM. Full genotypes appear in the Appendix Supplementary Methods. Note the reduced fluorescence recovery of Atg18a in *synj* null mutants and *synj* null mutants expressing *synj*<sup>RQ</sup> compared to wild-type controls. Even in wild-type Atg18a<sup>GFP</sup>, fluorescence never recovers more than 60%, suggesting an immobile pool of protein on the nascent autophagosome.
- F–J Transgenic larvae expressing Atg18a<sup>mEos3.2</sup> were imaged at 33 Hz. (F–F''') Representative low-resolution image of NMJ bouton (F), sptPALM trajectory map (F'), average intensity (F''), and diffusion coefficient (F''') of Atg18a<sup>mEos3.2</sup>. Scale bar, 5  $\mu$ m. (G) Comparison of MSD of Atg18a<sup>mEos3.2</sup> in fed and starved conditions ( $n \geq 6$  larvae and  $n \geq 18$  NMJ per condition). (H) Analysis of the area under the MSD curve ( $\mu$ m<sup>2</sup>s) showed significant decrease in starved compared to fed controls. (I) Diffusion coefficient distribution of Atg18a<sup>mEos3.2</sup> in fed and starved controls. (J) Mobile-to-immobile ratio for fed ( $13.4 \pm 1.8$ ) significantly reduced in starved conditions ( $7.1 \pm 0.5$ ). Statistical analysis by one-way ANOVA with Tukey's multiple comparison test, \*\* $P < 0.01$ . Error bars represent SEM.
- K–M Representative time-lapse images of mEos3.2 photoconversion experiment where the RFP fluorescence recovery on an individual Atg18a<sup>mEos3.2</sup> after GFP conversion of the neighboring bouton, an individual Atg18a<sup>mEos3.2</sup> dot (D42-Gal4 > Atg18a<sup>mEos3.2</sup>) was monitored at a synaptic bouton of a control (K) and of a *synj*<sup>RQ</sup> (L). (M) Quantification of the ratio RFP/GFP fluorescence intensities of an Atg18a<sup>mEos3.2</sup> dot (arrowheads) in the indicated genotypes (in % of final time point (10 min after photoconversion) RFP/GFP fluorescence ratio of the Atg18a<sup>mEos3.2</sup> dot), error bars represent SEM. Full genotypes appear in the Appendix Supplementary Methods. Statistical analysis comparing curves fitted by linear regression.  $n \geq 3$  larvae and  $n \geq 13$  NMJs per genotype. Note the reduced RFP/GFP fluorescence recovery of Atg18a<sup>mEos3.2</sup> in *synj*<sup>RQ</sup> compared to wild-type controls.

To find further evidence for our model, we also generated Atg18a<sup>mEos3.2</sup>-expressing flies. mEos is a photoconvertible fluorescent protein that shifts from green to red fluorescence when activated (61). We reasoned that Atg18a mobility would decrease after induction of autophagy, as more Atg18a would bind to newly forming autophagosomes. Therefore, we used single-particle tracking photoactivation localization (sptPALM) microscopy to track single molecules within synaptic boutons expressing Atg18a<sup>mEos3.2</sup> (62). Tracking each fluorescent molecule (Video EV1) allows us to generate trajectory maps of Atg18a<sup>mEos3.2</sup>, as well as intensity and instantaneous diffusion coefficient maps (Figure 4F–F'''). Moreover, we quantified Atg18a<sup>mEos3.2</sup> mobility by analyzing the mean square displacement (MSD) of sptPALM trajectories of single fluorescent localizations (Figure 4G). Compared to fed larvae, Atg18a mobility significantly decreases in starved larvae (Figure 4H), in good agreement with recruitment of cytosolic molecules to presynaptic autophagosomes. Analysis of the diffusion coefficient distribution reveals a decrease in the mobile population of Atg18a<sup>mEos3.2</sup> in starved conditions (Figure 4I). This is most apparent in the ratio of the mobile-to-immobile fractions (Figure 4J). This change in mobility of Atg18a after induction of autophagy is consistent with the recruitment of Atg18a to presynaptic autophagosomes.

We subsequently followed the accumulation of Atg18a on synaptic autophagosomes by converting a bouton pool of Atg18a<sup>mEos3.2</sup>. We converted Atg18a<sup>mEos3.2</sup> in one bouton and followed accumulation of red Atg18a<sup>mEos3.2</sup> on (green Atg18a<sup>mEos3.2</sup>-positive)

autophagosomes in the neighboring boutons of control and *synj<sup>RQ</sup>* knock-in flies. While the amount of red photoconverted Atg18a in the cytoplasm of controls and *synj<sup>RQ</sup>* is similar, the red Atg18a accumulates significantly less quickly on nascent autophagosomes in *synj<sup>RQ</sup>* compared to controls (Figure 4K-M). This slowed acquisition of red fluorescence indicates reduced exchange between membrane bound and soluble pools of Atg18a, and thus indicates that the SAC1 domain of Synj normally promotes Atg18a mobility at synaptic autophagosomes.

## **Synj<sup>RQ</sup> reduces lifespan upon starvation and causes neurodegeneration**

To more broadly assess the physiological consequences of the Synj<sup>RQ</sup> mutation, we examined whether this affects animal survival under starvation conditions, a readout that is strongly modulated by autophagy (63). While wild-type flies reared in these conditions can survive for ~4 days, we detect significantly reduced survival times for *synj* null mutants that express Synj<sup>RQ</sup> in neurons or *synj<sup>RQ</sup>* knock-in animals which display 100% lethality within 3 days (Figure 5A and A'). The results correlate with impaired autophagosome maturation in animals lacking Synj SAC1 activity, suggesting that presynaptic autophagy connects to an important survival mechanism during starvation in the fruit fly.

Next, we tested neuronal survival, another parameter sensitive to autophagy (63, 64). To induce neurodegeneration, flies were kept 7 days in constant light challenging photoreceptor neurons of the fly eye. In *synj* null mutant flies that express Synj<sup>RQ</sup>, a significant reduction in the number of intact ommatidia and an accumulation of vacuoles was observed. In contrast to control animals, when *synj* null mutant animals expressing Synj<sup>+</sup> or animals kept in dark for 7 days, these photoreceptors appear unaffected (Figure 5B-E). Finally, given the vulnerability of dopaminergic neurons in PD, we assessed the integrity of such neurons in fly brains of 30-day-old *synj<sup>RQ</sup>* knock-in animals using anti-TH labeling. In these mutants, anti-TH-positive neuronal cell bodies in the PPM3 and PPL1 dopaminergic neuron clusters were significantly reduced compared to controls (Figure 5F-F"). Hence, Synj SAC1 domain function is required for dopaminergic neuron survival in the fly brain.

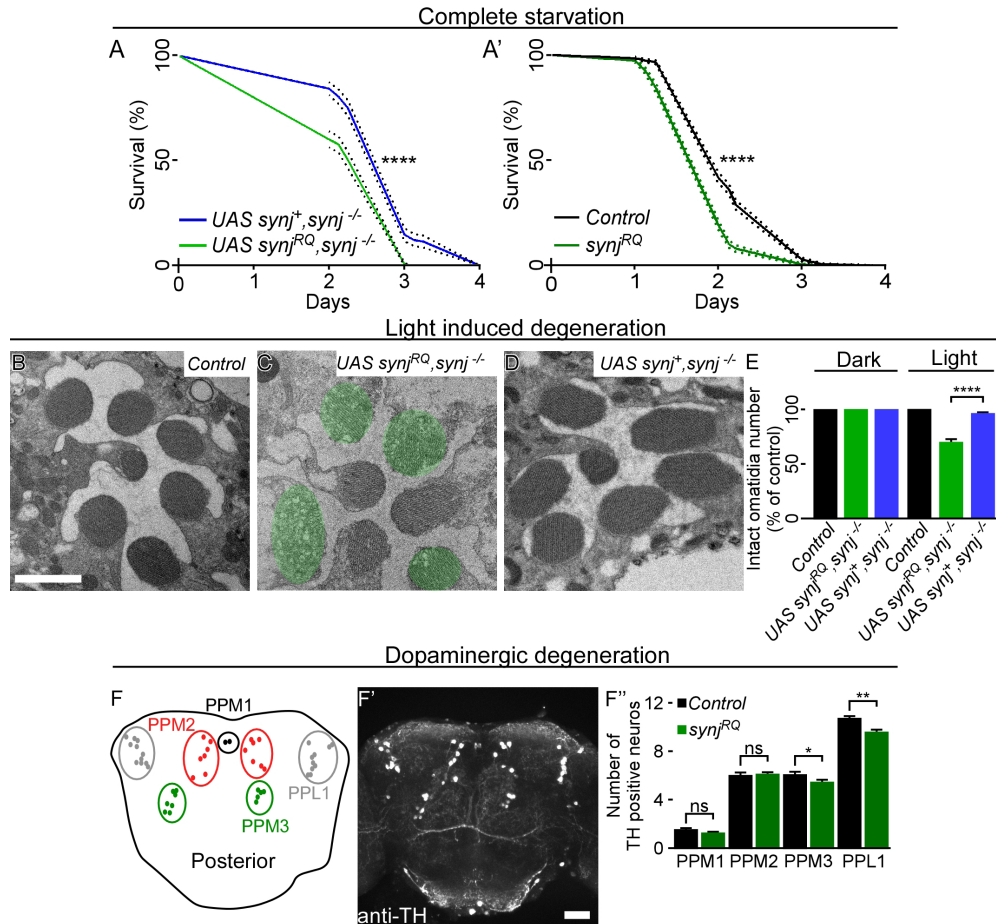


**Figure 5. Defects in synaptic autophagy result in reduced lifespan upon starvation and neurodegeneration**

**A, A'** Complete starvation (water-only diet) assay in *synj* null mutants expressing *synj<sup>RQ</sup>* (light green) or *synj<sup>+</sup>* (blue) (expressed using *nSyb-Gal4*) (A) and *synj<sup>RQ</sup>* knock-in animals (dark green) as well as controls (*w<sup>1118</sup>*, black) (A'). Statistical analysis of survival curves by log-rank (Mantel-Cox) test, \*\*\*\* $P < 0.0001$ ,  $n \geq 134$  flies per genotype for (A) and  $n \geq 292$  flies per genotype for (A'), dotted lines surrounding the curves indicate SEM. Note, *synj* null mutants expressing *synj<sup>RQ</sup>* as well as *synj<sup>RQ</sup>* knock-in flies have a shorter life span under these starvation conditions.

**B-E** Representative electron micrographs of the retina after 7 days of continuous light exposure of control (*nSyb-Gal4/+*) (B) and *synj* null mutants expressing *synj<sup>RQ</sup>* (C) or *synj<sup>+</sup>* (D) (expressed using *nSyb-Gal4*). Green highlighting in (C) shows disintegrating rhabdomeres as a sign of degeneration. Scale bar, 2  $\mu$ m. (E) Quantification of number of intact ommatidia per indicated genotype when flies were kept in complete darkness or when exposed to light. Full genotypes are in the Appendix Supplementary Methods. Statistical analysis by t-test, \*\*\*\* $P < 0.0001$ ,  $n=3-5$  flies per genotype. Error bars represent SEM.

**F-F''** Dopaminergic neuron degeneration assay in 30-day-old control (*w<sup>1118</sup>*) and *synj<sup>RQ</sup>* knock-in flies. Schematic representation (F) and image (z-stack, sum of slices) of posterior side of an anti-TH-labeled 30-day-old adult fly brain (F') to show the location of the different dopaminergic neuron cell bodies in this part of the brain. Scale bar, 40  $\mu$ m. (F'') Bar graph showing the number of dopaminergic neurons (TH-positive) in each cluster indicated in (F) in 30-day-old flies of control (black bars) and *synj<sup>RQ</sup>* knock-in (dark green bars) flies. Statistical analysis per dopaminergic cluster by t-test, \*\* $P < 0.01$ , \* $P < 0.05$ ,  $n \geq 15$  brains per genotype. Error bars represent SEM. Note at PPM3 and PPL1 dopaminergic neuron clusters the reduction of anti-TH-positive neuronal cell bodies in the of *synj<sup>RQ</sup>* mutant animals compared to controls.



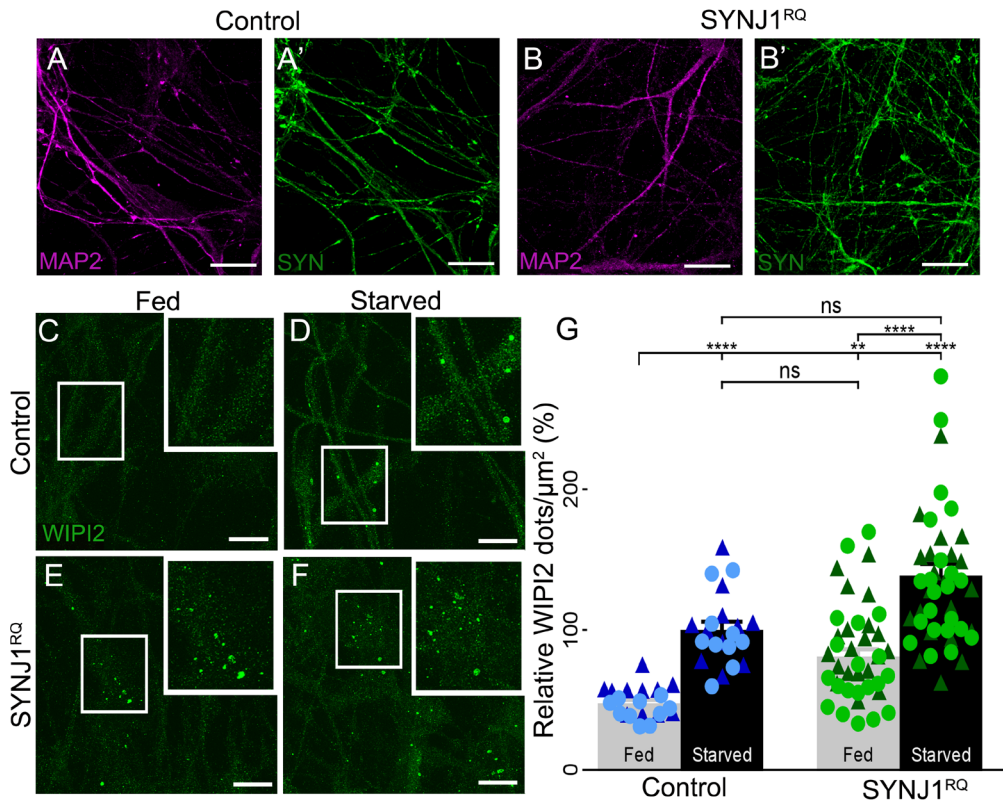


**Figure 6. WIPI2/Atg18a accumulates in neurites of SYNJ1 R258Q human patient iPSC-derived neurons**

A–B' Immunocytochemistry analysis of human iPSC-derived neurons (after 28 days of differentiation) showing expression of neuronal markers, anti-MAP2 (magenta) and anti-synapsin 1 (green) in control (A, A') and SYNJ1<sup>RQ</sup> (B, B'). Scale bars, 15  $\mu\text{m}$ .

C–G Images of neurons stained with anti-WIPI2 in fed and starved conditions of controls (C, D) and SYNJ1<sup>RQ</sup> (E, F). (G) Quantification of the number of WIPI2 dots of indicated genotypes (two control lines and two patients lines (NAP016 and 17), circles and triangles indicate separate lines for each genotype) under fed and starved conditions. Statistical analysis with one-way ANOVA Kruskal-Wallis followed by Dunn's multiple comparison post hoc test, \*\*\*\* $P < 0.0001$ , \*\* $P < 0.01$ , ns, not significant.  $n \geq 21$  images per condition per genotype. Error bars represent SEM; scale bar, 15  $\mu\text{m}$ . Note that SYNJ1<sup>RQ</sup> has increased number of WIPI2 dots under fed conditions.

## WIPI2/Atg18a accumulates in neurites of SYNJ1 R258Q patient-derived human induced neurons

To confirm our key findings in a disease-relevant condition, we resorted to human iPSC obtained from two patients with autosomal recessive, early-onset PD carrying the R258Q mutation in *SYNJ1* as well as two age-matched controls (Appendix Table S1). Following validation, including expression analysis of pluripotency and proliferation markers (Figure 6A–B', Appendix Figure S4 and Appendix Table S1), we differentiated these iPSC

into neurons. After 28 days of differentiation, we labeled the neurons with anti-WIP12 (mammalian Atg18a) and imaged the neurites (Figure 6C–F). Similar to our observations at fly synapses, we find a significant increase in the number of WIP12 dots in starved control neurons compared to fed control neurons (Figure 6C, D, and G). Moreover, in line with our observations made with fly *synj<sup>RQ</sup>* mutants, we find a significant increase in the number of WIP12 dots in fed *SYNJ1<sup>RQ</sup>* neurons compared to fed controls and which is even further increased in starved *SYNJ1<sup>RQ</sup>* neurons (Figure 6C and E–G). These data indicate that also in human neurons, Synj1 is required for autophagy, and further supports our model that implicates SYNJ1-SAC1 function in removing Atg18a/WIP12 from nascent autophagosomal membranes.

## Discussion

The presynaptic protein SYNJ1 contains two PtdInsP lipid phosphatase domains and is critical for neurotransmission. In this work, we take advantage of both flies and human iPSC-derived neurons obtained from patients carrying the *SYNJ1* R258Q mutation to examine the role of the Synj SAC1 phosphatase domain that is mutated in early-onset PD and that was previously shown to block PI(3)P dephosphorylation (15). We show that Synj has a previously unrecognized role in promoting autophagosome maturation within presynaptic terminals and that this is distinct to the relatively well-described function in synaptic vesicle recycling. This predicts that defective synaptic autophagy and protein clearance contributes to *SYNJ1*-PD pathology. Furthermore, given that Synj is a presynaptic protein, these data show the existence of a synapse-specific autophagy machinery and suggest this process may be disrupted in PD.

We detected that Synj has dual presynaptic functions in endocytosis and macroautophagy when comparing the impact of the SAC1-domain mutation and a null mutation. While the *Synj* null mutation causes larval lethality, *Synj<sup>RQ</sup>* knock-in animals or *synj* null mutants that neuronally express Synj<sup>RQ</sup> are viable. Similarly, synaptic endocytic mutants cause lethality in flies, while many of the mutants that disrupt macroautophagy are viable (13, 34, 37, 63). Hence, our observation that *synj<sup>RQ</sup>* flies live is in line with the mutation not disrupting endocytosis. Furthermore, we provide several additional lines of evidence that *Synj<sup>RQ</sup>* mutants have largely normal synaptic endocytosis. First, Synj<sup>RQ</sup> mutants have a largely normal number of synaptic vesicles. Second, they display normal presynaptic FM1-43 dye uptake at NMJs. Third, they do not develop the NMJ morphological defects

associated with impaired endocytosis. Fourth, we directly assessed how the SAC1 domain *synj*<sup>RQ</sup> PD mutation affects neurotransmission. Unlike endocytic mutants, we find that the *Synj*<sup>RQ</sup> mutant protein maintains NMJ neurotransmitter release during intense stimulation, as well as during normal neurotransmission between the fly eye and brain. These results all indicate that the *Synj*<sup>RQ</sup> protein can fulfill the endocytic function of *Synj* that is required for efficient synaptic vesicle cycling and is severely abnormal in *synj* null animals. Nevertheless, the RQ mutation in *Synj* does incapacitate aspects of *Synj* activity, as evidenced by loss of dopaminergic neurons and shorter lifespan of *Synj*<sup>RQ</sup>-expressing flies under starved conditions. We also find that synaptic boutons expressing *Synj*<sup>RQ</sup> fail to organize autophagy at presynaptic terminals. Instead, these boutons contain membrane structures positive for the early autophagosome marker Atg18a. Thus, given that under the used conditions, we see that *synj*<sup>RQ</sup> animals have severely abnormal autophagy alongside normal endocytosis, we conclude that *Synj* operates in both processes.

Our findings implicate *Synj* in autophagy at presynaptic terminals, which is surprising given the well-studied role of this protein at the synapse (10-13). We therefore hypothesize that the severe endocytic defects that occur upon *synj* loss made it difficult to detect the importance in autophagy. The conclusion that *Synj*1 is a dual endocytic and autophagic protein is consistent with the evolutionarily conserved presence of two distinct *Synj* PtdInsP phosphatase domains, SAC1 and 5-phosphatase, that have different preferences for PtdInsP species. This suggests a cooperativity between the domains and it is interesting to consider the possibility that the dual roles of *Synj* allow this protein to couple autophagy to levels of synaptic vesicle cycling and thus ensure sufficient protein turnover possibly depending on the level of synaptic activity.

We provide evidence that SAC1-dependent PI(3)P and PI(3,5)P<sub>2</sub> dephosphorylation is needed for normal autophagic flux at synapses using both *Synj*<sup>RQ</sup> and *SynjCS*, in line with the activities of the PI(3)P phosphatases Ymr1, INP52, and INP53 in yeast cells (65). These data in yeast and flies appear at odds with a study in zebrafish where expression of the SAC1 *Synj*<sup>C385S</sup> mutant results in a mild and partial rescue of autophagy in cone photoreceptors. While we currently do not understand the nature of this partial rescue, cone photoreceptors are tonically firing neurons (66, 67) and these cells may have different requirements for *Synj* activity than the spiking neurons at the fly NMJ or mouse hippocampal neurons. Nonetheless, the nature of the partial rescue of autophagy defects upon expression of *Synj*<sup>C385S</sup> in zebrafish suggests optimal SAC1 function is needed for normal autophagy. It will be interesting in this context to assess the effect of



the Synj Parkinson mutations in zebrafish as well.

While our data indicate an important role of the Synj SAC1 domain in synaptic autophagy, our data do not exclude that the Synj 5-phosphatase domain is—indirectly—needed for autophagy as well. The Synj 5-phosphatase domain dephosphorylates phosphoinositides critical for endocytosis and *synj* 5-phosphatase mutants strongly disrupt endocytosis in mouse neurons (33). Endocytosis itself is required for the maturation of autophagic markers, suggesting that ultimately, the 5-phosphatase domain may block autophagy as well (68-70). This idea is consistent with evidence from the zebrafish study where a Synj 5-phosphatase mutant (D732A) blocks autophagy in photoreceptor neurons (53). Further experiments to determine whether this mutant, similar to data in mouse neurons, also blocks endocytosis in zebrafish or fruit flies are awaited, but the data are consistent with endocytic defects to precede autophagy. Hence, we propose a direct function of the SAC1 domain in synaptic autophagosome flux by PI(3)P and PI(3,5)P<sub>2</sub> dephosphorylation and a potential indirect role of the 5-phosphatase domain by mediating synaptic endocytosis.

PtdInsP phosphatase enzymes are classic drivers of organelle biogenesis and function since they alter membrane lipid composition and thus which proteins interact with this membrane (24, 27). The biochemical basis of how Synj1 contributes to endocytosis is relatively well studied. The 5-phosphatase domain dephosphorylates PI(4,5)P<sub>2</sub>, thereby lowering the affinity of clathrin adaptors for the membrane of newly formed vesicles and promoting synaptic vesicle uncoating (10, 13, 28). Our data suggest that the Synj1 SAC1 domain that hydrolyzes PI(3)P, PI(4)P, and PI(3,5)P<sub>2</sub> may have a similar “uncoating” role, but acting during the early steps of autophagosome biogenesis. Indeed, it was previously established that the early-stage autophagosome membrane contains PI(3)P and PI(3,5)P<sub>2</sub> and that these phosphoinositides recruit PI(3)P/PI(3,5)P<sub>2</sub>-binding proteins, like Atg18a (29-32). Here, we observe that synapses expressing Synj<sup>RQ</sup> accumulate the Atg18a<sup>GFP</sup> marker of early autophagosomes, but produce far fewer mature Atg8-positive structures. Furthermore, using *in vivo* CLEM for neurons expressing Atg18a<sup>GFP</sup>, we ultrastructurally define that Atg18a is attached to cisternal-like membrane structures and these are overly abundant within Synj<sup>RQ</sup> synapses. Finally, live cell imaging shows that Atg18a<sup>GFP</sup> accumulations are immobilized within presynaptic terminals expressing Synj<sup>RQ</sup>, suggesting that the Synj SAC1 domain normally promotes Atg18a cycling between soluble and membrane-bound pools. Note that these data are inconsistent with a direct involvement of the 5-phosphatase domain (53) as this domain is responsible for the dephosphorylation of phosphoinositide species that Atg18a does not bind to.

We therefore propose a model, where Synj-mediated PI(3)P and PI(3,5)P<sub>2</sub> hydrolysis on nascent autophagosomes lowers the affinity for PI(3)P/PI(3,5)P<sub>2</sub>-binding proteins, including Atg18a, to release these from the membrane. This mechanism, regulated by the synapse-enriched Synj, is similar to that thought to be mediated by myotubularin (Ymr1) during autophagy in yeast cells (71). Interestingly, WIPI2 (the Atg18a homolog) cycling is known to recruit LC3/Atg8 to autophagosomes of non-neuronal cell types (72, 73), and thus, Atg18a immobilization can explain why the Synj SAC1 activity is needed for Atg8 accumulation at synapses. Hence, we propose that cycles of Atg18a recruitment followed by Synj SAC1 domain-dependent shedding allow the recruitment and concentration of Atg8 on the synaptic autophagosomal membrane, explaining why the Synj<sup>RQ</sup> protein fails to support the production of mature autophagosomes.

This model of Synj1 function has parallels with the roles of the yeast myotubularin Ymr1, INP52 and INP53 PtdInsP phosphatases in autophagosome biogenesis (65, 71, 74), which provides conceptual support to our finding that the PI(3)P phosphatase activity of Synj operates in autophagy at synapses. Given that Synj is presynaptic, we hypothesize that a different PI(3)P/PI(3,5)P<sub>2</sub>-hydrolyzing enzyme mediates autophagosome maturation in non-neuronal animal cells and neuronal cell bodies. In addition, our data do not preclude the possibility that PtdInsP dephosphorylation mediated by the Synj1 SAC1 domain also contributes to other cell biological processes, potentially including endocytosis under certain conditions, but thus far, we have found no evidence for this. It is intriguing to consider the evolutionary consequences of combining 5-phosphatase and SAC1 domains in Synj proteins throughout the animal kingdom. This is consistent with the idea that both domains contribute to a cell biological process, perhaps acting sequentially to drive multiple stages of organelle maturation. Alternatively, it is possible that the dual roles of Synj allow this protein to couple autophagy to levels of synaptic vesicle cycling, and thus ensure sufficient protein turnover depending on the level of synaptic activity.

Our data connect impaired presynaptic autophagy to PD pathology. This is consistent with the classical concept of abnormal protein homeostasis causing proteopathic stress and driving neurodegenerative disease. However, this role of Synj highlights the concept that protein homeostasis within presynaptic terminals has a particularly important role in these diseases. We demonstrate that the pathogenic R258Q mutation in the presynaptic PD protein SYNJ1 impairs synaptic macroautophagy, and we associate this with neurodegeneration including loss of dopaminergic neurons. Another presynaptic PD protein  $\alpha$ -synuclein affects membrane trafficking (75, 76), although its roles remain less well defined than those of Synj. The PD proteins Parkin and Pink1 are thought to

drive mitophagy, a specialized form of macroautophagy that targets mitochondria for degradation (77-79). In addition, LRRK2, the most commonly mutated protein in PD, also affects autophagy within synaptic terminals (34). In the case of LRRK2, this appears to occur via the essential presynaptic membrane factor EndophilinA (34) that, interestingly, is a key regulator of Synj activity (13, 80). Future work should continue to examine whether the presynaptic terminal has a unique network of proteins that control macroautophagy, a membrane-mediated mechanism to clear damaged proteins or organelles. It is important to discover whether mutations in different PD genes indeed converge onto this process and, if so, to consider synaptic autophagy as an important target for development of anti-PD therapies.

## Experimental Procedures

### Fly stocks and genetics

Flies were grown on standard cornmeal and molasses medium supplemented with yeast paste at 25°C. The following *Drosophila* stocks were obtained from the Bloomington Stock Center: *w; P{hs-I-CreI.R}1A Sb1/TM6, y(1) w(\*)*; *Mi{y(+mDint2)=MIC}Synj(MI11871)/SM6a* (35). The following fly stocks were obtained from the laboratory where the stock was first described: *w;UAS-mCherry-Atg8a* (81), *UAS GFP::Lamp1/CyO;TM6B/Sb bos1* (82), *w;;UAS-PLCd-PH-EGFP* (83), *yw,eyFLP GMR-LacZ;FRT42D synj<sup>1</sup>/CyO*, and *yw,eyFLP GMR-LacZ;FRT42D synj<sup>2</sup>/CyO* (13), *w;;atg18a(W3)/TM6b,Hu,Tb* and *w;;atg18a(W4)/TM6b,Hu,Tb* (84), genomic *w;;Atg9<sup>HA</sup>* (G. Juhász, unpublished).

### Transgenic flies

A list of fly genotypes used in this study can be found in the Appendix Supplementary Methods section. All constructs were generated using a seamless cloning method (Gibson Assembly, NEB). *UAS synj<sup>RO</sup>*, *UAS synj<sup>CS</sup>*, and *UAS synj<sup>+</sup>* were created using gBlocks (Integrated DNA Technologies, Inc.) and PCR products generated using primers listed in the Appendix Supplementary Methods section from CH322-135G1 P(acman) plasmid (BACPAC Resources Center (BPRC)) (85, 86), cloned into the EcoRI site of pUAST-attB, sequence-verified, and inserted into attP site VK37 (22A3) using PhiC31-mediated integration at BestGene Inc.

*synj<sup>RQ</sup>* knock-in flies were created as described in Vilain *et al.* (36). Targeting vector MiMIC 1322 pBS-KS-attB1-2 I-SceI *Synj<sup>RQ</sup>* I-CreI was generated using primers listed in the Appendix Supplementary Methods section from CH322-135G21 P(acman) plasmid (BPRC) and cloned first into XhoI and PstI sites of pSV004 (containing I-SceI and I-CreI sites, see Appendix Supplementary Methods section) followed by restriction with SmaI, gel purification, and cloning into BbsI sites of MiMIC 1322 pBS-KS-attB1-2 vector with an additional linker sequence containing BbsI sites (see Appendix Supplementary Methods section) into XbaI and EcoRI sites. Next, the construct was inserted into flies with Mi{MIC}*Synj<sup>MI11871</sup>* using PhiC31-mediated integration by in-house injection. Efficiencies were 30% for integration into the Mi{MIC}*Synj<sup>MI11871</sup>*, 15% for desired orientation, and 37% of I-CreI double-strand break/repair. After genomic manipulation, the whole locus was sequence-verified.

*UAS GFP::Atg18a*, *UAS GFP::Atg18b*, *UAS GFP::CG11975*, *UAS mEOS3.2::Atg18a*, *UAS eGFP-mCherry::Atg8a* were created using gBlocks (Integrated DNA Technologies, Inc.) and PCR products generated using primers listed in the Appendix Supplementary Methods section, all Atg18 homologues cDNAs as template were obtained from the Proteomic ORF Collection (87) (respectively, LD38705, GH07816, and LD32381), mEOS3.2 was PCR from Addgene plasmid #54550 and cloned into the XhoI site of pUAST-attB, and Atg8 was cloned in between the EcoRI and XbaI sites of pUAST-attB. All constructs were sequence-verified and inserted into attP site VK20 (99F8) using PhiC31-mediated integration at BestGene Inc or by in-house injection.

## Induction of autophagy by starvation, electrical stimulation, and chloroquine assay

Autophagy induction and flux assay were performed by placing early third-instar larvae on petri dishes containing 20% sucrose and 1% agarose for 3–4 h prior to experimentation (88). Electrical stimulation, 20 Hz for 30 min, to induce autophagy was conducted as described before (34). For the chloroquine assay, we fed third-instar larvae 4 h on standard and starvation food containing 10 mg/ml chloroquine diphosphate salt (Sigma).

## Correlative light and electron microscopic studies (CLEM and TEM)

Correlative light and electron microscopy studies were performed as described in Soukup *et al.* (34). Before dissection in HL3, larvae were starved for 3–4 h. The samples were directly fixed for 2 h at room temperature in the dark (0.5% glutaraldehyde, 2% paraformaldehyde in 0.1 M phosphate buffer, pH=7.2), followed by washing steps in 0.1 M phosphate buffer, pH=7.2. near-infrared branding (NIRB) was performed on a LSM 710 upright confocal microscope using the bleaching function as described (89). Before and after NIRB, z-stacks of the region of interest were acquired. Next, larvae were post-fixed in 1% glutaraldehyde, 2% paraformaldehyde in 0.1 M phosphate buffer, pH=7.2 at 4°C overnight or until further processing as described in Fernandes *et al.* (90). NIRB introduced branding marks were used as a guide to identify *Drosophila* NMJ boutons previously imaged with the confocal microscope. Electron and fluorescent micrographs overlay, and identification of Atg18a<sup>GFP</sup>-positive ultrastructural features and processing of micrographs using brightness and contrast were performed with NIH ImageJ and Adobe Photoshop Elements 14.

TEM studies of larval boutons were performed as described in Kasproicz *et al.* (91). Larvae were starved for 3–4 h prior to dissection and fixation. TEM of the adult fly heads was performed as described previously in Slabbaert *et al.* (92).

## Imaging and quantification

For live imaging of Atg8<sup>mCherry</sup>, Atg8<sup>GFP-mCherry</sup>, Atg18a<sup>GFP</sup>, Atg18b<sup>GFP</sup>, CG11975<sup>GFP</sup>, or Lamp1<sup>GFP</sup>, larvae expressing these markers were dissected in HL3 on sylgard plates and imaged on a Nikon A1R confocal microscope with a 60× NA 1.0 water-dipping lens. All images were collected with a pinhole of 1 airy unit and a resolution of 1,024 × 1,024. Imaging settings between experiments with the same marker were identical. Images are shown either in grayscale or using a 16-color lookup table (the LUT is shown in the figure).

Quantification of number of puncta or intensity was performed in NIH ImageJ. Atg8<sup>mCherry</sup>, Atg8<sup>GFP-mCherry</sup>, Atg18a<sup>GFP</sup>, or CG11975<sup>GFP</sup> dots were counted using particle analysis of a binary image combined with applying a threshold mask on the cytoplasmic signal to calculate the bouton area. Lamp1<sup>GFP</sup> fluorescence intensities were measured by first applying a threshold to mark the bouton areas followed by measuring the average pixel intensities in bouton areas. The different conditions were blinded before imaging and quantifying the data.

Fluorescence recovery after photobleaching (FRAP) was performed on third-instar larval fillets dissected in HL3 on sylgard-coated plates using a protocol adapted from Seabrooke *et al.* (93). Experiments were conducted on a Nikon A1R confocal microscope with a 60× NA 1.0 water-dipping lens. Before bleaching, 10 images were acquired to set the pre-bleach intensity. Next, bleaching (minimum 50% of the pre-bleach intensity, by two rapidly iterated laser bursts), using a 488-nm laser, was focused on an Atg18a<sup>GFP</sup> dot, directly followed by image acquisition for 120 s (60 scans with a 2.12-s interval). The fluorescence intensity of the selected Atg18a<sup>GFP</sup> dot was analyzed in NIH ImageJ.

Photoconversion of mEOS3.2 was performed on third-instar larval fillets dissected in HL3 on sylgard-coated plates; next, nerves were cut in HL3 with NAS (100  $\mu$ M) followed by mounting the larval prep on a glass slide in HL3 with NAS. Experiments were conducted on a Nikon A1R confocal microscope with a 60× NA1.4 oil lens; all images were collected with an open pinhole and a resolution of 1,024 × 1,024. Images of the Atg18a<sup>mEOS3.2</sup> dot of interest were taken before, directly after, and 5 and 10 min after photoconversion (conducted using a 405-nm laser) of the neighboring bouton. The fluorescence intensity of the selected Atg18a<sup>mEOS3.2</sup> dot was analyzed in NIH ImageJ.

## Single-particle tracking photoactivation localization microscopy (sptPALM)

SptPALM was carried out on transgenic Atg18a<sup>mEOS3.2</sup> third-instar *Drosophila* larvae dissected on sylgard base as previously described (62). Briefly, Atg18a<sup>mEOS3.2</sup> was imaged at the larva NMJ on muscles 6 and 7 of the second abdominal segments, using total internal reflection (TIRF) microscopy under oblique illumination. Dissected larvae on the sylgard base were inverted onto glass-bottomed imaging dishes (In Vitro Scientific). Localization and tracking of single Atg18a<sup>mEOS3.2</sup> molecules were carried out using a 63× water-immersion objective (1.2 numerical aperture, C-Apochromat) on the ELYRA PS.1 microscope (Zeiss). NMJs were located using 488-nm laser (18.72 mW) illumination. A 405-nm laser (0.6 mW) was used for photoconversion, while imaging of photoconverted Atg18a<sup>mEOS3.2</sup> molecules was done using 561-nm laser (20.6 mW) to spatially visualize and temporally distinguish individual molecules (405-nm laser was used at 0.009–0.3% power, while 75% power was used for 561 nm). Single-molecule fluorescence was collected by a sensitive electron-multiplying charge-coupled device (EMCCD) camera (Evolve, Photometric). Zen Black acquisition software (2012 version, Carl Zeiss) was used for movie acquisition. Images were captured at 33 Hz and 15,000 frames were obtained per NMJ. sptPALM analysis is described in Appendix Supplementary Methods section.

## Complete starvation

Complete starvation assay was performed as described in Juhász *et al.* (63), briefly 1-day-old fed flies were transferred to vials containing a gel of water (1% agarose in water) and transferred to a new vial every day. Dead flies were counted manually multiple times a day.

## Light-induced degeneration

Light-induced retinal degeneration studies were performed by rearing flies for 7 days in constant illumination at 1,300 lux and 25°C (4).

## Visualization of TH-positive neuronal clusters after aging adult flies

Aging and visualization of dopaminergic clusters was performed by aging 1- to 3-day-old adult flies for an additional 30 days at 25°C (flies were placed on fresh medium every 3 days). At day 30, fly brains were dissected and stained (see immunohistochemistry). Images of dopaminergic clusters (labeled by the anti-TH antibody) were captured with a Nikon A1R confocal microscope using a 20× objective 0.75 NA (Nikon). The total number of TH-positive neurons throughout the brain and in both hemispheres for the PPM1, PPM2, PPM3, and PPL1 clusters was counted manually.

## Neural progenitor differentiation

The iPSCs (generation and karyotyping described in Appendix Supplementary Methods and Appendix Table S1) were grown on irradiated MEFs and cultured in normal iPSC medium (DMEM/F12 Advanced (Gibco Life Technologies) supplemented with 20% KOSR, 2 mM L-glutamine, 0.1 mM MEM-NEAA, 0.1 mM 2-mercaptoethanol, 100 units/ml penicillin/streptomycin (all from Life Technologies)) and 10 ng/ml bFGF (Perprotech) at 37°C/5% CO<sub>2</sub>. Medium was changed daily and cells were passaged every 4–6 days either mechanically or enzymatically with collagenase type IV (100 U/ml) (Life Technologies), and addition of 10 μM ROCK inhibitor (Sigma) to the medium after passaging.

Neural progenitor cells (NPCs) were created according to published protocols (94, 95) with minor modifications. Briefly, for embryoid body (EB) generation, iPSCs were dissociated and transferred to non-adherent plates in normal iPSC medium without

bFGF and cultured on a shaker at 37°C/5% CO<sub>2</sub>. After 2 days *in vitro* (DIV), medium was replaced by neural induction medium (DMEM/F12 Advanced, 1:100 N2 supplement, 100 units/ml penicillin/streptomycin (all from Life Technologies) and 2 µg/ml heparin (Sigma)). After 7 DIV, the EBs were partially dissociated and plated on laminin-coated culture dishes in neural induction medium.

Neural progenitor cells growing out of the attached EB fragments were cultured for 8 DIV at 37°C/5% CO<sub>2</sub>, and medium was changed every other day. Subsequently, the NPCs were split between 1:2 and 1:6 with collagenase every 5–7 days and cultured on laminin (Sigma) coated plates. The NPCs were maintained in NPC medium (DMEM/F12 Advanced, 1:100 N2 supplement, 1:50 B27-RA supplement, 100 units/ml penicillin/streptomycin (all from Life Technologies), 1 µg/ml laminin (Sigma), and 20 ng/ml bFGF (Preprotech)).

## Neural differentiation

Neural progenitor cells were passaged 1:1 to poly-D-lysine (PDL) (Sigma)- and laminin (Sigma)-coated coverslips and cultured in neural differentiation medium (Neurobasal medium supplemented with 1:100 N2 supplement, 1:50 B27 supplement, 0.1 mM MEM-NEAA, 100 units/ml penicillin/streptomycin (all from Life Technologies), 20 ng/ml BDNF (ProspecBio), 20 ng/ml GDNF (ProspecBio), 1 µM db-cAMP (Sigma), 200 µM ascorbic acid (Sigma), and 2 µg/ml laminin (Sigma)). The differentiating cells were cultured for 28 DIV at 37°C/5% CO<sub>2</sub>, and medium was changed every other day.

## Neuron starvation

At 28 DIV, neurons were either incubated for 3 h in neural differentiation medium supplemented with 100 µM leupeptin (Roche) for the control condition, or in preconditioned EBSS (Life Technologies) supplemented with 100 µM leupeptin (Roche) for the starved condition.

## Statistics

GraphPad Prism 6 (San Diego, USA.) was used to determine statistical significance. Prior to this, datasets were tested for normal distribution using a D'Agostino–Pearson Omnibus test. Next, normally distributed data were tested with parametric tests: Student's



*t*-test was used when two datasets were compared and we used a one-way analysis of variance test (ANOVA) followed by a *post hoc* Tukey test when more than two datasets were compared. Non-normally distributed data were tested using non-parametric tests: when comparing two datasets, we used a Mann-Whitney test, and when comparing more than two datasets, we used an ANOVA Kruskal-Wallis test followed by a Dunn's *post hoc* test. Significance levels are defined as \*\*\*\* $P < 0.0001$ , \*\*\* $P < 0.001$ , \*\* $P < 0.01$ , \* $P < 0.05$ , ns (not significant)= $P > 0.05$ . "n" in the legends indicates either the number of animals used or the number of NMJs analyzed.

## Author contributions

RV, SFS, and PV conceived the study. RV, SFS, and PV analyzed data and wrote the paper. RV, SK, RM, AB, JM, NS, LB, SG, JS, SV, MP, PB, STM, FMSdV, SAK, NVG, WM, VB, FAM, SFS, and PV performed experiments and/or provided reagents, and NS performed the in-house injection. All the authors approved the final version of the manuscript.

## Acknowledgements

We thank T. Neufeld, H. Krämer, G. Juhász, and B. Ganetzky, the Bloomington *Drosophila* Stock Center the Developmental Studies Hybridoma bank for reagents and the VIB Bio-imaging core Leuven for help and BestGene Inc for *Drosophila* embryo injections. We thank Mehrnaz Ghazvini and Joost Gribnau from the Erasmus MC iPS core facility for generation of the iPSC lines, Bruno Van Swinderen (Queensland Brain Institute, The University of Queensland) for use of his fly facility and insightful discussions. We especially thank Rose Goodchild for excellent discussions throughout the study, Willem Van den Bergh for additional in-house injections, and Liesbeth Deaulmerie and the Verstreken laboratory members for help and consultation. Research support was provided by a Flanders Innovation Agency (IWT) Fellowship to RV (121324), KU Leuven (CREA, GOA), ERC CoG (646671), the Research Foundation Flanders (FWO grants G088515N, G094915N, G0D3317N, G0D3417N), the Hercules Foundation, the Interuniversity Attraction Pole program by BELSPO (P7/16), a Methusalem grant of the Flemish government, VIB, the Vlaamse Parkinson Liga, the Stichting ParkinsonFonds

(the Netherlands), the Dorpmans-Wigmans Stichting, an Erasmus MC MRace promotie grant to VB and WM, the EU Joint Programme—Neurodegenerative Disease Research (JPND) Memorabel (733051065) supported by the Nederlandse organisatie voor gezondheidsonderzoek en zorginnovatie (ZonMw) under the aegis of JPND to VB and an Hersenstichting Fellowship to FdV, the National Health and Medical Research Council (NHMRC) project grant (GNT1120381 to FAM) and Australian Research Council LIEF Grants (LE0882864 and LE130100078 to FAM). FAM is a National Health and Medical Research Council Senior Research Fellow (GNT1060075).

## References

1. Paus T, Pesaresi M, French L. White matter as a transport system. *Neuroscience*. 2014;276:117-25.
2. Burke RE, O'Malley K. Axon degeneration in Parkinson's disease. *Exp Neurol*. 2013;246:72-83.
3. Selkoe DJ. Alzheimer's disease is a synaptic failure. *Science*. 2002;298(5594):789-91.
4. Soukup SF, Pocha SM, Yuan M, Knust E. Dlin-7 is required in postsynaptic lamina neurons to prevent light-induced photoreceptor degeneration in *Drosophila*. *Curr Biol*. 2013;23(14):1349-54.
5. Klein C, Westenberger A. Genetics of Parkinson's disease. *Cold Spring Harb Perspect Med*. 2012;2(1):a008888.
6. Thomas B, Beal MF. Parkinson's disease. *Hum Mol Genet*. 2007;16 Spec No. 2:R183-94.
7. Lepeta K, Lourenco MV, Schweitzer BC, Martino Adami PV, Banerjee P, Catuara-Solarz S, et al. Synaptopathies: synaptic dysfunction in neurological disorders - A review from students to students. *J Neurochem*. 2016;138(6):785-805.
8. Schirinzi T, Madeo G, Martella G, Maltese M, Picconi B, Calabresi P, et al. Early synaptic dysfunction in Parkinson's disease: Insights from animal models. *Mov Disord*. 2016;31(6):802-13.
9. Vanhauwaert R, Verstreken P. Flies with Parkinson's disease. *Exp Neurol*. 2015;274(Pt A):42-51.
10. Cremona O, Di Paolo G, Wenk MR, Luthi A, Kim WT, Takei K, et al. Essential role of phosphoinositide metabolism in synaptic vesicle recycling. *Cell*. 1999;99(2):179-88.
11. Harris TW, Hartwig E, Horvitz HR, Jorgensen EM. Mutations in synaptobrevin disrupt synaptic vesicle recycling. *J Cell Biol*. 2000;150(3):589-600.
12. McPherson PS, Garcia EP, Slepnev VI, David C, Zhang X, Grabs D, et al. A presynaptic inositol-5-phosphatase. *Nature*. 1996;379(6563):353-7.
13. Verstreken P, Koh TW, Schulze KL, Zhai RG, Hiesinger PR, Zhou Y, et al. Synaptobrevin is recruited by endophilin to promote synaptic vesicle uncoating. *Neuron*. 2003;40(4):733-48.
14. Kirola L, Behari M, Shishir C, Thelma BK. Identification of a novel homozygous mutation Arg459Pro in SYNJ1 gene of an Indian family with autosomal recessive juvenile Parkinsonism. *Parkinsonism Relat Disord*. 2016;31:124-8.
15. Krebs CE, Karkheiran S, Powell JC, Cao M, Makarov V, Darvish H, et al. The Sac1 domain of SYNJ1 identified mutated in a family with early-onset progressive Parkinsonism with generalized seizures. *Hum Mutat*. 2013;34(9):1200-7.
16. Olgiati S, De Rosa A, Quadri M, Criscuolo C, Breedveld GJ, Picillo M, et al. *PARK20* caused by SYNJ1 homozygous Arg258Gln mutation in a new Italian family. *Neurogenetics*. 2014;15(3):183-8.
17. Quadri M, Fang M, Picillo M, Olgiati S, Breedveld GJ, Graafland J, et al. Mutation in the SYNJ1 gene associated with autosomal recessive, early-onset Parkinsonism. *Hum Mutat*. 2013;34(9):1208-15.
18. Van Epps HA, Hayashi M, Lucast L, Stearns GW, Hurley JB, De Camilli P, et al. The zebrafish nrc mutant reveals a role for the polyphosphoinositide phosphatase synaptobrevin 1 in cone photoreceptor ribbon anchoring. *J Neurosci*. 2004;24(40):8641-50.
19. Tsujishita Y, Guo S, Stolz LE, York JD, Hurley JH. Specificity determinants in phosphoinositide dephosphorylation: crystal structure of an archetypal inositol polyphosphate 5-phosphatase. *Cell*. 2001;105(3):379-89.
20. Whisstock JC, Romero S, Gurung R, Nandurkar H, Ooms LM, Bottomley SP, et al. The inositol polyphosphate 5-phosphatases and the apurinic/apyrimidinic base excision repair endonucleases share a common mechanism for catalysis. *J Biol Chem*. 2000;275(47):37055-61.
21. Guo S, Stolz LE, Lemrow SM, York JD. SAC1-like domains of yeast SAC1, INP52, and INP53 and of human synaptobrevin encode polyphosphoinositide phosphatases. *J Biol Chem*. 1999;274(19):12990-5.
22. Zhong S, Hsu F, Stefan CJ, Wu X, Patel A, Cosgrove MS, et al. Allosteric activation of the phosphoinositide phosphatase Sac1 by anionic phospholipids. *Biochemistry*. 2012;51(15):3170-7.
23. Di Paolo G, De Camilli P. Phosphoinositides in cell regulation and membrane dynamics. *Nature*. 2006;443(7112):651-7.
24. Lauwers E, Goodchild R, Verstreken P. Membrane Lipids in Presynaptic Function and Disease. *Neuron*. 2016;90(1):11-25.
25. Marat AL, Haucke V. Phosphatidylinositol 3-phosphates at the interface between cell signalling and membrane traffic. *EMBO J*. 2016;35(6):561-79.
26. Ueda Y. The role of phosphoinositides in synapse function. *Mol Neurobiol*. 2014;50(3):821-38.

27. Wenk MR, De Camilli P. Protein-lipid interactions and phosphoinositide metabolism in membrane traffic: insights from vesicle recycling in nerve terminals. *Proc Natl Acad Sci U S A*. 2004;101(22):8262-9.
28. Gad H, Ringstad N, Low P, Kjaerulf O, Gustafsson J, Wenk M, et al. Fission and uncoating of synaptic clathrin-coated vesicles are perturbed by disruption of interactions with the SH3 domain of endophilin. *Neuron*. 2000;27(2):301-12.
29. Dall'Armi C, Devereaux KA, Di Paolo G. The role of lipids in the control of autophagy. *Curr Biol*. 2013;23(1):R33-45.
30. Noda T, Matsunaga K, Taguchi-Atarashi N, Yoshimori T. Regulation of membrane biogenesis in autophagy via PI3P dynamics. *Semin Cell Dev Biol*. 2010;21(7):671-6.
31. Proikas-Cezanne T, Takacs Z, Donnes P, Kohlbacher O. WIP1 proteins: essential PtdIns3P effectors at the nascent autophagosome. *J Cell Sci*. 2015;128(2):207-17.
32. Simonsen A, Tooze SA. Coordination of membrane events during autophagy by multiple class III PI3-kinase complexes. *J Cell Biol*. 2009;186(6):773-82.
33. Mani M, Lee SY, Lucast L, Cremona O, Di Paolo G, De Camilli P, et al. The dual phosphatase activity of synaptotagmin1 is required for both efficient synaptic vesicle endocytosis and reavailability at nerve terminals. *Neuron*. 2007;56(6):1004-18.
34. Soukup SF, Kuenen S, Vanhauwaert R, Manetsberger J, Hernandez-Diaz S, Swerts J, et al. A LRRK2-Dependent EndophilinA Phosphoswitch Is Critical for Macroautophagy at Presynaptic Terminals. *Neuron*. 2016;92(4):829-44.
35. Venken KJ, Schulze KL, Haelterman NA, Pan H, He Y, Evans-Holm M, et al. MiMIC: a highly versatile transposon insertion resource for engineering *Drosophila melanogaster* genes. *Nat Methods*. 2011;8(9):737-43.
36. Vilain S, Vanhauwaert R, Maes I, Schoovaerts N, Zhou L, Soukup S, et al. Fast and efficient *Drosophila melanogaster* gene knock-ins using MiMIC transposons. *G3 (Bethesda)*. 2014;4(12):2381-7.
37. Verstreken P, Kjaerulf O, Lloyd TE, Atkinson R, Zhou Y, Meinertzhagen IA, et al. Endophilin mutations block clathrin-mediated endocytosis but not neurotransmitter release. *Cell*. 2002;109(1):101-12.
38. Ramaswami M, Krishnan KS, Kelly RB. Intermediates in synaptic vesicle recycling revealed by optical imaging of *Drosophila* neuromuscular junctions. *Neuron*. 1994;13(2):363-75.
39. Dickman DK, Lu Z, Meinertzhagen IA, Schwarz TL. Altered synaptic development and active zone spacing in endocytosis mutants. *Curr Biol*. 2006;16(6):591-8.
40. Burman C, Ktistakis NT. Regulation of autophagy by phosphatidylinositol 3-phosphate. *FEBS Lett*. 2010;584(7):1302-12.
41. D'Amelio M, Nistico R. Editorial: targeting synaptic dysfunction and neural connectivity in neurological and psychiatric disorders. *Curr Pharm Des*. 2013;19(36):6391-2.
42. Devereaux K, Dall'Armi C, Alcazar-Roman A, Ogasawara Y, Zhou X, Wang F, et al. Regulation of mammalian autophagy by class II and III PI 3-kinases through PI3P synthesis. *PLoS One*. 2013;8(10):e76405.
43. Hernandez D, Torres CA, Setlik W, Cebrian C, Mosharov EV, Tang G, et al. Regulation of presynaptic neurotransmission by macroautophagy. *Neuron*. 2012;74(2):277-84.
44. Maday S, Holzbaur EL. Autophagosome biogenesis in primary neurons follows an ordered and spatially regulated pathway. *Dev Cell*. 2014;30(1):71-85.
45. Stavoe AK, Hill SE, Hall DH, Colon-Ramos DA, KIF1A/UNC-104 Transports ATG-9 to Regulate Neurodevelopment and Autophagy at Synapses. *Dev Cell*. 2016;38(2):171-85.
46. Wang T, Martin S, Nguyen TH, Harper CB, Gormall RS, Martinez-Marmol R, et al. Flux of signalling endosomes undergoing axonal retrograde transport is encoded by presynaptic activity and TrkB. *Nat Commun*. 2016;7:12976.
47. Wang T, Martin S, Papadopoulos A, Harper CB, Mavlyutov TA, Niranjana D, et al. Control of autophagosome axonal retrograde flux by presynaptic activity unveiled using botulinum neurotoxin type A. *J Neurosci*. 2015;35(15):6179-94.
48. Williamson WR, Wang D, Haberman AS, Hiesinger PR. A dual function of V0-ATPase a1 provides an endolysosomal degradation mechanism in *Drosophila melanogaster* photoreceptors. *J Cell Biol*. 2010;189(5):885-99.
49. Zhu JY, Vereshchagina N, Sreekumar V, Burbulla LF, Costa AC, Daub KJ, et al. Knockdown of Hsc70-5/mortalin induces loss of synaptic mitochondria in a *Drosophila* Parkinson's disease model. *PLoS One*. 2013;8(12):e83714.
50. He C, Song H, Yoritatsu T, Monastyrska I, Yen WL, Legakis JE, et al. Recruitment of Atg9 to the preautophagosomal structure by Atg11 is essential for selective autophagy in budding yeast. *J Cell Biol*. 2006;175(6):925-35.
51. Tamura H, Shibata M, Koike M, Sasaki M, Uchiyama Y. Atg9A protein, an autophagy-related membrane protein, is localized in the neurons of mouse brains. *J Histochem Cytochem*. 2010;58(5):443-53.
52. Yamamoto H, Kakuta S, Watanabe TM, Kitamura A, Sekito T, Kondo-Kakuta C, et al. Atg9 vesicles are an important membrane source during early steps of autophagosome formation. *J Cell Biol*. 2012;198(2):219-33.
53. George AA, Hayden S, Stanton GR, Brockerhoff SE. Arf6 and the 5'phosphatase of Synaptotagmin 1 regulate autophagy in cone photoreceptors. *Inside Cell*. 2016;1(2):117-33.
54. Kabeya Y, Mizushima N, Ueno T, Yamamoto A, Kirisako T, Noda T, et al. LC3, a mammalian homologue of yeast Apg8p, is localized in autophagosome membranes after processing. *EMBO J*. 2000;19(21):5720-8.
55. Juhasz G, Hill JH, Yan Y, Sass M, Baehrecke EH, Backer JM, et al. The class III PI(3)K Vps34 promotes autophagy and endocytosis but not TOR signaling in *Drosophila*. *J Cell Biol*. 2008;181(4):655-66.
56. Marzella L, Ahlberg J, Glaumann H. Isolation of autophagic vacuoles from rat liver: morphological and biochemical characterization. *J Cell Biol*. 1982;93(1):144-54.
57. Chi C, Zhu H, Han M, Zhuang Y, Wu X, Xu T. Disruption of lysosome function promotes tumor growth and metastasis in *Drosophila*. *J Biol Chem*. 2010;285(28):21817-23.
58. Stauber WT, Hedge AM, Trout JJ, Schottelius BA. Inhibition of lysosomal function in red and white skeletal muscles by chloroquine. *Exp Neurol*. 1981;71(2):295-306.
59. DeVorkin L, Gorski SM. Monitoring Autophagy in *Drosophila* Using Fluorescent Reporters in the UAS-GAL4 System. *Cold Spring Harbor Protocols*. 2014(9):pdb.prot080341-prot.
60. Baskaran S, Ragusa MJ, Boura E, Hurley JH. Two-site recognition of phosphatidylinositol 3-phosphate by PROPPINs in autophagy. *Mol Cell*. 2012;47(3):339-48.
61. Zhang M, Chang H, Zhang Y, Yu J, Wu L, Ji W, et al. Rational design of true monomeric and bright photoactivatable fluorescent proteins. *Nat Methods*. 2012;9(7):727-9.
62. Bademosi AT, Lauwers E, Padmanabhan P, Odierna L, Chai YJ, Papadopoulos A, et al. In vivo single-molecule imaging of syntaxin1A reveals polyphosphoinositide- and activity-dependent trapping in presynaptic nanoclusters. *Nat Commun*. 2017;8:13660.
63. Juhasz G, Erdi B, Sass M, Neufeld TP. Atg7-dependent autophagy promotes neuronal health, stress tolerance, and longevity but is dispensable for metamorphosis in *Drosophila*. *Genes Dev*. 2007;21(23):3061-6.
64. Komatsu M, Waguri S, Chiba T, Murata S, Iwata J, Tanida I, et al. Loss of autophagy in the central nervous system causes neurodegeneration in mice. *Nature*. 2006;441(7095):880-4.

65. Parrish WR, Stefan CJ, Emr SD. Essential role for the myotubularin-related phosphatase Ymr1p and the synaptotagmin-like phosphatases Sjl2p and Sjl3p in regulation of phosphatidylinositol 3-phosphate in yeast. *Mol Biol Cell*. 2004;15(8):3567-79.
66. Heidelberger R, Thoreson WB, Witkovsky P. Synaptic transmission at retinal ribbon synapses. *Prog Retin Eye Res*. 2005;24(6):682-720.
67. Van Epps HA, Yim CM, Hurley JB, Brockerhoff SE. Investigations of photoreceptor synaptic transmission and light adaptation in the zebrafish visual mutant nrc. *Invest Ophthalmol Vis Sci*. 2001;42(3):868-74.
68. Hyttinen JM, Niittykoski M, Salminen A, Kaarniranta K. Maturation of autophagosomes and endosomes: a key role for Rab7. *Biochim Biophys Acta*. 2013;1833(3):503-10.
69. Jager S, Bucci C, Tanida I, Ueno T, Kominami E, Saftig P, et al. Role for Rab7 in maturation of late autophagic vacuoles. *J Cell Sci*. 2004;117(Pt 20):4837-48.
70. Puri C, Renna M, Bento CF, Moreau K, Rubinstein DC. Diverse autophagosome membrane sources coalesce in recycling endosomes. *Cell*. 2013;154(6):1285-99.
71. Cebollero E, van der Vaart A, Zhao M, Rieter E, Klionsky DJ, Helms JB, et al. Phosphatidylinositol-3-phosphate clearance plays a key role in autophagosome completion. *Curr Biol*. 2012;22(17):1545-53.
72. Dooley HC, Razi M, Polson HE, Girardin SE, Wilson MI, Tooze SA. WIP1 links LC3 conjugation with PI3P, autophagosome formation, and pathogen clearance by recruiting Atg12-5-16L1. *Mol Cell*. 2014;55(2):238-52.
73. Polson HE, de Lartigue J, Rigden DJ, Reedijk M, Urbe S, Clague MJ, et al. Mammalian Atg18 (WIP1) localizes to omegasome-anchored phagophores and positively regulates LC3 lipidation. *Autophagy*. 2010;6(4):506-22.
74. Cheng J, Fujita A, Yamamoto H, Tatsumatsu T, Kakuta S, Obara K, et al. Yeast and mammalian autophagosomes exhibit distinct phosphatidylinositol 3-phosphate asymmetries. *Nat Commun*. 2014;5:3207.
75. Chua CE, Tang BL. Rab, SNAREs and alpha-synuclein--membrane trafficking defects in synucleinopathies. *Brain Res Rev*. 2011;67(1-2):268-81.
76. Soper JH, Kehm V, Burd CG, Bankaitis VA, Lee VM. Aggregation of alpha-synuclein in *S. cerevisiae* is associated with defects in endosomal trafficking and phospholipid biosynthesis. *J Mol Neurosci*. 2011;43(3):391-405.
77. Kawajiri S, Saiki S, Sato S, Sato F, Hatano T, Eguchi H, et al. PINK1 is recruited to mitochondria with parkin and associates with LC3 in mitophagy. *FEBS Lett*. 2010;584(6):1073-9.
78. Narendra D, Tanaka A, Suen DF, Youle RJ. Parkin is recruited selectively to impaired mitochondria and promotes their autophagy. *J Cell Biol*. 2008;183(5):795-803.
79. Vincow ES, Merrihew G, Thomas RE, Shulman NJ, Beyer RP, MacCoss MJ, et al. The PINK1-Parkin pathway promotes both mitophagy and selective respiratory chain turnover in vivo. *Proc Natl Acad Sci U S A*. 2013;110(16):6400-5.
80. Schuske KR, Richmond JE, Matthies DS, Davis WS, Runz S, Rube DA, et al. Endophilin is required for synaptic vesicle endocytosis by localizing synaptotagmin. *Neuron*. 2003;40(4):749-62.
81. Chang YY, Neufeld TP. An Atg1/Atg13 complex with multiple roles in TOR-mediated autophagy regulation. *Mol Biol Cell*. 2009;20(7):2004-14.
82. Pulipparacharuvil S, Akbar MA, Ray S, Sevrioukov EA, Haberman AS, Rohrer J, et al. Drosophila Vps16A is required for trafficking to lysosomes and biogenesis of pigment granules. *J Cell Sci*. 2005;118(Pt 16):3663-73.
83. Verstreken P, Ohyama T, Haueter C, Habets RL, Lin YQ, Swan LE, et al. Tweek, an evolutionarily conserved protein, is required for synaptic vesicle recycling. *Neuron*. 2009;63(2):203-15.
84. Shen W, Ganetzky B. Autophagy promotes synapse development in Drosophila. *J Cell Biol*. 2009;187(1):71-9.
85. Venken KJ, Carlson JW, Schulze KL, Pan H, He Y, Spokony R, et al. Versatile P(acman) BAC libraries for transgenesis studies in Drosophila melanogaster. *Nat Methods*. 2009;6(6):431-4.
86. Venken KJ, He Y, Hoskins RA, Bellen HJ, P(acman): a BAC transgenic platform for targeted insertion of large DNA fragments in D. melanogaster. *Science*. 2006;314(5806):1747-51.
87. Yu C, Wan KH, Hammonds AS, Stapleton M, Carlson JW, Celniker SE. Development of expression-ready constructs for generation of proteomic libraries. *Methods Mol Biol*. 2011;723:257-72.
88. Scott RC, Schuldiner O, Neufeld TP. Role and regulation of starvation-induced autophagy in the Drosophila fat body. *Dev Cell*. 2004;7(2):167-78.
89. Urwyler O, Izadifar A, Dascenco D, Petrovic M, He H, Ayaz D, et al. Investigating CNS synaptogenesis at single-synapse resolution by combining reverse genetics with correlative light and electron microscopy. *Development*. 2015;142(2):394-405.
90. Fernandes AC, Uytterhoeven V, Kuenen S, Wang YC, Slabbaert JR, Swerts J, et al. Reduced synaptic vesicle protein degradation at lysosomes curbs TBC1D24/sky-induced neurodegeneration. *J Cell Biol*. 2014;207(4):453-62.
91. Kasprzowicz J, Kuenen S, Miskiewicz K, Habets RL, Smitz I, Verstreken P. Inactivation of clathrin heavy chain inhibits synaptic recycling but allows bulk membrane uptake. *J Cell Biol*. 2008;182(5):1007-16.
92. Slabbaert JR, Kuenen S, Swerts J, Maes I, Uytterhoeven V, Kasprzowicz J, et al. The Drosophila Homolog of SLC25A39/40, Is a Mitochondrial Carrier That Promotes Neuronal Survival. *J Neurosci*. 2016;36(6):1914-29.
93. Seabrooke S, Qiu X, Stewart BA. Nonmuscle Myosin II helps regulate synaptic vesicle mobility at the Drosophila neuromuscular junction. *BMC Neurosci*. 2010;11:37.
94. de Esch CE, Ghazvini M, Loos F, Schelling-Kazaryan N, Widagdo W, Munshi ST, et al. Epigenetic characterization of the FMR1 promoter in induced pluripotent stem cells from human fibroblasts carrying an unmethylated full mutation. *Stem Cell Reports*. 2014;3(4):548-55.
95. Gunhanlar N, Shpak G, van der Kroeg M, Gouty-Colomer LA, Munshi ST, Lendemeijer B, et al. A simplified protocol for differentiation of electrophysiologically mature neuronal networks from human induced pluripotent stem cells. *Mol Psychiatry*. 2018;23(5):1336-44.

# Supplementary Information

## Genotypes

vasaPhiC31;Mi{MIC}Synj<sup>MI11871</sup>/CyO  
 yw,ey::Flp GMR::lacZ; P{ry+ neoFRT}42D/FRT42D cl P(w+)  
 yw,ey::Flp GMR::lacZ; P{ry+ neoFRT}42D synj<sup>1</sup>/FRT42D cl P(w+)  
 w;;nSyb-Gal4/+  
 w;P{ry+ neoFRT}42D synj<sup>1</sup>/ P{ry+ neoFRT}42D synj<sup>2</sup>;nSyb-Gal4/+  
 w;UAS-synj<sup>RQ</sup>, P{ry+ neoFRT}42D synj<sup>1</sup>/ P{ry+ neoFRT}42D synj<sup>2</sup>;nSyb-Gal4/+  
 w;UAS-synj<sup>+</sup>, P{ry+ neoFRT}42D synj<sup>1</sup>/ P{ry+ neoFRT}42D synj<sup>2</sup>;nSyb-Gal4/+  
 w<sup>1118</sup>  
 w;synj<sup>RQ</sup>  
 w;Atg9;HA::Atg9 (unpublished)  
 w;;HA::Atg9 (unpublished)  
 w;synj<sup>RQ</sup>;HA::Atg9  
 w;UAS-mCherry::Atg8/+;D42-Gal4/+  
 w;P{ry+ neoFRT}42D synj<sup>1</sup>/UAS-mCherry::Atg8,synj<sup>2</sup>;D42-Gal4/+  
 w;UAS-synj<sup>RQ</sup>, P{ry+ neoFRT}42D synj<sup>1</sup>/UAS-mCherry::Atg8, P{ry+ neoFRT}42D synj<sup>2</sup>;D42-Gal4/+  
 w;UAS-synj<sup>CS</sup>, P{ry+ neoFRT}42D synj<sup>1</sup>/UAS-mCherry::Atg8, P{ry+ neoFRT}42D synj<sup>2</sup>;D42-Gal4/+  
 w;UAS-synj<sup>+</sup>, P{ry+ neoFRT}42D synj<sup>1</sup>/UAS-mCherry::Atg8, P{ry+ neoFRT}42D synj<sup>2</sup>;D42-Gal4/+  
 w;UAS-GFP::Lamp1 /+;D42-GAL4/+  
 w;P{ry+ neoFRT}42D synj<sup>1</sup>/UAS-GFP::Lamp1, P{ry+ neoFRT}42D synj<sup>2</sup>;D42-Gal4/+  
 w;UAS-synj<sup>RQ</sup>, P{ry+ neoFRT}42D synj<sup>1</sup>/UAS-GFP::Lamp1, P{ry+ neoFRT}42D synj<sup>2</sup>;D42-Gal4/+  
 w;UAS-synj<sup>+</sup>, P{ry+ neoFRT}42D synj<sup>1</sup>/UAS-GFP::Lamp1, P{ry+ neoFRT}42D synj<sup>2</sup>;D42-Gal4/+  
 w;;UAS-eGFP-mCherry::Atg8/D42-Gal4  
 w;synj<sup>RQ</sup>;UAS-eGFP-mCherry::Atg8/D42-Gal4  
 w;;atg18a(W3)/atg18a(W4)  
 w;;Da-Gal4,atg18a(W3)/ UAS-GFP::Atg18a,atg18a(W4)  
 w;;atg18a(W3)/UAS-GFP::Atg18a,atg18a(W4)  
 w;;UAS-GFP::Atg18a/D42-Gal4  
 w;;UAS-GFP::Atg18b/D42-Gal4  
 w;;UAS-GFP::CG11975/D42-Gal4  
 w;P{ry+ neoFRT}42D synj<sup>1</sup>/ P{ry+ neoFRT}42D synj<sup>2</sup>;UAS-GFP::Atg18a/D42-Gal4  
 w;UAS-synj<sup>RQ</sup>, P{ry+ neoFRT}42D synj<sup>1</sup>/ P{ry+ neoFRT}42D synj<sup>2</sup>;UAS-GFP::Atg18a/D42-Gal4  
 w;UAS-synj<sup>+</sup>, P{ry+ neoFRT}42D synj<sup>1</sup>/ P{ry+ neoFRT}42D synj<sup>2</sup>;UAS-GFP::Atg18a/D42-Gal4  
 w;synj<sup>RQ</sup>;UAS-GFP::Atg18a/D42-Gal4  
 w;UAS-mCherry::Atg8/+;UAS-GFP::Atg18a/D42-Gal4  
 w;;UAS-mEOS3.2::Atg18a/D42-Gal4  
 w;synj<sup>RQ</sup>;UAS-mEOS3.2::Atg18a/D42-Gal4  
 w;;UAS-PLCd-PH-EGFP/ D42-Gal4  
 w;P{ry+ neoFRT}42D synj<sup>1</sup>/ P{ry+ neoFRT}42D synj<sup>2</sup>;UAS-PLCd-PH-EGFP/ D42-Gal4  
 w;UAS-synj<sup>RQ</sup>, P{ry+ neoFRT}42D synj<sup>1</sup>/ P{ry+ neoFRT}42D synj<sup>2</sup>;UAS-PLCd-PH-EGFP/ D42-Gal4  
 w;UAS-synj<sup>+</sup>, P{ry+ neoFRT}42D synj<sup>1</sup>/ P{ry+ neoFRT}42D synj<sup>2</sup>;UAS-PLCd-PH-EGFP/ D42-Gal4

## FM 1-43

FM1-43 labeling and quantification of intensities was performed as described (Verstreken et al. 2008). Third instar larvae were dissected and stimulated using HL3 with 90 mM KCl in 1.5 mM  $\text{CaCl}_2$  for 1 min and followed by several washing steps before Imaging. Images were captured with a Nikon eclipse FN1 upright microscope and a 60x 1.0 NA W lens.

## Electrophysiology

Electroretinograms (ERGs) were recorded from 3-5 day old adult flies as described (Slabbaert et al. 2016), with the only difference that the repetitive light stimulus (1 s) was given by a white light-emitting diode. Raw data traces were transferred to Clampfit 10.5 (Molecular Devices) for quantification.

Two-electrode voltage clamp (TEVC) experiments to measure EJCs and mEJCs and current clamp experiments to measure EJPs were recorded as described in (Kasprovicz et al. 2014; Slabbaert et al. 2016). Third-instar larvae were dissected in  $\text{Ca}^{2+}$  free HL-3 (110 mM NaCl, 5 mM KCl, 10 mM  $\text{NaHCO}_3$ , 5 mM Hepes, 30 mM sucrose, 5 mM trehalose, and 10 mM  $\text{MgCl}_2$ , pH 7.2; Stewart et al., 1994). Next, fillets were bathed in HL-3 with 1 mM  $\text{CaCl}_2$  (EJC) or 2 mM  $\text{CaCl}_2$  (EJP) where nerves were severed and isolated using a suction electrode. Axons were stimulated at least 50% above threshold at 0.2 Hz in the presence of 1 or 2 mM  $\text{CaCl}_2$  for EJC or EJP recordings respectively. Recordings were measured in muscle 6, segment A2 or A3 using sharp electrodes (current clamp electrode (30 M $\Omega$ ), the voltage sensing electrode for TEVC (30 M $\Omega$ ) and the current passing electrode for TEVC (10-15 M $\Omega$ )) filled with a 3:1 solution of 3 M KCl and 3 M KAc. Only data recorded from muscle 6 with a resting membrane potential more hyperpolarized than -60 mV that during the recording did not deviate more than 15% were analyzed. For TEVC experiments the holding potential was -70 mV and the input resistance was  $\geq 4$  M $\Omega$ . For EJPs, motor neurons were stimulated at 10 Hz for 10 minutes. EJP sets were omitted when the recording did not hold its basal membrane potential throughout the 10 minute stimulation paradigm. Signals were amplified using the Axoclamp900A amplifier (Molecular Devices), filtered using a 1 kHz Bessel filter, and digitized at 10 kHz using a Digidata 1440A (Molecular Devices). Data were stored, processed and analyzed using Clampfit 10.5 (Molecular Devices). To calculate the EJC amplitude, 60 responses recorded at 0.2 Hz were averaged. The amplitude and frequency of mEJCs were measured using the Clampfit 10.5 event-detection algorithm. EJP amplitudes were quantified for each stimuli over the 10 minute stimulation period. Next, the EJP amplitudes were binned

for every 300 stimuli, except for the first 150 binned stimuli. Subsequently, the EJP amplitudes for each binned data point were normalized to the first binned data point of the first 150 stimuli.

## Immunoblotting

Adult flies were decapitated with a razor blade. Heads were homogenized on ice using a motorized pellet pestle in lysis buffer containing 50 mM Tris-HCl pH 6.8, 130 mM NaCl, 1% Triton, and protease inhibitor complete (Roche). Next, protein were reduced and denatured in 1x lithium dodecyl sulfate (LDS) sample buffer (Invitrogen) supplemented with 1%  $\beta$ -mercaptoethanol for 10 min at 80°C. Then, proteins were separated on NuPAGE Novex 4-12% Bis-Tris polyacrylamide gels (Invitrogen) in MOPS buffer and transferred to nitrocellulose membrane. Membranes were blocked in TBST (Tris-buffered saline + 0.05% Tween-20) with 5% BSA for 1 hour at room temperature before incubation with primary antibodies (rabbit  $\alpha$ -synj (1:5000 (Verstreken et al. 2003)) and mouse  $\alpha$ -Tubulin 12G10 (1:000 (Developmental Studies Hybridoma Bank)) diluted in blocking buffer. After incubation with primary antibodies at 4°C overnight, rabbit HRP-conjugated secondary antibodies were added at a concentration of 1:10,000 for 1 h at room-temperature. Signal was detected using the Western Lightning Plus ECL kit (Perkin Elmer) and imaged on a Fuji-Film digital imaging system, quantification was done using NIH ImageJ.

## Immunohistochemistry

For immunohistochemistry third instar larvae were dissected in HL3, fixed in 4% paraformaldehyde in HL3, permeabilized with 0.4% triton in PBS (PBT), preblocked with 10% NGS-PBT and incubated with primary antibodies overnight at 4°C, washed and followed by incubation with secondary antibodies in PBT with 10% NGS for 2 h at room temperature and washed before being mounted in Vectashield (Vector Laboratories). Immunohistochemistry of 30 day old adult brains was performed by dissecting brains in ice-cold PBS and fixing them with 3.7% formaldehyde in PBT (PBS + 0.1% Triton X-100). Subsequently, the brains were washed, blocked with 5% BSA in PBT and overnight incubated with primary antibody at 4°C, samples were washed followed by incubation with secondary antibodies, washed and mounted in Vectashield (Vector Laboratories).

The following antibodies were used to stain third instar *Drosophila* larvae or adult brains: chicken  $\alpha$ -GFP (1:1000 (Invitrogen; A10262)), rabbit  $\alpha$ -synj (1:500 (Verstreken et al. 2003)), guinea pig  $\alpha$ -EndoA (GP69) (1:1000 (Verstreken et al. 2002)), chicken  $\alpha$ -mCherry (1:1000



(Novus; NBP2-25158)), mouse  $\alpha$ -Dlg (1:500 (DSHB; 4F3)), rabbit  $\alpha$ -HRP (1:1000 (Jackson ImmunoResearch)), rabbit  $\alpha$ -TH (1:300 (Millipore)), Alexa Fluor 488-/Alexa Fluor 555-conjugated secondary antibodies: 1:1000 (Invitrogen). Fixed samples were imaged on a Nikon A1R confocal microscope through a 60X NA1.2 water immersion lens (for larval NMJ imaging) or a 20x NA0.75 air lens (for brain imaging).

Cells were fixed in 4% formaldehyde for 20 minutes, and washed with PBS. Subsequently, primary antibody incubation was performed overnight at 4°C in labeling buffer (50 mM Tris.Cl (pH 7.4), 0.9% NaCl 0.25% gelatin, 0.2% TritonX-100 (all from Sigma)). The next day coverslips were washed in PBS, followed by secondary antibody incubation in the dark for 1 hour at room temperature in labeling buffer. After washing in PBS, coverslips were mounted with Prolong Gold plus DAPI (Life Technologies). Primary antibodies: mouse anti-WIPI2 (AbD Serotec), rabbit anti-Synapsin 1 (Synaptic Systems) goat anti-human OCT3/4 (Santa Cruz Biotechnology), goat anti-human NANOG (R&D Systems), mouse anti-human TRA-1-80 (Santa Cruz Biotechnology) and guinea pig anti-MAP2 (Synaptic Systems). Secondary antibodies: donkey anti-mouse Alexa 488 (Jackson Immuno), goat anti-guinea pig Alexa 647 (Abcam), donkey anti-goat Cy2 (Jackson Immuno), donkey anti-mouse Cy3 (Jackson Immuno). Slides were analyzed on a Leica SP5 AOBS confocal laser scanning microscope with a HCX PL APO CS  $\times$ 40 objective (NA 1.25) or HCX PL APO CS  $\times$ 63 objective (NA 1.40). Image stacks were acquired with a step size of 494 nm over 9.88  $\mu$ m thickness and a resolution of 1,024 x 1,024 pixels at a zoom of 1.7x to visualize the WIPI2 dots. Data was quantified in NIH ImageJ. WIPI2 dots were counted using particle analysis of a binary image combined with applying a threshold mask on the cytoplasmic signal to calculate the area.

## Immunoprecipitation (IP)

IP of Atg9<sup>HA</sup> was performed similar as described (Soukup et al. 2016), briefly adult flies that express genomic Atg9<sup>HA</sup> or *w,<sup>synj<sup>ro</sup></sup>;Atg9<sup>HA</sup>* or controls (*w<sup>1118</sup>*) were frozen on dry ice and decapitated by vigorously vortexing. Heads were separated from the body by sieving. Heads were homogenized on ice using a motorized pestle, in 1 ml of homogenization buffer containing 300 mM sucrose, 4 mM HEPES (pH 7.4) and complete protease inhibitor (Roche). The homogenate was cleared from debris by centrifugation for 2 times 10 min at 10,000 x g. 150  $\mu$ l of the supernatant (added with 150 mM NaCl) was loaded onto 25  $\mu$ l of anti-HA magnetic beads (Pierce) and incubated for 30 minutes at RT on a shaker. HA-beads (preincubated with 5% BSA in TBS for 30 minutes) were magnetically separated and washed five times with 1x TBS.



For gel analysis, beads were resuspended in 15 µl homogenization buffer and 4 µl 4xSDS buffer, denatured for 10 min at 90°C and separated by SDS-PAGE. For Western blots, NuPAGE Novex 4-12% Bis-Tris polyacrylamide gels (Invitrogen) were used. Blots were transferred onto PVDF (Merck-Millipore), blocked with 2.5% BSA in TBST (Tris-buffered saline + 0.05% Tween-20) and incubated with antibodies using standard procedures (sequentially, with stripping for 30 min at 55°C with 2% SDS - TBS-T in between). Antibody dilutions used: rabbit α-synj (1:5000 (Verstreken et al. 2003)), rabbit α-SNAP (1: 5000 (gift from Leo Pallanck)), rabbit α-complexin (1:2000 (gift from Troy Littleton)) and mouse α-HA (1:1000 (Covance)), peroxidase-conjugated secondary antibodies 1:10,000. The ECL system (Perkin Elmer) was used for detection and chemiluminescence was imaged using LAS-3000 (Fuji Film).

## Wortmannin and YM201636 assay

PI(3)P or PI(3,5)P<sub>2</sub> production was inhibited by placing early third instar larvae on petri dishes containing 20% sucrose and 1% agarose and either 5 µM wortmannin (Vps34 inhibitor) (Sigma W3144-250UL) or 5 µM YM201636 (PIKfyve inhibitor) (Invitrogen YM201636) for 3 to 4 h prior to experimentation (Scott et al. 2004).

## sptPALM Analysis

PALM-Tracer, a customised-written software plugin in Metamorph (Molecular Devices) (Kechkar et al. 2013; Nair et al. 2013), was used to localize molecules and quantify the mobility of single molecules, yielding the diffusion coefficient ( $\mu\text{m}^2 \text{s}^{-1}$ ) values (equation 1) as well as mean square displacement ( $\mu\text{m}^2$ ) (MSD) values (equation 2). The parameters were set to isolate trajectories from molecules undergoing free cytosolic diffusion and associated with organelles. Only fluorescent molecules with sufficient threshold across a minimum of eight movie frames were tracked and used for data analysis. The PALM-Tracer software also generated trajectory maps as well as average intensity maps.

$$(1) \quad MSD(n \times \Delta t) = \sum_{i=1}^{N-n} \frac{[x((i+n) \times \Delta t) - x(i \times \Delta t)]^2 + [y((i+n) \times \Delta t) - y(i \times \Delta t)]^2}{N-n}$$

N is the number of data points,  $\Delta t$  is the time interval of each frame, x and y are the coordinates for each particle and D is the diffusion coefficient. The MSD was calculated for the time interval  $\tau = n\Delta t$  for the entire duration of each trajectory. The first 8 points of the MSD were averaged over all trajectories and graphed against time.

$$(2) \quad MSD(\tau) = a + 4D\tau$$

The diffusion coefficient,  $D$ , was calculated for each trajectory, from linear fits of the first four points of the MSD versus time function,  $a$  is the offset constant which incorporates the effects of localization error and finite camera exposure. The threshold for the mobile to immobile fraction was determined to be  $0.021 \mu\text{m}^2 \text{s}^{-1}$  as previously described (Bademosi et al. 2017).

Microsoft Excel was used to further analyse the MSDs to obtain their mean and standard error of mean (S.E.M.). Relative frequency distribution graphs and average MSD curves were plotted using Graph Prism (version 6.0).

## Generation of iPS cell lines

Primary cultures of dermal fibroblasts were established from punch biopsies of two siblings diagnosed with juvenile parkinsonism due to a homozygous R258Q mutation in the *SYNJ1* gene as described by (Quadri et al. 2013) (pedigree shown in Figure S4). The study procedures were approved by the medical ethical committee of the Erasmus MC Rotterdam, conformed to the principles set out in the WMA Declaration of Helsinki and the Department of Health and Human Services Belmont Report and all participating subjects provided written informed consent. The male patient (NAPO16) developed symptoms at 22 years of age and underwent the skin biopsy at the age of 50. The female patient (NAPO17) developed symptoms at the age of 28 and the skin biopsy was taken at the age of 35. In addition, primary cultures of dermal fibroblasts were established from skin puncture biopsies of two unaffected individuals. Control line 1.5 was derived from a healthy unrelated female donor (42 years), while the control line 2.1 was derived from a healthy unrelated male donor (57 years). Reprogramming of all patient and control lines used in this study was performed by The Erasmus MC iPS core facility as described previously with minor modifications (Warlich et al. 2011). Briefly, fibroblasts were transduced with a multicistronic lentiviral vector encoding OCT4, SOX2, KLF4, and MYC, and a dTomato reporter gene, under the control of a retroviral promoter (SFFV) which is rapidly silenced during the reprogramming process. Transduced fibroblasts were seeded on irradiated Mouse Embryo Fibroblasts (MEFs) and cultured with standard human embryonic stem cell (hESC) medium, until colonies could be picked. Selection of colonies was based on morphology, and the presence and subsequent loss of dTomato reporter expression, indicating proper silencing of the transgene. Multiple clones were characterized and selected based on karyotyping, expression of endogenous pluripotency factors and expression of differentiation associated markers after 8 days of Embryoid Body formation (Figure S4 & table S1). Furthermore, the mutation status was

confirmed in all patient iPSC lines (Figure S4).

## Karyotyping

iPSCs were harvested with TrypLE Express (Life Technologies), treated with colcemid (10 µg/ml) (Life Technologies) for 30 minutes at 37°C and then incubated in hypotonic solution 75 mM KCL for 30 minutes at 37°C and 10 minutes at room temperature. Cells were fixed using Carnoy's solution for 4 rounds of adding fixative, centrifuged for 10 min at 1100 rpm and aspiration of supernatant. Metaphases were mounted using Vectashield plus DAPI (Vector Laboratories).

## RT-Q-PCR

RNA was isolated directly from iPSCs and 8 day old EBs using RNA Bee (AMS Bio), according to the manufacturer's protocol. The RNA was then treated with DNase before a two-step reverse transcriptase PCR was performed with the iScript cDNA synthesis kit (Biorad) according to the manufacturer's protocol. Q-PCR using SYBR Green (KAPA Biosystems) was performed on 100 µl cDNA product. Cycling conditions were an initial denaturation of 3 minutes at 95°C, followed 40 cycles of 5 seconds 95°C and 30 seconds 60°C. GAPDH was used as a reference gene and the human ES cell line H9 was included for normalization of the gene expression.

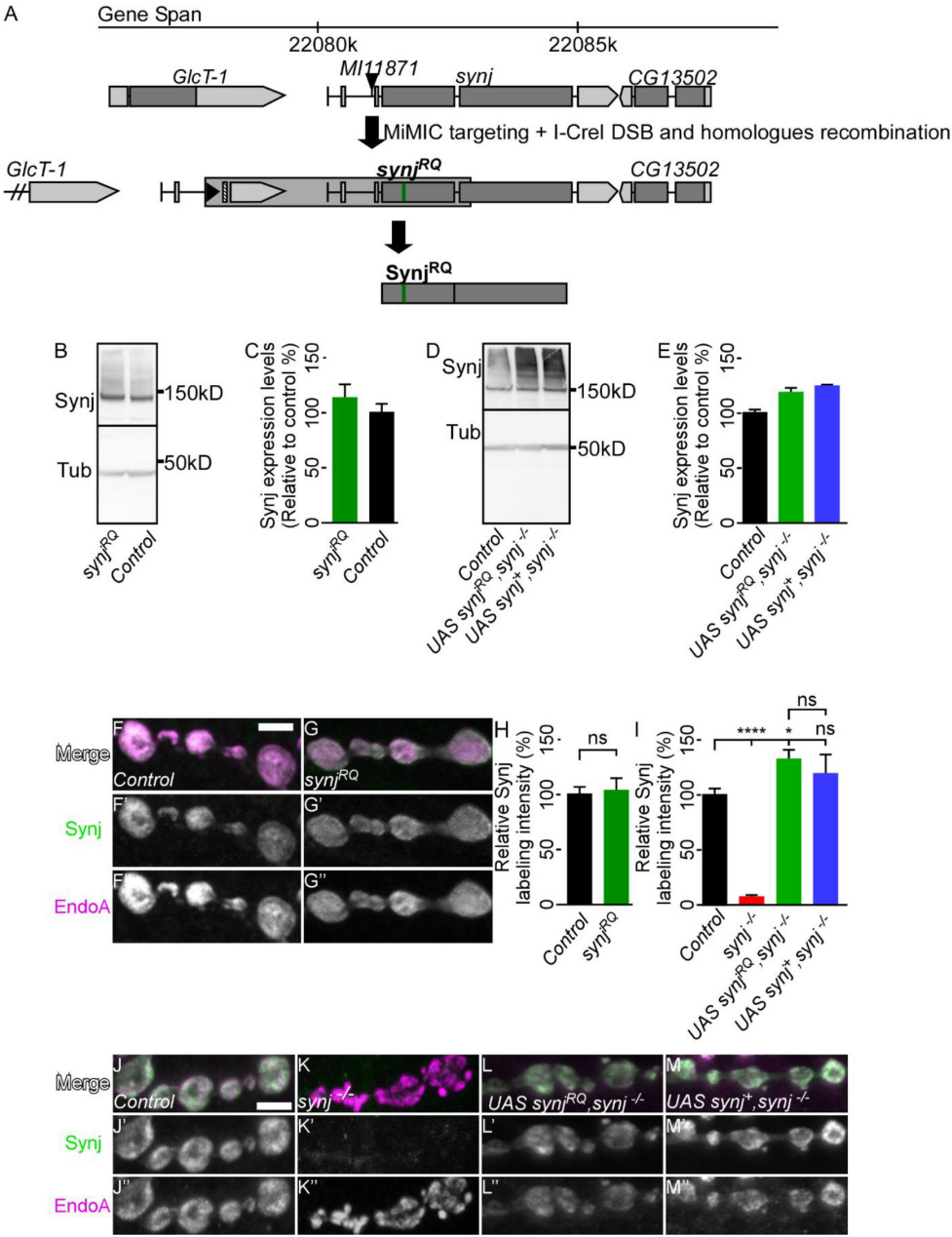
# Supplementary References

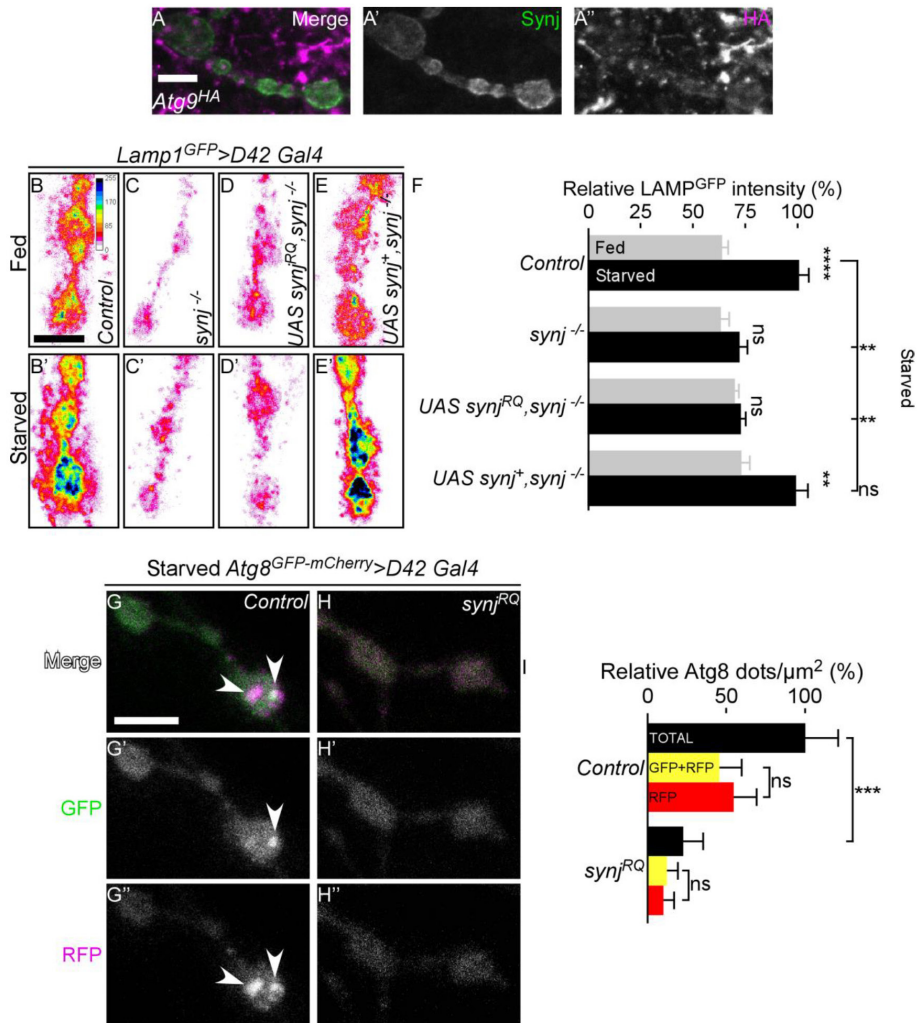
1. Bademosi AT, Lauwers E, Padmanabhan P, Odierna L, Chai YJ, Papadopoulos A, Goodhill GJ, Verstreken P, van Swinderen B & Meunier FA (2017) In vivo single-molecule imaging of syntaxin1A reveals polyphosphoinositide- and activity-dependent trapping in presynaptic nanoclusters. *Nat. Commun.* 8: 13660
2. Kasprówicz J, Kuenen S, Swerts J, Miskiewicz K & Verstreken P (2014) Dynamin photoinactivation blocks Clathrin and  $\alpha$ -adaptin recruitment and induces bulk membrane retrieval. *J. Cell Biol.* 204: 1141–56
3. Kechkar A, Nair D, Heilemann M, Choquet D & Sibarita J-B (2013) Real-time analysis and visualization for single-molecule based super-resolution microscopy. *PLoS One* 8: e62918
4. Nair D, Hosy E, Petersen JD, Constals A, Giannone G, Choquet D & Sibarita J-B (2013) Super-resolution imaging reveals that AMPA receptors inside synapses are dynamically organized in nanodomains regulated by PSD95. *J. Neurosci.* 33: 13204–24
5. Quadri M, Fang M, Picillo M, Olgiati S, Breedveld GJ, Graafland J, Wu B, Xu F, Erro R, Amboni M, Pappatà S, Quarantelli M, Annesi G, Quattrone A, Chien HF, Barbosa ER, International Parkinsonism Genetics Network, Oostra B a., Barone P, Wang J, et al (2013) Mutation in the SYNJ1 gene associated with autosomal recessive, early-onset Parkinsonism. *Hum. Mutat.* 34: 1208–15
6. Scott RC, Schuldiner O & Neufeld TP (2004) Role and regulation of starvation-induced autophagy in the *Drosophila* fat body. *Dev. Cell* 7: 167–78
7. Slabbaert JR, Kuenen S, Swerts J, Maes I, Uytterhoeven V, Kasprówicz J, Fernandes AC, Blust R & Verstreken P (2016) Shawn, the *Drosophila* Homolog of SLC25A39/40, Is a Mitochondrial Carrier That Promotes Neuronal Survival. *J. Neurosci.* 36: 1914–29
8. Soukup S-F, Kuenen S, Vanhauwaert R, Manetsberger J, Hernández-Díaz S, Swerts J, Schoovaerts N, Vilain S, Goukko N V., Vints K, Geens A, De Strooper B & Verstreken P (2016) A LRRK2-Dependent EndophilinA Phosphoswitch Is Critical for Macroautophagy at Presynaptic Terminals. *Neuron* 92: 829–844
9. Verstreken P, Kjaerulf O, Lloyd TE, Atkinson R, Zhou Y, Meinertzhagen I a & Bellen HJ (2002) Endophilin mutations block clathrin-mediated endocytosis but not neurotransmitter release. *Cell* 109: 101–12
10. Verstreken P, Koh T-W, Schulze KL, Zhai RG, Hiesinger PR, Zhou Y, Mehta SQ, Cao Y, Roos J & Bellen HJ (2003) Synaptotagmin is recruited by endophilin to promote synaptic vesicle uncoating. *Neuron* 40: 733–48
11. Verstreken P, Ohyama T & Bellen HJ (2008) FM 1-43 labeling of synaptic vesicle pools at the *Drosophila* neuromuscular junction. *Methods Mol. Biol.* 440: 349–69
12. Warlich E, Kuehle J, Cantz T, Brugman MH, Maetzig T, Galla M, Filipczyk A a, Halle S, Klump H, Schöler HR, Baum C, Schroeder T & Schambach A (2011) Lentiviral vector design and imaging approaches to visualize the early stages of cellular reprogramming. *Mol. Ther.* 19: 782–9

# Supplementary Figures and Tables

## Supplementary Figure S1. Generation of synjRQ knock-in and basic characterization of knock-in allele and overexpression constructs, related to Figure 1

- A** Genome editing using a MiMIC technology to knock in the R228Q mutation into the endogenous *Drosophila* *synj* locus (*synjRQ*). Schematic representation of the gene span around the MiMIC (Mi(MiC)SynjMI11871, 140bp upstream the ATG start codon of *synj*, which is being targeted with a targeting construct (highlighted by surrounding box) consisting of a duplication of *synj* harbouring the pathogenic mutation (R228Q) and flanked by *I-SceI* and *I-CreI* endonuclease sites. After genomic manipulation a new *synjRQ* knock-in allele is created.
- B-E** Western blot for *Synj* (134 kDa) using anti-Synj antibodies and for Tubulin (50 kDa) using anti-Tubulin antibodies as a loading control of the indicated genotypes. Quantification of *Synj* expression levels of the indicated genotypes.  $n \geq 10$  fly heads per genotype. Experiments were performed in independent duplicates. Error bars represent the SEM.
- F-H** Synaptic NMJ boutons of Control (w1118) and *synjRQ* and immunolabelled with anti-Synj and anti-EndoA antibodies, indicating correct localization and overlap with EndoA labelling, scale bar 5  $\mu$ m. Quantification of bouton *Synj* labelling intensity (H). For statistical analysis of intensities, t-test comparing genotypes,  $p > 0.05$ .  $n \geq 3$  larvae and  $n \geq 4$  NMJs per genotype. Error bars represent the SEM.
- I-M** Synaptic NMJ boutons of Control (D42-Gal4/+ (J-J')) and *synj*-/- null mutants (K-K'') either expressing *synjRQ* (L-L'') or *synj*+ (M-M'') under control of the D42-Gal4 driver and immunolabelled with anti-Synj and anti-EndoA antibodies, indicating correct localization and overlap with EndoA in labelling, scale bar 5  $\mu$ m. Full genotypes are included in the supplemental section. Quantification of *Synj* labelling intensity of indicated genotypes (I). For statistical analysis of intensities, t-test comparing genotypes, \*\*\*= $p < 0.0001$ , \*= $p < 0.05$ .  $n > 3$  larvae. Error bars represent the SEM.





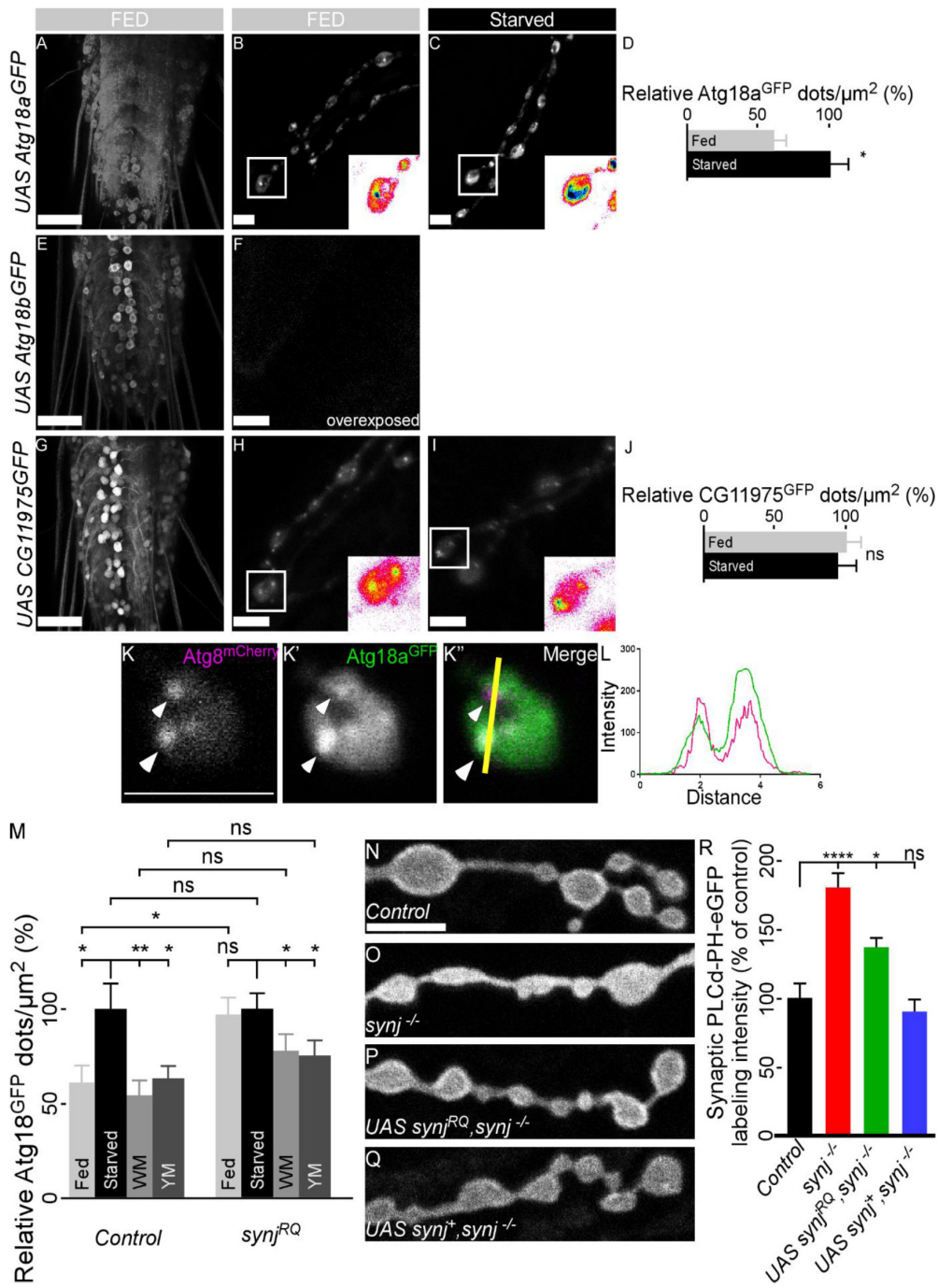
### Supplementary Figure S2. Synaptojanin is required for autophagy at synapses, related to Figure 2

**A-A''** Synaptic NMJ boutons expressing under endogenous promotor control the preautophagosomal marker Atg9<sup>HA</sup> and immunolabelled with anti-Synj and anti-HA antibodies, scale bar 5  $\mu$ m.

**B-F** Live imaging of fed (B,C,D,E) and 4 h-starved (B',C',D',E') NMJ boutons of Control (D42-Gal4> Lamp1<sup>GFP</sup>) (B-B') and synj<sup>-/-</sup> null mutants (C,C') either expressing synj<sup>RQ</sup> (D,D') or synj<sup>+</sup> (E,E') and also expressing Lamp1<sup>GFP</sup> (D42-Gal4> Lamp1<sup>GFP</sup>). Full genotypes are included in the supplemental section. Quantification of the Lamp1<sup>GFP</sup> intensities of indicated genotypes (F). Statistical analysis with 1-way ANOVA Kruskal-Wallis followed by Post Hoc test Dunn's multiple comparisons, \*\*= $p < 0.01$ , and each genotype individually Fed and Starved by t-test, \*\*\*\*= $p < 0.0001$ , \*\*= $p = 0.0040$ ,  $n \geq 9$  larvae and  $n \geq 18$  NMJs per genotype. Error bars represent the SEM, scale bar 5  $\mu$ m. Note that loss of Synj blocks the induction of Lamp1<sup>GFP</sup> and this is not rescued by expression of synj<sup>RQ</sup>.

**G-I** Live imaging of starved NMJ boutons of Control (D42-Gal4>Atg8<sup>GFP-mCherry</sup>) (G-G'') and synj<sup>RQ</sup> (H-H'') also expressing Atg8<sup>GFP-mCherry</sup>. Full genotypes are included in supplemental section. Quantification of the total number of Atg8 (GFP+RFP and RFP alone) dots and the number of yellow (GFP+RFP) and red (RFP) Atg8 dots (I). Statistical analysis by t-test comparing each genotype individually, \*\*\*= $p < 0.001$ ,  $n \geq 7$  larvae and  $n \geq 28$  NMJs per genotype. Error bars represent the SEM, scale bar 5  $\mu$ m. Note that in synj<sup>RQ</sup>, as already seen with the mCherry-Atg8 construct a severe reduction in Atg8 dots is observed and that when an Atg8 dot is observed in synj<sup>RQ</sup> this will be degraded as controls.

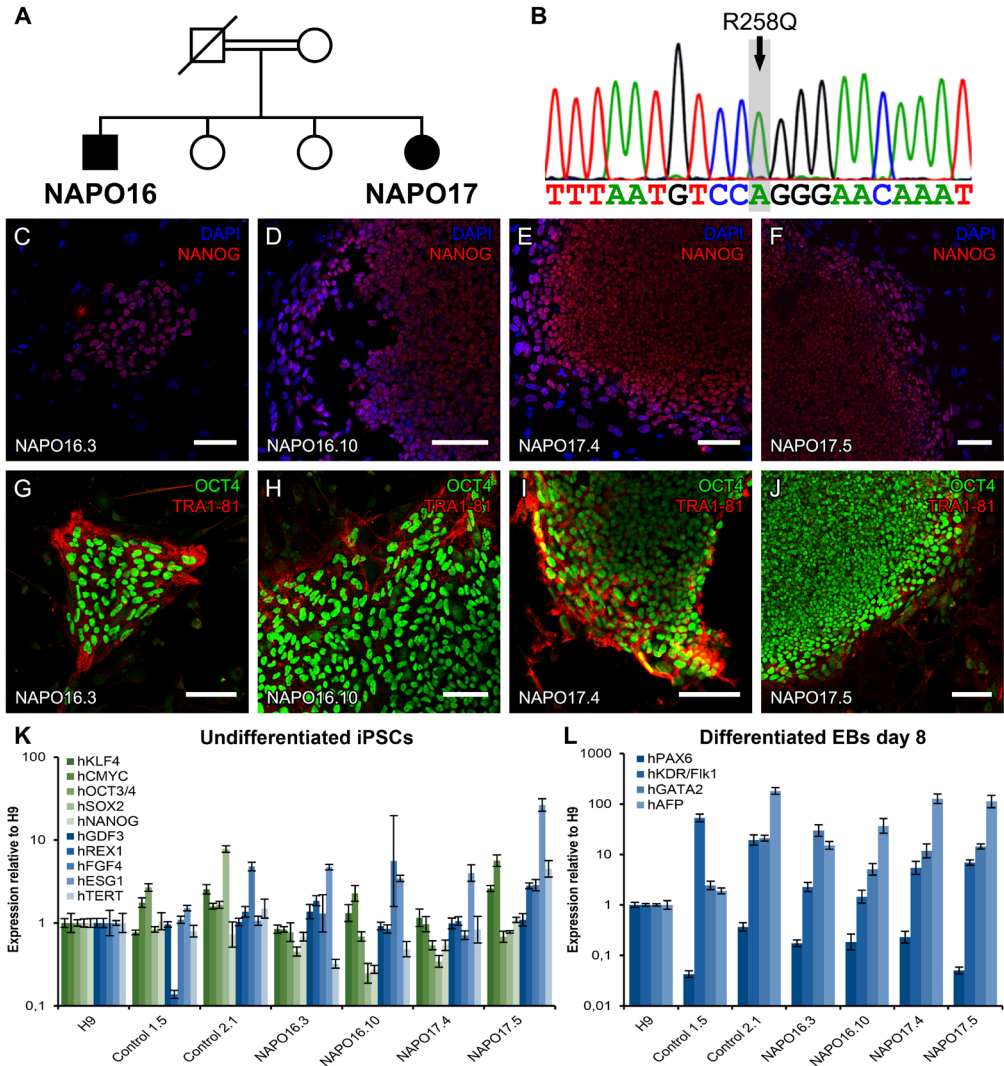




### Supplementary Figure S3 (previous page). *Drosophila* homologues of the PROPPIN WIPI2, related to Figure 3

- A-J Live imaging of ventral nerve cord (VNC) cell bodies and synaptic NMJ boutons of WIPI2 *Drosophila* homologues (Atg18a (A-C), Atg18b (E,F) and CG11975 (G-I)) N-terminally tagged with GFP in fed (A,B,E-H) and starved (C,I) conditions. Full genotypes are included in the supplemental section. Insets are magnification of indicated squares, using a 16 color lookup table. Scale for VNC images 50  $\mu$ m and 5  $\mu$ m for NMJs. (D) Quantification of Atg18a<sup>GFP</sup> dots at synaptic NMJ boutons, comparing fed and starved condition (data reused from Figure 3E) (J) Quantification of CG11975<sup>GFP</sup> dots, comparing fed and starved condition. For statistical analysis of number of dots, t-test comparing genotypes,  $p > 0.05$ ,  $n \geq 3$  larvae and  $n \geq 23$  NMJ per condition. Error bars represent the SEM.
- K-L Live imaging of a synaptic NMJ bouton expressing Atg8<sup>mCherry</sup> and Atg18a<sup>GFP</sup> (driven by D42-Gal4). Full genotypes are included in the supplemental section. Atg8 and Atg18a dots occasionally colocalize (arrowheads). Graph of a line scan view of the intensity profile through the indicated dots (arrowheads) of a bouton (line width and plot profile tools in NIH ImageJ) (L).
- M Live imaging NMJ boutons in Controls (D42-Gal4>Atg18a<sup>GFP</sup>) and *synj*<sup>RQ</sup> also expressing Atg18a<sup>GFP</sup>. Quantification of the number of Atg18a<sup>GFP</sup> dots of indicated genotypes under either fed, starved or starvation conditions combined with drugs that either block kinases that produce PI(3)P, wortmannin (WM) or PI(3,5)P2, YM201636 (YM) (M) (data of Fed and Starved Control obtained previously Figure 3E). Statistical analysis by t-test comparing each genotype individually,  $** = p < 0.01$  and  $* = p < 0.05$ ,  $n \geq 7$  larvae and  $n \geq 27$  NMJs per genotype. Error bars represent the SEM. Note that both PI(3)P and PI(3,5)P2 accumulate and are substrates for Atg18a both in controls and *synj*<sup>RQ</sup> mutants.
- N-R Live imaging of neuronal PI(4,5)P2 levels using the PLCd-PH-eGFP probe in synaptic NMJ boutons of Control (D42-Gal4> PLCd-PH-eGFP) (N) and *synj*<sup>-/-</sup> null mutants (O) either expressing *synj*<sup>RQ</sup> (P) or *synj*<sup>-</sup> (Q) also expressing PLCd-PH-eGFP under control of the D42-Gal4 driver. Scale bar 5  $\mu$ m. Quantification of PLCd-PH-eGFP levels (R). Statistical analysis with 1-way ANOVA Kruskal-Wallis followed by Post Hoc test Dunn's multiple comparisons,  $*** = p < 0.0001$ ,  $* = p < 0.05$ ,  $n \geq 10$  larvae per genotype. Error bars represent the SEM.





**Supplementary Figure S4. Characterisation of undifferentiated iPSC and embryoid bodies from patients carrying the SYNJ1 R258Q mutation and controls, related to Figure 6**

- A** The Italian pedigree with the SYNJ1 mutation. The black symbols denote individuals affected by juvenile parkinsonism.
- B** Electropherogram showing the homozygous SYNJ1 c.773G>A (p.Arg258Gln) mutation present in the patient iPSC lines.
- C-J** Immunocytochemistry analysis of patient iPSCs, showing expression of pluripotency markers. C-F are stained with anti-Nanog (red) and counterstained with DAPI (blue) and represent lines NAP016.3, NAP016.10, NAP017.4 and NAP017.5. Images G-J are stained with anti-OCT4 (green) and anti-Tra1-81 (red) and represent lines NAP016.3, NAP016.10, NAP017.4 and NAP017.5. Scale bars, 100  $\mu$ m.
- K** Expression analysis by RT-Q-PCR of pluripotency markers in the patient and control iPSCs.
- L** Expression analysis by RT-Q-PCR of differentiation markers in 8 day old embryoid bodies from the patient and control iPSCs.

**Supplementary Table S1. Summary of iPSC lines created and selected**

ID	Sex	Age at biopsy	Age of onset	Mutation	# of Lines created	Clone selected	Karyotype	Transgene silencing	Pluripotency markers	Differentiation markers
Control 1	F	42	NA	NA	6	Control 1.5	46,XX	Passed	Passed	Passed
Control 2	M	57	NA	NA	6	Control 2.1	46,XY	Passed	Passed	Passed
NAPO16	M	50	22	SYNJ1 R258Q	12	NAPO16.3	46,XY	Passed	Passed	Passed
						NAPO16.10	46,XY	Passed	Passed	Passed
NAPO17	F	35	28	SYNJ1 R258Q	12	NAPO17.4	46,XX	Passed	Passed	Passed
						NAPO17.5	46,XX	Passed	Passed	Passed





# Analysis of *PARK20* patient iPSC derived dopaminergic neurons connects Synaptojanin-1 to neurodevelopment and mitochondrial function

**Roy Masius**, Michelle Minneboo, Martyna Grochowska, Marialuisa Quadri, Emanuel Berger, Shashini T. Munshi, Femke M.S. de Vrij, Steven A. Kushner, Marina Picillo, Paolo Barone, Jens C. Schwamborn, Vincenzo Bonifati, Wim Mandemakers

## Summary

*PARK20* mutations in *SYNJ1*, encoding Synaptojanin-1, lead to early-onset Parkinsonism. We and others have previously shown that *PARK20* mutations strongly influence Synaptojanin-1 protein function, leading to disturbed synaptic autophagic flux and synaptic vesicle recycling. To obtain more insight into Synaptojanin-1 function and *PARK20* mutations in development of early onset Parkinsonism, we created induced pluripotent stem cell lines from *PARK20* patient and unaffected control skin-biopsy derived fibroblasts, and differentiated them to neural progenitors and dopaminergic neurons. Here we show that in spite of reduced PAX6 expression levels detected in *PARK20* derived neural progenitor cell lines, both *PARK20* patient and control neural progenitor cell lines were able to robustly differentiate into neurons (70-80%) and more specifically dopaminergic neurons (20-35%). Interestingly, we detected significantly increased levels of Parkin protein in neural progenitor cells and dopaminergic neurons derived from *PARK20* patient lines. Based on the role of Parkin in regulating mitophagy, we investigated mitochondrial function and mitophagy in *PARK20* patient and control cell lines. Strikingly, we observed improved mitochondrial function and normal mitophagic flux in *PARK20* patient cell lines. These findings stress the broad impact on cellular physiology of *PARK20* mutations in early-onset Parkinsonism.

# Introduction

Parkinson's disease (PD) is the second most common neurodegenerative disorder and with prevalence rising with age, it affects over 1% of the population above 60 (1). Due to the aging populations, incidence and prevalence are predicted to rise substantially over the next decades (2). PD is characterized by the selective loss of dopaminergic (DA) neurons in the substantia nigra, and the presence of Lewy Body (LB) inclusions in the remaining DA neurons. To date, animal models for PD have replicated many features of neurodegeneration and LB pathology; however, there is no model that fully recapitulates the human disease (3). Recent progress in the derivation and differentiation of human induced pluripotent stem cells (iPSCs) presented new possibilities for disease modelling (4). Furthermore, robust DA neuron differentiation protocols of human iPSCs combined with mutations identified in genetic forms of PD presents novel possibilities to study the specific cell type affected in PD in humans. iPSC derived models have been established from idiopathic and genetic forms of PD, including *PARK1*, *PARK2* and *PARK8*, with mutations in *SNCA*, *PRKN* and *LRRK2*, respectively (4). These models were successful in identifying pathological pathways and mechanisms in differentiated neurons, and from these studies several genetic forms of PD appear to converge toward shared pathological pathways, including synaptic, mitochondrial, proteasomal, vesicular trafficking, and lysosomal dysfunction (reviewed in (5)). *PARK20* is caused by mutations in *SYNJ1*, encoding Synaptojanin-1, and leads to autosomal recessive forms of early-onset Parkinsonism (6, 7). Synaptojanin-1 is a lipid phosphatase that in addition to other conserved protein domains also contains two consecutive phosphatase domains. The most N-terminal phosphatase domain (SAC1), predominantly dephosphorylates phosphatidylinositol (PI) substrates, monophosphates PI(3)P and PI(4)P, and biphosphate PI(3,5)P<sub>2</sub> (8) (Figure 1A). In addition, the 5'phosphatase domain primarily utilizes PI(4,5)P<sub>2</sub> and PI(3,4,5)P<sub>3</sub> as substrates (8, 9) (Figure 1A). The varied membrane PI phosphate composition of Golgi apparatus, endosomes, and plasma membranes infers a potential role for Synaptojanin-1 phosphatase activity in multiple different pathways. For example, Synaptojanin-1 has been proven to be essential for synaptic vesicle endocytosis, which is implicated as an important pathological pathway in PD (10, 11). Synaptojanin-1 is recruited to budding endocytic vesicles at synapses by Endophilin, where Synaptojanin-1 phosphatase activity is required for dephosphorylation of PI(4,5)P<sub>2</sub>. This results in shedding of the clathrin cages to allow maturation into synaptic vesicles, a necessity for normal synaptic function (10, 11). Mutations associated with the *PARK20* SAC1 domain and p.Arg258Gln abolish both PI(3)P and PI(4)P phosphatase activities, but does not affect the SAC1 PI(4,5)P<sub>2</sub>

phosphatase activity (7). Knockin and knockout animal models for *PARK20* have defects in synaptic vesicle recycling (9, 11). In a *Drosophila* knockin model for *PARK20* p.Arg258Gln mutation, autophagosome maturation in fly synapses is blocked, which was confirmed in our human neuronal model from *PARK20* patient derived iPSCs (12). This autophagosomal effect is explained by the SAC1 domain that dephosphorylates PI(3)P and PI(3,5)P<sub>2</sub> (Figure 1A), two lipids found in autophagosomal membranes (7, 12). Lack of Synaptojanin-1 SAC1 phosphatase activity, autophagosomes maturation is blocked, preventing subsequent fusion with lysosomes (12). Moreover, the *Drosophila* model showed neurodegeneration, including DA neuron loss, supporting that defective synaptic autophagy and protein clearance may contribute to SYNJ1-PD pathology (12). Also, DA neurons in the mouse *PARK20* knockin model show DA neuron specific axonal dystrophy, and synapses of these mice displayed endocytic defects, further implicating SAC1 activity in synaptic vesicle endocytosis (9). Loss of Synaptojanin-1 in HeLa, and SH-SY5Y cells, or the presence of the p.Arg258Gln mutation, in patient derived fibroblasts induces impaired endosomal recycling trafficking (13, 14). Interestingly, loss of both the SAC1 and 5'-phosphatase activity of SYNJ1 underlies a severe disorder with neonatal refractory epilepsy and a neurodegenerative disease course (15-17). In addition, SYNJ1 may also play a role in Alzheimer's Disease (AD), where it is linked to amyloid toxicity, swelling of early endosomes, and age-dependent long-term memory defects (14, 18). Finally, Synaptojanin-1 has been proposed to play a role in gliogenesis, where it has been shown that SYNJ1 5'-phosphatase activity is regulated by gliogenic stimuli (19, 20). This would explain the observed increased number and size of astrocytes in Down's syndrome brain where Synaptojanin-1 levels are elevated (21). It is also in line with the decrease in brain size of Synaptojanin-1 knockout mice as astrocytes are the major cell population in the brain (10). Together, these findings suggest a role for SYNJ1 mutations in various neurodegenerative diseases and indicate a strong phenotype-genotype correlation.

To gain more insight into the role of Synaptojanin-1 in DA neuronal development and function and the effect of the *PARK20* mutation, we established a patient derived *PARK20* DA neuron model and focussed on the role of Synaptojanin-1 in neuron development, endocytosis, and mitochondrial function (mitophagy, mitochondrial respiration, mitochondrial biogenesis). We show subtle effects of the *PARK20* mutation on neuron development and mitochondrial function, and find elevated levels of Parkin in neural progenitor cells and DA neurons. Our data point towards a potential role of Synaptojanin-1 SAC1 activity in neurodevelopment and mitochondrial function.



# Results

## Generation of iPSC lines from two siblings with *SYNJ1* homozygous mutation p.Arg258Gln

We previously described the generation of iPSC lines from human dermal fibroblasts from two siblings (Patient 1 and 2, (Figure 1B)) carrying the homozygous *SYNJ1* mutation c.773G>A, p.Arg258Gln and two age and gender matched unaffected controls (12). All clones have been previously characterized and selected based on karyotyping, expression of endogenous pluripotency factors and expression of differentiation associated markers after 8 days of Embryoid Body formation (12). Furthermore, the mutation status was confirmed in all patient iPSC lines (12). Examples of the iPSC clones are shown in figure 1C.

## Small-molecule neural progenitor cell characterisation from *PARK20* and Control iPSC lines

Several studies have shown that loss of Synaptojanin-1 leads to neurodevelopmental defects (10, 17). To determine the neurodevelopmental potential of *PARK20* patient and control iPSCs, a previously reported small-molecule differentiation paradigm was used that results in DA neuron enriched cultures (22) (Figure 1D). Western blot analysis demonstrated equal *SYNJ1* protein expression levels when comparing patient and control lines derived small molecule Neural progenitor cells (smNPC) (Figure 2A and B), indicating that the *PARK20* mutation has no effect on protein stability or expression, in line with previous observations (9). The neurogenic differentiation potential of *PARK20* and control smNPC was further analysed for by immunocytochemistry (ICC) staining of proteins that specify neural progenitor stages. Expression of pluripotency marker SOX2 and the neural progenitor marker Nestin was not changed in *PARK20* derived cells in comparison to control cells (Figure 2C). In addition, equal numbers of cells positive for the neuronal marker  $\beta$ III-Tubulin (TUJ1), revealing spontaneous differentiating smNPC to early maturing neurons, could be detected in both patient and control derived smNPC cultures (Figure 2D). Next, efficiency of smNPC formation was further characterized by investigation of transcription factor PAX6. ICC staining showed comparable, high levels of PAX6 expression in control smNPC (Figure 2D). However, in both patient lines, quantification of PAX6 revealed a 30% and 60% reduced number of PAX6-positive smNPCs in patient 1 and 2, respectively, when compared to control smNPC (Figure 2E).

Interestingly, no change in PAX6 levels is found when comparing patient and control at the iPSC stage (12) (Supplementary Figure S1). This indicates that the observed decrease in PAX6 expression in *PARK20* mutant cells is lineage specific.

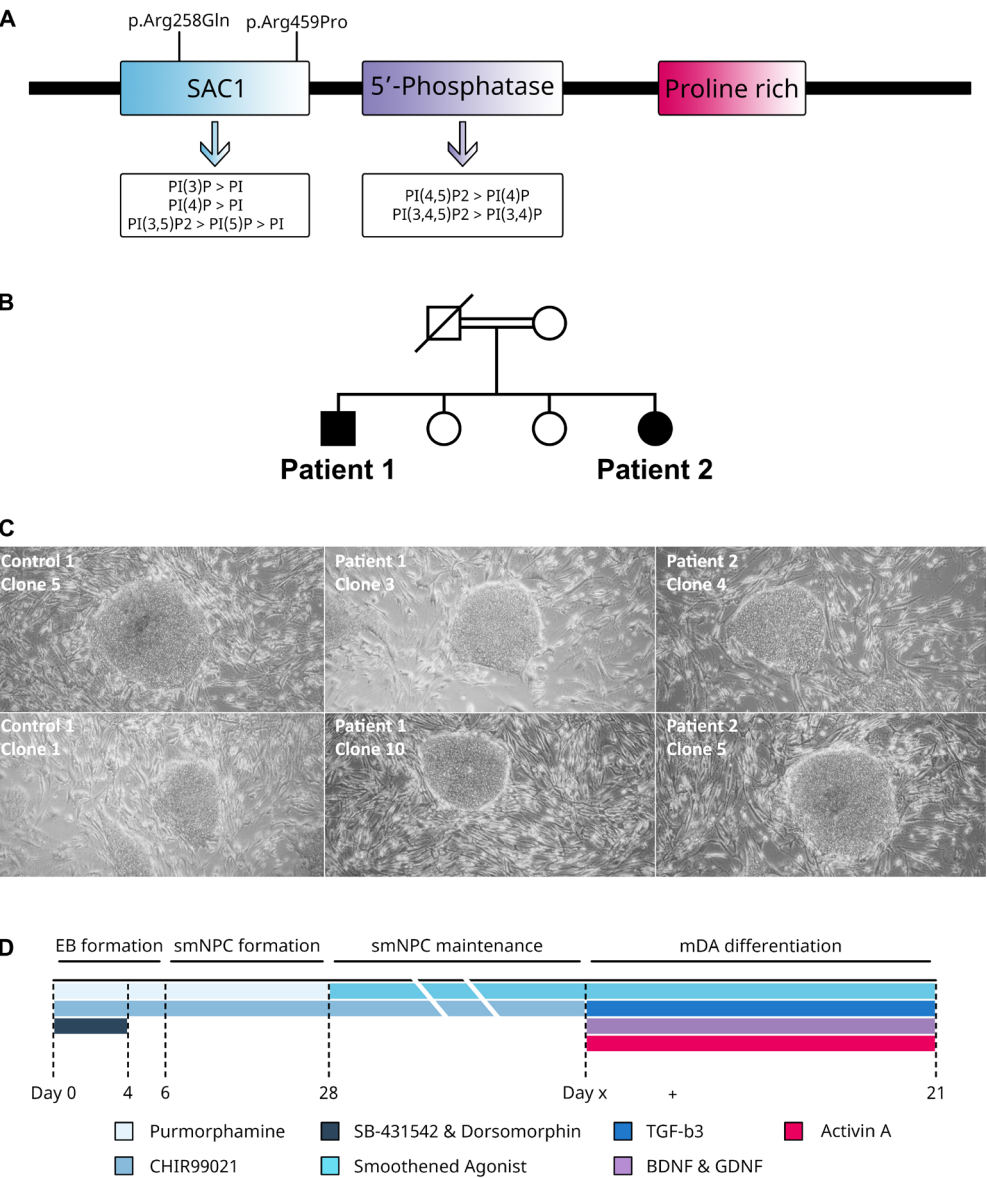


**Figure 1. Characteristics of the induced Pluripotent Stem Cells and the differentiation protocol**

(A) Schematic depiction of the Synaptojanin-1 protein with the functional domains, phosphatase activity and location of the *PARK20* mutation. (B) Family tree of the two *PARK20* patients of whom fibroblasts are reprogrammed to induced Pluripotent Stem Cells. (C) iPSC morphology imaged by ZEISS Primovert inverted microscope. (D) Schematic depiction of the differentiation protocol and the small-molecule factors used.

3



### Figure 2 (previous page). Western blot and Immunocytochemistry analysis of the generated smNPC

(A) Western blot analysis of Synaptojanin-1 of whole cell extracts of smNPC shows no difference in amount of protein present. Loading control used was GAPDH. (B) Quantification of Synaptojanin-1 in smNPC shows equal expression of both the wildtype form in the controls and the p.Arg258Gln mutant form in the patient lines. (C) NPC marker validation on control and patient smNPC shows nearly all cells to express the markers Nestin (green) and SOX2 (red). (D) smNPC characterization show a varying amount of PAX6 (green) positive NPCs and a small degree of spontaneous neuron differentiation marked by TUJ1 (magenta). (C-D) Cells are counterstained with DAPI (blue) to indicate the nucleus. Scale bars represent 50 nm. (E) Quantification of the percentage of the cell population expressing a marker for NPCs (SOX2, Nestin, and PAX6) or neuron (TUJ1) characterization. Patient lines show decreased levels of PAX6.

## Reliable differentiation to dopaminergic neurons regardless of mutation status

To compare the ability of *PARK20* and control smNPC to form DA neurons, smNPC were differentiated for 3 weeks according to a previously described protocol (22) (Figure 1D). Targeted differentiation of the smNPC of both patient and control lines resulted in neurons positive for TUJ1, and the dopamine neuronal marker Tyrosine Hydroxylase (TH) (Figure 3A). In addition, cells positive for GFAP or SOX2, indicating astrocytes or undifferentiated smNPC, respectively, were also detected (data not shown). This demonstrates that the differentiation protocol resulted in a mixed neuronal culture enriched for the presence of DA neurons as previously described (22). Comparison of neuronal marker TUJ1 versus the nuclear marker DAPI showed that 70-80% of cells formed neurons (Figure 3A, B), whereas the efficiency to generate TH-positive DA neurons was 21-35% of total number of cells, and up to 30-48% of total number of neurons (Figure 3A, B). No significant changes in differentiation efficiency were found between control and patient neurons, at 3 weeks after initiation of differentiation. These data suggest that in spite of the presence of the *PARK20* mutation, generation of neurons, and in particular DA neurons, during early *in vitro* development is unaffected.

## Upregulated Parkin in patient derived lines

In addition to SYNJ1, several proteins implicated by genetic studies in PD (e.g. DNAJC6, Parkin) are linked, directly or indirectly, to the endocytic pathway. To determine early effects of the SYNJ1 p.Arg258Gln mutation on synaptic vesicle recycling, we examined levels of endocytic and PD associated proteins in smNPC by Western blotting. Equal amounts of EEA1, Amphiphysin, DNAJC6 and Dynamin protein were detected comparing control and patient derived smNPCs (Figure 4A, B). In contrast, Parkin levels were consistently increased 48-51% for the two clones of patient 1 and 23-26% for those of patient 2 (Figure 4C, D). Increased Parkin protein expression was also detected after

3 weeks of differentiation to 55-63% for patient 1 and 58% for patient 2 (Figure 4E and F). Interestingly, increased Parkin levels have also been detected in brains of p.Arg258Gln knockin mice (9).

A

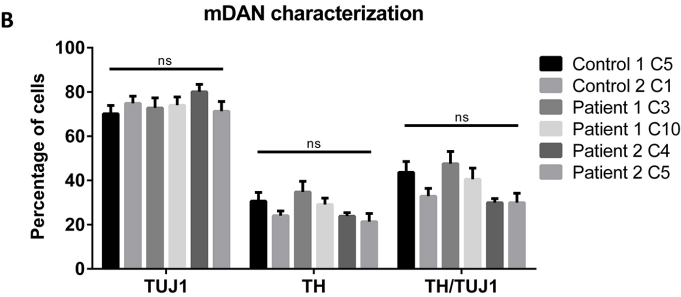
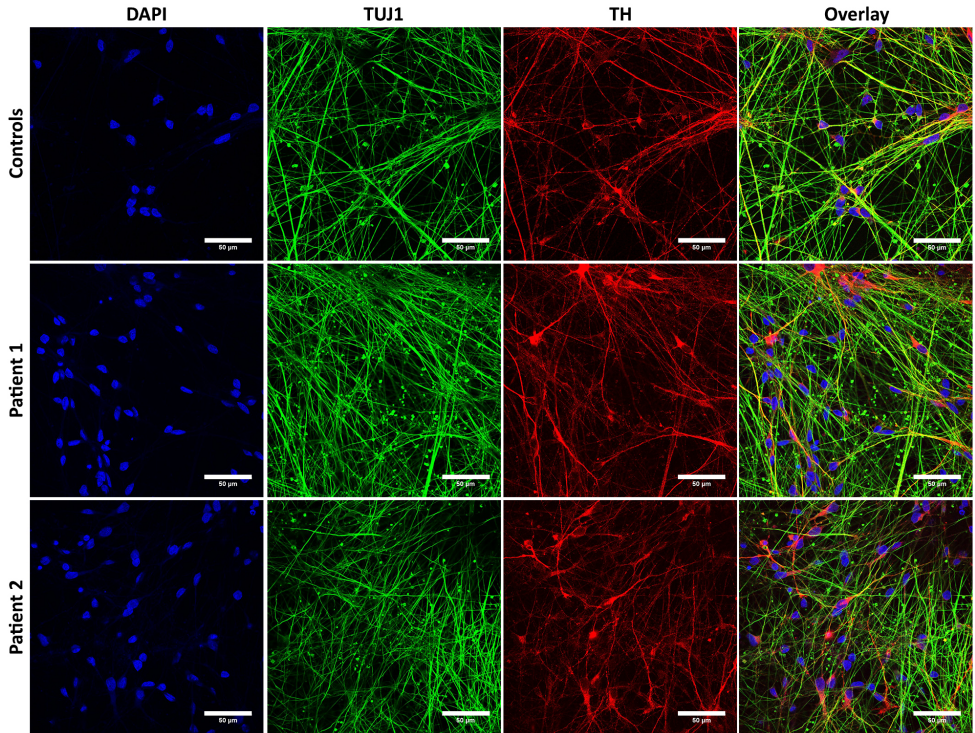


**Figure 3. Immunocytochemistry analysis and quantification of the generated dopaminergic neurons**

Three week differentiated control and patient cultures show neurons, marked by TUJ1 (green), of which a subset expresses TH (red), a marker of dopaminergic neuron identity. (A) Cells are counterstained with DAPI (cyan or blue) to indicate the nucleus. Scale bars represent 50 nm. (B) Quantification of the percentage of the cell population expressing a marker for neurons (TUJ1) or DA neuron (TH) characterization.



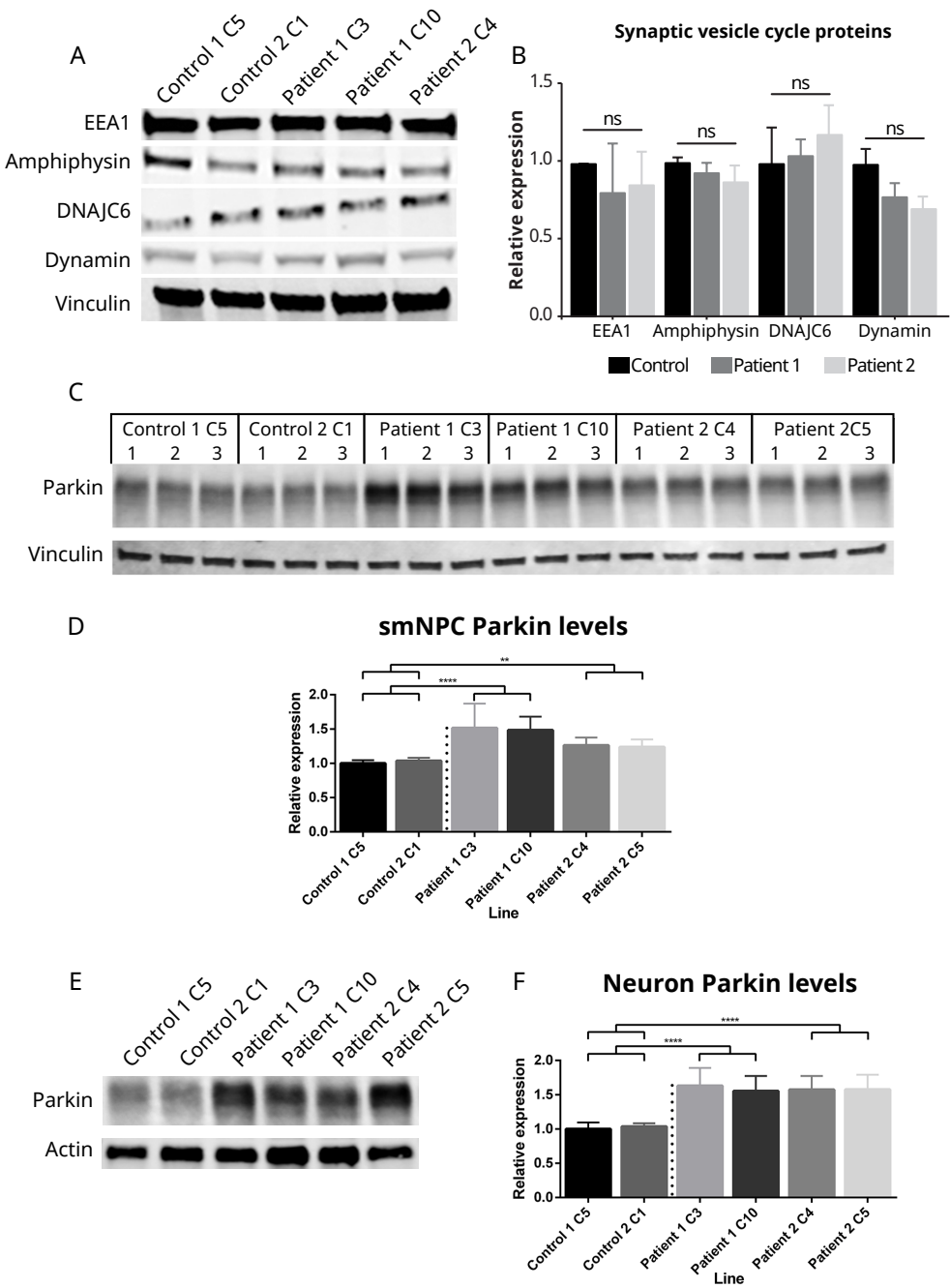


# Figure 4. Protein quantification of endocytosis associated proteins and Parkin

(A) Western blot analysis of smNPC proteins depicting relative level of expression of endocytosis markers EEA1, Amphiphysin, DNAJC6, and Dynamin, against loading control Vinculin. (B) Quantification of the levels of the endocytosis proteins in smNPCs shows no difference between controls and patients. (C) Western blot analysis of Parkin in smNPC over three biological replicates show a consistent upregulation of Parkin in patient lines. (D) Quantification of the protein levels of Parkin in smNPCs indicate an upregulation of Parkin in patient smNPCs. (E) Western blot analysis of Parkin in 3 week old dopaminergic neuron differentiation cultures, quantification (F) of these Parkin levels show upregulation of Parkin in patient lines.

## Functional mitochondrial stress response

Parkin has been shown to play an important role in regulating mitophagy (23). Based on significantly elevated Parkin protein levels detected in *PARK20* smNPC and 3 week old DA neurons, we probed the mitophagy response to the stressors Carbonyl cyanide m-chlorophenyl hydrazone (CCCP) and Valinomycin in control and *PARK20* smNPC. Parkin protein levels are significantly higher in patient lines in the control condition of DMSO exposure (Figure 5A, B). However, when smNPC were exposed to the CCCP or Valinomycin stressor, both control and patient line Parkin levels reduced to comparable levels (Figure 5A, B). These data show that mitophagy is equally functional in both control and *PARK20* patient lines. Next, ongoing mitophagy was measured by

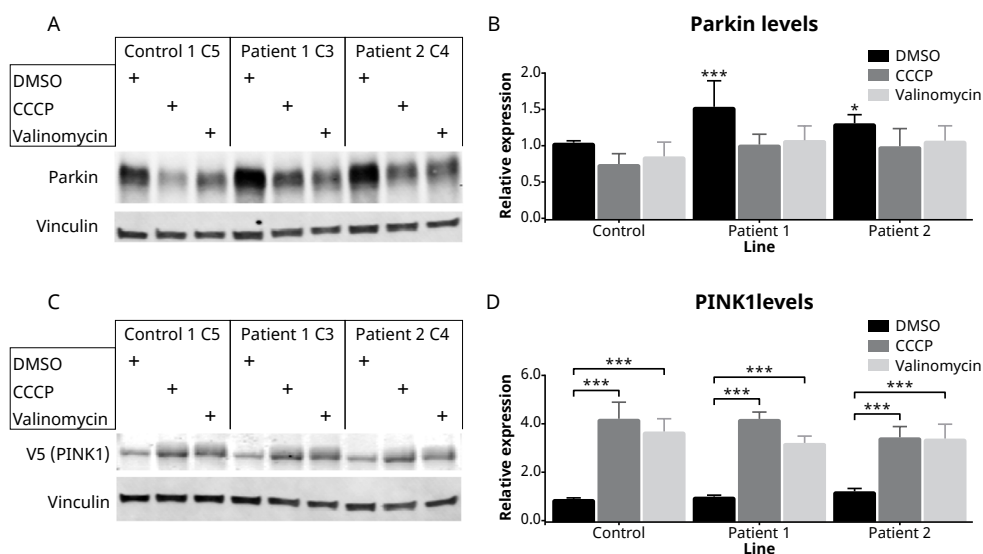


# Figure 5. Mitochondrial respiration, baselevel analysis and mitochondrial stress response in smNPC cultures

(A-D) Mitochondrial stress response of smNPC cultures to CCCP and Valinomycin exposure show both control and patient lines are able to perform PINK1- and Parkin-mediated mitophagy. This is measures in Parkin levels (A-B) and in PINK1 levels, monitored by overexpression of a V5-tagged PINK1 construct (C-D).

determining PINK1 levels in PINKV5 overexpressing cells. The first steps of the mitophagy are recruitment and stabilization of PINK1, which can be seen from the increase in PINK1-V5 levels. CCCP treatment showed PINK1V5 levels of 4.3 fold higher in controls and 4.3 and 3.5 fold higher in patient 1 and 2, respectively (Figure 5C, D). Valinomycin resulted in a 3.7 fold increase in PINK1V5 levels in controls and a 3.3 and 3.4 fold increase in patient 1 and 2, respectively (Figure 5C, D). The level of increased PINK1-V5 expression was not significantly altered in either treatment, when comparing patient and control cells. These data indicate that PINK1 is recruited normally to depolarized mitochondria in *PARK20* smNPC. Together, these findings show that the observed elevated steady-state Parkin levels in *PARK20* mutant cells does not affect the efficiency of Parkin/PINK1-mediated mitophagy caused by mitochondrial depolarization.

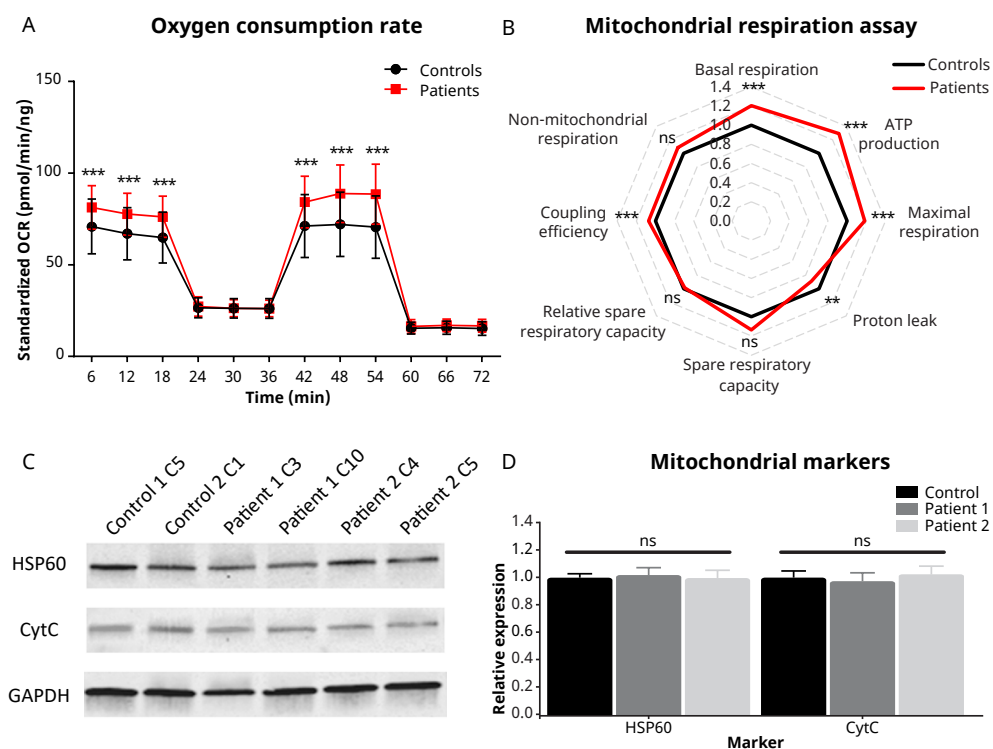


**Figure 6. Mitochondrial respiration and mitochondrial baselevel analysis in smNPC cultures**

(A-B) Mitochondrial respiration analysis of smNPC using the Agilent Seahorse XF Cell Mito Stress Test. The Oxygen consumption rate (A) is converted to fundamental parameters of mitochondrial function (B). Basal respiration, ATP turnover, proton leak, maximal respiration and spare respiratory capacity are then compared for control and patient smNPC (B). (C-D) Western blot analysis of mitochondrial markers HSP60 and CytC show no difference in amount of mitochondria present. Loading control used was GAPDH.



## Elevated mitochondrial activity in patient smNPCs

In addition to its role in mitophagy, Parkin has also been shown to influence mitochondrial respiration and biogenesis (24, 25). To investigate whether the observed elevated Parkin levels in *PARK20* mutant cell lines affect mitochondrial respiration, we performed a mitochondrial respiration assay. The Agilent Seahorse XF Cell Mito Stress Test revealed an elevated mitochondrial activity in patient smNPC (Figure 6A and B). This is observed by an increase of 20% in basal respiration, 29% in ATP production, 18% in maximal respiration and 7% in coupling efficiency when compared to age and gender matched controls (Figure 6C). Furthermore patient derived smNPC show an 11% reduction of the proton leak (Figure 6C). Next, to determine the effect of elevated Parkin levels in *PARK20* mutant cells on mitochondrial biogenesis we compared the amount of mitochondria present in the smNPC by quantifying the levels of the mitochondrial proteins HSP60 and CytC (Figure 6D). We observed no change in either of these markers, indicating that the detected increased Parkin levels in *PARK20* patient lines do not influence mitochondrial biogenesis.

## Discussion

Although cellular and animal models systems have provided valuable mechanistic insight into pathological pathways that lead to PD and other neurodegenerative diseases (3), it has recently become clear that certain species-specific traits associated with these diseases can only be detected in human model systems (26, 27). Therefore, in spite of insightful models for *PARK20* in mice, *Drosophila*, and cell lines that have provided valuable information on the role of Synaptojanin-1 in parkinsonism and other neurodegenerative diseases (9, 12, 13), a human *PARK20* DA neuronal model, established from patients could demonstrate important novel human-specific phenotypes. Here we show DA differentiation of *PARK20* patient and unaffected control derived iPSCs to investigate the role of Synaptojanin-1 in neuron development, endocytosis, and mitochondrial function (mitophagy, mitochondrial respiration, and mitochondrial biogenesis). First, during differentiation from iPSCs to smNPC both *PARK20* patient and control demonstrated similar expression levels of the pluripotency marker SOX2, the smNPC marker Nestin, and the neuronal marker TUJ1. However, we detected reduced expression of differentiation marker PAX6 in *PARK20* patient smNPC. It remains

unclear why PAX6 protein expression is decreased in our patient line. PAX6 is a major regulator required for cell fate specification and patterning of a variety of brain regions, accumulating at discrete areas of the forebrain and together with other PAX-genes at the hindbrain-midbrain boundary (28). Furthermore, the transcription factor plays a role in DA neuron neurogenesis (29), and complete loss of PAX6 has been shown to significantly reduce formation of DA neurons, skewing the proportion of neuron populations (30). Whereas, PAX6 expression is often shut down in most post mitotic neurons, DA neurons of the substantia nigra and in the olfactory bulb, retinal ganglion cells maintain expression (31). In these post-mitotic neurons, the transcription factor is thought to play a role in mediating axonal development (31). Moreover, study of mice lacking PAX6 showed altered pathfinding of axonal projections of DA neurons in the substantia nigra (32). This function in axonal development could be vital to the DA neurons, which form extensive axons and a huge number of synapses (33). However, the number of DA neurons formed in our human iPSCs derived model system is not affected, indicating that reduced PAX6 levels do not affect DA neuron differentiation in our model. This is in line with the observation in the *PARK20* mouse model, where also no changes in the number of DA neurons were detected (9). Nevertheless, reduced numbers of DA neurons were detected in the *PARK20* Drosophila model (12). These results might be explained by a transient developmental delay in the formation of DA neurons in human and mouse model systems caused by reduced PAX6 levels that can be overcome by expression of unknown PAX6 redundant factors, which are lacking in Drosophila. This possibility will require further investigation. To our knowledge, no common pathway has been discovered between PAX6 and SYNJ1; however, it remains possible that SYNJ1 indirectly and transiently affects PAX6 expression at the progenitor stage.

Although the formation of dopamine neurons is unaltered in the human *PARK20* iPSC model, it remains to be determined whether the *PARK20* iPSC derived DA neurons are more sensitive to stress, and more prone to neurodegeneration. Data by others indicate that this indeed might be the case as reduced numbers of DA neurons are detected in Drosophila *PARK20* model and also DA neurons in the mouse *PARK20* model show DA neuron specific axonal dystrophy. Long term cultures of the human *PARK20* iPSC might demonstrate DA neuron degeneration. Alternatively exposing the human *PARK20* DA neurons to stress could show increased neurodegeneration. Interestingly, preliminary data showed reduced number of TH-positive neurons in patient derived neuronal cultures when compared to control neuronal cultures (0.9-1.4%, vs. 2.2-3.6%, respectively) after Fluorescence-Activated Cell Sorting (FACS) to enrich the DA neuron cell population (data not shown). The stringent conditions used in FACS could expose

a higher sensitivity to stressors in *PARK20* patient derived DA neurons. This will require further investigation.

Association between Parkin and Synaptojanin-1 has been established, as this E3 ubiquitin ligase protein was already investigated in relation to the p.Arg258Gln mutation and SYNJ1 Knockout. Especially, p.Arg258Gln knockin mice with the mutation showed over 2-fold upregulation of Parkin in the brain (9). Conversely, the Synaptojanin-1 knockout mice did not show any fluctuation in the amount of Parkin in newborn brains (34). This would indicate that the loss of phosphatase function of the SAC1 domain is not the underlying cause of the aberration in Parkin. Instead, the mutation might have caused a gain of function directly or indirectly affecting Parkin transcription. The process leading to neonatal lethality in the knockout mice, possibly affects much more severely multiple cell types, which would correspond to the seizures and juvenile lethality associated with patients carrying mutations that affect both Synaptojanin-1 phosphatase domains (16, 17).

Furthermore, Synaptojanin-1 is ubiquitinated in the presence of Parkin (34). Endophilin is also known to undergo specific ubiquitination by Parkin and is a binding partner to Synaptojanin-1 (34). This binding is suggested to be the underlying reason that Synaptojanin-1 ubiquitination is affected by Parkin. Another major binding partner of Endophilin is Dynamin and this is also affected by Parkin in the same way as Synaptojanin-1 is (34). Suggesting Parkin may have a regulatory function on endophilin-containing endocytic protein complexes. However, these findings still do not explain how the specific mutation in SYNJ1 would affect the levels of Parkin, and further research is required to investigate this.

We also show that mitochondria in *PARK20* mutant cells display increased respiratory function. We speculate that this is caused by the increased levels of Parkin. Indeed, previous reports have also shown that Parkin plays a protective role in the maintenance of normal mitochondrial respiration (35). Further, Parkin plays an important role in mitochondrial quality control and promoting the selective autophagy of depolarized mitochondria (23). Parkin/PINK1-mediated mitophagy clears defective mitochondria by accumulation of PINK1 followed by recruitment of Parkin, adding an ubiquitin signal that triggers recruitment of the autophagy machinery. The need for PINK1 recruitment could limit the effect of the Parkin upregulation seen in our model (36, 37); however, Narendra et al. have shown that overexpression of Parkin alone already has an effect in accelerating mitophagy (38). More recently, Shin et al. have implicated Parkin in mitochondrial regulation via Parkin-Interacting Substrate (PARIS or ZNF746), which

represses PGC-1 $\alpha$  and NRF-1, both important mediators of mitochondrial biogenesis (24, 39, 40). In addition, Parkin has previously been shown to be involved in mitochondrial biogenesis by regulating mitochondrial DNA transcription and regulation (41). These findings indicate the upregulated Parkin in our patient lines might lead to increased mitochondrial biogenesis via degradation of PARIS, and indirect regulation of PGC-1 $\alpha$  and NRF1 and by regulating mitochondrial DNA transcription and regulation. The two effects of Parkin, namely the induction of mitophagy and mitochondrial biogenesis are counteracting each other on the mitochondrial homeostasis. While the upregulated Parkin may cause an earlier mitophagy response, the increased biogenesis would allow for generation of more mitochondria. This fine-tuned mechanism may be the cause that we see no change in amount of mitochondria as a result of the increase in Parkin. Furthermore, the improved mitochondrial function observed in *PARK20* smNPC could be explained as a younger population of mitochondria that would be the result from this higher mitochondrial turnover rate. This would require further investigation.

The increased Parkin levels however, stand in stark contrast to the loss of function *PRKN* mutations seen in *PARK2* patients. Likewise, the finding of improved mitochondrial function contradicts the impaired mitochondrial functionality normally associated to Parkinson's disease (23). Interestingly both may lead to preferential degeneration of DA neurons, indicating tight regulation of mitochondrial function is required in these neurons. The selective neurodegeneration could arise from the DA neurons being extra vulnerable to mitochondrial deficiencies because of their high activity and large number of synapses (33). Mitochondrial respiration would be required to provide for their high energy demand and to resist excitotoxic effects of neurotransmitter activation (42). Increased respiration activity, such as we found, has been linked to increased oxidative damage on the mitochondrial DNA (42). This damage in turn could diminish mitochondrial biogenesis, which ultimately may lead to neuronal death in the *PARK20* patients.

The strength of our model system is that we use patient derived cells to generate specifically the cell type (DA neurons) that is affected in the patients, providing a strong advantage over models from other species. We chose to use two clones from two patient lines in combination with two age matched controls. These controls were generated in the same way as the patient lines, without the need for additional steps. This allowed for swift investigation of the patient mutations while keeping the lines devoid of possible off-target mutations due to genome editing. However, we do recognize that there are limitations. Selection of lines with shared genetic background between the two siblings

might play a role in the effects we observe. If this is the case then the results might be inflated or mitigated. In future experiments, gene correction could be used to verify that the only the mutation, not the genetic background, is causative for the differences described. Targeted genome editing by CRISPR-Cas9 to correct the mutation would allow generation of isogenic controls (43, 44). The control lines could be edited to obtain the mutation in lines with different genetic backgrounds. Furthermore, the CRISPR-Cas9 technology would allow for generation and investigation of other mutations identified for *PARK20*.

In conclusion, developmental investigation of the generated model for *PARK20* shows significantly reduced PAX6 expression levels in neural progenitor cells, without interfering with the differentiation of iPSC into smNPC, neurons and DA neurons in vitro. Furthermore, increased levels of Parkin protein were detected in *PARK20* patient lines. Moreover, we observed improved mitochondrial function and normal mitophagic flux in patient cell lines. Further research is required to investigate whether and how the observed effects contribute to early-onset parkinsonism in *PARK20* patients. Nevertheless, these findings stress the broad impact on cellular physiology of *PARK20* mutations in early-onset Parkinsonism, and point toward a previously unidentified role for Synaptojanin-1 in mitochondrial function and biogenesis.

3

## Experimental procedures

### Generation of human induced Pluripotent Stem Cell Cultures

Primary cultures of dermal fibroblasts were established from punch biopsies of two siblings diagnosed with juvenile parkinsonism due to a homozygous p.Arg258Gln mutation in the *SYNJ1* gene as described by Quadri et al. (6). The study procedures were approved by the medical ethical committee of the Erasmus MC Rotterdam, conformed to the principles set out in the WMA Declaration of Helsinki and the Department of Health and Human Services Belmont Report and all participating subjects provided written informed consent. The male patient (Patient 1) developed symptoms at 22 years of age and underwent the skin biopsy at the age of 50. The female patient (Patient 2) developed symptoms at the age of 28 and the skin biopsy was taken at the age of 35. In addition, primary cultures of dermal fibroblasts were established from skin puncture biopsies of

two unaffected individuals. Control line 1 was derived from a healthy unrelated female donor (42 years), while the control line 2 was derived from a healthy unrelated male donor (57 years).

Reprogramming of all patient and control lines used in this study was performed by The Erasmus MC iPS core facility as described previously (12). Briefly, fibroblasts were transduced with a multicistronic lentiviral vector encoding OCT4, SOX2, KLF4, and MYC, and a dTomato reporter gene, under the control of a retroviral promoter (SFFV) which is rapidly silenced during the reprogramming process. Transduced fibroblasts were seeded on irradiated Mouse Embryo Fibroblasts (MEFs) and cultured with standard human embryonic stem cell (hESC) medium, until colonies could be picked. Following selection of colonies was based on morphology, and the presence and subsequent loss of dTomato reporter expression, indicating proper silencing of the transgene. Multiple clones were characterized and selected based on karyotyping, expression of endogenous pluripotency factors and expression of differentiation associated markers after 8 days of Embryoid Body formation. Furthermore, the mutation status was confirmed in all patient iPSC lines.

The iPSC lines were maintained on irradiated MEFs in normal iPSC medium DMEM/F12 Advanced supplemented with 20% KOSR, 2 mM L-glutamine, 0.1 mM MEM-NEAA, 0.1 mM 2-mercaptoethanol, 100 units/mL penicillin/streptomycin (all from Life Technologies) and 10 ng/mL bFGF (Peprotech) in a 5% CO<sub>2</sub> atmosphere of 37°C. Medium was changed daily and cells were passaged every 4 to 6 days, depending on growth rates. Passaging was done either mechanically or enzymatically with collagenase type IV (100 U/ml) (Life Technologies), 10 µM ROCK inhibitor (Sigma) was added to the culture medium after passaging. For storage, iPSCs were frozen in defined Fetal Bovine Serum (HyClone), supplemented with Dimethyl sulfoxide (Sigma) and stored in liquid nitrogen.

## Karyotyping

iPSCs were harvested with TrypLE Express (Life Technologies), treated with colcemid (10 µg/ml) (Life Technologies) for 30 minutes at 37°C and then incubated in hypotonic solution 75 mM KCL for 30 minutes at 37°C and 10 minutes at room temperature. Cells were fixed using Carnoy's solution for 4 rounds of adding fixative, centrifuged for 10 min at 1,100 rpm and aspiration of supernatant. Metaphases were mounted using Vectashield plus DAPI (Vector Laboratories).

## Reverse Transcription and Quantitative PCR

RNA was isolated directly from iPSCs and 8 day old Embryoid Bodies using RNA Bee (AMS Bio), according to the manufacturer's protocol. The RNA was then treated with DNase before a two-step reverse transcriptase PCR was performed with the iScript cDNA synthesis kit (Biorad) according to the manufacturer's protocol. Q-PCR using SYBR Green (KAPA Biosystems) was performed on 100 µl cDNA product. Cycling conditions were an initial denaturation of 3 minutes at 95°C, followed 40 cycles of 5 seconds 95°C and 30 seconds 60°C. GAPDH was used as a reference gene and the human ES cell line H9 was included for normalization of the gene expression.

## Sequencing

The *SYNJ1* mutation was verified using Sanger sequencing. PCR amplification of *SYNJ1* exon 5 was done using the primers listed below. Amplification reactions were performed in a total volume of 20 µl, containing 1XFastStart Taq DNA Polymerase buffer, 200 µM of each dNTP, 0.5 µM of forward primer, 0.5 µM of reverse primer, 0.5 units of FastStart Taq DNA Polymerase (Roche, Basel, Switzerland), and 40 ng of genomic DNA.

PCR conditions: 5 minutes 94°C initial denaturation followed by 30 cycles of 30 seconds at 94°C; 30 seconds at 60°C; 90 seconds at 72°C, with a final extension for 5 minutes at 72°C. PCR reactions (4 µl) were cleaned-up from unconsumed dNTPs and primers using 5 units of ExoI and 0.5 units of Fast AP (Thermo Fisher Scientific, Waltham, MA, USA), 45 minutes at 37°C, 15 minutes at 80°C.

Direct Sanger Sequencing was performed using Big Dye Terminator chemistry (version 3.1; Thermo Fisher Scientific) as recommended by the manufacturer. Dye terminators were removed using SephadexG50 (GE Healthcare, Little Chalfont, UK) and loaded on an ABI 3730XL Genetic Analyzer (Thermo Fisher Scientific). Generated sequences were analyzed using the software packages Seqscape v3.0 (Thermo Fisher Scientific) and Sequencing Analysis v6.0 (Thermo Fisher Scientific).

SYNJ1\_exon5F TCTCGTTTTATAGCCCTATCTTCTGATCC

SYNJ1\_exon5R AAGGCCCATTAAGTAACCAAGAACAATC

Expected PCR size: 545bp

## Small-molecule neural progenitor cell differentiation

Differentiation of hiPSCs was performed as described previously (22) with slight modifications. For generation of smNPCs from pluripotent stem cells, colonies were detached from the MEFs 3-4 days after splitting, using 2 mg/mL collagenase IV (100 U/ml) (Life Technologies). Pieces of colonies were collected by sedimentation and resuspended in hESC medium (without bFGF) supplemented with 10  $\mu$ M SB-431542 (Ascent Scientific), 1  $\mu$ M dorsomorphin (Tocris) for neural induction, as well as 3  $\mu$ M CHIR99021 (CHIR; Axon Medchem) and 0.5  $\mu$ M Purmorphamine (PMA; Alexis), and cultured in petri dishes. Medium was replaced on day 2 by N2B27 medium supplemented with the same small molecule supplements. N2B27 medium consisted of DMEM:F12 (Life Technologies) and Neurobasal (Life Technologies) 50:50 with 1:200 N2 supplement (Invitrogen), 1:100 B27 supplement without vitamin A (Invitrogen) with 1% penicillin/streptomycin (Life Technologies). On day 4, SB-431542 and dorsomorphin were withdrawn and 150  $\mu$ M Ascorbic Acid (AA; Sigma) was added to the medium. On day 6, the Embryoid Bodies, which showed intensive neuroepithelial outgrowth, were triturated with a 1000  $\mu$ L pipette into smaller pieces and plated on Matrigel-coated (Matrigel, growth factor reduced, high concentration; BD Biosciences) 12-well plates at a density of about 10–15 per well in smNPC medium (N2B27 with CHIR, PMA, and AA). For coating, Matrigel was diluted to a final dilution of 1:50 in sterile water (Baxter) and 500  $\mu$ L per well of a 12-well plate was added. The coated plates were prewarmed to 37°C prior to plating. The first split was performed at a 1:5 ratio on days 2 to 4 after plating. All the remaining splitting ratios were at least 1:10. After a maximum of 5 passages, cultures were virtually pure smNPCs. The smNPCs were maintained in N2B27 medium supplemented with 200  $\mu$ M AA, 3  $\mu$ M CHIR and 0.5  $\mu$ M Smoothed Agonist (Tocris).

## Dopaminergic neuron targeted differentiation

Differentiation was started either on coverslips in 12 well plates or without coverslips in 6 well plates. Coverslips were baked before coating. Plates and coverslips were coated with Poly-D-Lysine (Sigma) overnight at 4°C and Matrigel 30 min at 37°C prior to plating. N2B27 medium with 1 ng/mL GDNF (ProspecBio), 2 ng/mL BDNF (ProspecBio), 200  $\mu$ M Ascorbic Acid (Sigma) and 0.5  $\mu$ M Smoothed Agonist (Tocris) was refreshed every 2 days up to 6-8 days. Next, cells were refreshed with N2B27 medium with 2 ng/mL GDNF, 4 ng/mL BDNF, 200  $\mu$ L Ascorbic Acid, 1 ng/mL TGF- $\beta$ 3 (ProspecBio), 1:1000 dbcAMP (Sigma) and 50 ng/mL Activin A (ProspecBio) for 3 days. Then Activin A was switched to 2 ng/mL for the remaining time of 12 days.



## Immunohistochemistry and immunofluorescence imaging

Cells were fixed in 4% formaldehyde for 20 minutes, and washed with PBS. Subsequently, primary antibody incubation was performed overnight at 4°C in labeling buffer (50 mM Tris.Cl (pH 7.4), 0.9% NaCl 0.25% gelatin, 0.2% TritonX-100 (all from Sigma)). The next day coverslips were washed in PBS, followed by secondary antibody incubation in the dark for 1 hour at room temperature in labeling buffer. After washing in PBS, coverslips were mounted with Prolong Gold plus DAPI (Life Technologies). Primary antibodies: rabbit anti-SOX2 1:200 (Merck Millipore, AB5603), mouse antiNestin 1:200 (Millipore, MAB5326), mouse anti-PAX6 1:200 (Santa Cruz Biotechnology, sc-81649), mouse anti-TUJ1 1:500 (Abcam, ab78078), chicken anti-TUJ1 1:500 (Millipore, AB9354), sheep anti-TH 1:200 (Novus Biologicals, 300-110), guinea pig anti-MAP2 1:200 (Synaptic Systems, 188004). Secondary antibodies: donkey anti-mouse Alexa 488 (Jackson Immuno), donkey anti-mouse Cy3 (Jackson Immuno), goat anti-rabbit Alexa 488 (Jackson Immuno), goat anti-guinea pig Alexa 647 (Abcam), goat anti-sheep Alexa 647 (Life technologies), goat anti-chicken Alexa 568 (Abcam).

Slides were analyzed on a Leica SP5 AOBS confocal laser scanning microscope with a HCX PL APO CS ×40 objective (NA 1.25) or HCX PL APO CS ×63 objective (NA 1.40). Images were acquired by sequentially scanning for the used fluorophores at a resolution of 1,024 x 1,024 pixels. Data was quantified using FIJI software. Cell masks were created based on background fluorescence and images were measured for average fluorescent intensity per cell. A cell was considered positive for the marker if it reached an average fluorescent intensity above a set threshold. Thresholds were defined on the observed maximum average fluorescent intensity of a cell and the background intensity, thresholds were used of 20% of the maximum intensity over the background intensity.

## Extracellular flux analysis

Extracellular flux analysis has been performed as described previously (45). Briefly, human NESCs were seeded in a Matrigel coated XF 96-well plate (Agilent) at a density of 65k cells per well. Cells were incubated in a normal incubator for 6 h for attachment. Medium was removed and cells were washed 2x using Assay medium consisting of 1 mM Pyruvate (ThermoFisher), 21.25 mM D+glucose (Sigma), 2 mM glutamax (ThermoFisher) in DMEM (Sigma, D5030), at 37°C, pH 7.4. For equilibration, cells were left in assay medium at 37°C in air for 1 h. The assay was run in a Seahorse XFe96 Analyser according to manufacturer

instructions. Concentrations of compounds after the injection were 1  $\mu$ M oligomycin (Sigma, 75351), 1  $\mu$ M FCCP (Sigma, C2920), 1  $\mu$ M antimycin A (Sigma, A8674) and 1  $\mu$ M rotenone (Sigma, R8875). Three baseline measures and three measurements after each compound injection were performed. For normalization, the DNA content of each well was quantified using CyQUANT kit (ThermoFisher, C7026).

## Mitophagy treatments

Cells were seeded on 6 well plates and at 70-80% confluency medium was replaced with medium supplemented with either DMSO (Sigma), Carbonyl cyanide m-chlorophenyl hydrazone 25  $\mu$ M (CCCP) or Valinomycin (1  $\mu$ M). Cells were incubated for 12 hours at 37°C and 5% CO<sub>2</sub> before proteins were extracted and analysed on Western blot as described below. To be able to determine recruitment and stabilization of PINK1 in the mitophagy, PINK1-V5 constructs were overexpressed. For this, cells were transfected with 24 hours prior to treatments with DNA-In™ Neuro (MTI-GlobalStem).

## Western Blotting

Cells were lysed using using a RadioImmunoPrecipitation Assay (RIPA) buffer containing 150 mM Sodium Chloride (Sigma) with 50 mM Tris pH 8.0 (Sigma), 1.0% NP40 (Fluka Biochemika), 0.5% sodium deoxycholate (Sigma), 0.1% SDS (Sigma) and freshly added Protease inhibitor Complete® (Promega), 1:100 phosphatase inhibitor cocktail 2 and 3 (Sigma). Using a cellscraper the lysate was collected and subsequently centrifuged at 13,000x g for 15 min at 4°C. Protein concentration was measured using the Pierce Bradford concentration assay (Thermo Fisher scientific).

The protein extracts are run on a Criterion TGX 4-15% precast polyacrylamide gel from Bio Rad and blotted to a pre-cut PVDF or nitrocellulose membrane using the Trans Blot Turbo system (Bio Rad) for 15 minutes at 2.5 A and 25 V. Blots were blocked using 5% Elk skim milk powder (Campina) in PBS, 0.1% v/v TWEEN® 20 (Merck) for 30 minutes at room temperature. Primary antibody incubations were performed overnight at 4°C. Primary antibodies used: mouse anti-Amphiphysin-1 1:1000 (Biosciences, 610714), rabbit anti-DNAJC6 1:1000 (Thermo Fischer Scientific, pa5-26981), mouse anti-Dynamin 1:1000 (Biosciences, 610246), goat anti-EEA1 1:1000 (Santa Cruz Biotechnology, 6415), mouse anti-Parkin 1:1000 (Cell Signaling Technology, 4211), rabbit anti-SOX2 1:1000 (Merck Millipore, AB5603), mouse anti-Synapsin-1 (Synaptic Systems, 106001), rabbit anti-Synaptojanin-1 1:1000 (Abcam, ab84309), rabbit anti-HSP60 1:200 (Cell Signalling,

12165P), rabbit anti-CytC (Abcam, ab90529), mouse anti-V5 1:500 (Bio-Rad, mca1360ga), rabbit anti-actin 1:1000 (Abcam, ab8227), mouse anti-Vinculin 1:5000 (Santa Cruz Biotechnology, V284), and mouse anti-GAPDH 1:5000 (Genetex, gt239). After washing in PBS, 0.1% v/v TWEEN® 20, Blots were incubated for 1 hour at room temperature with fluorescently conjugated donkey anti-mouse (IRDye 800), donkey anti-rabbit (IRDye 680) and donkey anti-goat (IRDye 680) secondary antibodies (LI-COR Biosciences, Lincoln, NE, USA). After washing in PBS, 0.1% v/v TWEEN® 20, the fluorescent intensity is determined, analysed and quantified with a LI-COR Odyssey imager and software (LI-COR Biosciences). This is able to give relative intensity values for the protein bands. The corrected protein concentration is gotten by first dividing the bands intensity by the loading control intensity. Next the corrected concentrations are divided by the average corrected concentration of the control samples to give the relative concentration levels in each sample.

## Statistical analysis

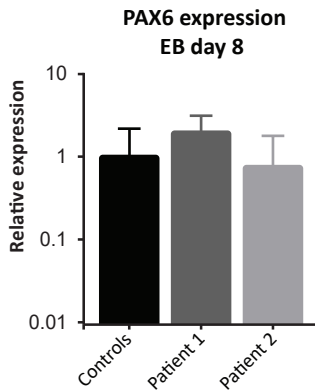
GraphPad Prism 6 (San Diego, USA.) was used to determine statistical significance. Data represent at least three independent experiments, presented as mean  $\pm$  SEM. Statistical significance was ascertained by One-way ANOVA or Two-way ANOVA with appropriate posthoc testing;  $p < 0.05$  was considered significant.

## References

1. Tysnes OB, Storstein A. Epidemiology of Parkinson's disease. *J Neural Transm (Vienna)*. 2017;124(8):901-5.
2. Savica R, Grossardt BR, Rocca WA, Bower JH. Parkinson disease with and without Dementia: A prevalence study and future projections. *Mov Disord*. 2018;33(4):537-43.
3. Jiang P, Dickson DW. Parkinson's disease: experimental models and reality. *Acta Neuropathol*. 2018;135(1):13-32.
4. Calatayud C, Carola G, Consiglio A, Raya A. Modeling the genetic complexity of Parkinson's disease by targeted genome edition in iPSC cells. *Curr Opin Genet Dev*. 2017;46:123-31.
5. Kalia LV, Lang AE. Parkinson's disease. *Lancet*. 2015;386(9996):896-912.
6. Quadri M, Fang M, Picillo M, Olgiati S, Breedveld GJ, Graafland J, et al. Mutation in the SYNJ1 gene associated with autosomal recessive, early-onset Parkinsonism. *Hum Mutat*. 2013;34(9):1208-15.
7. Krebs CE, Karkheiran S, Powell JC, Cao M, Makarov V, Darvish H, et al. The Sac1 domain of SYNJ1 identified mutated in a family with early-onset progressive Parkinsonism with generalized seizures. *Hum Mutat*. 2013;34(9):1200-7.
8. Drouet V, Lesage S. Synaptojanin 1 mutation in Parkinson's disease brings further insight into the neuropathological mechanisms. *Biomed Res Int*. 2014;2014:289728.
9. Cao M, Wu Y, Ashrafi G, McCartney AJ, Wheeler H, Bushong EA, et al. Parkinson Sac Domain Mutation in Synaptojanin 1 Impairs Clathrin Uncoating at Synapses and Triggers Dystrophic Changes in Dopaminergic Axons. *Neuron*. 2017;93(4):882-96 e5.
10. Cremona O, Di Paolo G, Wenk MR, Luthi A, Kim WT, Takei K, et al. Essential role of phosphoinositide metabolism in synaptic vesicle recycling. *Cell*. 1999;99(2):179-88.
11. Verstreken P, Koh TW, Schulze KL, Zhai RG, Hiesinger PR, Zhou Y, et al. Synaptojanin is recruited by endophilin to promote synaptic vesicle uncoating. *Neuron*. 2003;40(4):733-48.
12. Vanhauwaert R, Kuenen S, Masius R, Bademosi A, Manetsberger J, Schoovaerts N, et al. The SAC1 domain in synaptojanin is required for autophagosome maturation at presynaptic terminals. *EMBO J*. 2017;36(10):1392-411.

13. Fasano D, Parisi S, Pierantoni GM, De Rosa A, Picillo M, Amodio G, et al. Alteration of endosomal trafficking is associated with early-onset parkinsonism caused by SYNJ1 mutations. *Cell Death Dis.* 2018;9(3):385.
14. Cossec JC, Lavour J, Berman DE, Rivals I, Hoischen A, Stora S, et al. Trisomy for synaptotagmin1 in Down syndrome is functionally linked to the enlargement of early endosomes. *Hum Mol Genet.* 2012;21(14):3156-72.
15. Al Zaabi N, Al Menhali N, Al-Jasmi F. SYNJ1 gene associated with neonatal onset of neurodegenerative disorder and intractable seizure. *Mol Genet Genomic Med.* 2018;6(1):109-13.
16. Dymant DA, Smith AC, Humphreys P, Schwartzentruber J, Beaulieu CL, Consortium FC, et al. Homozygous nonsense mutation in SYNJ1 associated with intractable epilepsy and tau pathology. *Neurobiol Aging.* 2015;36(2):1222 e1-5.
17. Hardies K, Cai Y, Jardel C, Jansen AC, Cao M, May P, et al. Loss of SYNJ1 dual phosphatase activity leads to early onset refractory seizures and progressive neurological decline. *Brain.* 2016;139(Pt 9):2420-30.
18. Miranda AM, Herman M, Cheng R, Nahmani E, Barrett G, Micevska E, et al. Excess Synaptotagmin 1 Contributes to Place Cell Dysfunction and Memory Deficits in the Aging Hippocampus in Three Types of Alzheimer's Disease. *Cell Rep.* 2018;23(10):2967-75.
19. Herrera F, Chen Q, Fischer WH, Maher P, Schubert DR. Synaptotagmin-1 plays a key role in astrogliogenesis: possible relevance for Down's syndrome. *Cell Death Differ.* 2009;16(6):910-20.
20. Irie F, Okuno M, Pasquale EB, Yamaguchi Y. EphrinB-EphB signalling regulates clathrin-mediated endocytosis through tyrosine phosphorylation of synaptotagmin 1. *Nat Cell Biol.* 2005;7(5):501-9.
21. Arai Y, Ijuin T, Takenawa T, Becker LE, Takashima S. Excessive expression of synaptotagmin in brains with Down syndrome. *Brain Dev.* 2002;24(2):67-72.
22. Reinhardt P, Glatza M, Hemmer K, Tsytsyura Y, Thiel CS, Hoing S, et al. Derivation and expansion using only small molecules of human neural progenitors for neurodegenerative disease modeling. *PLoS One.* 2013;8(3):e59252.
23. Pickrell AM, Youle RJ. The roles of PINK1, parkin, and mitochondrial fidelity in Parkinson's disease. *Neuron.* 2015;85(2):257-73.
24. Shin JH, Ko HS, Kang H, Lee Y, Lee YI, Pletinkova O, et al. PARIS (ZNF746) repression of PGC-1alpha contributes to neurodegeneration in Parkinson's disease. *Cell.* 2011;144(5):689-702.
25. Zheng L, Bernard-Marissal N, Moullan N, D'Amico D, Auwerx J, Moore DJ, et al. Parkin functionally interacts with PGC-1alpha to preserve mitochondria and protect dopaminergic neurons. *Hum Mol Genet.* 2017;26(3):582-98.
26. La Manno G, Gyllborg D, Codeluppi S, Nishimura K, Salto C, Zeisel A, et al. Molecular Diversity of Midbrain Development in Mouse, Human, and Stem Cells. *Cell.* 2016;167(2):566-80 e19.
27. Burbulla LF, Song P, Mazzulli JR, Zampese E, Wong YC, Jeon S, et al. Dopamine oxidation mediates mitochondrial and lysosomal dysfunction in Parkinson's disease. *Science.* 2017;357(6357):1255-61.
28. Takahashi M, Osumi N. Pax6 regulates specification of ventral neurone subtypes in the hindbrain by establishing progenitor domains. *Development.* 2002;129(6):1327-38.
29. Osumi N, Shinohara H, Numayama-Tsuruta K, Maekawa M. Concise review: Pax6 transcription factor contributes to both embryonic and adult neurogenesis as a multifunctional regulator. *Stem Cells.* 2008;26(7):1663-72.
30. Thomas MG, Welch C, Stone L, Allan P, Barker RA, White RB. PAX6 expression may be protective against dopaminergic cell loss in Parkinson's disease. *CNS Neurol Disord Drug Targets.* 2016;15(1):73-9.
31. Sebastian-Serrano A, Sandonis A, Cardozo M, Rodriguez-Tornos FM, Bovolenta P, Nieto M. Palphax6 expression in postmitotic neurons mediates the growth of axons in response to SFRP1. *PLoS One.* 2012;7(2):e31590.
32. Mamelak M. Parkinson's Disease, the Dopaminergic Neuron and Gammahydroxybutyrate. *Neurol Ther.* 2018;7(1):5-11.
33. Cao M, Milosevic I, Giovedi S, De Camilli P. Upregulation of Parkin in endophilin mutant mice. *J Neurosci.* 2014;34(49):16544-9.
34. Gouspillou G, Godin R, Piquereau J, Picard M, Mofarrah M, Mathew J, et al. Protective role of Parkin in skeletal muscle contractile and mitochondrial function. *J Physiol.* 2018;596(13):2565-79.
35. Clark IE, Dodson MW, Jiang C, Cao JH, Huh JR, Seol JH, et al. Drosophila pink1 is required for mitochondrial function and interacts genetically with parkin. *Nature.* 2006;441(7097):1162-6.
36. Park J, Lee SB, Lee S, Kim Y, Song S, Kim S, et al. Mitochondrial dysfunction in Drosophila PINK1 mutants is complemented by parkin. *Nature.* 2006;441(7097):1157-61.
37. Narendra D, Tanaka A, Suen DF, Youle RJ. Parkin is recruited selectively to impaired mitochondria and promotes their autophagy. *J Cell Biol.* 2008;183(5):795-803.
38. Castillo-Quan JI. Parkin' control: regulation of PGC-1alpha through PARIS in Parkinson's disease. *Dis Model Mech.* 2011;4(4):427-9.
39. Scarpulla RC. Metabolic control of mitochondrial biogenesis through the PGC-1 family regulatory network. *Biochim Biophys Acta.* 2011;1813(7):1269-78.
40. Kuroda Y, Mitsui T, Kunishige M, Shono M, Akaike M, Azuma H, et al. Parkin enhances mitochondrial biogenesis in proliferating cells. *Hum Mol Genet.* 2006;15(6):883-95.
41. Wang W, Osenbroch P, Skinnies R, Esbensen Y, Bjoras M, Eide L. Mitochondrial DNA integrity is essential for mitochondrial maturation during differentiation of neural stem cells. *Stem Cells.* 2010;28(12):2195-204.
42. Jinek M, Chylinski K, Fonfara I, Hauer M, Doudna JA, Charpentier E. A programmable dual-RNA-guided DNA endonuclease in adaptive bacterial immunity. *Science.* 2012;337(6096):816-21.
43. Wang G, Yang L, Grishin D, Rios X, Ye LY, Hu Y, et al. Efficient, footprint-free human iPSC genome editing by consolidation of Cas9/CRISPR and piggyBac technologies. *Nat Protoc.* 2017;12(1):88-103.
44. Arias-Fuenzalida J, Jarazo J, Qing X, Walter J, Gomez-Giro G, Nickels SL, et al. FACS-Assisted CRISPR-Cas9 Genome Editing Facilitates Parkinson's Disease Modeling. *Stem Cell Reports.* 2017;9(5):1423-31.

# Supplementary Figures



**Supplementary Figure S1. PAX6 expression levels in 8 day old embryoid bodies from patient and control iPSCs**



## Chapter 4

# *LRP10* genetic variants in familial Parkinson's disease and dementia with Lewy bodies: a genome-wide linkage and sequencing study

Marialuisa Quadri\*, Wim Mandemakers\*, [Roy Masius](#)\*, Martyna M. Grochowska\*, Hanneke Geut†, Edito Fabrizio, Guido J. Breedveld, Demy Kuipers, Michelle Minneboo, Leonie J.M. Vergouw, Ana Carreras Mascaro, Ekaterina Yonova-Doing, Erik Simons, Tianna Zhao, Alessio B. Di Fonzo, Hsiu-Chen Chang, Piero Parchi, Marta Melis, Leonor Correia Guedes, Chiara Criscuolo, Astrid Thomas, Rutger W.W. Brouwer, Daphne Heijnsman, Angela M.T. Ingrassia, Giovanna Calandra Buonauro, Janneke P. Rood, Sabina Capellari, Annemieke J. Rozemuller, Marianna Sarchioto, Hsin Fen Chien, Nicola Vanacore, Simone Olgiati, Yah-Huei Wu-Chou, Tu-Hsueh Yeh, Agnita J.W. Boon, Susanne E. Hoogers, Mehrnaz Ghazvini, Arne S. IJpma, Wilfred F.J. van IJcken, Marco Onofrj, Paolo Barone, David J. Nicholl, Andreas Puschmann, Michele De Mari, Anneke J. Kievit, Egberto Barbosa, Giuseppe De Michele, Danielle Majoor-Krakauer, John C. van Swieten, Frank J. de Jong, Joaquim J. Ferreira, Giovanni Cossu, Chin-Song Lu, Giuseppe Meco, Pietro Cortelli, Wilma D.J. van de Berg, Vincenzo Bonifati, in collaboration with the International Parkinsonism Genetics Network

\* These authors contributed equally as first authors

† These authors contributed equally as second authors

**Lancet Neurology 2018;17(7):597-608.**

# Summary

## Background

Most patients with Parkinson's disease, Parkinson's disease dementia, and dementia with Lewy bodies do not carry mutations in known disease-causing genes. The aim of this study was to identify a novel gene implicated in the development of these disorders.

## Methods

Our study was done in three stages. First, we did genome-wide linkage analysis of an Italian family with dominantly inherited Parkinson's disease to identify the disease locus. Second, we sequenced the candidate gene in an international multicentre series of unrelated probands who were diagnosed either clinically or pathologically with Parkinson's disease, Parkinson's disease dementia, or dementia with Lewy bodies. As a control, we used gene sequencing data from individuals with abdominal aortic aneurysms (who were not examined neurologically). Third, we enrolled an independent series of patients diagnosed clinically with Parkinson's disease and controls with no signs or family history of Parkinson's disease, Parkinson's disease dementia, or dementia with Lewy bodies from centres in Portugal, Sardinia, and Taiwan, and screened them for specific variants. We also did mRNA and brain pathology studies in three patients from the international multicentre series carrying disease-associated variants, and we did functional protein studies in in-vitro models, including neurons from induced pluripotent stem-like cells.

## Findings

Molecular studies were done between Jan 1, 2008, and Dec 31, 2017. In the initial kindred of ten affected Italian individuals (mean age of disease onset 59.8 years [SD 8.7]), we detected significant linkage of Parkinson's disease to chromosome 14 and nominated *LRP10* as the disease-causing gene. Among the international series of 660 probands, we identified eight individuals (four with Parkinson's disease, two with Parkinson's disease dementia, and two with dementia with Lewy bodies) who carried different, rare, potentially pathogenic *LRP10* variants; one carrier was found among 645 controls with abdominal aortic aneurysms. In the independent series, two of these eight variants were detected in three additional Parkinson's disease probands (two from Sardinia and one



from Taiwan) but in none of the controls. Of the 11 probands from the international and independent cohorts with *LRP10* variants, ten had a positive family history of disease and DNA was available from ten affected relatives (in seven of these families). The *LRP10* variants were present in nine of these ten relatives, providing independent—albeit limited—evidence of co-segregation with disease. Post-mortem studies in three patients carrying distinct *LRP10* variants showed severe Lewy body pathology. Of nine variants identified in total (one in the initial family and eight in stage 2), three severely affected *LRP10* expression and mRNA stability (1424+5delG, 1424+5G>A, and Ala212Serfs\*17, shown by cDNA analysis), four affected protein stability (Tyr307Asn, Gly603Arg, Arg235Cys, and Pro699Ser, shown by cycloheximide-chase experiments), and two affected protein localisation (Asn517del and Arg533Leu; shown by immunocytochemistry), pointing to loss of *LRP10* function as a common pathogenic mechanism.

## Interpretation

Our findings implicate *LRP10* gene defects in the development of inherited forms of  $\alpha$ -synucleinopathies. Future elucidation of the function of the *LRP10* protein and pathways could offer novel insights into mechanisms, biomarkers, and therapeutic targets.

## Funding

Stichting ParkinsonFonds, Dorpmans-Wigmans Stichting, Erasmus Medical Center, ZonMw—Memorabel programme, EU Joint Programme Neurodegenerative Disease Research (JPND), Parkinson's UK, Avtal om Läkarutbildning och Forskning (ALF) and Parkinsonfonden (Sweden), Lijf and Leven foundation, and cross-border grant of AlzheimerNetherlands—Ligue Européenne Contre la Maladie d'Alzheimer (LECMA).

# Introduction

Parkinson's disease, the most common neuro-degenerative movement disorder, is clinically defined by bradykinesia, resting tremor, muscular rigidity, and a favourable response to levodopa or dopamine-agonist treatment (1). The pathological hallmarks of Parkinson's disease are loss of nigrostriatal dopaminergic neurons, with intracellular inclusions containing  $\alpha$ -synuclein protein (ie, Lewy bodies and Lewy neurites) in surviving neurons (1). Non-motor manifestations—eg, olfactory, cognitive, psychiatric, sleep, and autonomic disturbances—are nowadays recognised as frequent and relevant features of Parkinson's disease (1). Cognitive decline progresses into overt dementia in up to 80% of individuals with Parkinson's disease (2), leading to a diagnosis of Parkinson's disease dementia (3, 4). Furthermore, in patients with dementia with Lewy bodies, severe cognitive disturbances are the initial manifestation, often but not always followed by parkinsonism (3, 4). Dementia with Lewy bodies accounts for roughly 5% of dementia cases in elderly people (5) and is associated with severe and widespread pathological findings of Lewy bodies in the brain (4, 6).

Rare highly penetrant variants in *SNCA* (7, 8) and *LRRK2* (8, 9, 10) cause hereditary forms of dominantly transmitted, Lewy body-positive Parkinson's disease, Parkinson's disease dementia, and dementia with Lewy bodies. Moreover, common variants in *SNCA*, *LRRK2*, and *GBA* are risk factors for the same disorders (11, 12, 13). Pathological misfolding and aggregation of  $\alpha$ -synuclein seems to be central in several neurodegenerative diseases, including Parkinson's disease and dementia with Lewy bodies, collectively termed  $\alpha$ -synucleinopathies (14). These clinical, pathological, and molecular overlaps suggest that Parkinson's disease, Parkinson's disease dementia, and dementia with Lewy bodies are parts of a continuum of Lewy body diseases (15, 16). Yet, in most patients with familial forms of Parkinson's disease, Parkinson's disease dementia, or dementia with Lewy bodies, variants in the above-mentioned genes are not found, suggesting that other causative or predisposing genes remain to be identified. We aimed to identify a novel gene implicated in the development of familial Parkinson's disease, Parkinson's disease dementia, and dementia with Lewy bodies.

# Methods

## Study participants

Our study was done in three stages. For the first stage, we identified a large Italian family with Parkinson's disease segregating as an autosomal-dominant trait. We examined these family members neurologically and took biological specimens from them.

For the second stage, we analysed samples and clinical data that had been obtained from an international series of unrelated probands with Parkinson's disease, Parkinson's disease dementia, or dementia with Lewy bodies between Jan 1, 2000, and Dec 31, 2017. These participants were enrolled from the International Parkinsonism Genetics Network, the Netherlands Brain Bank at the Netherlands Institute of Neuroscience in Amsterdam (selected based on presence of  $\alpha$ -synuclein-positive pathology), and the Laboratory of Neuropathology at the University of Bologna in Italy (appendix). We also included as a control whole exome sequencing data from a Dutch study of patients with abdominal aortic aneurysms (unpublished data). Data for neurological diseases were not available in that study.

For the third study stage, we enrolled an independent series of unrelated patients with clinically diagnosed Parkinson's disease and unaffected controls from centres in Portugal, Sardinia, and Taiwan. As controls, we included population-matched series of spouses of individuals with Parkinson's disease or unrelated individuals examined at the same centres with no signs or family history of Parkinson's disease, Parkinson's disease dementia, or dementia with Lewy bodies.

We obtained written informed consent for use of clinical data and biological samples for this study from patients with a clinical diagnosis of Parkinson's disease, Parkinson's disease dementia, or dementia with Lewy bodies (or their next of kin, for patients with dementia) and unaffected relatives. For patients diagnosed pathologically from the Netherlands Brain Bank and the Laboratory of Neuropathology, written informed consent for brain autopsy and use of clinical information and material for research purposes had been obtained previously from the donor or from the next of kin. Participants in the abdominal aortic aneurysms study had provided written informed consent for use of whole exome sequencing data for genetic research. Relevant ethics authorities approved study protocols (appendix).

## Procedures

We made clinical diagnoses of Parkinson's disease according to the UK Parkinson's Disease Society Brain Bank criteria (17). We diagnosed Parkinson's disease dementia in patients developing dementia after 1 year from the onset of Parkinson's disease symptoms (3). We based our clinical diagnosis of dementia with Lewy bodies on the third report of the Dementia with Lewy Body Consortium (3).

In the first stage of the study, after confirming the absence of pathogenic mutations in genes causing autosomal-dominant Parkinson's disease (ie, *SNCA*, *LRKK2*, *VPS35*, and *CHCHD2*, as well as *GBA* variants; sequencing and multiplex ligation-dependent probe amplification [MLPA] protocols are reported in the appendix), we did genome-wide single nucleotide polymorphism (SNP) array genotyping in ten affected relatives from the Italian family. We also ran a parametric multipoint linkage analysis, assuming an autosomal-dominant mode of inheritance, and we did copy number analysis with Nexus Copy Number (appendix). We did whole exome sequencing in the index patient. We annotated variants with Annovar (version 2016 Feb 01) (18) and the Mendelian Clinically Applicable Pathogenicity (M-CAP) score (19). We then filtered variants located within the linkage interval using the following criteria: (I) the variant being present in the heterozygous state; (II) rarity, defined as a minor allele frequency (MAF) less than 0.1% by the Exome Aggregation Consortium (ExAC), dbSNP, the National Heart, Lung, and Blood Institute's Exome Sequencing Project exome variant server, Genome of the Netherlands (GoNL), and the genome aggregation database (gnomAD); (III) exonic and non-synonymous, or predicted to affect splicing in silico; and (IV) pathogenicity, defined as being predicted as pathogenic by at least five of 11 in-silico tools (appendix). This work led to nomination of *LRP10* (low-density lipoprotein receptor-related protein 10) as the candidate disease-causing gene in the Italian family. We used Sanger sequencing for validation and co-segregation analysis in all members of this family for whom DNA was available.

In the second stage of the study, we sequenced the entire *LRP10* open reading frame and exon-intron boundaries in 660 unrelated probands with Parkinson's disease, Parkinson's disease dementia, or dementia with Lewy bodies. We did Sanger sequencing in 659 participants and whole exome sequencing in one. Protocols and primers are detailed in the appendix. We judged of interest variants fulfilling the same criteria mentioned in the first study stage. We used Sanger sequencing for co-segregation analysis when DNA from additional relatives was available. We also searched for *LRP10* variants (entire coding region and exon-intron boundaries) in the whole exome sequencing database of

individuals from the abdominal aortic aneurysm study (average *LRP10* depth coverage 100.7 times). We included variants fulfilling the same, above-specified, criteria and compared their frequency with that in our series of 660 patients with Parkinson's disease, Parkinson's disease dementia, and dementia with Lewy bodies.

In stage three of the study, we used high-resolution melting analysis to study three of the identified *LRP10* variants in the independent population-matched series of patients and controls from Portugal, Sardinia, and Taiwan. We also used Sanger sequencing and MLPA to analyse genes causing autosomal-dominant Parkinson's disease (ie, *SNCA*, *LRK2*, *VPS35*, and *CHCHD2*, and the risk gene *GBA*) in all probands from the second and third study stages in whom *LRP10* variants were identified (appendix).

For pathological analyses, we obtained autopsy tissue blocks from 23 different brain regions in three patients from the international multicentre series of unrelated probands carrying *LRP10*-disease associated variants (appendix), which we then fixed in formalin, embedded in paraffin, and cut into 8  $\mu$ m sections. For staining of selected regions, we used haematoxylin and eosin, Congo red, Gallyas silver stain, and immunohistochemistry against  $\alpha$ -synuclein, amyloid- $\beta$ , and hyperphosphorylated tau (appendix). For quantitative mRNA expression studies in human brain tissue of two patients with *LRP10* disease-associated variants, we isolated RNA from the medial temporal gyrus of donors with Parkinson's disease, Parkinson's disease dementia, or dementia with Lewy bodies, and from elderly control donors (appendix). We used standard procedures to isolate DNA and RNA from blood and brain samples. We generated cDNA using total RNA and amplified *LRP10* cDNA fragments and analysed and sequenced them, as described in the appendix.

We studied the effect of the identified, potentially pathogenic variants of *LRP10* on stability of LRP10 protein and subcellular localisation. Details of methods, antibodies, and LRP10 expression constructs are in the appendix. We derived human induced neurons from previously characterised induced pluripotent stem cells (iPSCs) (20), according to published protocols (21), with minor modifications (appendix). For subcellular localisation, we transfected differentiated neurons with N-terminal V5-tagged LRP10 wildtype expression plasmid and processed them further for immunocytochemistry against V5-LRP10, TGOLN2 (also known as TGN46), EEA1, GGA1, and VPS35 (appendix).

## Statistical analysis

We describe continuous clinical variables (eg, age at disease onset, age at examination, disease duration) as mean (SD). We did parametric multipoint linkage analysis with the software MERLIN, version 1.1.2 (22), with affected-only analysis. We assumed an autosomal-dominant model of disease inheritance, equal markers allele frequency, a disease allele frequency of  $1 \times 10^{-5}$ , and penetrance of either 0.002 (wildtype), 0.99 (heterozygous carrier), or 0.99 (homozygous carrier). We judged  $\log_{10}$  of odds (LOD) scores of 3.3 or higher to be genome-wide significant, according to internationally accepted standards. We compared categorical data using Fisher's exact test. We judged a two-sided *p* value less than 0.05 to be significant. For stability and subcellular localisation of LRP10 protein, we did statistical analyses with Prism 7 (GraphPad Software, La Jolla, CA, USA; appendix).

## Role of the funding source

The funder had no role in study design, data collection, data analysis, data interpretation, or writing of the report. The corresponding author had full access to all the data in the study and had final responsibility for the decision to submit for publication.

## Results

The pedigree of the Italian family in the first stage of the study (family 1) is shown in figure 1A. 13 members of family 1 had Parkinson's disease and one had dementia with Lewy bodies, of whom ten were alive and examined personally by two investigators (EF, GM). 19 relatives in total were included in our study—nine with Parkinson's disease, one with dementia with Lewy bodies, and nine who were unaffected. Mean age at disease onset was 59.8 years (SD 8.7, range 46–73; table). Additional clinical features of family 1 are described in the appendix.

A Family 1 (Italy)

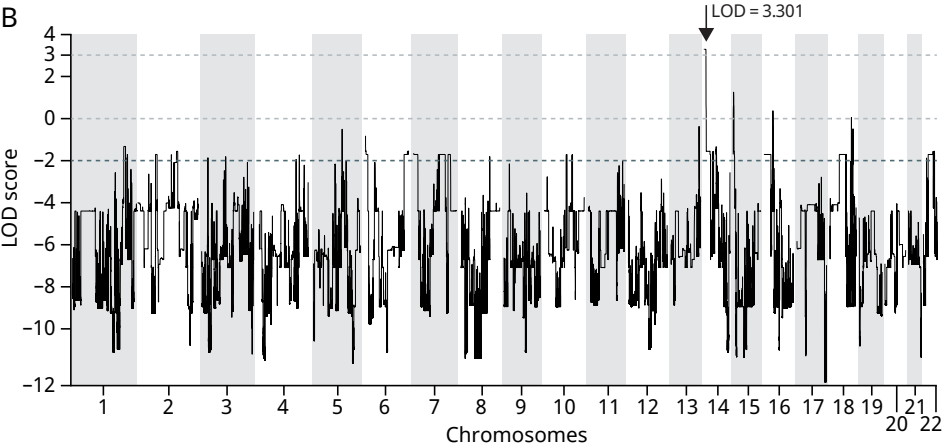
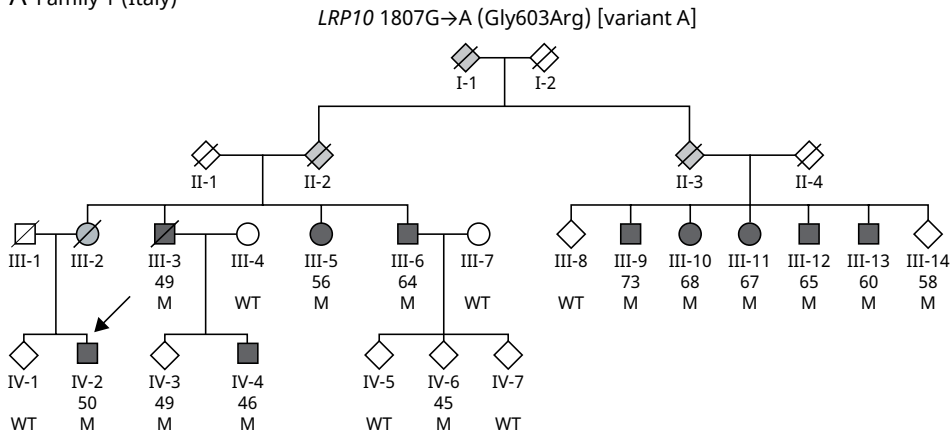


**Figure 1. Pedigree of the Italian family in the first study stage (family 1) and genome-wide linkage analysis**

(A) Pedigree of the *LRP10* 1807G>A (Gly603Arg) variant. Black symbols denote affected individuals; grey symbols indicate individuals reported with Parkinson's disease by history, but not examined personally within this study; diagonal lines indicate deceased individuals; circles indicate women; squares indicate men; diamonds indicate sex-disguised individual. Numbers below individual codes indicate age at symptom onset (for patients) or age at last examination (for living unaffected carriers). The arrow indicates the proband. M=heterozygous *LRP10* Gly603Arg variant carrier. WT=homozygous wildtype individual. (B) Genome-wide linkage analysis in this family yielded significant linkage to a novel locus on chromosome 14p13–q12 (red arrow, LOD score 3.301), spanning 25 Mb from the beginning of the chromosome until the marker rs1950946 (position chr14:0–26,396,221; GRCh37) and containing 243 genes. Dashed lines at LOD scores of –2 and 3 are for ease of reference. LOD=log<sub>10</sub> of odds.

**Table 1. Characteristics of study participants**

	Affected individuals		Controls		Genetic analyses	LRP10 pathogenic variant* (family reference; variant reference)
	Total participants (n) and disease characteristics	Mean (SD) age at onset (years)	Controls (n)	Mean (SD) age at examination (years)		
First study stage						
Italian family	10 (9 PD, 1 DLB)	59.8 (8.7)	..	..	Genome-wide SNP array genotyping and linkage analysis, WES in the index patient, co-segregation analysis (Sanger sequencing)	1807G>A ([Gly603Arg] family 1; variant A)
Second study stage						
Multicentre series (patients with clinically diagnosed familial PD and PDD)	430 (420 PD, 10 DLB)	54.6 (11.3)	..	..	Sanger sequencing, all LRP10 exons and exon-intron boundaries	..
Italy (31 centres)	274 (264 PD, 10 PDD)	..	..	..	..	2095C>T ([Pro699Ser] family 2 [Sardinia]; variant B); 919T>A ([Tyr307Asn] family 5; variant E)
UK (1 centre)	45 (PD)	..	..	..	..	..
Portugal (2 centres)	42 (PD)	..	..	..	..	1598G>T ([Arg533Leu] family 4; variant D)
Brazil (4 centres)	37 (PD)	..	..	..	..	..
Taiwan (3 centres)	15 (PD)	..	..	..	..	1424+5delG (family 3; variant C)
Sweden (1 centre)	9 (PD)	..	..	..	..	..
The Netherlands (4 centres)	8 (PD)	..	..	..	..	..
Multicentre series (patients clinically diagnosed with DLB)	62	69.6 (9.1)	..	..	Sanger sequencing, all LRP10 exons and exon-intron boundaries	..
The Netherlands (2 centres)	32 (1 possible DLB, 31 probable DLB)	..	..	..	..	1424+5G>A (family 6; variant F)
Italy (2 centres)	30 (2 possible DLB, 28 probable DLB)	..	..	..	..	..
Multicentre series (patients with pathologically confirmed PD, PDD, and DLB)	168 (49 PD, 74 PDD, 45 DLB)	76.9 (7.8)†	..	..	..	..
The Netherlands (1 centre)	167 (49 PD, 73 PDD, 45 DLB)	..	..	..	Sanger sequencing, all LRP10 exons and exon-intron boundaries	1549_1551delAAT ([Asn517del] family 8; variant H); 632dupT ([Ala212Serfs*17] family 9; variant I)
Italy (1 centre)	1 (PDD)	..	..	..	WES	703C>T ([Arg235Cys] family 7; variant G)
Control series (abdominal aortic aneurysm study)	..	..	645 (553 unrelated individuals, 92 relatives)	67.2 (10.1)	WES (average LRP10 depth coverage >100 times)	451C>T ([Arg151Cys] 1 individual)
Third study stage						
Consecutive series (unrelated patients with PD and controls)						
Italy (Sardinia; 2 centres)	412 (PD)	62.8 (11.0)	242	70.7 (11.7)	HRM	2095C>T ([Pro699Ser] family 10 [familial], family 11 [sporadic]; variant B)
Taiwan (3 centres)	831 (PD)	55.4 (12.1)	431	56.8 (16.3)	HRM	1424+5delG (family 12 [familial]; variant C)
Portugal (2 centres)	223 (PD)	59.2 (11.8)	138	69.0 (7.4)	HRM	..

*Details of centres are in the appendix. DLB=dementia with Lewy bodies. HRM=high-resolution melting analysis. PD=Parkinson's disease. PDD=Parkinson's disease dementia. SNP=single nucleotide polymorphism. WES=whole exome sequencing. \*National Center for Biotechnology Information reference sequence NM\_014045.4; all variants were heterozygous. †Age at death.*



By analysis of the ten members of family 1 with Parkinson's disease or dementia with Lewy bodies, one linkage peak of genome-wide significance (LOD 3.301) was identified on chromosome 14p13-q12 (figure 1B). Copy number aberrations within the linkage interval were not detected by SNP array analysis using Nexus. In the whole exome sequencing analysis of the index case (patient IV-2 in figure 1A), only three heterozygous variants—in the *OR11H12*, *POTEG*, and *LRP10* genes—located within the linkage region had MAF less than 0.1% (appendix). The *OR11H12* and *POTEG* variants were predicted as benign by most of the 11 in-silico tools and had a negative nucleotide conservation score (genomic evolutionary rate profiling [GERP] -0.993 and -0.546, respectively; appendix). However, the *LRP10* variant 1807G>A (Gly603Arg; variant A) was predicted to be damaging by seven of 11 in-silico tools, had a high GERP score (+4.9), and replaced a very conserved residue in the LRP10 protein. Furthermore, *LRP10* was the only one of these three genes with evidence of expression in human brain (appendix).

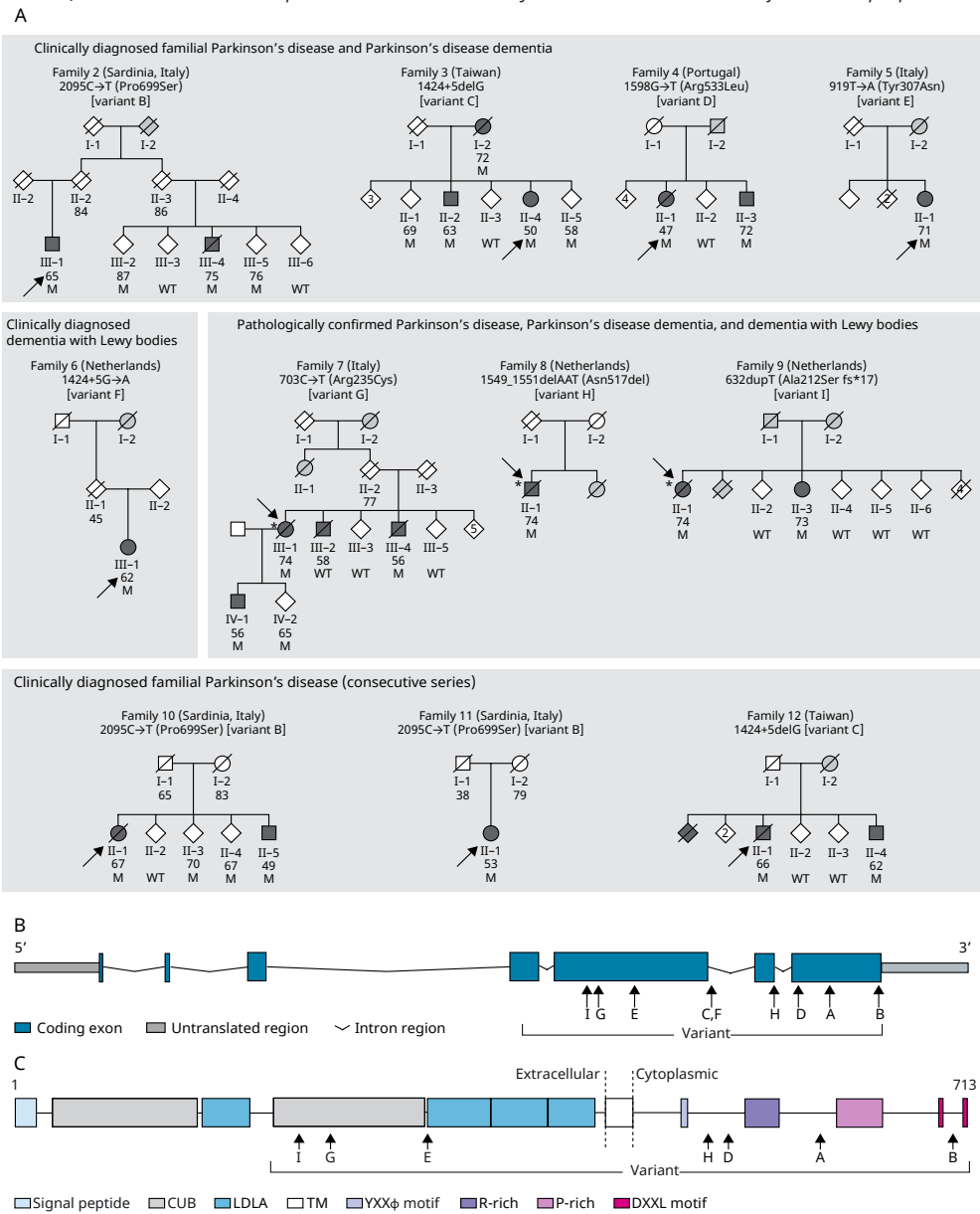
*LRP10* was nominated as the candidate disease-causing gene in family 1 (NM\_014045.4). We confirmed by Sanger sequencing the presence of variant A (1807G>A) in the index case (patient IV-2; appendix) and all nine affected relatives, and variant A was present in three unaffected relatives (patients III-14, IV-3, and IV-6; figure 1A; age at last examination 58 years, 49 years, and 45 years, respectively). Four unaffected relatives and two spouses did not carry the *LRP10* variant A.

In the second stage of the study, all *LRP10* exons and exon-intron boundaries underwent Sanger sequencing in an international cohort of 660 unrelated probands (table). Of these people, 430 were diagnosed clinically with either familial Parkinson's disease (n=420) or Parkinson's disease dementia (n=10), and 62 were diagnosed clinically with dementia with Lewy bodies; 168 had pathological confirmation of Parkinson's disease (n=49), Parkinson's disease dementia (n=74), or dementia with Lewy bodies (n=45). Eight variants were identified that fulfilled our criteria (variants B to I; table; appendix).

Five of these variants were identified in probands who were diagnosed clinically with either Parkinson's disease, Parkinson's disease dementia, or dementia with Lewy bodies (table). The first variant—2095C>T (Pro699Ser; variant B)—was detected in a Sardinian proband with Parkinson's disease, which was confirmed in a cousin with Parkinson's disease and two unaffected cousins (family 2; figure 2A). A second variant—deletion of guanine at position +5 in *LRP10* intron 5 (1424+5delG; variant C)—was identified in a Taiwanese proband with Parkinson's disease and confirmed in two relatives with Parkinson's disease and two unaffected relatives (family 3; figure 2A). The third variant was 1598G>T (Arg533Leu; variant D) and was identified in a Portuguese proband with

**Figure 2. Pedigrees of families carrying *LRP10* variants in the second and third study stages and structure of the *LRP10* gene and LRP10 protein**

(A) Pedigrees of families 2 to 12, carrying *LRP10* variants B to I, respectively. Black symbols denote individuals affected by Parkinson's disease, Parkinson's disease dementia, or dementia with Lewy bodies; grey symbols indicate individuals reported to have Parkinson's disease, Parkinson's disease dementia, or dementia with Lewy bodies by history, but not examined personally within this study; diagonal lines indicate deceased individuals; circles indicate women; squares indicate men; diamonds indicate sex-disguised individuals. Numbers below individual codes indicate age at symptom onset (for patients), age at last examination (for living unaffected carriers), or age at death (for deceased unaffected relatives). The arrows indicate the probands. Numbers within symbols indicate the number of additional people within



*the same family with that status. M=heterozygous variant carrier. WT=homozygous wildtype individual. \*Pathologically proven cases. (B) LRP10 gene structure. Capital letters indicate the position of the nine identified variants (ie, variant A in figure 1 and variants B to I in figure 2A). (C) LRP10 protein structure. Capital letters indicate the position of the seven coding variants identified (splicing variants C and F are not shown because they affect non-coding regions of the gene). Variant I leads to frameshift and premature protein truncation, and nonsense-mediated mRNA decay (appendix). CUB=complement C1R/C1S, urchin EGF, BMP1. LDLA=low-density lipoprotein receptor class A. TM=transmembrane domain. R-rich=arginine-rich domain. P-rich=proline-rich domain. YXXφ=a motif of a tyrosine plus two other aminoacids, then an aminoacid with a large bulky hydrophobic side chain. DXXLL=a motif of an aspartic acid, two other aminoacids, then two leucines.*

Parkinson's disease and a sibling with Parkinson's disease (family 4; figure 2A). In an Italian proband with Parkinson's disease dementia, a fourth variant (919T>A [Tyr307Asn]; variant E) was identified (family 5; figure 2A). In a Dutch proband who had probable dementia with Lewy bodies (family 6; figure 2A), a fifth variant was noted at position +5 in *LRP10* intron 5 (1424+5G>A; variant F). It is noteworthy that the same guanine that was deleted in variant C was replaced by adenine in variant F.

The other three variants were detected in brain DNA samples from the 168 probands with pathological confirmation of disease (table). These variants were characterised as germline by confirming their presence in DNA from blood samples of the same individuals. The sixth variant (703C>T [Arg235Cys]; variant G) was identified in an Italian proband with familial Parkinson's disease dementia (family 7; figure 2A). This patient was diagnosed initially with Parkinson's disease and later developed rapidly progressive dementia. Three affected relatives in family 7 developed a similar neurodegenerative illness, including parkinsonism, dementia, and neurological signs such as supranuclear gaze palsy and ideomotor apraxia (appendix). Variant G was present in two of these affected relatives; the remaining relative, who did not have this variant, had a similar disease (including supranuclear gaze limitation) but had a much longer disease course (roughly 20 years between symptom onset and death) compared with only 8–14 years in the relatives who carried the *LRP10* variant G, and might represent a phenocopy. One other relative in family 7 carried variant G but was unaffected. The seventh variant was an in-frame deletion of three nucleotides (1549\_1551delAAT [Asn517del]; variant H) and was identified in a Dutch proband with dementia with Lewy bodies (family 8; figure 2A). The eighth variant was a frameshift (632dupT [Ala212Serfs\*17]; variant I) and was detected in a Dutch proband with Parkinson's disease and severe parkinsonism and mild cognitive impairment. This variant I was confirmed in one sibling with dementia but in none of four unaffected siblings (family 9; figure 2A).

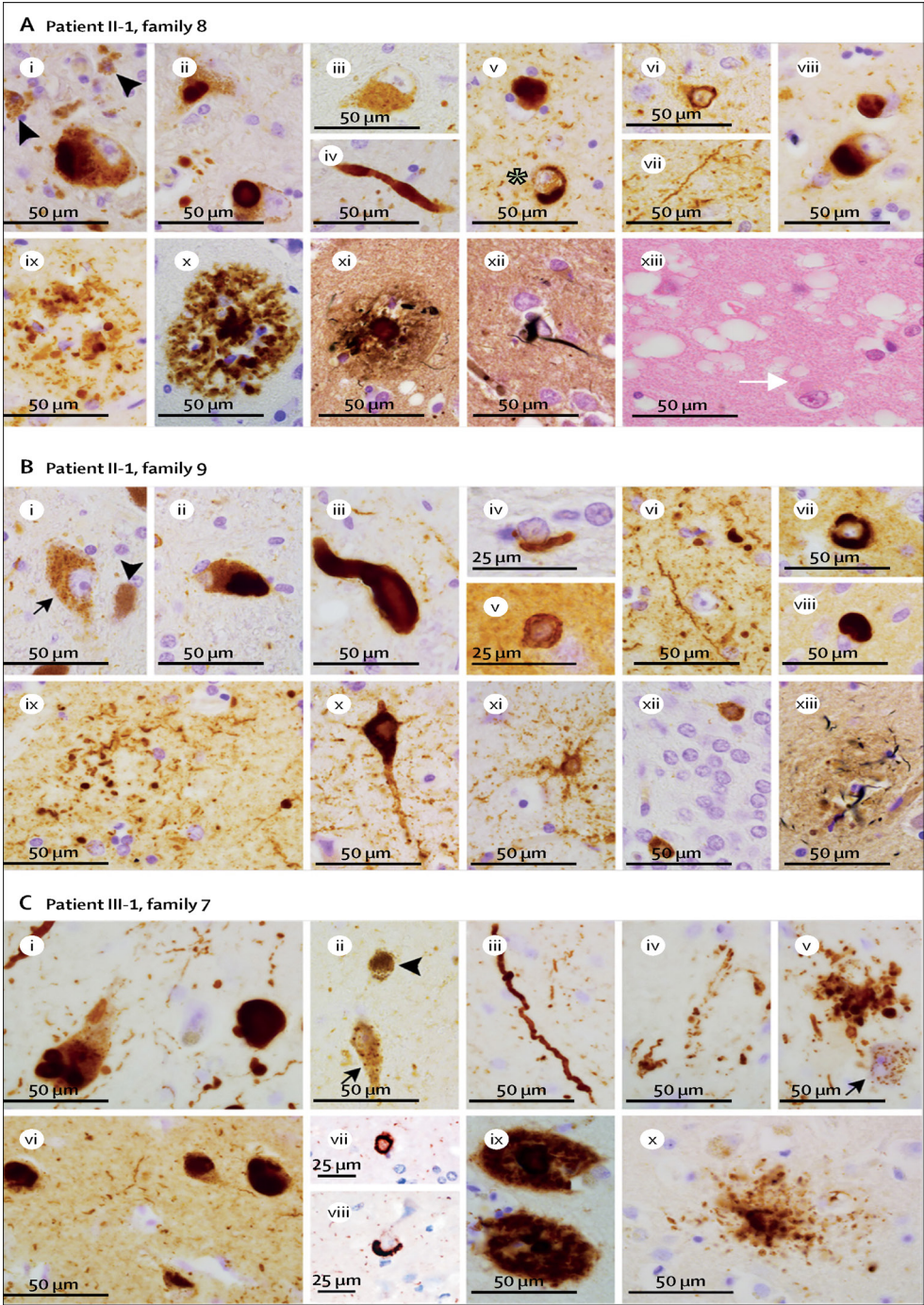
Whole exome sequencing data were obtained in the second stage of the study for 645 participants of a Dutch abdominal aortic aneurysm study, for use as a control (table). Only one carrier of an *LRP10* variant that fulfilled our criteria (451C>T [Arg151Cys]) was

identified, but the neurological status of this individual was not available. The frequency of *LRP10* variants in our probands of European ancestry (seven carriers in 608 probands [excluding 52 Brazilian and Taiwanese patients]) is significantly higher than that in the abdominal aortic aneurysms series (one carrier; two-sided Fisher's exact test,  $p=0.0306$ ; appendix).

Three variants identified in the second study stage (variants B, C, and D) underwent high-resolution melting analysis in an independent series of 1466 patients with Parkinson's disease who were unrelated to each other and to people in the previous study stages and 811 controls from centres in Portugal, Sardinia, and Taiwan (third study stage; table). Variant B (2095C>T [Pro699Ser]) was detected in two of 412 patients and none of 242 controls from Sardinia. Of these two probands, one had familial Parkinson's disease, and variant B was also found in one affected and two unaffected siblings (family 10; figure 2A); the other proband in whom variant B was found had sporadic Parkinson's disease (family 11; figure 2A). Variant C (1424+5delG) was found in one of 831 patients and none of 431 controls from Taiwan. This proband had familial Parkinson's disease, and variant C was also present in an affected sibling (family 12; figure 2A). Variant D (1598G>T [Arg533Leu]) was not detected in the case-control series from Portugal (223 patients and 138 controls).

### Figure 3. Brain pathology in three patients with *LRP10* variants

Brain tissue specimens are shown from (A) patient II-1 in family 8, (B) patient II-1 in family 9, and (C) patient III-1 in family 7. Specimens were stained with haematoxylin and eosin, Congo red, and Gallyas silver stain, and underwent immunohistochemical analysis. (Ai–ix, Bi–ix, Ci–viii) We used immunohistochemistry against  $\alpha$ -synuclein (clone KM51) to show  $\alpha$ -synuclein protein in brainstem, limbic, and neocortical regions in all three patients. We identified degenerating neuromelanin-containing neurons with loose neuromelanin in substantia nigra (arrowheads in Ai, Bi, Cii); brainstem-type Lewy bodies (Ai–ii, Bii, Ci); granular cytoplasmic staining (Aiii, and black arrows in Bi, Cii, and Cv); bulgy (Aiv, Biii, Ci, Ciii) and thin (Civ) Lewy neurites; globose (Av), crescent-shaped in Av (asterisk) and Cviii, and annular (Avi, Bvii, Cvii) inclusions in neurons; neuritic plaques (Bxii) and Lewy neurites (Avii, Bvi) in the amygdala; and Lewy bodies in neocortical regions (Aviii, Bviii, Cvi). We used immunohistochemistry against  $\alpha$ -synuclein (clone KM51) to show glial cytoplasmic inclusions in substantia nigra (Biv) and putamen (Bv); neuritic plaques in amygdala (Bxiii) and substantia nigra (Cv); and cored plaques in neocortex (Aix). We used Gallyas silver stain to show neuritic plaques in neocortex (Axi) and amygdala (Bxiii); and neurofibrillary tangles and threads in temporal regions (Axii, Bx). We used immunohistochemistry against amyloid- $\beta$  (clone 6f/3d) to show amyloid- $\beta$  cored plaques in neocortex (Ax, Cix), and immunohistochemistry against hyperphosphorylated tau (clone AT8) to show hyperphosphorylated tau in neurofibrillary tangles and threads in temporal regions (Bx), fuzzy astrocytes in entorhinal and temporal cortex (Bxi, and in patient III-1 in family 7 [data not shown]), ageing-related tau astroglialopathy and coiled bodies in the white matter next to the dentate gyrus (Bxii), and few neocortical neuritic plaques (Cx). We did haematoxylin and eosin staining to show Lewy bodies (white arrow Axiii) and spongiform changes in entorhinal cortex (Axiii). Images Aviii–xiii, Bviii, Bx–xi, Bxiii, Cvi, and Cix–x were taken in the middle temporal gyrus.





Analyses of genes known to cause Parkinson's disease (ie, *SNCA*, *LRRK2*, *VPS35*, and *CHCHD2*, and the risk gene *GBA*) in the 12 probands carrying *LRP10* variants A to I revealed no causative mutations by either Sanger sequencing or MLPA. Only one *GBA* risk variant (508C>T [Arg170Cys]; common nomenclature Arg131Cys) was present in the proband of family 11. The average age at symptom onset (Parkinson's disease, Parkinson's disease dementia, or dementia with Lewy bodies) of all 30 carriers of an *LRP10* variant (ten in family 1 and 20 in families 2–12) was 62.6 years (SD 9.2, range 46–75). Figure 2B shows the location of each of the variants A to I on the *LRP10* gene structure. Figure 2C shows the LRP10 protein structure and the position of the seven coding variants identified in our study (splicing variants C and F are not shown).

Macroscopic examination of brain tissue of three probands showed a pale substantia nigra and locus coeruleus, with only mild atrophy restricted to parietal regions (patient II-1 in family 8; figure 3A), an isolated small amygdala (patient II-1 in family 9; figure 3B), and moderate atrophy in the amygdala and hippocampus (patient III-1 in family 7; figure 3C). Microscopy showed severe loss of neuromelanin-containing neurons in the substantia nigra, and many Lewy bodies and Lewy neurites throughout the brain, compatible with the highest Braak  $\alpha$ -synuclein stage (stage 6; appendix). The dorsal motor nucleus of the vagal nerve, locus coeruleus, and substantia nigra showed classic brainstem-type Lewy bodies and Lewy neurites (figure 3). Moreover, crescent-shaped and annular  $\alpha$ -synuclein-immunoreactive neuronal inclusions were found in the CA3 region, particularly in the amygdala, similar to previous findings in patients with Parkinson's disease with pathogenic *SNCA* variants (23, 24). In patient II-1 from family 9 (figure 3B), many  $\alpha$ -synuclein-positive glial inclusions were present in the substantia nigra and putamen. Alzheimer's disease pathology (25) was of intermediate grade in brain tissue from patient II-1 in family 8 (figure 3A) and was mild in brain tissue from the other two patients.

The two splicing variants—1424+5delG (variant C) and 1424+5G>A (variant F) —were predicted to affect mRNA splicing by five in-silico tools (appendix). Thus, mRNA splicing was assessed in five patients from Taiwanese families carrying variant C (families 3 and 12) and the Dutch proband carrying variant F (family 6). *LRP10* cDNA amplification revealed an identical aberrant pattern in all patients carrying either variant C or F (appendix). Sequencing of the aberrant cDNA species revealed preferential usage of a different upstream splice donor site in exon 5 (position 517–518), resulting in incorporation of a much shorter aberrant exon 5, which missed 907 coding nucleotides

(518–1424 in RNA), and at protein level, a frameshift with premature truncation and removal of a large part of the LRP10 protein (Gly173Alafs\*34). Sanger sequencing of *LRP10* cDNA in the Dutch proband carrying variant I (632dupT [Ala212Serfs\*17]; patient II-1 in family 9) yielded only the wildtype transcript (appendix), suggesting nonsense-mediated mRNA decay. This finding was supported by reduced mRNA levels in brain tissue of this proband (patient II-1) compared with brain tissue from unaffected elderly controls and donors with idiopathic Parkinson's disease and dementia with Lewy bodies (appendix). mRNA expression and stability was normal in the Dutch proband carrying variant H (1549\_1551delAAT [Asn517del]; patient II-1 in family 8; appendix).

Functional studies showed that variants E (Tyr307Asn), A (Gly603Arg), G (Arg235Cys), and B (Pro699Ser) reduced LRP10 protein stability significantly compared with wildtype LRP10 (appendix). Variants H (Asn517del) and D (Arg533Leu) did not affect LRP10 protein stability but showed significantly increased surface labelling in cells overexpressing LRP10 (appendix), indicating that these variants affect LRP10 subcellular localisation. In 12-week-old human neuronal cultures, V5-tagged LRP10 localised to vesicular structures, including endosomes, the retromer complex, and the trans-Golgi network, in the neuronal soma and neurites (figure 4). Both in the cell soma and neurites, V5-tagged LRP10 strongly co-localised with the trans-Golgi network marker TGOLN2 (also known as) and GGA1. Furthermore, in the soma, V5-tagged LRP10 also partly co-localised with the early endosomal marker EEA1 and retromer marker VPS35.

## Discussion

During our study, we identified nine rare *LRP10* variants associated with familial Parkinson's disease, Parkinson's disease dementia, and dementia with Lewy bodies. Our findings provide initial evidence for a role of the LRP10 protein in the pathogenesis of neurodegenerative disorders with Lewy body pathology. By studying a large, multi-incident, Parkinson's disease kindred, we nominated *LRP10* as the candidate disease-causing gene. Subsequently, we found 11 probands who each carried one of eight potentially pathogenic variants of *LRP10*, and the same variants were detected in nine of ten affected relatives available for testing, providing independent—albeit limited—evidence of co-segregation with disease.

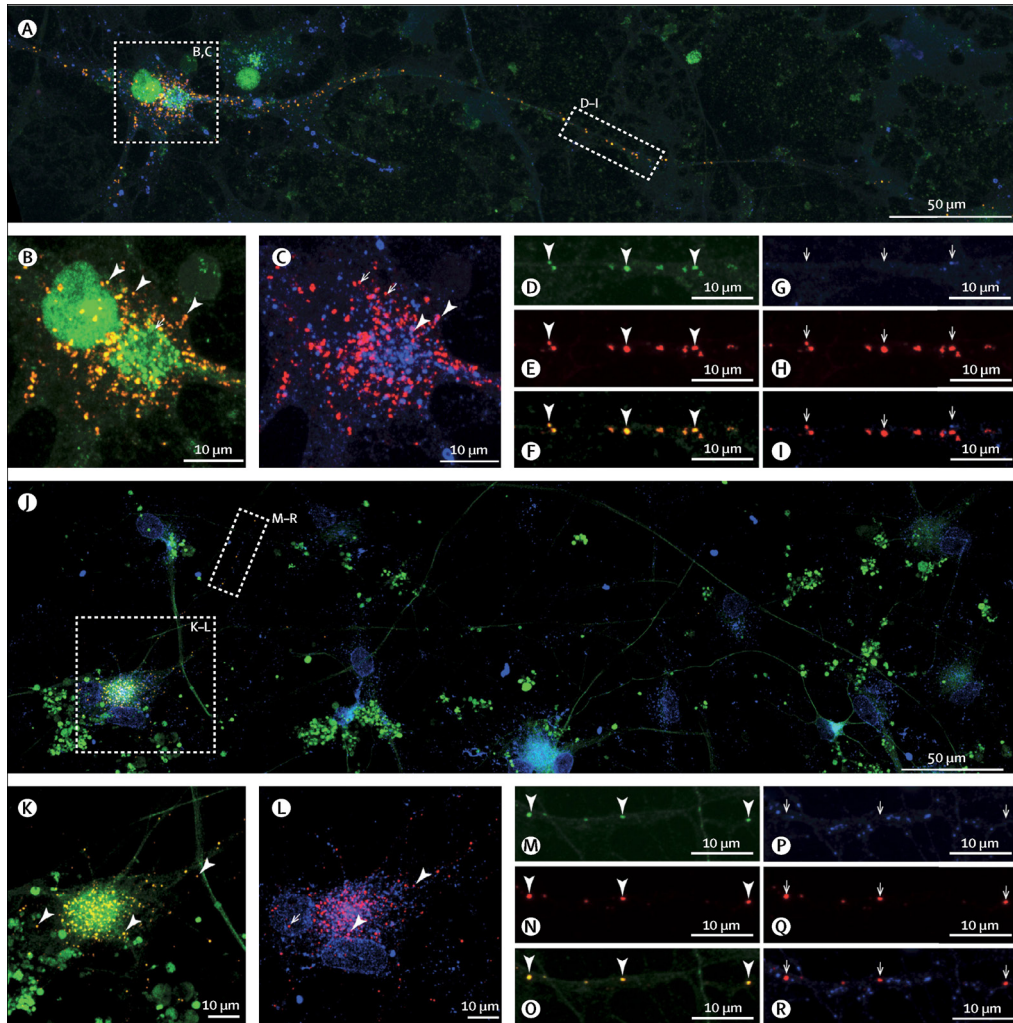


#### Figure 4. LRP10 expression studies in iPSC-derived neurons

Immunocytochemical analysis of 12-week-old induced neurons derived from iPSCs of a donor who did not have Parkinson's disease, Parkinson's disease dementia, or dementia with Lewy bodies. (A) V5-LRP10 transfected neuron, immune-labelled for the presence of V5-LRP10 (red), TGOLN2 (trans-Golgi network; green), and EEA1 (early endosomes; blue). White squares indicate enlarged regions shown in panels B–I. (B) V5-tagged LRP10 (red) co-localises with TGOLN2 (also known as TGN46; green) in the neuronal soma. (C) V5-tagged LRP10 (red) partly co-localises with EEA1 (blue) in the neuronal soma. Purple dots indicated by white arrowheads show co-localisation of LRP10 and EEA1. Red dots indicated by white arrows show lack of co-localisation of LRP10 and EEA1. (D) TGOLN2 (green), (E) V5-tagged LRP10 (red), and (F) merged image in the neurite. (G) EEA1 (blue), (H) V5-tagged LRP10 (red), and (I) merged image in the neurite. (J) V5-LRP10 transfected neurons, immune-labelled for the presence of V5-LRP10 (red), GGA1 (Golgi-associated trafficking proteins; green), and VPS35 (retromer-associated protein; blue). White squares indicate the enlarged regions shown in panels K–R. (K) V5-tagged LRP10 (red) co-localises with GGA1 (green) in the neuronal soma. (L) V5-tagged LRP10 (red) partly co-localises with VPS35 (blue) in the neuronal soma. (M) GGA1 (green), (N) V5-tagged LRP10 (red), and (O) merged image in the neurite. (P) VPS35 (blue), (Q) V5-tagged LRP10 (red), and (R) merged image in the neurite. White arrowheads indicate examples of co-localisation. White arrows indicate lack of co-localisation. iPSC=induced pluripotent stem cell.



A further observation is that the same guanine at position 1424+5 in *LRP10* intron 5 was the target of two different alterations (a deletion and a substitution), rare or absent in control databases, and detected in patients with Parkinson's disease or dementia with Lewy bodies from three families and two distant populations. These two variants result in an identical severe aberration at the level of mRNA splicing. Although small copy number variants within the linkage region and non-coding variants or repeat expansions could have been missed because whole genome sequencing was not done, altogether, our genetic data provide compelling evidence that implicate *LRP10* in the development of Parkinson's disease, Parkinson's disease dementia, and dementia with Lewy bodies.

The identification of *LRP10* variants in some unaffected family members suggests that the penetrance of at least some of these variants is age-related and perhaps incomplete. Three Gly603Arg carriers in family 1 were free from symptoms and clinical signs at age 58 years (III-14), 49 years (IV-3), and 45 years (IV-6), and four Pro699Ser carriers did not manifest disease symptoms or signs at age 87 years (III-2 in family 2), 76 years (III-5 in family 2), 70 years (II-3 in family 10), and 67 years (II-4 in family 10), suggesting a lower penetrance compared with the other *LRP10* variants. This notion would be in line with evidence of reduced penetrance for variants in *SNCA* (26), and particularly *LRRK2* (27). Follow-up studies of these and other *LRP10* families to be identified in the future might lead to accurate penetrance estimates. Furthermore, how *LRP10* variants relate to phenotypes varying from typical Parkinson's disease to Parkinson's disease dementia or dementia with Lewy bodies remains currently unknown. Other genetic or non-genetic modifiers are possibly implicated and further studies are warranted.

An abundance of  $\alpha$ -synuclein aggregation—in the form of brainstem and cortical Lewy bodies and Lewy neurites—was present in all three brains studied, which were from people who had different *LRP10* variants (Arg235Cys, Asn517del, and Ala212Serfs\*), suggesting important involvement of LRP10 in molecular cascades leading to  $\alpha$ -synucleinopathy. For most identified *LRP10* variants, we noted a striking effect at the level of transcript expression and transcript stability (1424+5delG, 1424+5G>A, Ala212Serfs\*17), protein stability (Gly603Arg, Tyr307Asn, Arg235Cys, Pro699Ser), or protein localisation (Arg533Leu, Asn517del), pointing towards loss of LRP10 protein function as a shared pathological mechanism.

Although very little is known about LRP10 protein function, previous studies have shown that LRP10 shuttles between the trans-Golgi network, endosomes, and plasma membrane (28-31). This finding accords with our observation that, in iPSC-derived neurons, LRP10 is localised to vesicular structures associated closely with proteins

implicated in trafficking between the trans-Golgi network and endosomes, including VPS35 and GGA1. VPS35, which is associated with autosomal-dominant Parkinson's disease (32, 33), regulates LRP10 subcellular localisation (34) and affects  $\alpha$ -synuclein aggregation (35, 36). Furthermore, GGA proteins interact with LRP10 (28, 30) and affect  $\alpha$ -synuclein oligomerisation and secretion and ameliorate its toxicity (37, 38). Collectively, these reports and our findings suggest intriguing links between VPS35, GGA proteins, and LRP10 in regulating  $\alpha$ -synuclein aggregation, intracellular trafficking, and cell-to-cell transmission (39).

Our study has some limitations. First, we did not have a second pedigree large enough to yield confirmation of linkage. Second, we enrolled fewer controls from Portugal and Sardinia compared with the number enrolled from Taiwan. Finally, our LRP10 functional studies were based on overexpression and they might not model accurately the behaviour of this protein at physiological expression levels. Despite these limitations, we provide strong evidence for involvement of *LRP10* in the development of inherited forms of Lewy body diseases. Future elucidation of the normal function of LRP10 protein and its signalling pathways might offer crucial insights into the molecular mechanisms of inherited, and perhaps sporadic,  $\alpha$ -synucleinopathies, pointing to novel biomarkers and therapeutic targets.

## Contributors

MQ designed, undertook, and supervised genetic experiments. WM designed, undertook, and supervised functional experiments. MMG, RM, MMi, ACM, and TZ designed and undertook functional experiments. GJB, DK, EY-D, ES, ABDF, CC, SO, and AMTI designed and undertook genetic experiments. HG and WDJvdB selected Parkinson's disease and dementia with Lewy body donors from the Netherlands Brain Bank cohort for genetic screening. HG, AJR, PP, and WDJvdB assessed neuropathology in brains with *LRP10* pathogenic variants. EF, LJMv, H-CC, MMe, LCG, CC, AT, GCB, JPR, SC, MS, HFC, NV, Y-HW-C, T-HY, AJWB, SEH, MO, PB, DJN, AP, MDM, AJK, EB, GDM, DM-K, JcVs, FjDj, JJF, GC, C-SL, GM, and PC undertook clinical and genealogical studies and provided clinical data and biological specimens from patients. WFJvI undertook whole exome sequencing. RWWB, DH, and ASI undertook variant calling and bioinformatic analyses on whole exome sequencing data. MG generated, characterised, and provided the induced pluripotent stem cell control line. HG, PP, and WDJvdB wrote sections on clinical and pathological information of the brain donors with *LRP10* pathogenic variants and produced figure 3. MQ and WM analysed and interpreted data and wrote the initial draft of the report. VB

provided overall study direction, supervision, and revised the manuscript. All authors critically reviewed the report and approved the final version.

## Declaration of interests

WM reports grants from Stichting Parkinson Fonds and Erasmus Medical Center, during the conduct of the study. GCB reports other financial support from UCB Pharma, Zambon Italia, and Abbvie, outside the submitted work. SO reports compensation from Cergentis BV and Bluebee BV, outside the submitted work. JJF reports grants from GlaxoSmithKline, Grunenthal, Fundação MSD (Portugal), TEVA, MSD, Allergan, Novartis, and Medtronic; personal fees from Faculdade de Medicina de Lisboa, CNS (Campus Neurológico Sénior), and Centro Hospitalar Lisboa Norte; and other financial support from Novartis, GlaxoSmithKline, TEVA, Lundbeck, Solvay, BIAL, Merck-Serono, Merz, Ipsen, Biogen, Acadia, Allergan, Abbvie, Sunovion, and Medtronic, outside the submitted work. PC reports other financial support from Allergan Italia, Chiesi Farmaceutici, Eli-Lilly, Novartis, Teva, UCB Pharma, and Zambon, outside the submitted work. WDJvdB reports grants and non-financial support from Roche Pharma (Basel); personal fees from UCB Pharma (Belgium); other financial support from Centre for Human Drug Research (CHDR; Netherlands); and grants from Lysosomal Therapeutics (USA), ZonMW Memorabel, Stichting Parkinson Fonds, and Alzheimer Netherlands–Ligue Européenne Contre la Maladie d'Alzheimer (LECMA), outside the submitted work. VB declares personal fees from the International Parkinson and Movement Disorder Society and from the Sun Pharmaceutical Laboratories (India) for lecturing honoraria, outside the submitted work. All other authors declare no competing interests.

## Acknowledgments

We thank all participants for their contribution, and the Netherlands Brain Bank (Netherlands Institute for Neuroscience, Amsterdam) for providing tissue and data. This work was supported by research grants (to VB and WM) from Stichting Parkinson Fonds (Netherlands), Dorpmans-Wigmans Stichting (Netherlands), Erasmus Medical Center (MRace promotie grant), and Nederlandse organisatie voor gezondheidsonderzoek en zorginnovatie (ZonMw)–Memorabel programme (grant 733051065, under the aegis of the EU Joint Programme—Neurodegenerative Disease Research [JPND]). VB acknowledges financial support to his research from the Centre for Human Drug Research (CHDR; Netherlands). DJN acknowledges financial support from Parkinson's

UK. AP acknowledges financial support from Avtal om Läkarutbildning och Forskning (ALF) and Parkinsonfonden (Sweden). DM-K acknowledges financial support from the Lijf and Leven Foundation. WDJvdB acknowledges financial support from Stichting Parkinson Fonds (Netherlands), ZonMw-Memorabel, and cross-border grant of Alzheimer Netherlands–Ligue Européenne Contre la Maladie d’Alzheimer (LECMA).

## References

- Obeso JA, Stamelou M, Goetz CG, et al. Past, present, and future of Parkinson’s disease: a special essay on the 200th anniversary of the shaking palsy. *Mov Disord* 2017; 32: 1264–310.
- Hely MA, Reid WG, Adena MA, Halliday GM, Morris JG. The Sydney multicenter study of Parkinson’s disease: the inevitability of dementia at 20 years. *Mov Disord* 2008; 23: 837–44.
- McKeith IG, Dickson DW, Lowe J, et al. Diagnosis and management of dementia with Lewy bodies: third report of the DLB Consortium. *Neurology* 2005; 65: 1863–72.
- McKeith IG, Boeve BF, Dickson DW, et al. Diagnosis and management of dementia with Lewy bodies: fourth consensus report of the DLB Consortium. *Neurology* 2017; 89: 88–100.
- Hogan DB, Fiest KM, Roberts JL, et al. The prevalence and incidence of dementia with Lewy bodies: a systematic review. *Can J Neurol Sci* 2016; 43 (suppl 1): S83–95.
- Walker Z, Possin KL, Boeve BF, Aarsland D. Lewy body dementias. *Lancet* 2015; 386: 1683–97.
- Polymeropoulos MH, Lavedan C, Leroy E, et al. Mutation in the alpha-synuclein gene identified in families with Parkinson’s disease. *Science* 1997; 276: 2045–47.
- Singleton AB, Farrer MJ, Bonifati V. The genetics of Parkinson’s disease: progress and therapeutic implications. *Mov Disord* 2013; 28: 14–23.
- Zimprich A, Biskup S, Leitner P, et al. Mutations in LRRK2 cause autosomal-dominant parkinsonism with pleomorphic pathology. *Neuron* 2004; 44: 601–07.
- Paisan-Ruiz C, Jain S, Evans EW, et al. Cloning of the gene containing mutations that cause PARK8-linked Parkinson’s disease. *Neuron* 2004; 44: 595–600.
- Sidransky E, Nalls MA, Aasly JO, et al. Multicenter analysis of glucocerebrosidase mutations in Parkinson’s disease. *N Engl J Med* 2009; 361: 1651–61.
- Nalls MA, Duran R, Lopez G, et al. A multicenter study of glucocerebrosidase mutations in dementia with Lewy bodies. *JAMA Neurol* 2013; 70: 727–35.
- Chang D, Nalls MA, Hallgrimsdottir IB, et al. A meta-analysis of genome-wide association studies identifies 17 new Parkinson’s disease risk loci. *Nat Genet* 2017; 49: 1511–16.
- Goedert M, Spillantini MG, Del Tredici K, Braak H. 100 years of Lewy pathology. *Nat Rev Neurol* 2013; 9: 13–24.
- Langston JW, Schule B, Rees L, Nichols RJ, Barlow C. Multisystem Lewy body disease and the other parkinsonian disorders. *Nat Genet* 2015; 47: 1378–84.
- Friedman JH. Dementia with Lewy bodies and Parkinson disease dementia: it is the same disease! *Parkinsonism Relat Disord* 2018; 46 (suppl 1): S6–9.
- Hughes AJ, Daniel SE, Kilford L, Lees AJ. Accuracy of clinical diagnosis of idiopathic Parkinson’s disease: a clinicopathological study of 100 cases. *J Neurol Neurosurg Psychiatry* 1992; 55: 181–84.
- Wang K, Li M, Hakonarson H. ANNOVAR: functional annotation of genetic variants from high-throughput sequencing data. *Nucleic Acids Res* 2010; 38: e164.
- Jagadeesh KA, Wenger AM, Berger MJ, et al. M-CAP eliminates a majority of variants of uncertain significance in clinical exomes at high sensitivity. *Nat Genet* 2016; 48: 1581–86.
- Vanhauwaert R, Kuenen S, Masius R, et al. The SAC1 domain in synaptotagmin is required for autophagosome maturation at presynaptic terminals. *EMBO J* 2017; 36: 1392–411.
- Reinhardt P, Glatza M, Hemmer K, et al. Derivation and expansion using only small molecules of human neural progenitors for neurodegenerative disease modeling. *PLoS One* 2013; 8: e59252.
- Abecasis GR, Cherny SS, Cookson WO, Cardon LR. Merlin: rapid analysis of dense genetic maps using sparse gene flow trees. *Nat Genet* 2002; 30: 97–101.
- Pasanen P, Myllykangas L, Siitonen M, et al. Novel alpha-synuclein mutation A53E associated with atypical multiple system atrophy and Parkinson’s disease-type pathology. *Neurobiol Aging* 2014; 35: 2180.
- Kiely AP, Ling H, Asi YT, et al. Distinct clinical and neuropathological features of G51D SNCA mutation cases compared with SNCA duplication and H50Q mutation. *Mol Neurodegener* 2015; 10: 41.
- Montine TJ, Phelps CH, Beach TG, et al. National Institute on Aging–Alzheimer’s Association guidelines for the neuropathologic assessment of Alzheimer’s disease: a practical approach. *Acta Neuropathol* 2012; 123: 1–11.
- Papadimitriou D, Antonelou R, Miligkos M, et al. Motor and nonmotor features of carriers of the p.A53T alpha-synuclein mutation: a longitudinal study. *Mov Disord* 2016; 31: 1226–30.
- Goldwurm S, Tunesi S, Tesi S, et al. Kin-cohort analysis of LRRK2-G2019S penetrance in Parkinson’s disease. *Mov Disord* 2011; 26: 2144–45.
- Brodeur J, Larkin H, Boucher R, et al. Calnuc binds to LRP9 and affects its endosomal sorting. *Traffic* 2009; 10: 1098–114.
- Brodeur J, Theriault C, Lessard-Beaudoin M, Marcil A, Dahan S, Lavoie C. LDLR-related protein 10 (LRP10) regulates amyloid precursor protein (APP) trafficking and processing: evidence for a role in Alzheimer’s disease. *Mol Neurodegener* 2012; 7: 31.

30. Boucher R, Larkin H, Brodeur J, Gagnon H, Theriault C, Lavoie C. Intracellular trafficking of LRP9 is dependent on two acidic cluster/dileucine motifs. *Histochem Cell Biol* 2008; 130: 315–27.
31. Doray B, Knisely JM, Wartman L, Bu G, Kornfeld S. Identification of acidic dileucine signals in LRP9 that interact with both GGAs and AP-1/AP-2. *Traffic* 2008; 9: 1551–62.
32. Zimprich A, Benet-Pages A, Struhal W, et al. A mutation in VPS35, encoding a subunit of the retromer complex, causes late-onset Parkinson disease. *Am J Hum Genet* 2011; 89: 168–75.
33. Vilarino-Guell C, Wider C, Ross OA, et al. VPS35 mutations in Parkinson disease. *Am J Hum Genet* 2011; 89: 162–67.
34. Steinberg F, Gallon M, Winfield M, et al. A global analysis of SNX27-retromer assembly and cargo specificity reveals a function in glucose and metal ion transport. *Nat Cell Biol* 2013; 15: 461–71.
35. Follett J, Norwood SJ, Hamilton NA, et al. The Vps35 D620N mutation linked to Parkinson's disease disrupts the cargo sorting function of retromer. *Traffic* 2014; 15: 230–44.
36. Tang FL, Erion JR, Tian Y, et al. VPS35 in dopamine neurons is required for endosome-to-Golgi retrieval of Lamp2a, a receptor of chaperone-mediated autophagy that is critical for alpha-synuclein degradation and prevention of pathogenesis of Parkinson's disease. *J Neurosci* 2015; 35: 10613–28.
37. von Einem B, Eschbach J, Kiechle M, et al. The Golgi-localized, gamma ear-containing, ARF-binding (GGA) protein family alters alpha synuclein (alpha-syn) oligomerization and secretion. *Aging (Albany NY)* 2017; 9: 1677–97.
38. Chen YC, Farzadfard F, Gharaei N, Chen WCW, Cao J, Lu TK. Randomized CRISPR-Cas transcriptional perturbation screening reveals protective genes against alpha-synuclein toxicity. *Mol Cell* 2017; 68: 247–57.
39. Lee HJ, Bae EJ, Lee SJ. Extracellular alpha-synuclein—a novel and crucial factor in Lewy body diseases. *Nat Rev Neurol* 2014; 10: 92–98.

## Supplementary Information

### Participating subjects

The patients and controls were examined and enrolled in several neurological centers (Appendix). Study protocols were approved by the relevant Ethical Authorities of the Erasmus MC, Rotterdam, the Netherlands (NL38860.078.11, NL53037.078.15); the VU University Medical Center, Amsterdam, the Netherlands (NL25907.029.08); the Chang Gung Memorial Hospital, Taoyuan, Taiwan; the Brotzu General Hospital, Cagliari, Italy; the Instituto de Medicina Molecular, Faculty of Medicine, University of Lisbon, Portugal; the University of São Paulo, São Paulo, Brazil; and the regional ethical review board in Lund, Sweden. All subjects enrolled into the genetic studies, patients and controls, provided written informed consent.

Human brain tissue from Patient II-1, Family 8, and Patient II-1, Family 9, was obtained from the Netherlands Brain Bank (NBB; [www.brainbank.nl](http://www.brainbank.nl)), Netherlands Institute for Neuroscience, Amsterdam. Brain tissue from Patient III-1, Family 7, was obtained from the Laboratory of Neuropathology, University of Bologna (LNUB). In both centres, written informed consent for brain autopsy and the use of the material and clinical information for research purposes had been obtained from the donor or from the next of kin.

A series of 645 Dutch subjects with abdominal aortic aneurysms (AAA study) enrolled in a research project within the Department of Clinical Genetics (Erasmus MC, Rotterdam,

the Netherlands) approved by the relevant Ethical Authorities of the Erasmus MC, Rotterdam, the Netherlands (MEC-2010-078) were used as controls in Stage II of this study. These subjects were not systematically evaluated for signs of Parkinson's disease or dementia.

## SNP array data and linkage analysis

The Gentra Puregene Kit (Qiagen, Hilden, Germany) was used for isolation and purification of high-molecular weight genomic DNA from blood and brain specimens.

DNA samples from 10 affected members of Family 1 underwent genome-wide SNP array genotyping with HumanCNV370 bead chip (356,075 markers; Illumina, San Diego, CA, USA). Analysis of copy number variants on the chr14q locus was performed using Nexus Copy Number, Discovery Edition, v.8 (BioDiscovery, El Segundo, CA, USA).

## Whole exome sequencing

In patient IV-2 of Family 1, whole exome sequencing (WES) was performed using in-solution capturing (Illumina TruSeq kit), and an Illumina HiSeq2000 sequencer with 100 paired-end sequencing. The average coverage was >90X with 85% of the target regions covered >20X. Reads were aligned to the human reference genome build 19 (hg19) using Burrows-Wheeler-Aligner (BWA-MEM) (1). Variant calling was done with GATK v3 (Genome-Analysis-Tool-Kit) (2).

In Family 7, WES was performed using the Agilent Technologies (Santa Clara, CA, USA) SureSelect clinical relevant exons (CRE) capture kit, and an Illumina HiSeq2500 sequencer with paired-ends 101bp + 9bp index (III-1, III-4, and IV-1), or an Illumina HiSeq4000 sequencer with paired-ends 150bp + 9bp index (Patient III-2). The average coverage was >90X, with 97% of the target regions covered more than 20X. The reads were aligned against the human reference genome build 19 (hg19) using BWA-MEM (1). Subsequently, genetic variants were called using GATK v3 (2).

Variants were filtered using Cartagenia Bench Lab NGS v.5.0.1 (Agilent Technologies). Within the genomic linkage region located on chromosome 14q variants were reported if they were i) heterozygous, ii) had a minor allele frequency (MAF) less than 0.1% in dbSNP, Exome Variant Server NHLBI GO Exome Sequencing Project (ESP), 1000 Genomes (<http://www.internationalgenome.org/1000-genomes-browsers>), Genome of

the Netherlands (GoNL), Exome Aggregation Consortium (ExAC), Genome aggregation database (GnomAD) iii) were exonic non-synonymous, iv) were within 5bp from a splice site. The splicing effect was evaluated *in silico* according to 5 splicing prediction programs (SpliceSiteFinder-like, MaxEntScan, NNSPLICE, GeneSplicer, and Human Splicing Finder) integrated in Alamut Visual version 4.2 (Interactive Biosoftware, Rouen, France). Variants were annotated using Annovar (3), and Mendelian clinically applicable pathogenicity score (M-CAP). The expression of genes harboring candidate variants according the afore-mentioned criteria was investigated using multiple datasets accessible in GeneCards® Human gene Database (<http://www.genecards.org/>) and in Unigene catalog (<https://www.ncbi.nlm.nih.gov/unigene>).

In the AAA study, WES was performed at Erasmus MC (Biomics), using an Illumina HiSeq2500 or HiSeq4000 sequencer. Of these samples, 464 were enriched using Agilent's HaloPlex Target Enrichment System. The other 181 samples were enriched for clinically relevant exons using the Agilent Technologies SureSelect Clinical Research Exome (CRE) capture kit. Reads were aligned to the reference genome (hg19) using BWA, and variants were called using the GATK software. Annotation was done using Annovar (3).

The average whole exome coverage was >90 times, with 90% of the target regions covered more than 20 times. The average coverage of the *LRP10* gene (coding exons, and intronic regions including 5 bp flanking the splicing sites) was 100.7 times, of which 99% was covered more than 10 times. Variants were followed up if they had a MAF less than 0.1% in ExAC, dbSNP, ESP, 1000 Genomes, GoNL, and GnomAD; if they were exonic non-synonymous, within 5 bp from a splice site, and if they were predicted to be pathogenic with  $\geq 5$  *in silico* tools.

Using these criteria, only a single carrier of a *LRP10* variant was identified among the entire group of 645 controls (1290 alleles). However, for our statistical analyses, a smaller number of alleles (n=1248) were considered, as a result of the following procedure: 553 subjects were unrelated probands in the AAA study, contributing therefore 1106 independent *LRP10* alleles to our analysis; 50 subjects were close relatives of probands; our direct, systematic inspection of their WES data at the *LRP10* locus revealed that they did not share any of their 2 haplotypes with their relative included in the 553 probands; therefore, these 50 relatives contribute another 100 independent alleles to our analysis; 42 subjects were close relatives of other probands, and our inspection of their WES data at the *LRP10* locus revealed that they shared only one haplotype with their relative included in the 553 probands; therefore, these 42 relatives contribute another 42 independent alleles to our analysis.

## Sequence analysis on genomic DNA

Primers for the PCR amplification of *LRP10* (all exons), *LRRK2* (exons 29-48, coding for the functional LRRK2 protein domains, where the PD-causing mutations are located), *SNCA* (all exons), *CHCHD2* (all exons), *GBA* (all exons), and *VPS35* (fragment where the p.Asp620Asn pathogenic variant is located) are in the Supplementary Table 6 and Supplementary Table 9.

Amplification reactions were performed in a total volume of 20 µl, containing 1X FastStart Taq DNA Polymerase buffer, 200 µM of each dNTP, 0.5 µM of forward primer, 0.5 µM of reverse primer, 0.5 units of FastStart Taq DNA Polymerase (Roche, Basel, Switzerland), and 40 ng of genomic DNA. Exon 1 was amplified with the addition of 1X GC-RICH solution (Roche).

PCR conditions: 5 minutes 94 °C initial denaturation followed by 30 cycles of 30 seconds at 94 °C; 30 seconds at 60 °C; 90 seconds at 72 °C, with a final extension for 5 minutes at 72 °C. PCR reactions (4 µl) were cleaned-up from unconsumed dNTPs and primers using 5 units of ExoI and 0.5 unit of Fast AP (Thermo Fisher Scientific, Waltham, MA, USA), 45 minutes at 37 °C, 15 minutes at 80 °C. Direct Sanger Sequencing was performed using Big Dye Terminator chemistry (version 3.1; Thermo Fisher Scientific) as recommended by the manufacturer. Dye terminators were removed using SephadexG50 (GE Healthcare, Little Chalfont, UK) and loaded on an ABI 3730XL Genetic Analyzer (Thermo Fisher Scientific). Generated sequences were analyzed using the software packages Seqscape v3.0 (Thermo Fisher Scientific) and Sequencing Analysis v6.0 (Thermo Fisher Scientific).

*LRP10* NM\_014045.4, *LRRK2* NM\_198578.3, *SNCA* NM\_000345.3, *CHCHD2* NM\_016139.3, *GBA* NM\_000157.3, and *VPS35* NM\_018206 NCBI reference sequences were adopted for sequence variants annotation, and human genome variome society (HGVS) recommendations (4) were followed for variants nomenclature.

Multiple ligation probe amplification assay (MLPA, kit P051, MRC Holland, the Netherlands) was used to screen for copy number variants in the *SNCA* gene.

High-resolution melting (HRM) analysis was adopted for studying *LRP10* c.2095C>T (p.Pro699Ser) variant in an additional series of patients and controls from Sardinia; *LRP10* c.1424+5delG variant in an independent series from Taiwan; and *LRP10* c.1598G>T (p.Arg533Leu) variant in an independent series from Portugal. In each experiment, positive and negative controls were included. The reaction was performed in a total volume of 11 µl, containing 5 µl SsoFast™ EvaGreen® supermix (Bio-Rad, Hercules,



CA, USA), 2  $\mu$ M primer forward and primer reverse, and 25 ng of genomic DNA. HRM condition: 3 minutes 98°C initial denaturation followed by 39 cycles of 5 seconds at 98°C; and 10 seconds at 58°C. The melting curve was set between 70°C and 95°C. Carriers of variants identified during these experiments were confirmed by Sanger sequencing using the above-mentioned protocols. *LRP10* variants that did not pass our filtering criteria mentioned above are reported in Supplementary Table 7.

## RNA isolation, cDNA preparation, and full length cDNA amplification

The RNeasy procedure (RNeasy Mini Kit, Qiagen) was used to isolate and purify total RNA from different tissues as recommended by the manufacturer.

cDNA synthesis was performed in the first step using total RNA (0.5  $\mu$ g) primed with random primers using the SuperScript® III First-Strand Synthesis System for RT-PCR (Thermo Fisher Scientific), followed by a RNase H digestion to remove the RNA template from the cDNA:RNA hybrid molecule.

In the second step, full length cDNA *LRP10* NM\_014045.4 fragments were amplified in a total volume of 20  $\mu$ l, containing 1X GC Buffer II (5 mM Mg<sup>2+</sup> plus), 400  $\mu$ M of each dNTP, 0.5  $\mu$ M of forward primer, 0.5  $\mu$ M of reverse primer, 1 unit TaKaRa LA Taq (TAKARA Bio Inc., Kusatsu, Shiga, Japan) and 1  $\mu$ l cDNA template. PCR conditions: 1 minute 94°C initial denaturation followed by 30 cycles of 30 seconds at 94°C; 30 seconds at 60°C; 2 minutes at 72°C, with a final extension for 5 minutes at 72°C. Fragments were analyzed on a 1.2% agarose gel, and sized using a 1 Kb Plus DNA Ladder (Thermo Fisher Scientific).

## LRP10 quantitative expression analysis in the brain

A real-time quantitative PCR (qPCR) experiment was set up including *LRP10* and three house-keeping genes (HKG) for the normalization (*POLR2A*, *RPL27* and *EIF4G2*), in order to determine the expression levels among 11 elderly non-demented controls of European ancestry (mean age at death: 80.9, SD  $\pm$ 8.3), 18 donors with idiopathic PD, PDD, and DLB of European ancestry (mean age at onset 71.4, SD  $\pm$ 9.0; mean age at death 82.2, SD  $\pm$ 4.7), and two cases carrying *LRP10* pathogenic variants (Patient II-1 Family 8, and Patient II-1 Family 9).

Medial temporal gyrus (GTM) total RNAs (1µg) from the above-mentioned donors were reverse transcribed using SuperScript™ II reverse transcriptase (Thermo Fisher Scientific). TaqMan (Thermo Fisher Scientific) assays spanning genomic intron-exon junctions were designed and, if possible, located at 3' gene sequence. The following primers were purchased from Eurogentec S.A. (Liege, Belgium), and suitable probes were selected from the Human Universal Probe Library (Roche Applied Science, Penzberg, Germany). Primer sequences: *LRP10* fwd, CAG CAA GGA ACA GAC TGT CAC; *LRP10* rev, GTG CCT CAC ACA GGG AGA T; *POLR2A* fwd, CGC ATC ATG AAC AGC GAT GAG; *POLR2A* rev, GCA GGG TCA TAT CTG TCA GCA T; *EIF4G2* fwd, GCA AGG CTT TGT TCC AGG T; *EIF4G2* rev, TTG GCT GGT TCT TTA GTC AG; *RPL27* fwd, CAA TCA CCT AAT GCC CAC AAG; *RPL27* rev, CTT CAA ACT TGA CCT TGG CC. TaqMan assay conditions: *LRP10*, 95 °C for 15 seconds initial denaturation, followed by 40 cycles of 95 °C for 15 seconds, 58 °C for 30 seconds and 65 °C for 30 seconds; *POLR2A*, 95 °C for 15 seconds initial denaturation, followed by 40 cycles of 95 °C for 15 seconds, 59 °C for 30 seconds and 65 °C for 40 seconds; *EIF4G2*, 95 °C for 15 seconds initial denaturation, followed by 40 cycles of 95 °C for 15 seconds, 57 °C for 35 seconds and 65 °C for 30 seconds; *RPL27*, 95 °C for 15 seconds initial denaturation, followed by 40 cycles of 95 °C for 15 seconds, 60 °C for 35 seconds and 65 °C for 30 seconds.

All PCR reactions were prepared with TaqMan Fast Universal PCR Master Mix (Thermo Fisher Scientific) and performed using a StepOne Plus Real-Time PCR instrument (Thermo Fisher Scientific). Standard curves were generated for each assay run. The reaction volume per well was 20 µl (cDNA was 50 ng). All samples were run in triplicate; a negative control generated without the reverse transcriptase enzyme was included for each assay. Per each gene, three plates were run, and threshold values were kept the same. The relative expression ratio of each target gene was calculated using the efficiency-corrected delta-delta C<sub>q</sub> method (5). The normalization was made using the geometric mean of the three HKGs.

## Neuropathological characterization

Human brain tissue from Patient II-1 Family 8 and Patient II-1 Family 9 was obtained from The Netherlands Brain Bank (NBB), Netherlands Institute for Neuroscience, Amsterdam. Patient III-1 Family 7 was obtained from the brain tissue collection at the Laboratory of Neuropathology, University of Bologna (LNUB). In both collections, written informed consent for a brain autopsy and use of the material, and clinical information for research purposes had been obtained from the donor or next of kin.

At autopsy, tissue blocks of the three cases were obtained from 23 different regions including frontal, occipital, cingulate, parietal, temporal, pre- and postcentral cortex, hippocampus, amygdala, substantia nigra, pons, medulla oblongata, cervical cord (not available for Patient III-1 Family 7), caudate, putamen, globus pallidus, insular and olfactory cortex, subthalamus and thalamus, cerebellum and meninges. In addition, tissue blocks from basal forebrain and hypothalamus were available from Patient III-1 Family 7 donor.

Tissue was fixed in formalin, embedded in paraffin and cut into 8  $\mu$ m sections. Staining of selected regions was performed using hematoxylin and eosin, Congo red, Gallyas silver stain, and immunohistochemistry against  $\alpha$ -synuclein (clone KM51, 1:500, Monosan, Uden, the Netherlands), amyloid-beta (clone 6f/3d, 1:100, , Agilent Technologies, and clone 4G8, 1:5,000, BioLegend, San Diego, CA, USA) and hyperphosphorylated tau (clone AT8, 1:100, Fujirebio Europe N.V., Ghent, Belgium). For pathological staging of  $\alpha$ -synuclein, amyloid-beta, neurofibrillary and neuritic plaque pathology, diagnostic criteria were used according to the BrainNet Europe (6, 7) and the National Institute on Aging-Alzheimer's Association guidelines (8-10). Transmission light microscopy images were taken using a Leica DM500 microscope (Leica Microsystems, Wetzlar, Germany) with a 63x oil lens (HC PL-APO, numerical aperture 1.40) and Leica Application Suite version 44 software (Leica Microsystems).

## Cycloheximide chase experiments

HEK293 cell lines were expanded in growth medium (DMEM, BE12-604F/U1, Lonza, Basel Switzerland, 10% FCS,), and plated on 6-well culture plates in growth medium. At 80% confluency, cells were transfected with Cterminal V5-tagged LRP10 wildtype and variant expression constructs using Genejuice® transfection reagent (Merck, Darmstadt, Germany) according to manufactures' specifications and incubated at 37°C/5% CO<sub>2</sub>. After 48 hrs, Cycloheximide (C7698-1G, Merck) was added to each well at 40 $\mu$ g/ml (final concentration), and cells were incubated at 37°C/5% CO<sub>2</sub> for indicated time points. After treatment, cells were washed with PBS, and further processed for Western blotting analysis.

## Western blot analysis

HEK293 cells were lysed in RIPA lysis buffer (150 mM NaCl, 1.0% IGEPAL® CA-630, 0.5% sodium deoxycholate, 0.1% SDS, and 50 mM Tris, pH 8.0) containing protease inhibitor

Complete® (Merck). Lysates were cleared by centrifugation at 10,000 g for 10 min at 4°C. Protein concentrations were determined via Pierce™ BCA Protein Assay Kit (Thermo Fisher scientific). For Western blotting, proteins were separated on 4-15% Criterion TGX precast gels (Bio-Rad), and transferred to nitrocellulose using the Trans-Blot® Turbo™ Transfer System (Bio-Rad). Blots were blocked using 5% blotting grade blocker nonfat milk (Bio-Rad) in PBS, 0.1% v/v TWEEN® 20 (Merck) for 30 minutes at room temperature. Primary antibody incubations were performed overnight at 4°C. Primary antibodies used: anti-V5-Tag (D3H8Q) rabbit monoclonal antibody (Cell Signaling Technologies, Danvers, MA, USA, 13202s, 1:2000 dilution); anti-Vinculin mouse monoclonal antibody (V284) (Santa Cruz Biotechnology, Dallas TX, USA, 1:2000 dilution). After washing in PBS, 0.1% v/v TWEEN® 20, Blots were incubated for 1 hour at room temperature with fluorescently conjugated Goat antimouse (IRDye 800) and goat anti-rabbit (IRDye 680) secondary antibodies (LI-COR Biosciences, Lincoln, NE, USA). After washing in PBS, 0.1% v/v TWEEN® 20, the blots were imaged and analyzed using an Odyssey Imaging system (LI-COR Biosciences).

## Cell-surface labeling of live cells

HEK293 cell lines were expanded in growth medium (DMEM, BE12-604F/U1, Lonza, 10% FCS), and plated on glass coverslips placed in 12-well culture plates in growth medium. At 80% confluency, cells were transfected in duplicate with N-terminal V5-tagged LRP10 wildtype and variant expression constructs using Genejuice® transfection reagent (Merck) according to manufactures' specifications and incubated at 37°C/5% CO<sub>2</sub>. After 48 hrs, one set of the coverslip with transfected cells was used for cell-surface labelling (surface LRP10) and the other set of coverslips was used for labelling of permeabilized cells (total LRP10). The surface LRP10 cells were placed on an ice, and medium was replaced with ice-cold DMEM/HEPES (pH 7.4, 25 mM) for 5 minutes to block endocytosis. The total LRP10 cells remained in the incubator at 37°C/5% CO<sub>2</sub>. Subsequently, on the surface LRP10 cells, DMEM/HEPES was replaced with ice-cold DMEM/HEPES containing anti-V5-Tag (D3H8Q) rabbit monoclonal antibody (Cell Signaling Technologies 13202s, 1:500 dilution) and cells were incubated for 1 hour on ice to achieve cell-surface labeling of N-terminal V5-tagged LRP10. Next, after washing the coverslips in ice-cold PBS, cells on coverslips were fixed with 4% paraformaldehyde for 10 minutes. At this point the total LRP10 cells were also fixed with 4% paraformaldehyde for 10 minutes. After washing in PBS, the surface LRP10 cells were incubated for 30 minutes with blocking buffer (2% [w/v] bovine serum albumin [BSA, A- 3294, Merck], 0.1M Glycine in PBS). The

total LRP10 cells were incubated for 30 minutes with blocking buffer containing 0.1% Triton X-100 to permeabilize the cells (2% [w/v] BSA, 0.1 M glycine, 0.1% [v/v] Triton X-100 in PBS). Secondary antibody incubation of surface LRP10 cells was performed overnight at 4°C in PBS containing 2% BSA, with the Alexa Fluor® 488 AffiniPure donkey anti-rabbit IgG antibody (Jackson ImmunoResearch Laboratories, West Grove, PA, USA, 711-545-152, 1:500). Primary antibody incubation of Triton X-100 permeabilized total LRP10 cells was performed overnight at 4°C in PBS containing 2% BSA, with the anti-V5-Tag (D3H8Q) rabbit monoclonal antibody (Cell Signaling Technologies 13202s, 1:500 dilution). The next day, the surface LRP10 cells were washed 3 times in PBS, once in water, air dried and mounted in ProLong Gold with DAPI (Thermo Fisher Scientific, P-36931). Triton X-100 permeabilized total LRP10 cells were washed 3 times in PBS, and secondary antibody incubation of cell-surface labelled cells was performed for 1 hour at room temperature in PBS containing 2% BSA, with the Alexa Fluor® 488 AffiniPure donkey antirabbit IgG antibody (Jackson ImmunoResearch Laboratories, 711-545-152, 1:500). The above-mentioned PBS washing was repeated, followed by one wash in water, and subsequently the cells were air dried and mounted in ProLong Gold with DAPI (Thermo Fisher Scientific, P-36931). Staining was analyzed using a Leica SP5 confocal microscope (Leica Microsystems) and images were processed using Fiji software (11) keeping intensity levels constant for all images. Briefly, in Fiji software, cells of each condition were selected and outlines of the cells of interest were drawn using the bright field exposure of the field and the freeform drawing tool of Fiji software. Measurements were set from the analyze menu selecting: area, integrated density and mean gray value. Next, by selecting the 'measure' option from the analyze menu, area and intensity values of each cell were calculated, and transported to Excel software. Background signal from areas surrounding the cells were selected for normalization purposes. Corrected total cell fluorescence (CTCF) were calculated in Excel (CTCF=Integrated Density - [Area of selected cell X Mean fluorescence of background readings]). Cells were counted from 3 independent experiments with at least 40 cells counted per condition.

## Statistical analysis

For cycloheximide chase experiments, signal intensities of C-terminal V5-tagged LRP10 protein expression at each time point were normalized to Vinculin expression levels of the same time point. Subsequently, C-terminal V5-tagged LRP10 protein expression levels at time point 0 (untreated sample) were set at 100% and C-terminal V5-tagged LRP10 protein expression levels at all subsequent time points were expressed as percentage

of untreated control for all analyzed C-terminal V5-tagged LRP10 wildtype and variant protein expression constructs. All experiments were repeated at least 4 times. Statistical significance levels were determined by Prism 7 software (Graphpad Software, Inc., Sand Diego, CA, USA). Column statistical analysis showed normal distribution of the data, and therefore a One-way ANOVA and Dunnett's multiple comparisons test was adopted. Values passing the threshold for statistical significance of  $p < 0.05$  were reported. For cell-surface labeling of live cells CTCF values of cell-surface N-terminal V5-tagged LRP10 wildtype and variant expression levels were counted from 3 independent experiments with at least 40 cells counted per condition. Mean CTCF values were calculated and Statistical significance levels were determined by Prism 7 software (Graphpad Software, Inc.). Column statistical analysis showed that the data were not normally-distributed, and therefore a Kruskal-Wallis and Dunn's multiple comparisons test was adopted. Values passing the threshold for statistical significance of  $p < 0.05$  were reported.

## Antibodies and LRP10 expression constructs

Primary antibodies: anti-V5-Tag (D3H8Q) rabbit monoclonal antibody (Cell Signaling Technologies 13202s); anti-Vinculin mouse monoclonal antibody (V284) (Santa Cruz Biotechnology);  $\alpha$ -synuclein (clone KM51, Monosan, Uden, the Netherlands); amyloid-beta (clone 6f/3d, Agilent Technologies); hyperphosphorylated tau (clone AT8, Fujirebio Europe N.V., Ghent, Belgium); anti-TGN46 sheep polyclonal antibody (Bio-Rad, ahp500gt), anti-EEA1 mouse monoclonal antibody (BD Biosciences, Los Angeles, CA, USA, clone 14, 610456); anti-GGA1 mouse monoclonal (Santa Cruz Biotechnology, D-6, sc-271927), anti-VPS35 goat polyclonal antibody (Abcam, Cambridge, UK, ab10099).

Secondary antibodies: goat anti-mouse IRDye 800CW (LI-COR Biosciences, 926-32210); goat anti-rabbit IRDye 680RD (LI-COR Biosciences, 926-32221); Alexa Fluor® 488 AffiniPure donkey anti-rabbit IgG antibody (Jackson ImmunoResearch Laboratories, 711-545-152); Alexa Fluor® 647-conjugated donkey antisheep (Jackson ImmunoResearch Laboratories); Alexa Fluor® 594-conjugated donkey anti-rabbit (Jackson ImmunoResearch Laboratories); Alexa Fluor® 488-conjugated donkey anti-mouse (Jackson ImmunoResearch Laboratories); Indodicarbocyanine, Cy5-conjugated donkey anti-mouse (Jackson ImmunoResearch Laboratories); Alexa Fluor® 488-conjugated donkey anti-goat (Jackson ImmunoResearch Laboratories).

Cloning of LRP10 expression constructs: the MGC Human LRP10 Sequence-Verified cDNA was subcloned from the human LRP10-pCR4-TOPO plasmid (Dharmacon, Inc., Lafayette,

CO, USA, Clone ID: 8322768) into pcDNA™3.1/V5-His-TOPO® using the pcDNA™3.1/V5-His TOPO® TA Expression Kit (Thermo Fisher Scientific, K480001) according to manufacturers' specifications. This generated the C-terminal V5-tagged LRP10 wildtype expression construct. This construct was used to generate the N-terminal V5-tagged LRP10 wildtype expression construct. Briefly, via PCR-cloning the C-terminal V5 tag was removed and replaced by a translational stop signal following the last amino acid coding for full length LRP10. Next, a BspE1 site was introduced directly following the LRP10 signal peptide cleavage site (after amino acid 16). Sense and antisense oligonucleotides coding for the N-terminal V5-tag and a BspEI complementary overhang were generated (Integrated DNA Technologies, Inc., Coralville, IA, USA) and annealed. The annealed oligonucleotides were cloned into the BspEI digested transition construct, generating a N-terminal V5-tag in frame with the mature LRP10 coding sequence resulting in the N-terminal V5-tagged LRP10 wildtype expression construct. Introduction of the p.Gly603Arg, p.Pro699Ser, p.Arg533Leu, p.Tyr307Asn, p.Arg235Cys, p.Asn517del, variants in C-terminal V5-tagged and N-terminal V5-tagged LRP10 wildtype expression constructs was achieved using the QuikChange Lightning Site-Directed Mutagenesis Kit (Agilent Technologies, 210518) according to manufactures' specifications. The N-terminal V5-tagged LRP10 Δ2DXXLL mutant construct was generated via PCR-cloning, creating a translational stop signal following amino acid 689, removing the two DXXLL sorting motifs at the C-terminal tail of LRP10 (12, 13). The two DXXLL sorting motifs located in LRP10 C-terminal are necessary for LRP10 internalization from the plasma membrane, and therefore the LRP10 Δ2DXXLL construct is used as an artificial positive control. All expression constructs were verified by Sanger sequencing.

## Human iPSC culture and neural differentiation

The iPSC control line 1 was provided by the Erasmus MC iPS core facility, and it has been characterized and described previously (14). Briefly, the iPSCs were grown on irradiated MEFs and cultured in normal iPSC medium (DMEM/F12 Advanced (Thermo Fisher Scientific) supplemented with 20% KOSR, 2 mM l-glutamine, 0.1 mM MEM-NEAA, 0.1 mM 2-mercaptoethanol, 100 U/ml penicillin/streptomycin (all from Thermo Fisher Scientific) and 10 ng/ml bFGF (Peprotech) at 37°C/5% CO<sub>2</sub>. Medium was changed daily and cells were passaged every 4–6 days either mechanically or enzymatically with collagenase type IV (100 U/ml) (Thermo Fisher Scientific), and addition of 10 μM ROCK inhibitor (Merck) to the medium after passaging.

Small molecule neural progenitor cells (smNPCs) were created and differentiated into neurons according to published protocols (15) with minor modifications. Briefly, iPSC colonies were detached from the MEFs 3–4 days after splitting, using 2 mg/mL collagenase IV. Pieces of colonies were collected by sedimentation and resuspended in iPSC medium (without FGF2) supplemented with 10  $\mu$ M SB-431542 (Abcam), 1  $\mu$ M dorsomorphin (Tocris Bioscience, Bristol, UK) for neural induction, as well as 3  $\mu$ M CHIR 99021 (Axon MedChem, Groningen, the Netherlands) and 0.5  $\mu$ M PMA (Enzo Biochem. Inc., Farmingdale, NY, USA), and cultured in petri dishes. Medium was replaced on day 2 by N2B27 medium supplemented with the same small molecule supplements. N2B27 medium consisted of DMEM-F12 (Invitrogen)/Neurobasal (Thermo Fisher Scientific) 50:50 with 1:200 N2 supplement (Thermo Fisher Scientific), 1:100 B27 supplement lacking vitamin A (Thermo Fisher Scientific) with 1% penicillin/streptomycin/glutamine (PAA). On day 4, SB-431542 and dorsomorphin were withdrawn and 150  $\mu$ M ascorbic acid (AA; Merck) was added to the medium. On day 6, the embryoid bodies (EBs), which showed intensive neuroepithelial outgrowth, were triturated with a 1,000  $\mu$ L pipette into smaller pieces and plated on matrigel-coated (matrigel, growth factor reduced, high concentration; BD Biosciences) 12-well plates at a density of about 10–15 pieces per well in smNPC expansion medium (N2B27 with CHIR, PMA, and AA). The first split was performed at a 1:5 to 1:10 ratio on days 2 to 4 after plating. All the remaining splitting ratios were at least 1:10. After passage 4 PMA was switched to 0.5  $\mu$ M smoothened agonist (SAG). After a maximum of 5 splits, cultures were virtually free of contaminating nonsmNPCs.

To start differentiation into neurons, a homogeneous suspension of 50,000 to 100,000 smNPCs were seeded onto PDL and matrigel-coated coverslips in 150  $\mu$ L droplets of patterning medium (N2B27 with 1 ng/mL GDNF, 2 ng/mL BDNF, 200  $\mu$ M AA, 0.5  $\mu$ M SAG). Patterning medium was changed every other day. After six to eight days in patterning medium, the medium was changed to maturation medium (N2B27 with 2 ng/mL GDNF, 2 ng/mL BDNF, 1 ng/mL TGF- $\beta$ 3, 200  $\mu$ M AA, 100  $\mu$ M dbcAMP). The first time when the maturation medium was added, include 5 ng/mL activinA. All other changes of maturation medium, 2 ng/mL activinA was included. Maturation medium was exchanged every third day. Mature neurons were processed for imaging 12 weeks after the start of differentiation.



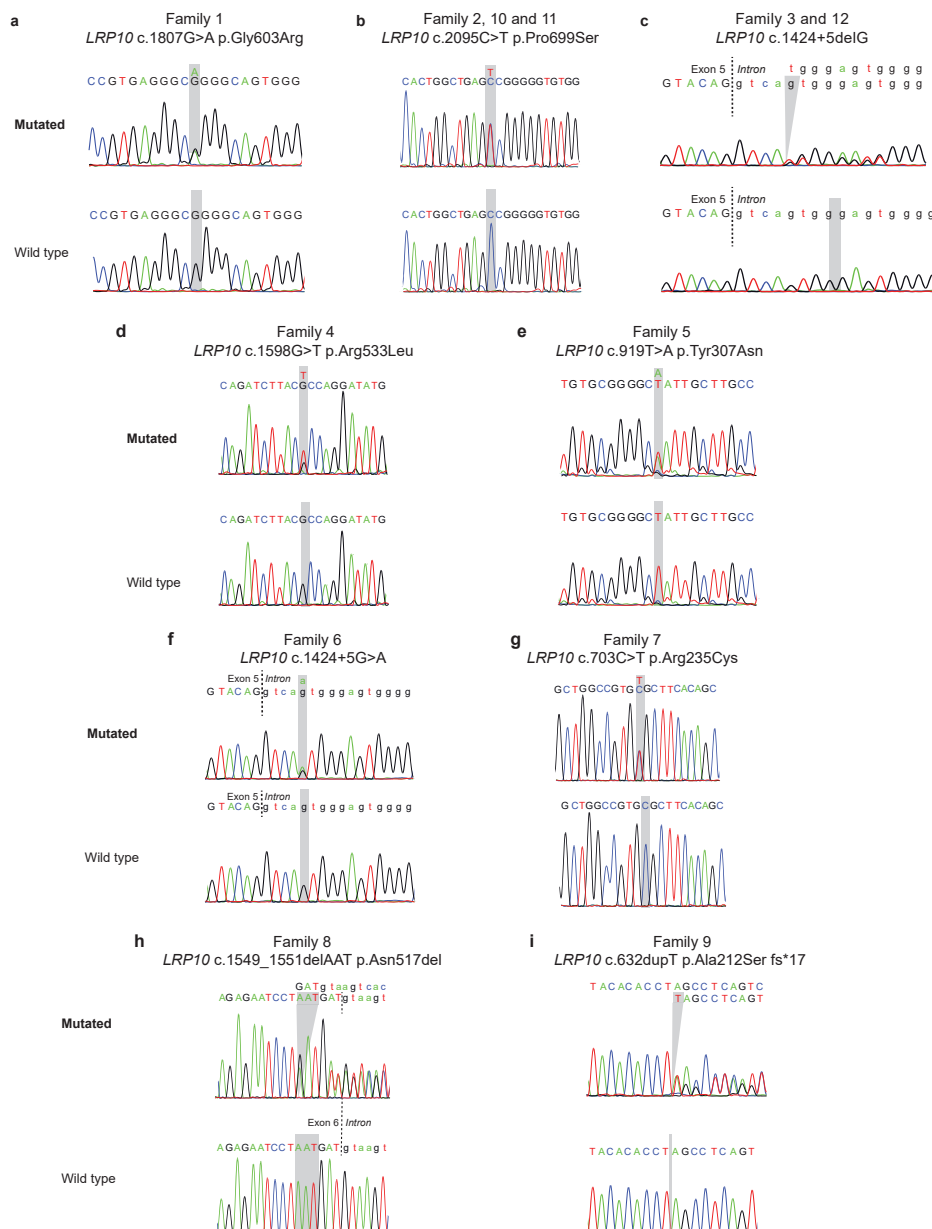
## Transfection and Immunocytochemistry in neurons

Differentiated neurons were transfected two times on subsequent days with N-terminal V5-tagged LRP10 wildtype expression plasmid using DNA-In® neuro transfection reagent according to manufacturer's specifications (Thermo Fisher Scientific). After 4 days, Cells were fixed for 20 minutes, and washed with PBS. Subsequently, primary antibody incubation was performed overnight at 4°C in labeling buffer (50 mM Tris.Cl [pH 7.4], 0.9% NaCl 0.25% gelatin, 0.2% TritonX-100 [all from Merck]). The next day coverslips were washed in PBS, followed by secondary antibody incubation in the dark for 1 hour at room temperature in labeling buffer. After washing in PBS, coverslips were mounted with Prolong Gold plus DAPI (Thermo Fisher Scientific). Primary antibodies: anti-V5-tag (D3H8Q) rabbit monoclonal antibody (Cell Signaling Technologies 13202s, 1:500 dilution), sheep anti-TGN46 (Bio-Rad, ahp500gt, 1:200), mouse anti-EEA1 (BD Biosciences, [clone 14], 610456, 1:200), mouse anti-GGA1 (Santa Cruz Biotechnology, [D-6], sc-271927, 1:100), goat anti-VPS35 (Abcam, ab10099, 1:200). Secondary antibodies: Alexa Fluor® 647-conjugated donkey anti-sheep (Jackson); Alexa Fluor® 594-conjugated donkey anti-rabbit (Jackson ImmunoResearch Laboratories), Alexa Fluor® 488-conjugated donkey anti-mouse (Jackson ImmunoResearch Laboratories). indodicarbocyanine, Cy5-conjugated donkey anti-mouse (Jackson ImmunoResearch Laboratories); Alexa Fluor® 488-conjugated donkey anti-goat. Slides were analyzed on a Leica SP5 AOBS confocal laser scanning microscope with a HCX PL APO CS ×40 objective (NA 1.25) or HCX PL APO CS ×63 objective (NA 1.40). Image stacks were acquired with a step size of 494 nm over 9,88 µm thickness and a resolution of 1024x1024 pixels. Images were processed using Fiji software.

# Supplementary References

1. Li H, Durbin R. Fast and accurate short read alignment with Burrows-Wheeler transform. *Bioinformatics* 2009; 25(14): 1754-60.
2. McKenna A, Hanna M, Banks E, et al. The Genome Analysis Toolkit: a MapReduce framework for analyzing next-generation DNA sequencing data. *Genome Res* 2010; 20(9): 1297-303.
3. Wang K, Li M, Hakonarson H. ANNOVAR: functional annotation of genetic variants from highthroughput sequencing data. *Nucleic Acids Res* 2010; 38(16): e164.
4. den Dunnen JT, Dalgleish R, Maglott DR, et al. HGVS Recommendations for the Description of Sequence Variants: 2016 Update. *Hum Mutat* 2016; 37(6): 564-9.
5. Pfaffl MW. A new mathematical model for relative quantification in real-time RT-PCR. *Nucleic Acids Res* 2001; 29(9): e45.
6. Alafuzoff I, Ince PG, Arzberger T, et al. Staging/typing of Lewy body related alpha-synuclein pathology: a study of the BrainNet Europe Consortium. *Acta Neuropathol* 2009; 117(6): 635-52.
7. Alafuzoff I, Arzberger T, Al-Sarraj S, et al. Staging of neurofibrillary pathology in Alzheimer's disease: a study of the BrainNet Europe Consortium. *Brain Pathol* 2008; 18(4): 484-96.
8. Hyman BT, Phelps CH, Beach TG, et al. National Institute on Aging-Alzheimer's Association guidelines for the neuropathologic assessment of Alzheimer's disease. *Alzheimers Dement* 2012; 8(1): 1-13.
9. Mirra SS, Heyman A, McKeel D, et al. The Consortium to Establish a Registry for Alzheimer's Disease (CERAD). Part II. Standardization of the neuropathologic assessment of Alzheimer's disease. *Neurology* 1991; 41(4): 479-86.
10. Thal DR, Rub U, Orantes M, Braak H. Phases of A beta-deposition in the human brain and its relevance for the development of AD. *Neurology* 2002; 58(12): 1791-800.
11. Schindelin J, Arganda-Carreras I, Frise E, et al. Fiji: an open-source platform for biological-image analysis. *Nat Methods* 2012; 9(7): 676-82.
12. Boucher R, Larkin H, Brodeur J, Gagnon H, Theriault C, Lavoie C. Intracellular trafficking of LRP9 is dependent on two acidic cluster/dileucine motifs. *Histochem Cell Biol* 2008; 130(2): 315-27.
13. Doray B, Knisely JM, Wartman L, Bu G, Kornfeld S. Identification of acidic dileucine signals in LRP9 that interact with both GGAs and AP-1/AP-2. *Traffic* 2008; 9(9): 1551-62.
14. Vanhauwaert R, Kuenen S, Masius R, et al. The SAC1 domain in synaptojanin is required for autophagosome maturation at presynaptic terminals. *EMBO J* 2017; 36(10): 1392-411.
15. Reinhardt P, Glatza M, Hemmer K, et al. Derivation and expansion using only small molecules of human neural progenitors for neurodegenerative disease modeling. *PLoS One* 2013; 8(3): e59252.

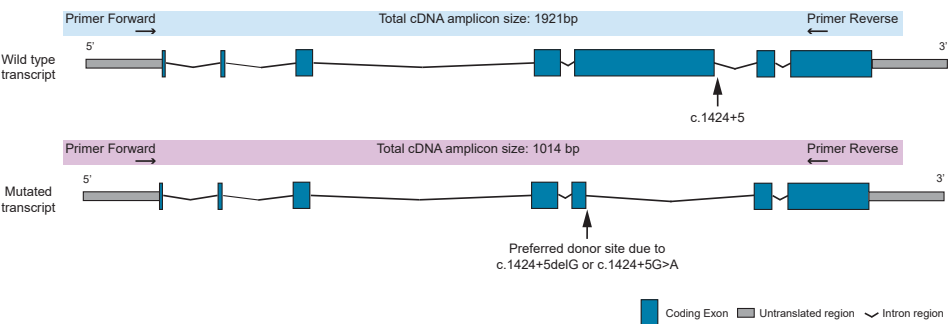
# Supplementary Figures and Tables



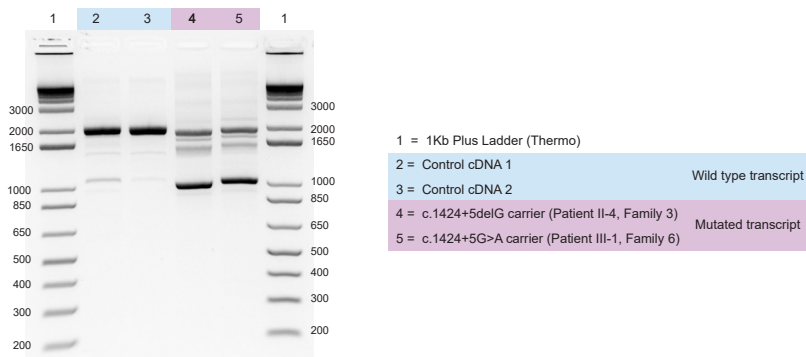
## Supplementary Figure 1. Electropherograms of *LRP10* variants

Electropherograms of *LRP10* variants identified in this study in genomic DNA from patients with Parkinson's disease, Parkinson's disease dementia, and Dementia with Lewy Bodies. Family codes are as in Figure 1 and 2 in the main manuscript.

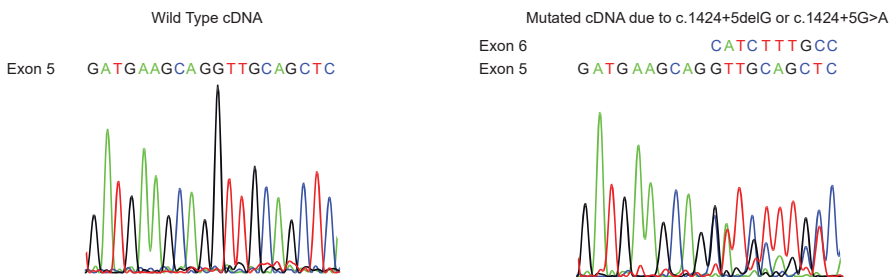
A *LRP10* transcript schematic representation



B Agarose gel picture



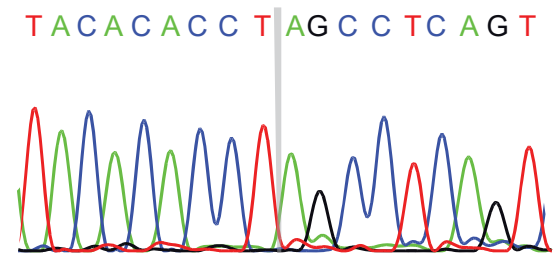
C Electropherograms



**Supplementary Figure 2. Effect of the c.1424+5 variants on *LRP10* mRNA splicing**

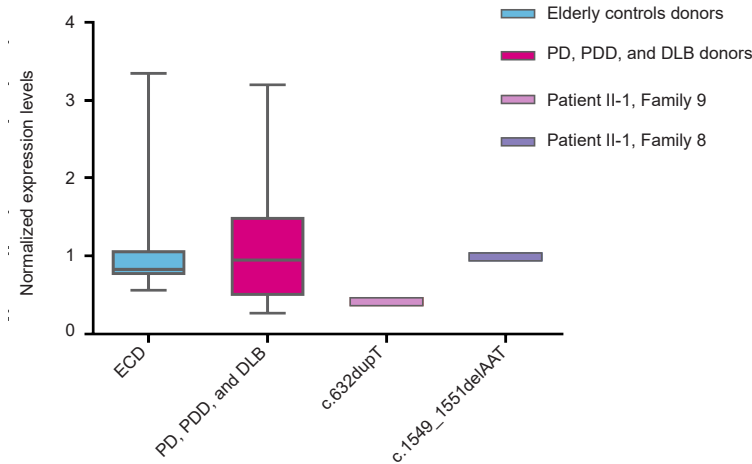
Panel a - Schematic representation of *LRP10* wild type and aberrant splicing due to the c.1424+5delG and c.1424+5G>A mutations (transcript NM\_014045). The c.1424+5 nucleotide (targeted by the mutations in Families 3, 12, and 6) is indicated by an arrow in the wild type transcript. In the mutant transcript, due to the c.1424+5delG or the c.1424+5G>A mutation, the normal exon 5 splice donor site is weakened and an alternative upstream donor site, located within the exon 5 (arrow) prevails, resulting in exclusion of a large part of this exon from the mature transcript and, at protein level, frameshift and premature truncation (p.Gly173Alafs\*34). Panel b - Agarose gel analysis of the *LRP10* transcripts. In comparison to normal controls, in patients carrying the c.1424+5delG or the c.1424+5G>A heterozygous mutation, a 1014-bp band becomes markedly more abundant, whereas the larger 1921-bp band, corresponding to the full-length *LRP10* transcript, is much decreased. Panel c - Sanger sequencing of *LRP10* cDNA showing identical aberrations in carriers of the c.1424+5delG and the c.1424+5G>A mutations: incorporation of a much shorter exon 5 lacking 907 nucleotides (r.518\_1424del).

Patient II-1, Family 9  
cDNA analysis  
*LRP10* c.632dupT p.Ala212Ser fs\*17



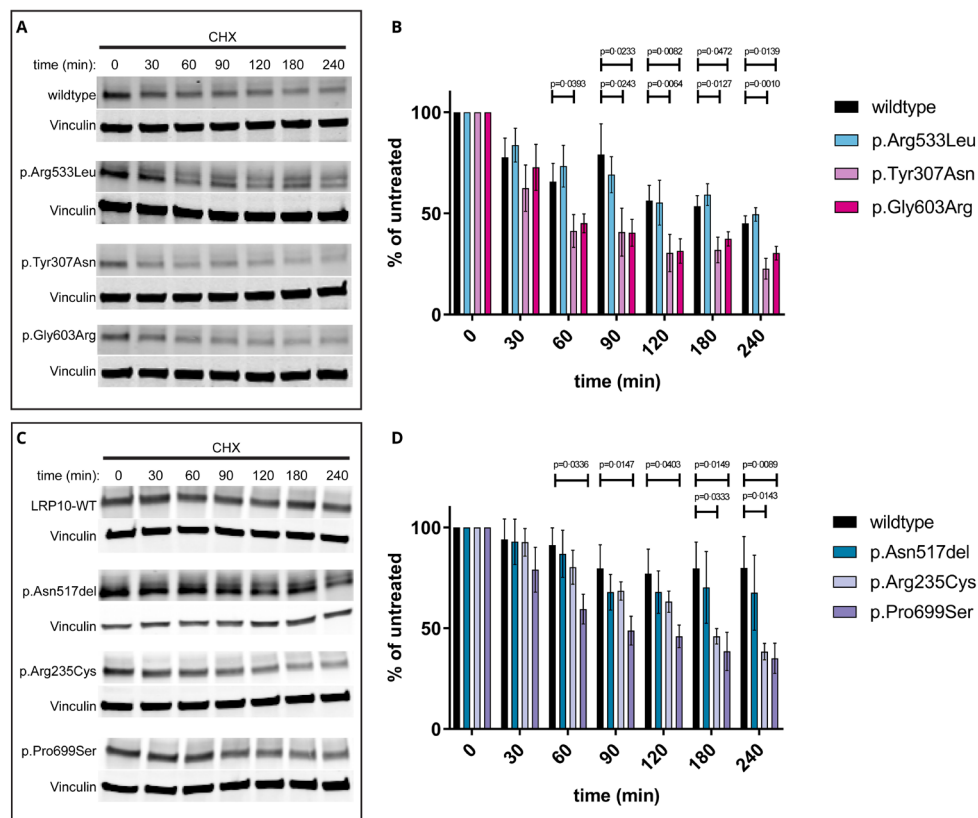
**Supplementary Figure 3. Nonsense-mediated mRNA decay of a *LRP10* frame-shift variant**

*LRP10* cDNA sequence from the patient carrying the c.632dupT (p.Ala212Serfs\*17) heterozygous mutation (patient II-1 in Family 9). Only the sequence from the wild type transcript is detected, in keeping with the mutant transcript undergoing nonsense-mediated mRNA decay (see also Supplementary Fig.4). The grey bar indicates the position of the mutation detected in genomic DNA (confront Supplementary Fig.1, panel i).

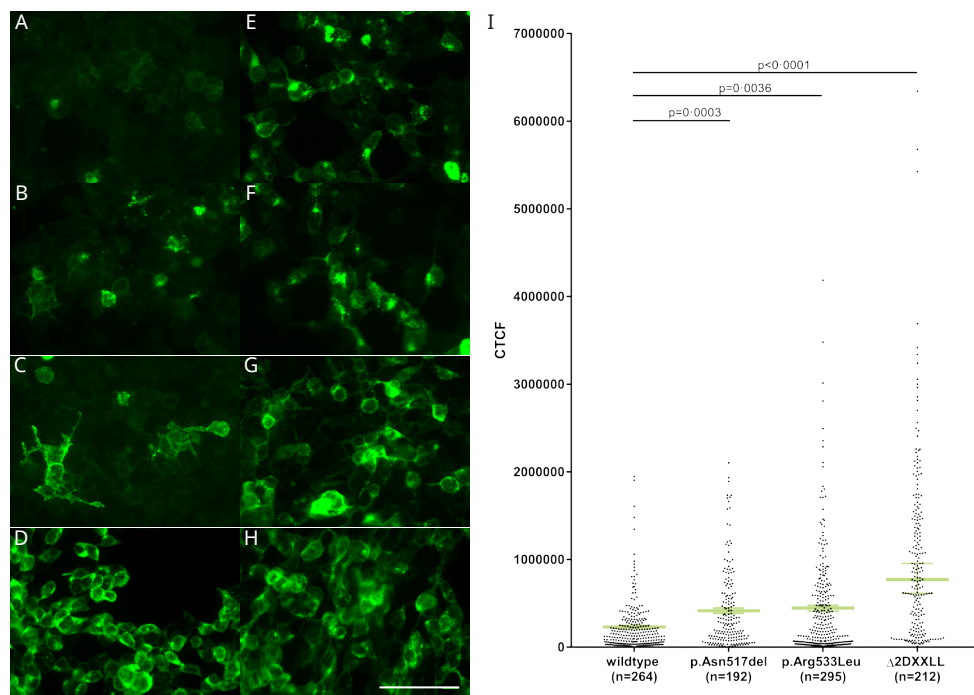


**Supplementary Figure 4. *LRP10* quantitative mRNA expression studies in human brain**

Real-time qPCR analysis of *LRP10* and three housekeeping genes (*POLR2A*, *RPL27*, *EIF4G2*). The expression of *LRP10* is reduced in the patient carrying the c.632dupT mutation (in keeping with this mutant transcript undergoing nonsense-mediated mRNA decay) (see also Supplementary Fig.3), whereas it is normal in the carrier of the in-frame deletion c.1549\_1551delAAT, when compared to elderly control donors or donors with idiopathic PD or DLB. RNA was isolated from the medial temporal gyrus of 11 elderly control donors, 18 donors with idiopathic Parkinson's disease, Parkinson's disease dementia, or dementia with Lewy bodies (PD, PDD and DLB), Patient II-1 from Family 9 (frameshift mutation carrier), and Patient II-1 from Family 8 (in-frame deletion carrier).



**Supplementary Figure 5. Effect of missense variants on LRP10 protein stability**  
HEK-293 cells expressing V5-tagged wildtype or LRP10 variants were treated with cycloheximide (CHX) for indicated times, followed by Western blot (WB) analysis. LRP10 protein levels were detected with anti-V5-tag antibody; Vinculin levels were used as loading controls. Panel a. Representative WB images comparing wildtype, p.Arg533Leu, p.Tyr307Asn, and p.Gly603Arg expression levels. Panel b. Quantification of WB analysis comparing wildtype, p.Arg533Leu, p.Tyr307Asn, and p.Gly603Arg expression levels. Panel c. Representative WB images comparing wildtype, p.Asn517del, p.Arg235Cys, and p.Pro699Ser expression levels. Panel d. Quantification of WB analysis comparing wildtype, p.Asn517del, p.Arg235Cys, and p.Pro699Ser expression levels. The bars in Panel c and d indicate mean LRP10 levels at each time point as percentage of untreated cells at time=0. Error bars are SEM of  $n \geq 4$  independent experiments. One-way ANOVA and Dunnett's multiple comparisons test. Only significant changes  $p < 0.05$  are shown.



### Supplementary Figure 6. Effect of missense variants on LRP10 cell surface localization

Immunofluorescence analysis in HEK293 cells transfected with N-terminal V5-tagged LRP10 wildtype (Panel a,e), p.Asn517del (Panel b,f), or p.Arg533Leu (Panel c,g) missense mutant expression constructs. A N-terminally V5-tagged LRP10 construct lacking two C-terminal DXLL motifs, which has been previously shown to increase LRP10 cell surface localization, was used as a positive control ( $\Delta 2DXXLL$ )<sup>27,28,30</sup> (Panel d,h). Cells were labelled with anti-V5 antibody (green signal) without cell membrane permeabilization (Panel a-d) or after the cell membranes were permeabilized (Panel e-h). Parallel staining of permeabilized cells demonstrates that intracellular LRP10 expression and transfection efficiencies were comparable among wildtype and all variants (Panel e-h). The corrected total cell fluorescence (CTCF) of non-permeabilized cells labelled with intensities above background was quantified (Panel i). Number of cells counted (n) for each condition is indicated. Median and 95% confidence interval are shown in green. Cells were counted from 3 independent experiments. Kruskal-Wallis and Dunn's multiple comparisons test was performed. Values passing the threshold for statistical significance of  $p < 0.05$  compared to wildtype are shown.

**Supplementary Table 1. Clinical features in patients carrying *LRP10* pathogenic variants**

Family	Patient	Variant	Clinical Diagnosis	AAO	DD	Mean AAO (SD, range); DD (SD, range)	IS	B	R	RT	L-Dopa/DA
1	III-3	p.Gly603Arg	PD	49	34	59.8 (8.7; 46-73); 11.5 (8.6; 4-34)	T	+	+	+	+
1	III-5	p.Gly603Arg	PD	56	9		B	+	+	+	+
1	III-6	p.Gly603Arg	PD	64	16		B, T	+	+	-	+
1	III-9	p.Gly603Arg	PD	73	5		R, T	+	+	+	n.t.
1	III-10	p.Gly603Arg	PD	68	4		B, T	+	+	+	n.t.
1	III-11	p.Gly603Arg	PD	67	13		T	+	+	+	+
1	III-12	p.Gly603Arg	DLB	65	4		Cognitive impairment	-	-	-	n.t.
1	III-13	p.Gly603Arg	PD	60	5		RT	+	-	+	n.t.
1	IV-2	p.Gly603Arg	PD	50	14		T	+	+	+	+
1	IV-4	p.Gly603Arg	PD	46	11		B	+	+	+	+
2	III-1	p.Pro699Ser	PD	65	14	70 (5.0; 65-75); 10.5 (3.5; 7-14)	T	+	+	+	+
2	III-4	p.Pro699Ser	PD	75	7		R, B	+	+	-	+
3	I-2	c.1424+5del	PD	72	13	61.7 (9.0; 50-72); 17.5 (10.5; 7-28)	R	+	+	-	+
3	II-2	c.1424+5del	PD	63	9		B	+	+	-	+
3	II-4	c.1424+5del	PD	50	18		B	+	+	-	+
4	II-1	p.Arg533Leu	PD	47	28	59.5 (12.5; 47-72); 13.3 (10.5; 7-28)	T	+	+	+	+
4	II-3	p.Arg533Leu	PD	72	7		B	+	+	-	n.t.
5	II-1	p.Tyr307Asn	PDD	71	4	-	T	+	+	+	+
6	III-1	c.1424+5G>A	DLB	62	6	-	Cognitive impairment	-	-	-	n.t.
7	III-1*	p.Arg235Cys	PDD	74	8	62.0 (8.5; 56-74); 10.7 (2.5; 8-14)	RT	+	+	+	+
7	III-4	p.Arg235Cys	PDD	56	10		Cognitive impairment	-	+	-	n.t.
7	IV-1	p.Arg235Cys	DEM	56	14		Behavioral disturbances	-	-	-	n.t.
8	II-1*	p.Asn517del	DLB	74	5	-	Cognitive impairment	-	-	-	n.t.
9	II-1*	p.Ala212Serfs*17	PD	74	16	73.5 (0.5; 73-74); 13.0 (3.0; 10-16)	B, R	+	+	-	+
9	II-3	p.Ala212Serfs*17	DEM	73	10		Memory complaints	-	-	-	-
10	II-1	p.Pro699Ser	PD	67	5	58 (9.0; 49-67); 7.5 (2.5; 5-10)	B, R	+	+	+	+
10	II-5	p.Pro699Ser	PD	49	10		RT	+	+	+	+
11	II-1	p.Pro699Ser	PD	53	26	-	R	+	+	+	+
12	II-1	c.1424+5del	PD	66	1	64.0 (2.0; 62-66); 6.0 (5.0; 1-11)	T	+	+	+	+
12	II-4	c.1424+5del	PD	62	11		T	+	+	+	+
				Mean	62.6	11.2					
				SD	9.2	7.4					
				Range	46-75	1-34					

AAO=age at onset, DD=disease duration, IS=initial symptoms at disease onset, signs at examination: B=bradykinesia, R=rigidity, RT=resting tremor, L-Dopa/DA=response to L-Dopa or dopamine agonist, T=tremor, +=present, -=absent, n.t.=not treated, \*=autopsy-proven Lewy body-positive pathology, PD=Parkinson's disease, PDD=Parkinson's disease with dementia, DLB=Dementia with Lewy bodies, DEM=degenerative dementia in advanced stage (additional characterization of disease or more specific diagnosis not available).



Supplementary Table 2. Details of *LRP10* pathogenic variants identified in PD, PDD, and DLB patients

Chr	Genomic coordinates (GRCh37)	Reference allele	Alternative allele	Nucleotide change NM_014045.4	Amino acid change NM_014045.4	Variant type	Pedigrees (Country of origin)	N. of affected carriers (N. of available individuals)	N. of asymptomatic carriers (mean age at examination; SD)	MAF GnomAD (N. of alleles)	rs number	Functional predictions: pathogenic (total)	Splicing predictions: deleterious (total)
14	23346401	G	A	c.1807G>A	p.Gly603Arg	Missense	Family 1 (Italy)	10 (10)	3 (50.6; 5.4)	0.0019% (5)	rs142287402	8 (11)	n.a.
14	23346689	C	T	c.2095C>T	p.Pro699Ser	Missense	Family 2, 10, 11 (Italy, Sardinia)	2(2), 2(2), 1(1)	2(81; 5; 5.5), 2(68.5; 1.5), n.d.	0.0012% (3)	rs753191017	6 (11)	n.a.
14	23345586	G	-	c.1424+5delG		Splicing	Family 3, 12 (Taiwan)	3(3), 2(2)	2(62.5), n.d.	0.0020% (5)	rs778728855	n.a.	5 (5)
14	23346192	G	T	c.1598G>T	p.Arg533Leu	Missense	Family 4 (Portugal)	2(2)	n.d.	n.d.	n.d.	9 (11)	n.a.
14	23345076	T	A	c.919T>A	p.Tyr307Asn	Missense	Family 5 (Italy)	1(1)	n.d.	0.0052% (13)	rs139650807	9 (11)	n.a.
14	23345586	G	A	c.1425+5G>A		Splicing	Family 6 (The Netherlands)	1(1)	n.d.	n.d.	n.d.	n.a.	5 (5)
14	23344860	C	T	c.703C>T	p.Arg235Cys	Missense	Family 7 (Italy)	3(4)	1(58)	0.0021% (6)	rs374479224	5 (11)	n.a.
14	23346022_23346024	AAT	-	c.1549_1551 delAAT	p.Asn517del	In frame deletion	Family 8 (The Netherlands)	1(1)	n.d.	n.d.	n.d.	n.a.	n.a.
14	23344789	-	T	c.632dupT	p.Ala212Ser fs*17	Frameshift insertion	Family 9 (The Netherlands)	2(2)	n.d.	n.d.	n.d.	n.a.	n.a.

GRCh37=genomic reference consortium human 37, NM\_014045.4=NCBI reference sequence, SD=standard deviation, MAF=minor allele frequency, GnomAD=genomes aggregation database, n.a.=not available, n.d.=not detected.

**Supplementary Table 3. In-silico pathogenicity predictions for *LRP10* pathogenic missense variants, and for *OR11H12* and POTEg variants identified in Family 1**

Pedigrees	Nucleotide Change	Amino Acid Change	Gerp	Variant-effect predictions software (scores)										
				SIFT	Polyphen2 HDIV	Polyphen2 HVAR	LRT	Mutation Taster	Mutation Assessor	FATHMM	Radial SVM	LR	CADD phred	M-CAP
Family 1 (LRP10)	c.1807G>A	p.Gly603Arg	4.9	T (0.19)	D (0.999)	P (0.888)	N (0.043)	D (1.000)	L (1.39)	D (-3.31)	D (0.638)	D (0.811)	13.77	PP (0.334)
Family 2, 10, and 11 (LRP10)	c.2095C>T	p.Pro699Ser	4.97	T (0.49)	B (0.384)	B (0.113)	D (0.000)	D (1.000)	L (1.39)	D (-2.99)	T (-0.118)	D (0.583)	15.54	PP (0.161)
Family 4 (LRP10)	c.1598G>T	p.Arg533Leu	5.13	T (1)	D (1.0)	D (0.947)	D (0.000)	D (1.000)	L (1.795)	D (-3.56)	D (0.593)	D (0.846)	23	PP (0.300)
Family 5 (LRP10)	c.919T>A	p.Tyr307Asn	5.97	T (0.2)	D (0.999)	D (0.942)	D (0.000)	D (1.000)	L (1.87)	D (-3.32)	D (0.771)	D (0.848)	19.09	PP (0.140)
Family 7 (LRP10)	c.703C>T	p.Arg235Cys	5.73	D (0.01)	B (0.086)	B (0.036)	D (0.000)	D (0.998)	M (2.08)	T (2.16)	T (-1.097)	T (0.073)	14.15	LB (0.011)
Family 1 (OR11H12)	c.213C>A	p.His71Gln	-0.993	T (0.11)	D (0.957)	P (0.557)	D (0.000)	N (0.998)	L (1.415)	T (2.38)	T (-1.042)	T (0.035)	8.267	LB (0.007)
Family 1 (POTEG)	c.649C>T	p.Arg217Trp	-0.546	D (0)	P (0.917)	B (0.17)	N (0.559)	N (1.000)	L (1.145)	T (0.58)	T (-0.978)	T (0.090)	8.623	LB (0.003)

GERP=genomic evolutionary rate profiling, SIFT=sorting intolerant from tolerant, Polyphen2 HDIV=polyorphism phenotyping version 2 human diversity, Polyphen2 HVAR=polyorphism phenotyping version 2 human variation, LRT=likelihood ratio test, FATHMM=functional analysis through hidden Markov models, SVM=support vector machine, LR=logistic regression, CADD=combined annotation dependent depletion, M-CAP=Mendelian clinically applicable pathogenicity, I=tolerated, D=damaging, PP=probably pathogenic, P=possibly damaging, N=neutral, L=low, B=benign, M=medium, LB=likely benign. Transcript NM\_014045.4 has been used for *LRP10* variants nomenclature, NM\_001013354.1 for *OR11H12* variant nomenclature, and NM\_001005356.2 for *POTEg* variant nomenclature.

**Supplementary Table 4. *LRP10* c.1424+5 variants – in-silico predictions on mRNA splicing**

Splicing prediction Method [Range], Threshold	LRP10 WT	LRP10 mut	
	c.1424+5G	c.1424+5delG	c.1424+5G>A
SSF [0-100], ≥70	90.12	72.71 (-19.3%)	77.97 (-13.5%)
MaxEnt [0-12], ≥0	8.94	3.35 (-62.5%)	4.06 (-54.6%)
NNSPLICE [0-1], ≥0,4	0.84	0 (-100%)	0 (-100%)
GeneSplicer [0-15], ≥0	8.25	0.85 (-89.7%)	2.27 (-72.5%)
HSF [0-100], ≥65	94.97	80.72 (-15%)	82.81 (-12.38%)

Effect on *LRP10* exon 5 splicing due to *LRP10* c.1424+5 variants, according to five splicing prediction tools (*SpliceSiteFinder-like*, *MaxEntScan*, *NNSPLICE*, *GeneSplicer*, and *Human Splicing Finder*) integrated in *Alamut Visual* version 4.2 (*Interactive Biosoftware*, Rouen, France). Listed are the splicing scores resulting from the reference and the mutated sequences (including their relative percentage), and the complete range of possible values for each method (only values passing the method-specific threshold are reported).

**Supplementary Table 5. Neuropathological features in three patients with *LRP10* variants**

	Family 7, III-1	Family 8, II-1	Family 9, II-1
Gender	Female	Male	Female
Age at onset	74	74	74
Age at death	82	79	90
Disease duration (years)	8	5	16
Clinical diagnosis	PDD	DLB	PD
Cognitive functioning	Dementia	Dementia	Mild cognitive impairment
Family history	Two siblings and one son with parkinsonism and dementia	Sister with dementia	Father with dementia
Neuropathological diagnosis	LB disease	LB disease	LB disease
Atrophy	Mild in cerebral cortex, moderate in amygdala and hippocampus	Parietal enlargement of ventricles	Not present
Braak $\alpha$ -synuclein stage	6	6	6
Thal phase for amyloid- $\beta$	4	3	3
Braak NFT stage	3	4	3
CERAD	A	B	A
CAA	Not present	Not present	Moderate (type 2)
Spongiform changes	Focal, parahippocampal gyrus	Temporal, entorhinal, insular cortex and striatum	Not present

PDD=Parkinson's disease dementia, DLB=dementia with Lewy bodies, PD=Parkinson's disease, LB=Lewy bodies, NFT=neurofibrillary tangles, CERAD=consortium to establish a registry for Alzheimer's disease, CAA=cerebral amyloid angiopathy.

**Supplementary Table 6. PCR primers for *LRP10* genomic regions and cDNA**

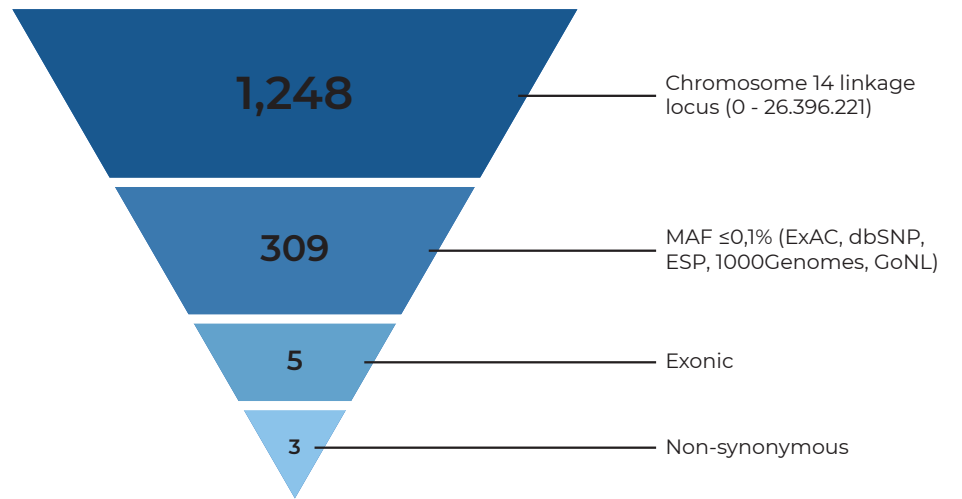
LRP10 genomic DNA NM_014045.4		
Primer name	Primer sequence 5'>3'	Amplicon size (bp)
LRP10-ex1-fwd	CAAAGTTTGGCCCGAAGAGG	522
LRP10-ex1-rev	GGGCAGGCAGGATAGAGTGC	
LRP10-ex2-fwd	CGGATGGCTCCCTTGAGTTG	287
LRP10-ex2-rev	CACACCGAGCCTCAGCTTCC	
LRP10-ex3-fwd	CCTCCTTGAGAGCCCAGAC	325
LRP10-ex3-rev	GAAGTGATCCCTGAAGACTTCCAATG	
LRP10-ex4-fwd	GCACCAGGGGAGGAGAAAGC	367
LRP10-ex4-rev	GCAGAGGCACCATGGAGAGG	
LRP10-ex5A-fwd	GCCAAGGTAGGCTGGACAGG	446
LRP10-ex5A-rev	GCATCTCCAAAGCCCAAGTCC	
LRP10-ex5Bfwd	GTCCCCCTCCCTGCCTTGC	593
LRP10-ex5B-rev	TGGTAGTTGCAGCGGTCAGC	
LRP10-ex5C-fwd	TGACGGCTCATGGGACTGTG	565
LRP10-ex5C-rev	TCAGGATCTGGACCTGTCCCTTAC	
LRP10-ex6-fwd	GGGAAAGCCATGGCACAGC	342
LRP10-ex6-rev	GGCCAAAGGCTGAATGAAGG	
LRP10-ex7A-fwd	CCTCCTGGTCCCAGTTCTGC	485
LRP10-ex7A-rev	TGGCTCTAGGGGCAGTGAGG	
LRP10-ex7B-fwd	CAGTGGGTGGGCAAGATGG	462
LRP10-ex7B-rev	CCCACCAAGTCCCTGAAATCC	
LRP10 coding DNA		
Primer name	Primer sequence 5'>3'	Amplicon size (bp)
LRP10-cDNA-1-3fwd	CCCTGGCATCCAGAGTACGG	1921
LRP10-cDNA-5-7rev	TCAAGGGGAGCAGCAGAAGG	
LRP10-cDNA-1-3fwd	CCCTGGCATCCAGAGTACGG	293
LRP10-cDNA-1-3rev	GACCAGGGGCCTCTGTAAGG	
LRP10-cDNA-2-4fwd	CCATCCAGACCGGATTATTTTCC	197
LRP10- cDNA-2-4rev	AGCCACAGGCCAGGTGTAGC	
LRP10- cDNA-3-5fwd	TGCAGGGCACCTTACAGAGG	430
LRP10- cDNA-3-5rev	CCAGGGAAGGGGTCTGAGC	
LRP10- cDNA-4-6fwd	CCAGGGCTTCCTGCTCTCC	1122
LRP10 -cDNA-4-6rev	ATGAGCTGCCCCGTAGGAAGG	
LRP10- cDNA-5-7fwd	CCCCGCAAGGTCATTACAGC	458
LRP10- cDNA-5-7rev	TCAAGGGGAGCAGCAGAAGG	
LRP10- cDNA-6-3UTRfwd	GGGTGCCATCCCACCTGTAG	832
LRP10- cDNA-6-3UTRrev	TCTCCCTGCCTGAGGGACAC	

Supplementary Table 7. Additional LRP10 variants identified in this study

Chr	Genomic coordinates (GRCh37)	Reference allele	Alternative allele	Nucleotide change	Amino acid change	Variant type	N. of carriers (MAF)	MAF GnomAD (N. of alleles)	rs number
14	23341108	G	A	c.-405G>A	-	SNP	1 (0.07%)	0.15% (47)	rs775535542
14	23341328	A	G	c.-185A>G	-	SNP	1 (0.07%)	2.32% (714)	rs56248501
14	23341459	T	C	c.-54T>C	-	SNP	1 (0.07%)	0.72% (222)	rs115799735
14	23341666	G	C	c.34+120G>C	-	SNP	1 (0.07%)	31.9% (9,268)	rs8011536
14	23341934	G	A	c.35-13G>A	-	SNP	1 (0.07%)	8 x 10-4 (2)	rs780055634
14	23341951	C	T	c.39C>T	p.=(Gly13=)	SNP	18 (1.36%)	2.75% (7,637)	rs342944471
14	23342077	G	A	c.79+86G>A	-	SNP	2 (0.15%)	0.10% (32)	rs189303378
14	23342113	T	G	c.79+122T>G	-	SNP	1 (0.07%)	0.01% (4)	rs367925650
14	23342497	G	A	c.80-23G>A	-	SNP	7 (0.53%)	0.70% (1,924)	rs145476957
14	23342499	G	A	c.80-21G>A	-	SNP	1 (0.07%)	0.02% (58)	rs200843875
14	23344572	A	G	c.415A>G	p.Met139Val	SNP	7 (0.53%)	0.69% (1,920)	rs28534929
14	23344653	G	A	c.496G>A	p.Gly166Ser	SNP	1 (0.07%)	-	-
14	23345874	C	T	c.1425-24C>T	-	SNP	1 (0.07%)	1 x 10-3 (4)	rs775144383
14	23345884	C	G	c.1425-14C>G	-	SNP	1 (0.07%)	-	-
14	23346059	T	G	c.1554+32T>G	-	SNP	2 (0.15%)	-	-
14	23346094	C	T	c.1555-55C>T	-	SNP	1 (0.07%)	-	-
14	23346279	G	A	c.1685G>A	p.Arg562His	SNP	3 (0.22%)	0.71% (1,980)	rs142153001
14	23346757_23346782del	ACCTGGGGGTCTA CTGAGGCCTCTCC	A	*21_*46del	-	Indel	2 (0.15%)	0.14% (346)	rs551804669
14	23346936	C	T	c.*200C>T	-	SNP	3 (0.22%)	0.25% (80)	rs151223810

Chr=chromosome, GRCh37=genome reference consortium human 37, MAF=minor allele frequency, GnomAD=genome aggregation database, SNP=single nucleotide polymorphism

**Supplementary Table 8. Filtering of variants in the linkage region – Family 1**



	Variant 1	Variant 2	Variant 3
<i>Chromosome</i>	14	14	14
<i>Start</i>	19377806	19559003	23346401
<i>End</i>	19377806	19559003	23346401
<i>Reference Allele</i>	C	C	G
<i>Alternative Allele</i>	A	T	A
<i>Transcript</i>	NM_001013354.1	NM_001005356.2	NM_014045.4
<i>Gene</i>	OR11H12	POTEG	LRP10
<i>Variant type</i>	SNP	SNP	SNP
<i>Exon</i>	1	3	7
<i>Variant nomenclature</i>	c.213C>A het p.His71Gln	c.649C>T het p.Arg217Trp	c.1807G>A het p.Gly603Arg
<i>dbSNP</i>	rs376279854	n.a.	rs142287402
<i>ExAC (Alleles)</i>	MAF: 0.01% (11)	MAF: 0.01% (11)	MAF: 0.003% (4)
<i>GnomAD (Alleles)</i>	MAF: 0.006% (17)	MAF: 0.008% (20)	MAF: 0.001% (5)
<i>GERP Score</i>	-0.993	-0.546	4.9
<i>Predictions (total tools)</i>	3 (11)	2 (11)	7 (11)
<i>Expression in the brain</i>	Not expressed	Not expressed	Expressed

MAF=minor allele frequency, ExAC=exome aggregation consortium, dbSNP=NCBI database single nucleotide polymorphism, ESP=exome variant server NHLBI GO exome sequencing project, GoNL=genome of the Netherlands, het=heterozygous, n.a.=not available, GnomAD=genome aggregation database, GERP=genomic evolutionary rating profiling (scores ranges from negative value of -12.36 until positive value of 6.18)

**Supplementary Table 9. Primers for PCR amplification of the known PD genes**

Primer Name	NM 198578.4 Primer Sequence	Amplicon Size
LRRK2_ex29_For	GGTGATTTTACCAACATTATCAACTACCC	584
LRRK2_ex29_Rev	TTAGGAGAAATGAAGGCTTTGG	
LRRK2-ex30F	TGATCGGTTGCTGACAAATATGC	427
LRRK2-ex30R	AGCAATTGTTTGCCCAAAATAAATTAAAC	
LRRK2_ex31_For	TTGTTCTTTTCTTCTCTGAAGTCTGC	591
LRRK2_ex31_Rev	CGGTCTCTTAGTTTCTCTCAGGTTCC	
LRRK2_ex32_For	TTGCCTCTGAATCAACAATTTTCC	543
LRRK2_ex32_Rev	TCAGTGGCCTATTAAAGAACCGTATG	
LRRK2_ex33_For	CCATAGGATGCACAGCTTCTAGTCC	390
LRRK2_ex33_Rev	TCTATGTGAAATGTCCACAGTTTTC	
LRRK2_ex34_For	TGCCCCCTGGGCTTCTAGG	545
LRRK2_ex34_Rev	AAAGTGTGAGATGCAATGTTTTATTCC	
LRRK2_ex35_For	TCTGAGCATGCATTGAATTGG	527
LRRK2_ex35_Rev	TGCCTACTCCAAGGTTTTATGAGC	
LRRK2-ex3637F	GCTTAACAGCATCAACCTGAAATGG	933
LRRK2-ex3637R	GCTCAATAAGCCAGCATTCAAACC	
LRRK2-ex38F	CAGCAGTTCAGAATTCTACAAGTGAACG	592
LRRK2-ex38R	TGATCCTAGTCTACATGATTATGTGCAAAAC	
LRRK2_ex39_For	GCTTAACAGCATCAACCTGAAATGG	414
LRRK2_ex39_Rev	CACAACGAAAAGACAACTAGGATTGC	
LRRK2_Ex40_For	GAAGAAATGGAAAGTTTGCTATGATCC	468
LRRK2_Ex40_Rev	TCAGGGAAATGGTAGTTTTTCATCC	
LRRK2-ex41F	GGACAAAGTGAGCACAGAATTTTGA	377
LRRK2-ex41R	TCTGTTTTCTCTTTGACTCTTCTGAAGTC	
LRRK2_ex42_For_New	GCCTAAGTGATGCCTCCTTGG	590
LRRK2_ex42_Rev_New	CACCTCCAAGAAAACGAAAACATTCC	
LRRK2_ex43_For	GGAGATAATATTTTTCTTTGCAATGTCTGG	413
LRRK2_ex43_Rev	GGCATATGGGAGCATGTGAGG	
LRRK2_ex44_For	TTGGGTTCCAGTTTAACAGTTTTAGG	476
LRRK2_ex44_Rev	AAGCAAAACACATTGCTCTTGAATAC	
LRRK2_Ex45_For	GATGTCATCTTGATAGGCAAAACTTG	547
LRRK2_Ex45_Rev	TCTCTGTGACCTTCCACAATTCC	
LRRK2-ex46F	GGTCCTTGGAAAAGACATTCTTGG	465
LRRK2-ex46R	AGGATCTACTGTGTTCAAGATTTTATGAAGC	
LRRK2-ex47F	GCTACTGATTTCTGTATGTTGATTTTGAATCC	733
LRRK2-ex47R	CAAAGTTGATTGTCTTCCAATTTTCATGTC	
LRRK2-ex48F	TCAATTCAGAAATGGTTAGGGAAGAATATG	413
LRRK2-ex48R	CAGAGGCAGAAAGGAAGAAAAATCC	
Primer Name	NM 000345.3 Primer Sequence	Amplicon Size
SNCA_EX1_For	AGCAGCTGACGGGAAAAGC	690
SNCA_EX1_Rev	CCCCAAAGGGACAAGTACTCACC	
SNCA_EX2_For	AATGCCAGAGCTAAAAATGTCTGC	435
SNCA_EX2_Rev	GACTCAGTCCACCTTTTGTGACAAGC	
SNCA_EX3_F_new	AATTGGAGAGGACCTCCTGTTAGC	376
SNCA_EX3_Rev	TGCTCAGTGATTGTTTTACAATTTTCATAGG	
SNCA_EX4_F_NEW	CCAAATCACTCATGGCTTTACATTCC	548
SNCA_EX4_Rev	TTCACAAGGGGAGGGTCAGG	
SNCA_EX5_For	CATGTTGCCGCAATGTTTCC	688
SNCA_EX5_R_NEW	TCATCCCATTTGGACATGTATGG	
SNCA_EX6_For	GCAGAATATTTGCAAAAACATTGATTG	532
SNCA_ex6_R_bis	AATCACTAAACACTTCTGAACAACAGC	
Primer Name	NM 018206 Primer Sequence	Amplicon Size
VPS35-p.Asp620Asn-FWD	GCTGCAGAAAGTCTCACAGGATGG	444
VPS35-p.Asp620Asn-REV	CAAGCACCCCAAATGTTTCACC	
Primer Name	NM 016139.3 Primer Sequence	Amplicon Size
CHCHD2-ex1F	CCTGGCGCCAAGTTCAGG	506
CHCHD2-ex1R	ATGCCTTTCCCGTTGTTTGG	
CHCHD2-ex2F	CTGGGCAACAAGAGCGAAGC	535
CHCHD2-ex2R	CAGTGGGTTCTAAATCAAAGACAATTCC	
CHCHD2-ex3F	AGGCGTGAGCCACCATGTTT	436
CHCHD2-ex3R	AAACACAGATTACCCTAAGTTCTACAGGAT	
CHCHD2-ex4F	AGCACTCTGGAAGGCCAAGG	405
CHCHD2-ex4R	GAGTAGGGACACCCCACTTCC	





## Chapter 5

# General Discussion



# Discussion

The induced Pluripotent Stem Cell (iPSC) culture system with its potential for *in vitro* neuronal differentiation is an important tool for neurodegenerative research as it allows new possibilities for disease modelling of human cell types that are otherwise unattainable. Over the last decade this field has seen an exponential increase in available cell types, techniques and protocols for generating disease models. In the case of Parkinson's disease (PD) modelling, this has resulted in many different protocols for generating midbrain dopaminergic (DA) neurons *in vitro* (1). However, a major problem in modelling PD with iPSCs is that most models are unable to reproduce the neurodegeneration, making the current models unfit for research of this key hallmark of the disease (2). The hurdles for the iPSC modelling of PD are threefold. First, an obvious difference between the *in vitro* models and the disease in patients is the age of the cells after terminal differentiation, because by reverting adult cells to a stem cell state, markers of age are erased (3). This reset of cellular age may be the underlying reason why we do not observe increased neuronal death in PD patient derived iPSC based DA neuronal models without applying additional stress to the cells (**chapters 1 – 3**). The reset age may be overcome by applying age-associated insults, such as ROS exposure over time, which could induce DA neuronal death from accumulation of said insults. On the other hand, maintaining long term iPSC-derived DA neuronal cultures for the time needed to detect neuronal death is (currently) limited, which would especially be required for analysis of the late onset forms of PD. To master this problem, different techniques could be applied to mimic cellular aging, such as Progerin overexpression (4) or telomerase manipulation (5). These do not reproduce all aspects of normal aging (6), but may enhance the emergence of phenotypes associated with the disease. Alternatively, individual aging mechanisms (i.e. mitochondrial dysfunction) can be targeted to identify an alternative stress response in the PD modelling neurons.

Second, most DA neuron differentiation protocols use strong differentiation driving factors, which are not present during DA neuronal differentiation *in vivo* (1). It is therefore crucial that we characterize the iPSC derived cells carefully, to make sure they are comparable to those formed during embryonic development *in vivo*. Standardizing the characterisation would also allow for accurate comparison between the multitude of differentiation protocols available now. Currently, the major criterion used for indicating DA neurons is the presence of Tyrosine Hydroxylase (TH) (1). Although, the enzyme TH is present in all DA neurons, it cannot discern between neurons of the retrorubral area (RR,

A8), substantia nigra pars compacta (SNc, A9) and the ventral tegmental area (VTA, A10) (7). Additionally, TH is not only expressed in DA neurons, but also in all catecholaminergic neurons in the brain (i.e. noradrenergic neurons of the locus coeruleus), further diminishing the suitability of TH as a specific marker (8). Inclusion of markers such as the transcription factor SOX6, and the potassium channel GIRK2 in the characterisation would support identification of the SNc neuron population (7). This is essential in PD modelling as these are the cells that undergo selective neurodegeneration in patients. Furthermore, the neurons should be functionally characterised based on standardized criteria, such as dopamine secretion, and the characteristic electrophysiological activity of mature DA neurons to compare the maturity of the formed neurons from the different protocols.

Third, in the attempt to obtain functional and mature iPSC-derived DA neurons, most protocols used, are tailored to increase as much as possible the amount of DA neurons in the cultures, whereas also astrocytes, oligodendrocytes and GABAergic neurons are needed to support mature DA neuronal function to more accurately mimic the *in vivo* situation (9). Co-culture with other cell types could assist to further increase maturity of the DA neurons. This co-culture is already inherent to the protocols based on brain organoids, where the different cell types are even self-organising to form spatially patterned structures (10, 11). The organisation of the cells simulates the *in vivo* situation much more closely than single cell type cultures and possibly leads to more functional DA neurons. Moreover, as a human model for the midbrain, brain organoids could be used for drug testing once a phenotype is discovered, and could also allow for the detection of phenotypes that could otherwise not be detected in a 2D-culture system. However, organoid models still require optimization and standardization, and need to overcome technical issues such as cell death in the core of the organoids (10). Furthermore, analysis of the specific neurons of interest is much more complicated in these multi cell type models due to the interaction with other cell types that might mask a phenotype of the DA neurons, or even cause their own phenotype.

Our own research first focussed on generating *PARK20* patient iPSCs, and differentiating these into neurons to investigate the effect on autophagy (**chapter 2**). We found an impairment of autophagic flux based on accumulation of WIPI2 after 28 days terminal differentiation, confirming the finding in *Drosophila* *SYN<sup>RQ</sup> PARK20* model of the Verstreken group (Figure 1). Together, we show that Synaptojanin-1 has a role in promoting autophagosome maturation within presynaptic terminals and that this is distinct to the Synaptojanin-1 function in synaptic vesicle recycling. This predicts that defective synaptic

autophagy and abnormal protein homeostasis within presynaptic terminals contributes to *PARK20* pathology. Interestingly, the location of the *PARK20* mutation further supports the importance of the role of autophagy in PD, as the involved lipids PI(3)P and PI(3,5)P<sub>2</sub> are targeted by the SAC1 domain, which contains both *PARK20* mutations. In contrast, the function of Synaptojanin-1 in the synaptic vesicle cycle is affected by the 5'-phosphatase hydrolysis of PI(4,5)P<sub>2</sub>. The autophagosome maturation is impeded as the p.Arg258Gln mutated Synaptojanin-1 protein is unable to dephosphorylate the PI(3)P and PI(3,5)P<sub>2</sub> lipids of the autophagosome membrane (12, 13). Therefore, the lack of this Synaptojanin-1 function during autophagy, results in increased levels of PI(3)P and PI(3,5)P<sub>2</sub>, explaining the increased detection of WIPI2 protein binding to these autophagosomes, which normally is released after Synaptojanin-1 mediated dephosphorylation during maturation and subsequent fusion with lysosomes.

Although  $\alpha$ -synuclein has not yet been investigated in *PARK20* patients, it would be interesting to see whether the combination of increased levels or presence of mutated forms of the  $\alpha$ -synuclein protein with the impaired autophagic flux in the iPSC *PARK20* model system would lead to increased  $\alpha$ -synuclein protein accumulation or toxicity. Interestingly, Synaptojanin-1 has been found to be in the immediate vicinity of  $\alpha$ -synuclein in living neurons by using APEX-tag based labelling (14). Additionally, deletion of *SYNJ1* yeast homolog, combined with low, non-toxic, expression of  $\alpha$ -synuclein in yeast produced a strong and synergistic growth defect (15). This suggests that  $\alpha$ -synuclein toxicity and *SYNJ1* expression and/or function are linked, and it would therefore also be interesting to pathologically analyse brain material from deceased *PARK20* patients for the presence of  $\alpha$ -synuclein pathology (i.e. Lewy Bodies).

Based on our observations of the blocked autophagosome maturation in our *PARK20* iPSC model system, one remaining question is: What happens to the immature autophagosomes that cannot progress normally? One possible alternative mechanism, that could remove the excess of vesicles and their contents from immature autophagosomes, has been observed in a similar impairment of autophagosome maturation and fusion with lysosomes by p25 $\alpha$  overexpression (16). There, autophagic vesicles that are blocked in maturation are re-routed to the plasma membrane where their content is released into the extracellular space (16). We speculate that the affected protein clearance in *PARK20* iPSC-derived neurons might also be crucial in  $\alpha$ -synuclein clearance, necessary to prevent accumulation that could give rise to aggregation and toxicity (17). In fact, upon increase of the autophagosome pool, overexpressed mutated  $\alpha$ -synuclein has been shown to exit the cell through this pathway (Figure 1) (16).

This unconventional secretion of monomeric and aggregated  $\alpha$ -synuclein, introduces a possible route for cell to cell transmission of  $\alpha$ -synuclein. One possibility, to investigate both the  $\alpha$ -synuclein toxicity and the unconventional secretion in relation to defective synaptic autophagy, we could use our iPSC derived *PARK20* model for DA neurons (**chapter 3**) in combination with overexpression or pre-formed fibrils of  $\alpha$ -synuclein (18). The autophagy impairment first needs to be checked by staining with markers for autophagosomes and autolysosomes as we did in **chapter 2**. Alternatively we could overexpress a tandem fluorescent-tagged LC3 construct that marks autophagosomes and changes fluorescence upon fusion with a lysosome for live imaging of the vesicles (19). Next  $\alpha$ -synuclein accumulation can be determined using quantitative immunocytochemistry and RT-PCR analyses for  $\alpha$ -synuclein and neuronal markers (20). Neuron survival should also be verified by a Cell Viability Assay (20). Finally, the used culture medium should be collected and analysed for secreted  $\alpha$ -synuclein (16). Additionally, autophagy dependant exophagy could be regulated using trehalose to enhance or *ATG5* shRNA to reduce exophagy related secretion (16).

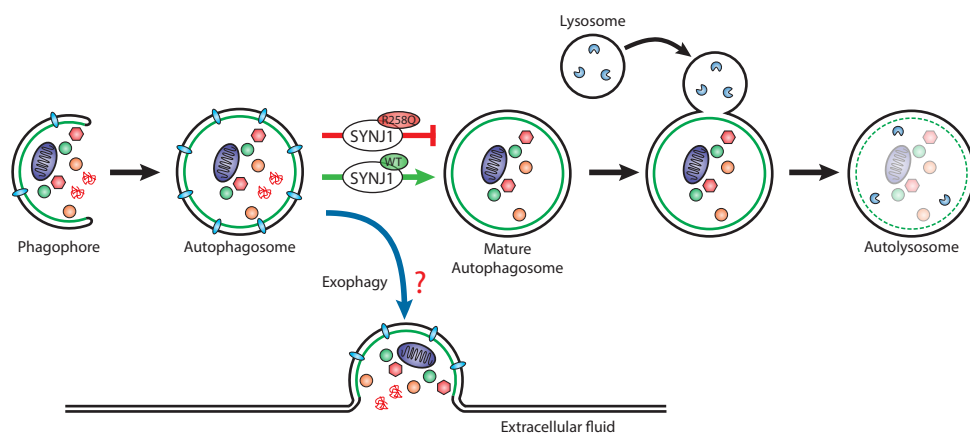


**Figure 1. Suggested exophagy route as a result of autophagosome accumulation**  
*Autophagosome maturation is impaired by the SYNJ1 p.Arg258Gln mutation, preventing fusion with a lysosome and content breakdown. Sequestered autophagosomes might secrete their contents by exophagy.*

Other results from our research into a human iPSCs derived DA neuron model for *PARK20* showed early reduction of PAX6, increase in Parkin levels and elevated mitochondrial activity (**chapter 3**). These findings are highly interesting as they propose multiple possible pathways to be affected in PD and suggest a previously unidentified role for Synptojanin-1 in mitochondrial function and biogenesis.

The reason behind the upregulation of Parkin is still unclear as the increase in Parkin is observed in human and mouse p.Arg258Gln mutants, but not in *SYNJ1* knockout mice (21, 22). The knockout mouse model also displays neonatal lethality, possibly due to multiple cell types being severely affected as both Synaptojanin-1 phosphatase domains are missing (21). However, the Parkin upregulation may not be visible in the knockout mice due to strongly increased mitophagy which could bring Parkin back to normal levels as we can see from the mitophagy induction experiments in **chapter 3**. Alternatively, Parkin could be upregulated by a gain of function of the p.Arg258Gln mutation, explaining the difference of Parkin expression with the knockout model. To test whether the increased expression is due to a gain or loss of function, we propose to generate human knockout lines from our patient lines using mutagenesis to create a non-sense mutation. Expression analysis of the following *SYNJ1* knockout human smNPCs could then be applied to identify Parkin upregulation, regardless of protein degradation by mitophagy.

In addition to the well-established function of Parkin in PINK1/Parkin mediated mitophagy, and increasing amount of evidence supports a role for Parkin in mitochondrial biogenesis (23-25). Mitophagy clears defective mitochondria by accumulation of PINK1 followed by recruitment of Parkin, which targets the mitochondria for degradation (26); however, Narendra et al. have shown that overexpression of Parkin alone already has an effect in accelerating mitophagy (27). Moreover, recent research into mitophagy further argues that the protein accumulation of PINK1 may not be important for the recruitment of Parkin to mitochondria (28). In addition, Parkin has previously been shown to be involved in mitochondrial biogenesis by regulating mitochondrial DNA transcription and regulation (23). Shin et al. have implicated Parkin in mitochondrial biogenesis regulation via inhibition of Parkin-Interacting Substrate (PARIS or ZNF746), which represses PGC-1 $\alpha$  and NRF-1, both important mediators of mitochondrial biogenesis (24, 25, 29). Finally, it has been shown that Parkin plays a protective role in the maintenance of normal mitochondrial respiration (30). Combining these data and our findings, we hypothesise that Parkin acts as a master regulator of mitochondrial homeostasis, and that increased levels of Parkin cause a higher turnover rate for mitochondria. This higher turnover rate would result in younger mitochondria, which may explain our finding of elevated mitochondrial activity. To confirm the hypothesis and assumptions our smNPCs should be tested for changes in protein levels of PARIS and PGC-1 $\alpha$  to verify the regulation by Parkin (25). Next the mitochondrial turnover should be determined; one way to achieve this is to transfect smNPCs to overexpress the so called “MitoTimer” protein (31). This mitochondria-targeted fluorescent protein transitions from green to red over 48 hours,

allowing for identification of newly formed mitochondria. The ratio of green to red will be indicative for mitochondrial turnover, where an increase in green fluorescent mitochondria means a higher turnover. Unfortunately mitochondria do contain the full range of DNA repair mechanisms that operate in the nucleus, mtDNA damage may therefore accumulate over the increased replications (32).

To further verify that the loss of SAC1 domain function is causing the phenotypes, the p.Arg459Pro Synaptojanin-1 mutation could be investigated. Although the effect of the p.Arg459Pro mutation on the phosphatase activity is unknown, a malachite-green based assay can be used to verify the impaired SAC1 phosphatase function. The p.Arg459Pro mutation could be generated by targeted mutagenesis using CRISPRCas9 and phenotypes detected in *PARK20* iPSC derived smNPCs/neurons could then be replicated. As both the p.Arg258Gln and p.Arg459Pro mutations are located within the same domain, this strongly implicates loss of SAC1 domain function as the cause for *PARK20* pathogenesis. Although the loss of function of the SYNJ1 SAC1 domain is responsible for the development of parkinsonism, loss of SYNJ1 dual phosphatase activity leads to a much more severe disease of neonatal refractory epilepsy with a neurodegenerative disease course (33-35). Conversely, increased SYNJ1 expression levels have been associated with Alzheimer's disease (36, 37). The association of SYNJ1 with these different diseases supports a strong genotype-phenotype correlation, and indicates that normal SYNJ1 expression levels are highly important and need to be tightly regulated to prevent disease.

Our identification of a novel gene *LRP10*, associated with familial PD, PD dementia (PDD), and dementia with Lewy bodies (DLB), allows for new opportunities for modelling (**chapter 4**) (38). This finding of a common gene between the diseases is especially important, because this highlights the common areas between the Lewy body diseases. Of the nine variants described, three severely affected *LRP10* expression and mRNA stability, four others reduced protein stability, and the last two mutations showed altered protein localisation. Based on these observations, it is highly likely that the phenotype is caused by a *LRP10* loss-of-function. Nevertheless, the mutations in the *LRP10* gene are likely to represent subtypes of an  $\alpha$ -synuclein-associated disease spectrum ranging from PD to PDD to DLB (39). Moreover, modelling of this gene may lead to the identification of a shared mechanism causing Lewy Bodies. Preliminary investigation of the *LRP10* protein in iPSC derived human neuronal cultures show strong co-localisation of *LRP10* with ADP-ribosylation factor-binding protein GGA1 in cell soma and neurites and partial co-localisation with retromer marker VPS35 in neuronal soma. The association with



VPS35 and GGA1 is worth investigating as these proteins may link LRP10 to  $\alpha$ -synuclein aggregation and Lewy Body disease. VPS35, in which mutations are known to cause familial PD, is described to be required for lysosomal degradation of  $\alpha$ -synuclein (40, 41). Furthermore, GGA1 function has been linked to alter  $\alpha$ -synuclein oligomerization and secretion (42). Interestingly, the distant LRP family member LRP1 has been described to potentially function as an efflux transporter of  $\alpha$ -synuclein (43). From these associations and the aberrant mutant LRP10 localisation, we can speculate that the mutations in LRP10 could impair correct protein transport of  $\alpha$ -synuclein, possibly leading to accumulation and toxicity. However, still only little is known about LRP10 and it would be interesting to first analyse the protein connections of wild type LRP10, for example via pulldown experiments. From there, one can identify cellular localisation and co-localisation with interacting proteins and compare this to localisation of the LRP10 mutants. This could possibly identify a defect in protein transport.

The PD patient derived iPSC model systems described above present the possibilities of employing the human iPSC-derived neuron model for functional studies into PD. However, the biggest opportunity for the iPSC based models lies in the possible application in cell replacement therapy. Whereas midbrain organoids are very suitable for disease modelling, these cells are unable to be transplanted for cell replacement therapy. For cell replacement therapy, pure cell populations of DA neurons are preferred to replenish the lost neurons. To make sure the correct DA neurons are transplanted, thorough characterisation is required. Furthermore, flow cytometry should be applied to purify the cell cultures and exclude any undifferentiated cells. A strong advantage is that the iPSC derived DA neurons are actually rejuvenated during the process of reprogramming into iPSCs (6). Features of cellular and molecular aging are reset, including telomere lengths, mitochondrial fitness, DNA damage foci, and reduced sensitivity to reactive oxygen species (3). While this poses a problem for modelling the neurodegeneration, it is beneficial for cell replacement therapy as the younger cells may take a long time to develop the same defects as the cells they are replacing. Furthermore, at symptom onset the DA neuron population is already decreased by 50-70% (44), indicating that the dopamine system can compensate up to that point. Therefore, already a small addition of healthy DA neurons might restore movement control for an extended period of time. In the cases of PD with identified genetic variants, the variants can even be corrected, though currently the risk of off-target effects would caution against it (45). These off-target effects are unpredictable and might cause problems in long term engraftment.

The main challenge in the therapy is to eliminate any risk of teratoma formation due

to transplantation of proliferating cells. Therefore, it is important that the iPSCs are created via non-integrating reprogramming, minimizing residual expression and reactivation of transgenes. This can be achieved using recently developed techniques of Adenovirus, Sendai virus, Episomal vector, mRNA or small molecule mediated reprogramming, resulting in high quality footprint-free iPSCs (46). Another challenge is that the reprogramming fails to completely reset the epigenetic profile, affecting gene expression levels in the derived cells (6). Further research is needed, but these changes might affect functionality in the long-term engraftments. An additional threat to the cell replacement therapy is the PD pathological mechanism itself. Researchers have shown that  $\alpha$ -synuclein aggregates could spread from one cell to another in a prion like fashion (47), which would mean that transplanted healthy and *SNCA* mutation free neurons may yet develop *SNCA* aggregates by cell-to-cell transmission. However, there is currently insufficient evidence that  $\alpha$ -synuclein aggregation is sufficient for toxicity. If the  $\alpha$ -synuclein aggregates do lead to neuronal death, PD will be difficult to cure by cell replacement therapy only, though the extra DA neurons would still keep symptoms at bay for a time. One could speculate that a combination therapy of cell replacement, in combination with for instance addition of compounds that keep  $\alpha$ -synuclein spreading at bay could increase the efficacy of the treatment. This needs to be further investigated.

## Conclusion

Patient derived iPSC models for Parkinson have successfully modelled many aspects of PD and thereby have further illustrated the pathogenic pathway of the disease. The investigation of the *PARK20* iPSC model for neurons and DA neurons has not given one definitive answer, but instead identified multiple possible pathways that could lead to neurodegeneration. In addition, the identification of the *LRP10* gene for Parkinson's disease, Parkinson's disease dementia, and dementia with Lewy bodies opens a new range of models to investigate for PD and Lewy body disease. By applying our DA neuron model to probe the cellular localisation of the newly discovered causative gene *LRP10*, we were able to identify a possible role of LRP10 in vesicular transport. Further modelling using LRP10 patient iPSC derived DA neurons will allow for further clarification of the proposed disease mechanism. In general, modelling PD using iPSC derived DA neurons has provided more insight into PD mechanisms, and will create new possibilities for the development of novel cell replacement and drug therapies.

# References

- Arenas E, Denham M, Villaescusa JC. How to make a midbrain dopaminergic neuron. *Development*. 2015;142(11):1918-36.
- Zhang Q, Chen W, Tan S, Lin T. Stem Cells for Modeling and Therapy of Parkinson's Disease. *Hum Gene Ther*. 2017;28(1):85-98.
- Vera E, Studer L. When rejuvenation is a problem: challenges of modeling late-onset neurodegenerative disease. *Development*. 2015;142(13):3085-9.
- Miller JD, Ganat YM, Kishinevsky S, Bowman RL, Liu B, Tu EY, et al. Human iPSC-based modeling of late-onset disease via progerin-induced aging. *Cell Stem Cell*. 2013;13(6):691-705.
- Vera E, Bosco N, Studer L. Generating Late-Onset Human iPSC-Based Disease Models by Inducing Neuronal Age-Related Phenotypes through Telomerase Manipulation. *Cell Rep*. 2016;17(4):1184-92.
- Mahmoudi S, Brunet A. Aging and reprogramming: a two-way street. *Curr Opin Cell Biol*. 2012;24(6):744-56.
- Anderegge A, Poulin JF, Awatramani R. Molecular heterogeneity of midbrain dopaminergic neurons—Moving toward single cell resolution. *FEBS Lett*. 2015;589(24 Pt A):3714-26.
- Tank AW, Xu L, Chen X, Radcliffe P, Sterling CR. Post-transcriptional regulation of tyrosine hydroxylase expression in adrenal medulla and brain. *Ann N Y Acad Sci*. 2008;1148:238-48.
- Tepper JM, Lee CR. GABAergic control of substantia nigra dopaminergic neurons. *Prog Brain Res*. 2007;160:189-208.
- Monzel AS, Smits LM, Hemmer K, Hachi S, Moreno EL, van Wuellem T, et al. Derivation of Human Midbrain-Specific Organoids from Neuroepithelial Stem Cells. *Stem Cell Reports*. 2017;8(5):1144-54.
- Jo J, Xiao Y, Sun AX, Cukuroglu E, Tran HD, Goke J, et al. Midbrain-like Organoids from Human Pluripotent Stem Cells Contain Functional Dopaminergic and Neuromelanin-Producing Neurons. *Cell Stem Cell*. 2016;19(2):248-57.
- Krebs CE, Karkheiran S, Powell JC, Cao M, Makarov V, Darvish H, et al. The Sac1 domain of SYN1 identified mutated in a family with early-onset progressive Parkinsonism with generalized seizures. *Hum Mutat*. 2013;34(9):1200-7.
- Proikas-Cezanne T, Takacs Z, Donnes P, Kohlbacher O. WIPI proteins: essential PtdIns3P effectors at the nascent autophagosome. *J Cell Sci*. 2015;128(2):207-17.
- Chung CY, Khurana V, Yi S, Sahni N, Loh KH, Auluck PK, et al. In Situ Peroxidase Labeling and Mass-Spectrometry Connects Alpha-Synuclein Directly to Endocytic Trafficking and mRNA Metabolism in Neurons. *Cell Syst*. 2017;4(2):242-50 e4.
- Khurana V, Peng J, Chung CY, Auluck PK, Fanning S, Tardiff DF, et al. Genome-Scale Networks Link Neurodegenerative Disease Genes to alpha-Synuclein through Specific Molecular Pathways. *Cell Syst*. 2017;4(2):157-70 e14.
- Ejlerskov P, Rasmussen I, Nielsen TT, Bergstrom AL, Tohyama Y, Jensen PH, et al. Tubulin polymerization-promoting protein (TPPP/p25alpha) promotes unconventional secretion of alpha-synuclein through exophagy by impairing autophagosome-lysosome fusion. *J Biol Chem*. 2013;288(24):17313-35.
- Wong YC, Krainc D. alpha-synuclein toxicity in neurodegeneration: mechanism and therapeutic strategies. *Nat Med*. 2017;23(2):1-13.
- Volpicelli-Daley LA, Luk KC, Lee VM. Addition of exogenous alpha-synuclein preformed fibrils to primary neuronal cultures to seed recruitment of endogenous alpha-synuclein to Lewy body and Lewy neurite-like aggregates. *Nat Protoc*. 2014;9(9):2135-46.
- Zhou C, Zhong W, Zhou J, Sheng F, Fang Z, Wei Y, et al. Monitoring autophagic flux by an improved tandem fluorescent-tagged LC3 (mTagRFP-mWasabi-LC3) reveals that high-dose rapamycin impairs autophagic flux in cancer cells. *Autophagy*. 2012;8(8):1215-26.
- Chung SY, Kishinevsky S, Mazzulli JR, Graziotto J, Mrejeru A, Mosharov EV, et al. Parkin and PINK1 Patient iPSC-Derived Midbrain Dopamine Neurons Exhibit Mitochondrial Dysfunction and alpha-Synuclein Accumulation. *Stem Cell Reports*. 2016;7(4):664-77.
- Cao M, Milosevic I, Giovedi S, De Camilli P. Upregulation of Parkin in endophilin mutant mice. *J Neurosci*. 2014;34(49):16544-9.
- Cao M, Wu Y, Ashrafi G, McCartney AJ, Wheeler H, Bushong EA, et al. Parkinson Sac Domain Mutation in Synaptotagmin 1 Impairs Clathrin Uncoating at Synapses and Triggers Dystrophic Changes in Dopaminergic Axons. *Neuron*. 2017;93(4):882-96 e5.
- Kuroda Y, Mitsui T, Kunishige M, Shono M, Akaike M, Azuma H, et al. Parkin enhances mitochondrial biogenesis in proliferating cells. *Hum Mol Genet*. 2006;15(6):883-95.
- Castillo-Quan JL. Parkin's control: regulation of PGC-1alpha through PARIS in Parkinson's disease. *Dis Model Mech*. 2011;4(4):427-9.
- Shin JH, Ko HS, Kang H, Lee Y, Lee YI, Pletnikova O, et al. PARIS (ZNF746) repression of PGC-1alpha contributes to neurodegeneration in Parkinson's disease. *Cell*. 2011;144(5):689-702.
- Pickrell AM, Youle RJ. The roles of PINK1, parkin, and mitochondrial fission in Parkinson's disease. *Neuron*. 2015;85(2):257-73.
- Narendra D, Tanaka A, Suen DF, Youle RJ. Parkin is recruited selectively to impaired mitochondria and promotes their autophagy. *J Cell Biol*. 2008;183(5):795-803.
- Xiao B, Goh JY, Xiao L, Xian H, Lim KL, Liou YC. Reactive oxygen species trigger Parkin/PINK1 pathway-dependent mitophagy by inducing mitochondrial recruitment of Parkin. *J Biol Chem*. 2017;292(40):16697-708.
- Scarpulla RC. Metabolic control of mitochondrial biogenesis through the PGC-1 family regulatory network. *Biochim Biophys Acta*. 2011;1813(7):1269-78.
- Gouspillou G, Godin R, Piquereau J, Picard M, Mofarrahi M, Mathew J, et al. Protective role of Parkin in skeletal muscle contractile and mitochondrial function. *J Physiol*. 2018;596(13):2565-79.
- Laker RC, Xu P, Ryall KA, Sujkowski A, Kenwood BM, Chain KH, et al. A novel MitoTimer reporter gene for mitochondrial content, structure, stress, and damage in vivo. *J Biol Chem*. 2014;289(17):12005-15.
- Cline SD. Mitochondrial DNA damage and its consequences for mitochondrial gene expression. *Biochim Biophys Acta*. 2012;1819(9-10):979-91.
- Al Zaabi N, Al Menhali N, Al-Jasmi F. SYN1 gene associated with neonatal onset of neurodegenerative disorder and intractable seizure. *Mol Genet Genomic Med*. 2018;6(1):109-13.
- Dymont DA, Smith AC, Humphreys P, Schwartzentruber J, Beaulieu CL, Consortium FC, et al. Homozygous nonsense mutation in SYN1 associated with intractable epilepsy and tau pathology. *Neurobiol Aging*. 2015;36(2):1222 e1-5.

35. Hardies K, Cai Y, Janelle C, Jansen AC, Cao M, May P, et al. Loss of SYN1 dual phosphatase activity leads to early onset refractory seizures and progressive neurological decline. *Brain*. 2016;139(Pt 9):2420-30.
36. Miranda AM, Herman M, Cheng R, Nahmani E, Barrett G, Micevska E, et al. Excess Synaptojanin 1 Contributes to Place Cell Dysfunction and Memory Deficits in the Aging Hippocampus in Three Types of Alzheimer's Disease. *Cell Rep*. 2018;23(10):2967-75.
37. Cossec JC, Lavour J, Berman DE, Rivals I, Hoischen A, Stora S, et al. Trisomy for synaptojanin1 in Down syndrome is functionally linked to the enlargement of early endosomes. *Hum Mol Genet*. 2012;21(14):3156-72.
38. Quadri M, Mandemakers W, Grochowska MM, Masius R, Geut H, Fabrizio E, et al. LRP10 genetic variants in familial Parkinson's disease and dementia with Lewy bodies: a genome-wide linkage and sequencing study. *Lancet Neurol*. 2018;17(7):597-608.
39. Jellinger KA. Dementia with Lewy bodies and Parkinson's disease-dementia: current concepts and controversies. *J Neural Transm (Vienna)*. 2018;125(4):615-50.
40. Miura E, Hasegawa T, Konno M, Suzuki M, Sugeno N, Fujikake N, et al. VPS35 dysfunction impairs lysosomal degradation of alpha-synuclein and exacerbates neurotoxicity in a Drosophila model of Parkinson's disease. *Neurobiol Dis*. 2014;71:1-13.
41. Follett J, Bugarcic A, Yang Z, Ariotti N, Norwood SJ, Collins BM, et al. Parkinson Disease-linked Vps35 R524W Mutation Impairs the Endosomal Association of Retromer and Induces alpha-Synuclein Aggregation. *J Biol Chem*. 2016;291(35):18283-98.
42. von Einem B, Eschbach J, Kiechle M, Wahler A, Thal DR, McLean PJ, et al. The Golgi-localized, gamma ear-containing, ARF-binding (GGA) protein family alters alpha synuclein (alpha-syn) oligomerization and secretion. *Aging (Albany NY)*. 2017;9(7):1677-97.
43. Sui YT, Bullock KM, Erickson MA, Zhang J, Banks WA. Alpha synuclein is transported into and out of the brain by the blood-brain barrier. *Peptides*. 2014;62:197-202.
44. Liu LX, Du D, Zheng T, Fang Y, Chen YS, Yi HL, et al. Detecting dopaminergic neuronal degeneration using diffusion tensor imaging in a rotenone-induced rat model of Parkinson's disease: fractional anisotropy and mean diffusivity values. *Neural Regen Res*. 2017;12(9):1485-91.
45. Kosicki M, Tomberg K, Bradley A. Repair of double-strand breaks induced by CRISPR-Cas9 leads to large deletions and complex rearrangements. *Nat Biotechnol*. 2018;36(8):765-71.
46. Schlaeger TM, Daheron L, Brickler TR, Entwistle S, Chan K, Cianci A, et al. A comparison of non-integrating reprogramming methods. *Nat Biotechnol*. 2015;33(1):58-63.
47. Prusiner SB, Woerman AL, Mordes DA, Watts JC, Rampersaud R, Berry DB, et al. Evidence for alpha-synuclein prions causing multiple system atrophy in humans with parkinsonism. *Proc Natl Acad Sci U S A*. 2015;112(38):E5308-17.





Chapter 6

# Appendix

# Summary

Parkinson's disease (PD) is characterized by progressive neurodegeneration that primarily depletes dopaminergic neurons in the substantia nigra pars compacta, resulting in the PD quintessential motor symptoms. Animal models for PD have replicated many features of the neurodegeneration and LB pathology; however, there is no model that fully reproduces the human disease. Therefore, a human model of PD neurons is needed to accurately investigate the underlying molecular mechanisms. Recent advancements in the field of stem cell research have opened up new possibilities for modelling of difficult-to-obtain cell types. In 2006, Yamanaka et al. were the first to dedifferentiate fibroblasts into induced pluripotent stem cells (iPSCs), and thereby identifying the necessary transcription factors to express that mediate dedifferentiation. With an improved delivery method these factors remain the basis for today's iPSCs. Combined with a directed differentiation, it is possible to create a new replenishable source of human derived neurons. This is especially important for PD, as research suffers from lack of access and availability of affected human midbrain dopaminergic neurons. Research in this thesis applies these new techniques to set up models based on patients with familial PD and aims to find affected cellular mechanisms in PD.

A *Drosophila* model for the SYNJ1 p.Arg258Gln mutation shows the effects of this mutation on macroautophagy in **Chapter 2**. The known function of the lipid phosphatase Synaptojanin-1 is to allow synaptic endocytosis by dephosphorylating PI(4,5)P<sub>2</sub> at the synaptic membrane. Though, we present that Synaptojanin-1 is required for macroautophagy, and that this effect is inhibited by the Parkinson's disease mutation p.Arg258Gln. By advanced imaging we observe accumulation of the PI(3)P/PI(3,5)P<sub>2</sub>-binding protein Atg18a in *Synaptojanin*<sup>RQ</sup> mutant fly synapses, indicating an obstruction of autophagosome maturation. Using the human iPSC derived neuron model with the same mutation we were able to verify accumulation of autophagosomes, exemplified by increased levels of WIPI2 protein, the human counterpart of Atg18 in p.Arg258Gln patient derived neurons. Additionally, neurodegeneration, including dopaminergic neuron loss, is observed in *Synaptojanin*<sup>RQ</sup> flies. These findings link presynaptic-specific autophagy defects to PD.

In **Chapter 3** we present, to our knowledge, the first model with iPSC generated dopaminergic neurons from *PARK20* patients with the homozygous SYNJ1 mutation c.773G>A, p.Arg258Gln. Starting from cells from patients with this early-onset form of



PD the model might allow us to demonstrate origins of neuron degeneration without inducing *in vitro* aging. To determine the early causes, we examined three stages of cell development: the generated iPSCs, the neuron progenitor intermediate, and the dopamine neurons. The resulting iPSCs were indistinguishable between control and patient lines; however, from the progenitor stage on Parkin was upregulated while PAX6 was downregulated in patient lines. Furthermore, mitochondrial respiration was higher in patient lines which may indicate a higher mitochondrial turnover. These findings highlight the importance of Synaptojanin-1 in various cellular mechanisms and suggest a previously unidentified role for Synaptojanin-1 in mitochondrial function and biogenesis.

We also apply the model of human dopaminergic neurons to the first steps in functional investigation of a newly discovered gene for familial PD and dementia with Lewy bodies in **Chapter 4**. Our study identified nine rare *LRP10* variants associated with familial PD, PD dementia, and dementia with Lewy bodies. Of the nine variants described, three severely affected LRP10 expression and mRNA stability (1424+5delG, 1424+5G>A, and Ala212Serfs\*17), which was determined by cDNA analysis. Four others affected protein stability (Tyr307Asn, Gly603Arg, Arg235Cys, and Pro699Ser, shown by cycloheximide-chase experiments. The last two mutations (Asn517del and Arg533Leu) affected protein localisation displayed by immunocytochemistry. Together these findings indicate loss of LRP10 function as the pathogenic mechanism. We used iPSC derived, 12week old, human neuronal cultures overexpressing V5-tagged LRP10 to determine the subcellular localisation. In these neurons the protein localised to vesicular structures in the neuronal soma and neurites, including endosomes, the retromer complex, and the trans-Golgi network.

Together, the work presented in this thesis shows the possibilities of employing the human iPSC-derived neuron model for PD. This application allowed the discovery of new mechanisms involved in PD; proving itself a powerful tool in the further clarification of the underlying mechanisms that cause PD. The model also gave first insights into the workings of the newly discovered gene for familial PD, PD dementia and dementia with Lewy bodies, LRP10. In future research, a combination of the model with gene editing would even allow for investigation of all genetic forms of PD, without the need for specific patient material. Eventually, gene corrected human iPSC-derived dopaminergic neurons might even be used in transplantation therapies to replenish the diminishing population in PD patient brains.

# Samenvatting

De ziekte van Parkinson wordt gekenmerkt door progressieve neurodegeneratie, die voornamelijk dopaminerge neuronen in de substantia nigra pars compacta aantast, resulterend in de motorische symptomen typisch voor Parkinson. Diermodellen voor Parkinson hebben veel kenmerken van de neurodegeneratie en LB-pathologie gerepliceerd; er is echter geen model die de menselijke ziekte volledig reproduceert. Daarom is een menselijk model van Parkinson-neuronen nodig om de onderliggende moleculaire mechanismen nauwkeurig te onderzoeken. Recente ontwikkelingen op het gebied van stamcelonderzoek bieden nieuwe mogelijkheden voor het modelleren van moeilijk te verkrijgen celtypen. Yamanaka et al. waren in 2006 de eersten om fibroblasten terug te laten ontwikkelen tot geïnduceerde pluripotente stamcellen (iPSCs) en identificeerden hierbij de daarvoor nodige expressie factoren. De toedieningsmethode is verbeterd, maar deze factoren zijn nog steeds de basis voor hedendaagse iPSCs. Gecombineerd met een gerichte celdifferentiatie is het mogelijk om een nieuwe bron van menselijke neuronen te creëren. Deze nieuwe en continu aanvulbare bron van neuronen is vooral belangrijk voor de ziekte van Parkinson, omdat het onderzoek lijdt aan een gebrek aan toegankelijkheid en beschikbaarheid van de aangetaste dopaminerge neuronen van de menselijke middenhersenen. Het onderzoek in dit proefschrift past deze nieuwe technieken toe om modellen op te stellen op basis van patiënten met familiale vormen van de ziekte van Parkinson en is gericht op het vinden van aangetaste cellulaire mechanismen bij de ziekte van Parkinson.

Met een *Drosophila*-model voor de SYNJ1 p.Arg258Gln-mutatie toont **Hoofdstuk 2** de effecten op macroautofagie. De bekende functie van de lipidefosfatase Synaptojanin-1 is om synaptische endocytose mogelijk te maken door PI(4,5)P<sub>2</sub> te defosforyleren op het synaptische membraan. Echter, wij opperen dat Synaptojanin-1 ook vereist is voor macroautofagie, en dat dit effect wordt geremd door de Parkinson mutatie p.Arg258Gln. Door middel van geavanceerde imaging observeren we de accumulatie van het PI(3)P/PI(3,5)P<sub>2</sub>-bindende eiwit Atg18a in Synaptojanin<sup>RQ</sup>-mutant vlieg-synapsen, wat wijst op een obstructie van de maturatie van autofagosomen. Met behulp van het menselijke iPSC-afgeleide neuronmodel voor dezelfde mutatie konden we ook accumulatie van WIPI2, de menselijke tegenhanger van Atg18, verifiëren. Bovendien wordt neurodegeneratie, inclusief dopaminerge neuronverlies, waargenomen bij de Synaptojanin<sup>RQ</sup>-vliegen. Deze bevindingen koppelen de presynaptisch-specifieke autofagische defecten aan de ziekte van Parkinson.

In **Hoofdstuk 3** presenteren we, naar ons weten, het eerste model met iPSC gegenereerde dopaminere neuronen van *PARK20*-patiënten met de homozygote *SYNJ1*-mutatie c.773G> A, p.Arg258Gln. Beginnend met cellen van patiënten met deze vroege vorm van Parkinson kunnen we mogelijk met het model de oorsprong van neuron degeneratie aantonen zonder in vitro veroudering te induceren. Om de vroegtijdige oorzaken te bepalen, onderzochten we drie stadia van celontwikkeling: de gegenereerde iPSCs, de neuron voorlopercel en de dopamine neuronen. De resulterende iPSCs waren niet te onderscheiden tussen controle- en patiëntlijnen; echter, vanaf het neuron voorloperstadium werden niveaus van Parkin verhoogd en van PAX6 verlaagd in patiëntlijnen. Bovendien was de mitochondriale respiratie hoger in patiëntlijnen, wat kan duiden op een versnelde mitochondriale levenscyclus. Deze bevindingen onderstrepen het belang van Synaptojanin-1 in diverse cellulaire mechanismen en suggereren een voorheen onbekende rol voor Synaptojanin-1 in de mitochondriale functie en aanmaak.

We pasten het model van menselijke dopaminerge neuronen ook toe op de eerste stappen in functioneel onderzoek van een nieuw ontdekt gen voor familiale Parkinson en dementie met Lewylichaampjes in **Hoofdstuk 3**. Ons onderzoek identificeerde negen zeldzame *LRP10*-varianten geassocieerd met familiale Parkinson, de ziekte van Parkinson met dementie en dementie met Lewylichaampjes. Van de negen beschreven varianten, tasten drie ernstig *LRP10*-expressie en mRNAstabiliteit aan (1424+5delG, 1424+5G>A, en Ala212Serfs\*17), dit werd vastgesteld door cDNA-analyse. Vier anderen beïnvloeden de eiwitstabiliteit (Tyr307Asn, Gly603Arg, Arg235Cys en Pro699Ser, aangetoond met cycloheximide-chase-experimenten). De laatste twee mutaties (Asn517del en Arg533Leu) hadden invloed op de eiwitlokalisatie, dit werd weergegeven door immunocytochemie. Samen duiden ze op verlies van de *LRP10*-functie als het pathogene mechanisme. We gebruikten iPSC-afgeleide, 12 weken oude, humane neuronale culturen die V5-gelabeld *LRP10* tot overexpressie brachten om de subcellulaire lokalisatie te bepalen. In deze neuronen is het eiwit gelokaliseerd in vesiculaire structuren in de neuronale soma en neurieten, waaronder endosomen, het retromercomplex en het trans-Golgi-netwerk.

Het werk dat in dit proefschrift wordt gepresenteerd toont de mogelijkheden van het gebruik van het menselijke iPSC-afgeleide neuron model. De toepassing van het model maakte de ontdekking mogelijk van nieuwe mechanismen die betrokken zijn bij de ziekte van Parkinson. Hiermee heeft het zichzelf bewezen als een krachtig hulpmiddel bij het verder ophelderen van de onderliggende mechanismen die Parkinson veroorzaken. Het model gaf ook de eerste inzichten in de werking van het nieuw ontdekte gen

voor familiale Parkinson en dementie met Lewy-lichamen, LRP10. Bovendien zou in vervolgonderzoek, combinatie van het model met genediting zelfs onderzoek van alle genetische vormen van de ziekte van Parkinson mogelijk maken, zonder de noodzaak voor specifiek patiëntmateriaal. Dit zou uiteindelijk kunnen leiden tot gen-gecorrigeerde menselijke iPSC-afgeleide dopaminerge neuronen die voor transplantaties gebruikt kunnen worden om de afnemende populatie neuronen in de hersenen van de Parkinson patiënt aan te vullen.

# List of publications

Quadri M, Mandemakers W, Grochowska MM, **Masius R**, Geut H, Fabrizio E, Breedveld GJ, Kuipers D, Minneboo M, Vergouw LJM, Carreras Mascaro A, Yonova-Doing E, Simons E, Zhao T, Di Fonzo AB, Chang HC, Parchi P, Melis M, Correia Guedes L, Criscuolo C, Thomas A, Brouwer RWW, Heijnsman D, Ingrassia AMT, Calandra Buonauro G, Rood JP, Capellari S, Rozemuller AJ, Sarchioto M, Fen Chien H, Vanacore N, Olgiati S, Wu-Chou YH, Yeh TH, Boon AJW, Hoogers SE, Ghazvini M, Ijpma AS, van Ijcken WFJ, Onofrj M, Barone P, Nicholl DJ, Puschmann A, De Mari M, Kievit AJ, Barbosa E, De Michele G, Majoor-Krakauer D, van Swieten JC, de Jong FJ, Ferreira JJ, Cossu G, Lu CS, Meco G, Cortelli P, van de Berg WDJ, Bonifati V; International Parkinsonism Genetics Network. LRP10 genetic variants in familial Parkinson's disease and dementia with Lewy bodies: a genome-wide linkage and sequencing study, *Lancet Neurology* 2018 Jul;17(7):597-608. doi: 10.1016/S1474-4422(18)30179-0.

Vanhauwaert R, Kuenen S, **Masius R**, Bademosi A, Manetsberger J, Schoovaerts N, Bounti L, Gontcharenko S, Swerts J, Vilain S, Picillo M, Barone P, Munshi ST, de Vrij FM, Kushner SA, Gounko NV, Mandemakers W, Bonifati V, Meunier FA, Soukup SF, Verstreken P. The SAC1 domain in synaptojanin is required for autophagosome maturation at presynaptic terminals, *EMBO Journal* 2017 May 15;36(10):1392-1411. doi: 10.15252/embj.201695773.

W. Beukers, R. Kandimalla, **R.G. Masius**, M. Vermeij, R. Kranse, G.J.H.L. van Leenders, E.C. Zwarthoff, Stratification based on methylation of TBX2 and TBX3 into three molecular grades predicts progression in patients with pTa bladder cancer, *Modern Pathology* 2015 Apr;28(4):515-22. doi: 10.1038/modpathol.2014.145.

Y. Allory, W. Beukers, A. Sagrera, M. Flández, M. Marqués, M. Márquez, K.A. van der Keur, L. Dyrskjot, I. Lurkin, M. Vermeij, A. Carrato, J. Lloreta, J.A. Lorente, E. Carrillo-de Santa Pau, **R.G. Masius**, M. Kogevinas, E.W. Steyerberg, A.A.G. van Tilborg, C. Abas, T.F. Orntoft, T.C.M. Zuiverloon, N. Malats, E.C. Zwarthoff, F.X. Real, Telomerase Reverse Transcriptase Promoter Mutations in Bladder Cancer: High Frequency Across Stages, Detection in Urine, and Lack of Association with Outcome, *European Urology*, Volume 65, Issue 2, February 2014, pages 360–366, doi: 10.1016/j.eururo.2013.08.052

R. Kandimalla, **R. Masius**, W. Beukers, C.H. Bangma, T.F. Orntoft, L. Dyrskjot, N. van Leeuwen, H. Lingsma, A.A. van Tilborg, E.C. Zwarthoff, A 3-plex methylation assay combined with the FGFR3 mutation assay sensitively detects recurrent bladder cancer in voided urine, *Clinical Cancer Research*, Volume 19, Issue 17, September 2013, pages 4760–4769, doi: 10.1158/1078-0432.CCR-12-3276.

W. Beukers, R. Kandimalla, **R. Masius**, M. Vermeij, E.C. Zwarthoff, Validation of TBX2, TBX3, GATA2, and ZIC4 as pTa-specific prognostic bladder cancer markers, *European Urology Supplements*, Volume 12, Issue 1, March 2013, Page e54, doi: 10.1016/S1569-9056(13)60547-3.

R. Kandimalla, Tilborg A.G. Van, **R. Masius**, L. Kompier, D. Stumpel, R. Stam, C. Bangma, E.C. Zwarthoff, Genome-wide analysis of CpG island methylation in bladder cancer identifies novel biomarkers for diagnosis and prediction of progression, *European Urology Supplements*, Volume 11, Issue 1, February 2012, Page e328, doi: 10.1016/S1569-9056(12)60325-X.

# Curriculum Vitae

## Personal information:

Name: Masius  
First names: Roy Geordi  
Date of birth: 13 September 1988  
Address: Russischestraat 62A  
Zip code: 3028 BH  
City: Rotterdam  
Phone number: +31 681148624  
E-mail address: rg.masius@gmail.com

## Professional experience

*Erasmus MC, Rotterdam, The Netherlands*

PhD Student in the group of Prof. Dr. V. Bonifati, Department of Clinical Genetics

November 2014 – October 2018

We established human iPSC-derived neurons as a model for Parkinson's disease. We focus on functional analysis of these neurons to gain insight into the function of Parkinson's disease related genes and the effect of their associated disease causing mutations.

*Josephine Nefkens Institute, Rotterdam, The Netherlands*

Research analyst in the group of Prof. Dr. E.C. Zwarthoff, Department of Pathology

September 2011 – September 2013

The work focused on validation of epigenetic markers for the prediction of progression, and the reactivation of methylated genes and the role of DNA methylation in non-promoter CpG islands. The work performed contributed to publication in European Urology, European Urology Supplements, and Modern Pathology.

## Education

*Leiden University, Leiden, the Netherlands*

Master of Science in Life Science and Technology (2014)

Thesis: The effect of pathogenic mutations on FBXO7 protein function in Parkinson's disease

*Hogeschool Zeeland, Vlissingen, the Netherlands.*

Bachelor of Applied Sciences in Chemistry, majoring in Life Sciences (2011)

Thesis: Genome-Wide DNA Methylation Profiling in Bladder Cancer and Identification of Diagnostic and Prognostic Markers

## Internships

*Erasmus MC, Rotterdam, The Netherlands*

Group of Prof. Dr. Vincenzo Bonifati, supervision of Dr. Wim Mandemakers

Internship for Master of Science in Life Science and Technology

The project of the internship was about the determining the function of F-Box Only Protein 7 which is mutated in familial cases of early onset parkinsonism.

*Josephine Nefkens Institute, Rotterdam, The Netherlands*

Group of Prof. Dr. E.C. Zwarthoff, supervision of Dr. Raju Kandimalla

Internship for Bachelor of Applied Sciences in Chemistry

The project of the internship was about the development of a urine based diagnostic assay for the detection of Bladder Cancer recurrences. The internship thesis was nominated for the Gouden Spatel award 2011. The work performed contributed to publication in Clinical Cancer Research and European Urology Supplements.

# PhD Portfolio

	Year	ECTS
<b>Courses:</b>		
Scientific Integrity	2014	0,5
Genetics	2015	3
Functional Imaging and Super Resolution	2015	2
Special topics course on Chromatin	2015	2
Biomedical English Writing and Communication	2018	3
Safely working in the Laboratory	2018	0,25
<b>Workshops:</b>		
21st MGC PhD student workshop, Münster	2014	1
22nd MGC PhD student workshop, Maastricht	2015	1
23rd MGC PhD student workshop, Dortmund	2016	1
24th MGC PhD student workshop, Leuven	2017	1
<b>(Inter)National Meetings:</b>		
Dutch Society for Stem Cell research (DSSCR) annual meeting, Utrecht	2015	0,5
Annual iPSC user meeting, Nijmegen	2015	0,5
IAPRD 2015 - XXI World Congress on Parkinson's disease and related disorders, Milan	2015	2
ISSCR/CRTD's Stem Cell Models of Neural Regeneration and Disease International Symposium, Dresden	2016	1
EU Joint Programme – Neurodegenerative Disease Research (JPND), 3DPD project kick-off meeting, Luxembourg	2016	0,5
Dutch Society for Stem Cell research (DSSCR) annual meeting, Utrecht	2016	0,5
13th International Conference on Alzheimer's & Parkinson's , Vienna	2017	2
Dutch Society for Stem Cell research (DSSCR) annual meeting, Utrecht	2017	0,5
EU Joint Programme – Neurodegenerative Disease Research (JPND), 3DPD project annual meeting, Münster	2017	0,5
JPco-fuND 2015 intermediate symposium, Den Haag	2017	0,5
EU Joint Programme – Neurodegenerative Disease Research (JPND), 3DPD project annual meeting, Rotterdam	2018	0,5
<b>Presentations:</b>		
Poster, Dutch Society for Stem Cell research (DSSCR) annual meeting, Utrecht	2015	0,25
Poster, Dutch Society for Stem Cell research (DSSCR) annual meeting, Utrecht	2016	0,25
Poster, 23rd MGC PhD student workshop, Dortmund	2016	0,25
Poster, 13th International Conference on Alzheimer's & Parkinson's , Vienna	2017	0,25
Oral presentation JPND, 3DPD project annual meeting, Münster	2017	0,5
Oral presentation 24th MGC PhD student workshop, Leuven	2017	0,5
Poster, JPco-fuND 2015 intermediate symposium, Den Haag	2017	0,25
Oral presentation EU Joint Programme – Neurodegenerative Disease Research (JPND), 3DPD project annual meeting, Rotterdam	2018	0,5



	Year	ECTS
<b>Teaching:</b>		
Supervision of Master student Feb-May	2015	1
Supervision of Bachelor student Feb-Jul	2015	2
Supervision of Master student Okt-Apr	2015/2016	2
Supervision of Master student Okt-Apr	2016/2017	2
Supervision of Master student Okt-Jun	2016/2017	2
<b>Other activities:</b>		
Organizing committee 23rd MGC PhD student workshop, Dortmund	2015/2016	2
<b>Total ECTS</b>		<b>37,5</b>

# Dankwoord

Dear Vincenzo, thank you for giving me the opportunity to work in your group. We first met five years ago during my masters when I was looking for an internship position. From the start your passion and enthusiasm for science have inspired me and over the years, your deep knowledge and experience have thought me a lot. Moreover, your warm personality has made your group very pleasant to work in. Thank you for believing in me and helping me to become a better scientist.

Beste Wim, heel erg bedankt voor je begeleiding tijdens mijn stage en PhD onderzoek. We hebben wat tijdrovende tegenslagen gehad maar met jouw hulp heb ik mijn PhD project toch binnen 4 jaar met succes weten af te ronden. Je uitgebreide kennis en vele ideeën zijn hierbij onmisbaar geweest en hebben mij in de tussentijd veel geleerd. We zaten al vaak op een lijn, maar ook wanneer ik andere ideeën had kreeg ik de ruimte en vrijheid om die uit te werken, wat ik erg kan waarderen. Ook met het schrijven van mijn dissertatie en afronden van mijn PhD heb ik nog veel van je mogen leren en ik ben blij met het boekje dat ik neer hebben kunnen zetten. Het was erg fijn met je samen te werken de afgelopen jaren.

I would like to thank Prof. Dr. R.J. Pasterkamp, Prof. Dr. J.C. Schwamborn, and Prof. Dr. R. Willemsen for taking part in the reading committee, and for evaluating my thesis. I also want to thank the other members of the committee, Prof. Dr. J.H. Gribnau and Prof. Dr. S.A. Kushner.

Mijn paranimfen Michelle en Fenne ben ik uiteraard ook dankbaar. Michelle, bedankt voor alle hulp met m'n experimenten en met name ook voor het bijspringen in de weekenden en vakanties voor het kweken van de cellen. Je was altijd erg attent en vriendelijk naar iedereen die naar je toe kwam. We hebben samen ook een tijd lang de celkweek op orde proberen te krijgen en al was dat misschien vanaf het begin al een hopeloze zaak, was het erg handig dat ik jou op mensen kon afsturen als ze weer eens hun dienst verzaakten. Bedankt dat je mijn paranimf wilde zijn. Fenne bedankt voor de gezellige MGC workshops en de biertjes die we gedronken hebben. Je vriendelijkheid en aandachtig luisteren maakten voor fijne gesprekken zowel op als buiten het werk. Ik wens je heel erg veel succes met het schrijven van je eigen boekje en je verdediging volgend jaar. Ook jij bedankt dat je mijn paranimf wilde zijn.

Verder wil ik iedereen bedanken uit de Parkinson groep: Guido, Marialuisa, Martyna, Demy, Ana, Simone, Josja, Christian, Victor, Brenda, Naomi, en mijn eigen studenten, Lina, Jordi, Stephanie, Sara, en Lieke. Bedankt voor jullie input in de wekelijkse werkbesprekingen en voor een vriendelijke en fijne werkomgeving. Jullie bijdrage en steun stel ik erg op prijs en ik wens jullie veel geluk in je verdere carrières. Guido, bedankt voor de ondersteuning bij experimenten en Martyna, voor het helpen met de celkweek tijdens vakanties. En mijn laatste student, Lieke, heel erg bedankt voor jouw bijdrage aan mijn thesis en ik hoop van harte dat je verder gaat in de research.

Alle andere mensen op de research afdeling van de klinische genetica wil ik ook graag bedanken. Het hoofd van de afdeling, Robert, en de PI's, Annelies, Grazia, Pim, Tjakko, Renate, en Stefan, bedankt voor de fijne discussies bij de research meetings en ik wens jullie veel nieuwe ontdekkingen toe. Natuurlijk mijn collega's van de verschillende labs bedank ik voor alle hulp en gezelligheid: Saif, Laura V, Kathrine, Atze, Erik, Mike, Laura K, Elena, Pablo, Rodrigo, Kyra, Wojtek, Natasha, Judith, Rob V, Lies-Anne, Shami, Herma, Erwin, Stijn, Joon, Rachel S, Esmay, Gerben, Tom, Bianca, William, Mark, Leontine, Marianne, Jeanette, Bep, Marike, Rachel N, Ronald, Helen, Wim, Maria, Merel, Rhiana, Quishi, Monica, Douglas, Rajendra, and Danny.

Dan wil ik nog Mehrnaz en haar team van de *Erasmus MC iPS core facility* bedanken voor de ondersteuning met het maken en kweken van de iPS cellen. Ook de leden van groep van Prof. Dr. S.A. Kushner waarmee, onder leiding van Femke, we wekelijkse werkbesprekingen hielden over iPS celkweek wil ik bedanken: Femke, Sashini, Guy, Mark, Bas, Nilhan, Stefano, Roberto, Ineke, Michelle, Sakshi, Hilde, en Giuseppe. In bijzonder Femke en Shashini dank ik voor het helpen met de eerste differentiatie protocollen.

Next I would like to thank all the collaborators that have made the research in this thesis possible. First, Prof. Dr. P. Verstreken and his team for the collaboration that led to the publication of the autophagosome maturation defect caused by SYNJ1 mutations. Especially Roeland, for his fine work in this paper. Also the members of the *3D-PD - brain on a chip*, JPND collaboration, Prof. Dr. J.C. Schwamborn, Prof. Dr. H.R. Schöler, Prof. Dr. P. Ertl, Prof. Dr. D. Seliktar, and their labmembers. Particularly Emanuel Berger from LCSB for performing the extracellular flux analysis experiments. Also, special thanks to Thomas Rauen and Anna-Lena Hallmann for recently creating isogenic controls of our patient iPSC lines.

Natuurlijk wil ik ook al mijn vrienden en familie bedanken voor de afleiding die ze boden buitenom het werk. De gezellige momenten samen gaven me de energie die ik soms nodig had om door te gaan. Bedankt voor alle feestjes, gezellige avondjes, potjes tennissen en droge humor!

Pa en ma, zonder jullie was ik nooit zover gekomen. Jullie hebben me altijd gesteund en gestimuleerd om te doen wat ik leuk en interessant vond. Ook tijdens mijn PhD hebben jullie mij gesteund en interesse getoond voor mijn onderzoek. Nu rest alleen nog de verdediging en ik hoop dan eindelijk goed uit te leggen wat ik nou de laatste jaren heb gedaan.

Lieve Sigrid, jij bent er voor me geweest vanaf het begin van mijn PhD tot nu, de laatste loodjes. Ik was niet altijd even gezellig met vaak werken in de weekenden en nu het vele schrijven, maar jij hebt me altijd gesteund. Onze supergave vakanties waren voor mij ook altijd een moment van rust, weg van het onderzoek. Ik hoop dat we nog veel avonturen mogen beleven samen. Ontzettend bedankt voor al je geduld en alles wat je voor me hebt gedaan. Ik houd van je!

-The day I met you, my world became a little brighter-



